

**Titre:** Porcine Spine Finite Element Model of Progressive Experimental Scoliosis and Assessment of a New Dual-Epiphyseal Growth Modulating Implant  
**Title:**

**Auteur:** Bahe Hachem  
**Author:**

**Date:** 2016

**Type:** Mémoire ou thèse / Dissertation or Thesis

**Référence:** Hachem, B. (2016). Porcine Spine Finite Element Model of Progressive Experimental Scoliosis and Assessment of a New Dual-Epiphyseal Growth Modulating Implant [Thèse de doctorat, École Polytechnique de Montréal]. PolyPublie. <https://publications.polymtl.ca/2122/>  
**Citation:**

 **Document en libre accès dans PolyPublie**  
Open Access document in PolyPublie

**URL de PolyPublie:** <https://publications.polymtl.ca/2122/>  
**PolyPublie URL:**

**Directeurs de recherche:** Carl-Éric Aubin, & Stefan Parent  
**Advisors:**

**Programme:** Génie biomédical  
**Program:**

UNIVERSITÉ DE MONTRÉAL

PORCINE SPINE FINITE ELEMENT MODEL OF PROGRESSIVE EXPERIMENTAL  
SCOLIOSIS AND ASSESSMENT OF A NEW DUAL-EPIPHYSEAL GROWTH  
MODULATING IMPLANT

BAHE HACHEM

INSTITUT DE GÉNIE BIOMÉDICAL  
ÉCOLE POLYTECHNIQUE DE MONTRÉAL

THÈSE PRÉSENTÉE EN VUE DE L'OBTENTION  
DU DIPLÔME DE PHILOSOPHIAE DOCTOR  
(GÉNIE BIOMÉDICAL)

AVRIL 2016

© Bahe Hachem, 2016.



UNIVERSITÉ DE MONTRÉAL

ÉCOLE POLYTECHNIQUE DE MONTRÉAL

Cette thèse intitulée:

PORCINE SPINE FINITE ELEMENT MODEL OF PROGRESSIVE EXPERIMENTAL  
SCOLIOSIS AND ASSESSMENT OF A NEW DUAL-EPIPHYSEAL GROWTH  
MODULATING IMPLANT

présentée par : HACHEM Bahe

en vue de l'obtention du diplôme de : Philosophiae Doctor

a été dûment acceptée par le jury d'examen constitué de :

Mme VILLEMURE Isabelle, Ph. D., présidente

M. AUBIN Carl-Éric, Ph. D., membre et directeur de recherche

M. PARENT Stefan, M. D., Ph. D., membre et codirecteur de recherche

M. YAHIA L'Hocine, Ph. D., membre

Mme LAFAGE Virginie, Ph. D., membre externe

## ACKNOWLEDGEMENTS

I would like to give my special and sincere thanks to Dr. Carl-Eric Aubin, my research director. Dr. Aubin's passion for research, his scientific rigour, and his extended expertise were crucial factors for supporting and guiding this thesis project. As a great mentor, he has guided me throughout this work both on a scientific, professional, and personal level, shaping me as a researcher. Dr. Aubin never hesitated to take time from his busy schedule to discuss future career avenues and encouraged knowledge acquisition both on an intellectual and practical basis.

I would also like to express my gratitude to Dr. Parent, my research co-director, for his continued support. Dr. Parent has ensured our engineering concepts and applications posed no health complications by suggesting perceptive and fresh recommendations. He truly believed in our proposed project and assured its successful completion. I would like to thank the members of my MEDITIS advisory committee, Drs Isabelle Villemure and Yvan Petit, for their precious and constructive counseling. I thank Brian Murrell, John Coleman, and Jeremy Rawlinson for their warm reception during my MEDITIS internship at Medtronic Spine and Biologics, Memphis, TN. Moreover, Dr. Rawlinson's continued contribution and constructive input were imperative to this doctoral project.

I would like to also thank the animal care unit, namely, Denise Carrier, Sonya L'Espérance, and Véronique Pellerin, and Michael Cademartori for his continued technical support. I would like to acknowledge the contribution of Dr. Aurélie Benoit, Vivane Lalande, and Dr. Irène Londono for aiding me in the difficult experimental stages of this project.

To all my lab colleagues, notably Rohan-Jean Bianco, Franck Le Navéaux, Juan Henao (the MEDITIS warriors) thank you for your continued support, constructive discussions, and cherished memories, and Mark Driscoll and Julien Clin, my mentors and idols. Most importantly, I thank my wife Anna for encouraging me to pursue my path as a biomedical engineer and for her unconditional support as of day one of this constructive journey.

Finally, I would like to thank the Natural Sciences and Engineering Research Council of Canada, Medtronic of Canada, and MEDITIS training program for their financial support and for allowing realization of this research work.

## RÉSUMÉ

La scoliose est une déformation tridimensionnelle de la colonne vertébrale dont l'étiologie reste encore à élucider. Il est généralement admis que la progression de la déformation scoliotique pédiatrique est liée au principe d'Hueter-Volkman qui stipule une réduction de la croissance suite à des contraintes en compression excessives au niveau de la concavité de la courbure scoliotique vs. sa convexité. Les stratégies de traitement des courbures sont difficiles, surtout chez les jeunes enfants. Typiquement, une intervention chirurgicale avec une instrumentation rachidienne accompagnée d'une arthrodèse segmentaire est nécessaire pour des courbures progressant au-delà de 40° d'angle de Cobb.

De nouveaux dispositifs visent à manipuler la croissance vertébrale en exploitant le principe d'Hueter-Volkman pour contrôler la progression de et corriger la courbure. Ces implants sans fusion exploitent la croissance vertébrale résiduelle en manipulant des gradients de croissance pour localement inverser la cunéiformisation vertébrale et, au fil du temps, réaligner la colonne vertébrale globalement. Des essais cliniques ont démontré une correction prometteuse pour les courbures généralement inférieures à 45°; cependant, les dispositifs actuels chevauchent l'espace du disque intervertébral et le compriment augmentant les risques de dégénérescence du disque à long terme. Par ailleurs, les implants nouvellement conçus sont généralement testés en utilisant des modèles animaux équivalents pour évaluer leur efficacité à corriger des déformations par l'intermédiaire de l'approche inverse (création d'une déformation) ou l'approche à 2-étapes (création d'une déformation suivie d'une correction). Néanmoins, une plate-forme de conception efficace est nécessaire pour évaluer la manipulation de la croissance à court et long termes par de nouveaux implants et de raccourcir le transfert de connaissances vers des applications cliniques.

L'objectif général de cette thèse était de développer et de vérifier un modèle par éléments finis porcin (MEFp) unique en tant qu'une plateforme alternative pour la simulation de scolioses expérimentales progressives et des implants sans fusion, et d'évaluer un nouvel implant double-épiphysaire local ne chevauchant pas l'espace du disque sur des porcs immatures. Ainsi, les objectifs spécifiques suivants ont été complétés : 1) développer et

vérifier un MEFp du rachis et de la cage thoracique, 2) développer et tester, in vivo, un implant double-épiphytaire incluant un mécanisme d'expansion spécifique, 3) exploiter le MEFp pour investiguer les différences entre les approches inverse et à 2-étapes couramment utilisés pour tester les nouveaux implants sans fusion, 4) exploiter le MEFp pour évaluer la contribution biomécanique de la cage thoracique et son rôle dans l'instrumentation sans fusion.

Dans le contexte de cette thèse, les objectifs spécifiques ont été proposés pour vérifier les hypothèses de recherche suivantes : 1) un modèle par éléments finis de la colonne vertébrale porcine, incluant la croissance épiphysaire et la cage thoracique, peut représenter le comportement biomécanique et la modulation de la croissance des implants sans fusion avec un angle de Cobb simulé à moins de 5°, une cunéiformisation vertébrale à moins de 2°, et une rotation axiale apicale à moins de 3° de leurs valeurs réelles, 2) moduler la croissance des plaques épiphysaires supérieures et inférieures simultanément avec un implant local ne chevauchant pas l'espace du disque intervertébral peut augmenter, d'au moins deux fois, l'angle de Cobb progressif et la cunéiformisation vertébrale comparé à une instrumentation locale sur une seule plaque 3) l'impact des implants sans fusion en chirurgie expérimentale est moins important par l'intermédiaire de l'approche à 2-étapes comparé à l'approche inverse, 4) la contribution biomécanique de la cage thoracique se manifeste par une augmentation de la rigidité thoracique menant à une réduction de l'impact des implants sans fusion suite à un changement dans la distribution des contraintes sur les plaques de croissance.

Un modèle par éléments finis paramétrique de la colonne vertébrale osséo-ligamentaire et de la cage thoracique porcine a été développé en utilisant des données morphométriques publiées et mesurées à l'interne. Une charge de type "Follower Load" a reproduit les forces physiologiques et la gravité. La croissance vertébrale et sa modulation ont été programmées selon le principe de Hueter-Volkman, stipulant une réduction/augmentation de la croissance suite à un accroissement/réduction des contraintes en compression. Un modèle in vivo porcin bien-établi a été simulé pour vérifier la reproduction de scoliose progressive. Ainsi, la création d'une déformation suite à l'insertion d'un ligament postérieur longitudinal (8 niveaux) combiné avec un tethering ipsi-latéral des côtes (5 niveaux) a été simulé sur 10 semaines de croissance.

Subséquentement, une correction via un tether installé latéralement sur la vertèbre apicale  $\pm 2$  niveaux et visant à corriger l'aspect tridimensionnel de la courbure a été simulé sur 20 semaines supplémentaires. Une étape de vérification supplémentaire a été effectuée en simulant l'induction d'une déformation par un « hemi-staple » et une agrafe rigide sur 12 et 8 semaines, respectivement. L'angle de Cobb simulé, la cunéiformisation vertébrale, et la rotation axiale étaient à moins de  $5^\circ$ ,  $2^\circ$ , et  $3^\circ$  de leurs valeurs réelles, respectivement. De plus, les simulations comparatives ont démontré que l'approche à 2 étapes était la mieux adaptée pour évaluer les nouveaux implants sans fusion puisque le comportement biomécanique de la colonne vertébrale déformée imitait les comportements attendus d'une colonne scoliotique sous instrumentation sans fusion. En outre, les simulations comparatives ont également montré l'importante contribution biomécanique de la cage thoracique en chirurgie sans fusion puisqu'elle augmente la rigidité de la région thoracique, et donc son omission en simulation numérique entraîne une exagération des contraintes au niveau des plaques de croissance, et par la suite une augmentation de l'effet à long-terme de l'implant simulé.

Suite à une revue de la littérature et des essais numériques effectués sur le MEFp, un nouveau dispositif sans fusion a été conçu à partir d'un implant épiphysaire breveté au sein de notre équipe. Il s'agit d'une agrafe double-épiphysaire, qui agit localement sur les plaques de croissance épiphysaires proximales et distales sans chevaucher l'espace du disque intervertébral. L'implant se compose de deux parties distinctes, une pièce supérieure et une inférieure, tenues ensemble par un outil et un mécanisme d'expansion spécialisé, permettant de régler la hauteur de l'implant en intra-opératoire pour satisfaire des morphologies vertébrales diverses.

Un essai expérimental *in vivo* a été réalisé en utilisant 7 porcs femelles immatures (instrumentées) et 4 porcs contrôles. Le dispositif a été inséré localement sur les vertèbres T7-T9. La croissance vertébrale et les changements subis par la colonne vertébrale ont été suivis pendant 3 mois. Des radiographies mensuelles ont été acquises pour évaluer la courbure induite, la cunéiformisation vertébrale et la différence de hauteur vertébrale entre les côtés concave/convexe. L'angle de Cobb final mesuré entre T7-T9 était de  $25.0^\circ \pm 4.2^\circ$  avec aucun changement significatif dans le plan sagittal. La cunéiformisation vertébrale ( $18.2^\circ \pm 2.7^\circ$ ) a été constamment plus élevée à T9, avec  $45.4^\circ$  de

cunéiformisation vertébrale cumulative, démontrant un phénomène de cunéiformisation discale inverse. Un arrêt de la croissance complet a été atteint avec une différence de hauteur vertébrale de  $3.9 \pm 1.0$  mm, moins importante du côté de l'implant. Les indices cliniques mesurés étaient significativement plus élevés que leurs équivalents contrôles, à l'exception de l'angle sagittal. En outre, des échantillons de régions instrumentées ont été acquis pour l'imagerie  $\mu$ -CT. Des observations préliminaires des coupes  $\mu$ -CT ont indiqué une perte d'os du côté de l'instrumentation dans 3/7 cas suggérant un phénomène de "stress-shielding" de l'os sous-jacent l'implant et la présence de croissance périphérique des vertèbres. Des analyses complémentaires sont nécessaires pour confirmer ces observations.

Suite à ce travail de thèse, plusieurs aspects peuvent être mis en évidence pour l'avancement de chirurgies expérimentales et des implants sans fusion. Le MEFp unique était capable de simuler la scoliose progressive d'un modèle de scoliose *in vivo* bien établi, a reproduit l'effet sur la croissance de deux implants sans fusion, a souligné l'importante différence entre les approches inverses et à 2 étapes utilisées pour les essais expérimentaux des implants sans fusion, et a souligné la contribution biomécanique de la cage thoracique en chirurgie sans fusion. Le modèle développé pourra être exploité pour simuler différentes approches de création d'un modèle de scoliose progressive. Finalement, le nouveau modèle par éléments finis porcine a établi une plateforme alternative pour concevoir et tester de nouveaux implants manipulant la croissance vertébrale avant de procéder à des essais expérimentaux finaux et le transfert des connaissances acquises à des applications cliniques humaines. Enfin, l'agrafe double-épiphysaire a démontré des résultats expérimentaux prometteurs, pouvant être transférés pour le traitement de la scoliose dans une colonne en pleine croissance. En outre, l'analyse histologique permettra de vérifier l'état de santé du disque et de la sécurité en vue d'une application future chez les humains.

## ABSTRACT

Scoliosis is a complex three-dimensional deformity of the spine whose etiology is yet to be elucidated. The pathomechanism of scoliosis progression is believed to be linked to the Hueter-Volkman principle, by which growth is reduced due to increased growth plate compression, with the inverse also valid. Treatment strategies are challenging, especially in young children. Curves progressing beyond 40° Cobb angle are typically treated via invasive surgical interventions requiring spinal instrumentation accompanied by segmental spinal arthrodesis, impairing spinal mobility.

New devices aim at manipulating vertebral growth by exploiting the Hueter-Volkman principle to control curvature progression. These fusionless implants harness remaining vertebral growth by manipulating growth gradients to reverse vertebral wedging locally and, over time, globally realign the spine. Clinical trials have demonstrated promising deformity correction for curves generally below 45°; however, current devices bridge the intervertebral disc gap and predominantly compress the disc increasing the risks of long-term disc degeneration. Moreover, in a time-consuming manner, newly designed implants are commonly tested using equivalent animal models to assess their efficacy in correcting spinal deformities via the inverse (creation of a deformity) or the 2-step approaches (creation of a deformity followed by its subsequent correction). Nevertheless, a solid design platform is required to evaluate the short- and long-term growth manipulating efficacy of new implant designs and shorten knowledge transfer to clinical applications.

The general objective of this thesis was to develop and verify a unique porcine spine finite element model (pFEM) as an alternative testing platform for the simulation of progressive experimental scoliosis and fusionless implants, and assess a new localized dual-epiphyseal implant on immature pigs. Thus, specific objectives were devised as follows: 1) develop and verify a distinctive pFEM of the spine and ribcage, 2) develop and test, *in vivo*, a dual-epiphyseal implant incorporating a custom expansion mechanism, 3) exploit the developed pFEM to investigate differences between the inverse and 2-step fusionless implant testing approaches, and 4) exploit the pFEM to evaluate the biomechanical contribution of the ribcage in fusionless scoliosis surgery.



In the context of this thesis, the objectives were devised to verify the following hypotheses:

1) a porcine spine finite element model, including the ribcage and epiphyseal growth dynamics, can represent the appropriate biomechanical behaviour and growth modulating effect of fusionless implants with simulated Cobb angle within  $5^{\circ}$ , vertebral wedging within  $2^{\circ}$ , and vertebral rotation within  $3^{\circ}$  of their measured values, 2) modulating the growth of the superior and inferior epiphyseal plates, simultaneously via a local implant which does not bridge the intervertebral disc space, can increase, by at least two folds, progressive Cobb angle and vertebral wedging compared to single growth plate alteration, 3) the growth modulating impact of fusionless implants is less prominent via the 2-step versus the inverse experimental approaches, 4) the biomechanical contribution of the ribcage is manifested by an increase in thoracic rigidity leading to a reduction in the impact of fusionless implants following a change in growth plate stress distribution.

A parametric finite element model of an osseo-ligamentous porcine spine and ribcage was developed using published and in-house morphometric measurements. Physiological forces and gravitational loads were replicated using a follower type load. Vertebral growth and its modulation were modeled at the epiphyseal growth plates. Growth behaviour was governed by the Hueter-Volkman principle to address changes in epiphyseal growth in response to compressive stresses. An established porcine scoliosis *in vivo* model was simulated to verify replication of progressive scoliosis. As such, scoliosis induction was simulated via a posterior longitudinal tether and 5-level ipsi-lateral rib tethering over 10 weeks of growth. Subsequently, curve correction was simulated over 20 weeks using a custom anterior tether aiming at correcting the 3D aspect of the induced deformity, as previously reported experimentally. An additional verification step was performed by simulating induced deformities using a hemi- and rigid staples, over 12 and 8 weeks, respectively. Simulated Cobb angle, apical vertebral wedging, and apical vertebral rotation were within  $5^{\circ}$ ,  $2^{\circ}$ , and  $3^{\circ}$ , respectively, for the progressive curve, its correction, and the simulated implants. Further investigational simulations demonstrated the 2-step approach was best suited to assess new fusionless implants as the biomechanical environment of the spine mimicked, as closely as possible, expected behaviours in deformed spines for progressive scoliosis treatment. Moreover, comparative simulations also showed the important biomechanical contribution of the ribcage in fusionless surgery

as it increases the rigidity in the thoracic region, the lack of which resulted in exaggerated simulated implant influence.

Following extensive simulations and a detailed literature review, an existing patented fusionless device was revised and features added, resulting a dual-epiphyseal staple, which acted locally on the proximal and distal epiphyseal growth plates without spanning the disc space. The implant consisted of separate parts, an upper and a lower piece, held together by a custom tool and expansion mechanism, which allowed for intra-operative implant height adjustment for various vertebral morphologies.

An *in vivo* animal trial was conducted using 7 instrumented healthy immature female pigs with 4 age-matched controls. The device was inserted locally over T7-T9 vertebrae and vertebral growth and spinal changes were followed over 3 months. Monthly radiographs were acquired to evaluate induced spinal deformities, vertebral wedging, and concave/convex vertebral body height differences. Final induced instrumented Cobb angle was  $25.0^{\circ} \pm 4.2^{\circ}$  with no significant changes in the sagittal plane. Vertebral wedging ( $18.2^{\circ} \pm 2.7^{\circ}$ ) was consistently highest at T9, with  $45.4^{\circ}$  cumulative vertebral wedging, evidence of reversed disc wedging phenomenon. Full growth restraint was achieved with  $3.9 \pm 1.0$  mm vertebral height shorter ipsi-lateral to the device. Measured indices were significantly higher than normal counterparts, except for sagittal angles. Moreover, instrumented region samples were harvested for  $\mu$ -CT imaging. Preliminary  $\mu$ -CT observations have indicated bone loss at instrumentation site in 3/7 cases suggesting the implant stress shielded the underlying bone with the presence of peripheral vertebral growth. Further analysis is required for conclusive affirmation.

Upon completion of this thesis work, several aspects can be highlighted towards the future advancement of fusionless devices and experimental surgery. The unique pFEM was capable of simulating progressive scoliosis via a well-established *in vivo* scoliosis model, reproduced the growth modulation of two distinct fusionless implants, highlighted important differences between the inverse and 2-steps fusionless implants testing approaches, and outlined the important biomechanical contribution of the ribcage in fusionless surgery. The developed model can be used to simulate different scoliosis progressive models. This novel porcine spine finite element model established an

alternative design and testing platform for newly conceived growth-sparing implants prior to proceeding to final experimental testing and transferring acquired understandings to human clinical applications. Finally, the devised dual-epiphyseal implant demonstrated promising experimental results, which may be translated for the treatment of scoliosis in the growing spine. Further histological analyses are necessary to verify maintained disc health and support the safety of its future application on human spines.

## TABLE OF CONTENTS

ACKNOWLEDGEMENTS .....	III
RÉSUMÉ.....	V
ABSTRACT .....	IX
TABLE OF CONTENTS.....	XIII
LIST OF TABLES .....	XVI
LIST OF FIGURES .....	XVII
LIST OF SYMBOLS AND ABBREVIATIONS .....	XXIV
LIST OF APPENDICES.....	XXVI
INTRODUCTION .....	1
CHAPTER 1      LITERATURE REVIEW .....	4
1.1      ANATOMY OF THE HUMAN SPINE .....	4
1.1.1    Vertebrae.....	5
1.1.2    Intervertebral discs.....	7
1.1.3    Ligaments .....	8
1.1.4    Ribcage .....	9
1.1.5    Porcine Spine and Thorax Anatomy .....	10
1.2      BIOMECHANICS OF THE SPINE .....	15
1.2.1    Spinal Loads .....	15
1.2.2    Spinal Motion .....	19
1.3      PHYSIOLOGY OF BONE TISSUE.....	25
1.3.1    Composition of bone and cartilage tissue .....	25
1.3.2    Epiphyseal Growth Plate.....	26
1.3.3    Bone Growth .....	27
1.3.4    Growth Modulation .....	30
1.4      SCOLIOSIS .....	34
1.4.1    Scoliosis pathogenesis and pathomechanism .....	36
1.4.2    Treatment.....	38
1.4.3    Fusionless devices.....	41

1.5	BIOMECHANICAL MODELING OF THE SCOLIOTIC SPINE .....	55
1.5.1	Finite Element Modeling .....	56
CHAPTER 2	RESEARCH RATIONAL, OBJECTIVES, AND HYPOTHESES .....	62
CHAPTER 3	IN VIVO ASSESSEMENT OF A DUAL-EPIPHYSEAL IMPLANT .....	66
3.1	PRESENTATION OF THE DUAL-EPIPHYSEAL IMPLANT .....	66
3.2	ARTICLE 1 : LOCAL EPIPHYSEAL GROWTH MODULATION FOR THE EARLY TREATMENT OF PROGRESSIVE SCOLIOSIS: EXPERIMENTAL VALIDATION USING A PORCINE MODEL .....	72
3.2.1	Introduction .....	76
3.2.2	Material and Methods .....	77
3.2.3	Results .....	80
3.2.4	Discussion .....	81
3.2.5	Conclusion .....	84
3.2.6	References .....	84
3.3	ADDITIONAL EX-VIVO OBSERVATIONS AND PROSPECTIVE ANALYSES OF THE INSTRUMENTED VERTEBRAE .....	91
3.3.1	$\mu$ -CT investigation .....	92
CHAPTER 4	FINITE ELEMENT MODEL FOR THE SIMULATION OF PROGRESSIVE EXPERIMENTAL SCOLIOSIS .....	97
4.1	FRAMEWORK OF THE SECOND ARTICLE .....	97
4.2	ARTICLE 2: PORCINE SPINE FINITE ELEMENT MODEL: A COMPLEMENTARY TOOL TO EXPERIMENTAL SCOLIOSIS FUSIONLESS INSTRUMENTATION .....	98
4.2.1	Introduction .....	99
4.2.2	Methods .....	101
4.2.3	Results .....	103
4.2.4	Discussion .....	104
4.2.5	References .....	107
4.3	ADDITIONAL DETAILS: MODEL'S CALIBRATION AND VERIFICATION/VALIDATION .....	114
4.4	INVERSE VS 2-STEP EXPERIMENTAL APPROACHES: A NUMERICAL INVESTIGATION .....	116
4.4.1	Introduction .....	116
4.4.2	Methodology .....	116
4.4.3	Results .....	119
CHAPTER 5	BIOMECHANICAL STUDY OF THE ROLE OF RIBCAGE .....	124

5.1	INTRODUCTION .....	124
5.2	METHODOLOGY .....	124
5.3	RESULTS .....	126
CHAPTER 6	GENERAL DISCUSSION .....	130
CHAPTER 7	CONCLUSION AND RECOMMENDATIONS .....	143
BIBLIOGRAPHY.....		146
APPENDICES.....		172

## LIST OF TABLES

Table 1-1: Anatomical differences between humans and pigs .....	11
Table 1-2: Differences between the porcine and human ribcage anatomy .....	12
Table 1-3: Conventional scoliosis treatment strategies .....	39
Table 1-4: Summary of experimental fusionless implant testing and development of animal scoliosis models .....	51
Table 1-5: Summary of current finite elements models in scoliosis research .....	57
Table 3-1: $\mu$ -CT qualitative observations.....	94
Table 4-1: Reported and calibrated mechanical properties attributed to the different spinal anatomical structures .....	110

## LIST OF FIGURES

Figure 0-1 : Outline of the thesis .....	3
Figure 1-1 Spinal column. From left to right: Antero-Posterior, Postero-Anterior, and Lateral views (Wikimedia commons).....	5
Figure 1-2: Thoracic Vertebrae depicting the body and posterior bony structures (Left: Lateral View, Right: Top View) (Modified from [2]).....	6
Figure 1-3: Cross-sectional view of a lumbar spine illustrating the cortical shell and cancellous bone interior (Adopted from [2]) .....	6
Figure 1-4: The intervertebral disc depicting the nucleus pulposus and annulus fibrosis (top). The lamellated structure of the annulus is shown with intermittent fibres orientation between layers allowing a spring-damper response as the disc is compressed by physiological loading as the nucleus forces itself on the annular lamellae (lower-right figure) (Modified from [5]). .....	8
Figure 1-5: Six major spinal ligaments. The intertransverse ligament is not shown; it spans between the transverse processes of adjacent vertebrae (Modified from [2]) .....	9
Figure 1-6: The Ribcage and intercostal ligaments (Modified from [2]).....	10
Figure 1-7: Difference between swine and human thoracic vertebrae (Modified from [13]) .....	11
Figure 1-8: Skeleton of a pig showing the ribcage. 14 pairs of ribs articulate from T1 to T15 (Modified from [14] and [15]).....	12
Figure 1-9: Porcine T2 (left) showing the subchondral bone and growth plate, similar to the human epiphysis in long bones (right) (Modified from [13] and [2]) .....	13
Figure 1-10: L3-L4 intradiscal pressure variation as a function of posture when compared to standing (Modified from [31]) .....	16
Figure 1-11: Graphical representation of the correlation between body weight and spinal segmental loading as developed by [32].....	17



Figure 1-12: a) Ventrally directed gravitational force vectors in quadrupeds, b) Dorsal and Ventral muscle co-activation to stabilize the spine in the sagittal plane (Modified from [43]) .....	18
Figure 1-13: Shear vector direction in the loaded quadruped and primates (A) and human (B) spines (Modified from [44]) .....	19
Figure 1-14: Vertebral translations and rotations. Along the x-axis: antero-posterior translation and lateral left/right bending, along y-axis: medio-lateral translation and Flex./Ext., and along z-axis: proximo-distal translation and axial rotation. ....	20
Figure 1-15: Segmental flexion/extension, lateral bending, and axial rotation along the human spine (obtained and modified on 01-03-2016 from <a href="http://wings.buffalo.edu/academic/departement/eng/mae/courses/417-517/Orthopaedic%20Biomechanics/Lecture%2012.pdf">http://wings.buffalo.edu/academic/departement/eng/mae/courses/417-517/Orthopaedic%20Biomechanics/Lecture%2012.pdf</a> ).....	21
Figure 1-16: Facet joint orientation in the thoracic and lumbar regions and their functional contribution to axial rotation .....	21
Figure 1-17: Coupled spinal motion (Modified from [55]) .....	23
Figure 1-18: Porcine spine segmental range of motion for the cervical, thoracic, and lumbar regions (Modified from [56]) .....	24
Figure 1-19: Macroscopic composition of bone (Obtained from: <a href="http://www.training.seer.cancer.gov/anatomy/skeletal/tissue.html">http://www.training.seer.cancer.gov/anatomy/skeletal/tissue.html</a> on 08/01/2016). ..	26
Figure 1-20: Vertebral epiphyseal growth plate and its zonal divisions: the reserve, proliferative, and hypertrophic zones (obtained from <a href="http://www.nzdl.org/gsdl/collect/ccgi/archives/HASHee86.dir/p133.jpg">http://www.nzdl.org/gsdl/collect/ccgi/archives/HASHee86.dir/p133.jpg</a> on 03-01-2016) .....	27
Figure 1-21: Appositional (Left) and endochondral (right) growth. Arrows indicate growth direction and wavy lines illustrate ossification centers (Modified from [4]).....	28
Figure 1-22: Pig growth as a function of age (Adopted from [75]).....	30
Figure 1-23: Growth rate alterations as a function of applied load on vertebral growth plates of various species (Modified from [74]).....	32

Figure 1-24: Chondral growth force response curve (Modified from [92]).....	34
Figure 1-25: Scoliosis viewed from the back and Cobb angle measurement (Modified from: <a href="http://www.kwikfit4u.com/wp-content/uploads/2014/07/scoliosis.jpg">http://www.kwikfit4u.com/wp-content/uploads/2014/07/scoliosis.jpg</a> on 02/10/2015) .....	35
Figure 1-26: Transvers view of the trunk illustrating the differences between normal and scoliotic spines ( <a href="http://rad.washington.edu/about-us/academic-sections/musculoskeletal-radiology/teaching-materials/online-musculoskeletal-radiology-book/scoliosis/">http://rad.washington.edu/about-us/academic-sections/musculoskeletal-radiology/teaching-materials/online-musculoskeletal-radiology-book/scoliosis/</a> on 01/03/2016 (Left) and [96] (Right)).....	36
Figure 1-27: Vicious cycle for scoliosis progression pathomechanism .....	38
Figure 1-28: Patient treated with a standard brace (Modified from [146]) .....	40
Figure 1-29: Before (left) and after (right) radiograph examples of spinal instrumentation .....	41
Figure 1-30: Compression-based fusionless implant's cycle of deformity correction .....	41
Figure 1-31: Radiographic examples of: 1- Growing rods, 2- Magnetic growing rod, 3- VEPTR, 4- Shilla, 5- modern Luque trolley (1 to 4 modified from [159], 5 modified from [163]).....	43
Figure 1-32: ApiFix system (left) insert on the concavity of the apical region. Daily exercise for system elongation via a ratchet system (Modified from [164]) .....	43
Figure 1-33: Shape memory alloy staples clinical example (Modified from [152], [153])	44
Figure 1-34: Vertebral body tether: Postero-Anterior view (left), lateral view (right) (Modified from [168]) .....	46
Figure 1-35: Custom stainless steal staple and bone screw fixation (Modified from [181]) .....	47
Figure 1-36: Bovine thoracic vertebral stainless steel cable tethering (Modified from [183]) .....	49
Figure 1-37: Hemi-staple design. Fluoroscopy images of excised thoracic spine after 3-months curve induction on immature pigs (Modified from [190]) .....	51

Figure 1-38: Hybrid anterior tether aiming at correcting rotational deformity (Modified from [76]) .....	54
Figure 1-39: Hinged implant design aiming at correcting all three anatomical planes as the spine grows (Modified from [195]) .....	54
Figure 2-1: Methodology diagram and related manuscripts and chapters .....	65
Figure 3-1: Concept Dual-Epiphyseal implant: Growth modulation over time. Superior vertebral wedging corrected. ....	67
Figure 3-2: Top and lower implant slots and screw locations for different applications modes. Slots are depicted in Figure 3-1 for each of the implant components. Vertically stacked slots correspond to the top implant component and a single slot corresponds to the bottom implant component. ....	68
Figure 3-3: Hyperelastic material stress-strain curve. Target zone indicates hyperelastic ligament elongation zone for controlled/constant load (Modified from: <a href="http://abaqusdoc.ucalgary.ca/v6.9/books/gsa/default.htm?startat=ch10s06.html">http://abaqusdoc.ucalgary.ca/v6.9/books/gsa/default.htm?startat=ch10s06.html</a> )..	69
Figure 3-4: DUAL-Epiphyseal staple simulations on human and porcine FEMs. Potential correction in human and promising induction in pigs. ....	70
Figure 3-5: Final implant design and surgical steps. ....	70
Figure 3-6: Concept to application. CAD design followed by Sawbones feasibility and <i>in vivo</i> trials .....	71
Figure 3-7: Intraoperative fluoroscopic image of dual-staple insertion site. The implant's height is adjusted intraoperatively while mounted on a custom tool. Two screws are used for implant fixation. ....	87
Figure 3-8: Postoperative postero-anterior radiograph showing implant positioning. ....	88
Figure 3-9: Example of manual left bending under fluoroscopic imaging showing sustained mobility in instrumented and off-instrumented regions when compared to control spines. ....	89
Figure 3-10: Close-up radiographs in the coronal view 1 and 12 weeks postoperative and fluoroscopic image of the excised deformed region at study completion. Progressive	

local and global deformity are evidenced at 12 weeks and post-harvest (at 12 weeks) showing important vertebral coronal wedging at T7, T8, and T9. ....	89
Figure 3-11: Instrumented vs. control temporal coronal T7-T9 regional (a) and T9 vertebral coronal wedging (b) coronal T8-T9 intervertebral disc wedging (c). Results presented as means $\pm$ standard deviation. ....	90
Figure 3-12: Illustration of excised segments and projected study allocation .....	92
Figure 3-13: Mid-coronal CT slices. Top row shows instrumented T7-T9 vertebrae, and bottom row reflects control counterparts. Numbers identify animal tags.....	93
Figure 3-14: Mid-transverse CT slices. Top 3 rows correspond to instrumented T7, T8, and T9 while the bottom row corresponds to control counterparts. Numbers identify animal tags.....	94
Figure 3-15: Instrumented vs. Control transverse CT cuts showing possible signs of restrained bone growth, bone drift phenomenon, and fibrous callus formation. ....	95
Figure 4-1: Parametric porcine spine model featuring the vertebral bodies (T1-T15, L1-L6). a) Lateral and b) postero-Anterior views c) Intervertebral disc nucleus pulposus and annulus fibrosis. D) L6 vertebra and growth plate zonal details.....	110
Figure 4-2: Growth model algorithm. Growth plate stresses are computed after physiological load application. An equivalent growth is the calculated as a function of stress differential. The model's geometry is then updated for clinical indices identification. ....	111
Figure 4-3: Simulated intraoperative posterior and rib tether insertion deformity induction and anterior curve correction (a). The above models (global and apical thoracic vertebra) are at 0w, 10w induction, and 20w after correction. Intercostal ligaments not shown.....	112
Figure 4-4: Cobb angle and vertebral wedging for the hemi-staple (a) [190] and rigid staple (b) [181]. Comparison between simulated and experimental data showing global and local simulated deformity after 3 months (hemi-staple) and 2 months (rigid staple) of growth .....	113

Figure 4-5: Porcine spine finite element model calibration, verification/validation, and predictive assessment as per ASME V&V-40 standards .....	114
Figure 4-6: Diagram showing methodology for comparative simulation between Correction versus induction using 4 implants simulated at the apex $\pm 2$ . The arrows indicate the location of the simulated implants. ....	117
Figure 4-7: Absolute correction and induction of the simulated implants and expected curve progression. Negative values indicate a right convex curve. ....	120
Figure 4-8: Relative curve evolution for correction and induction. Angles are presented as delta change with respect to the initial deformity (Corr.) or non-instrumented spine (Ind.). ....	121
Figure 4-9: Relative apical vertebral wedging evolution for correction and induction. .	122
Figure 4-10: Apical growth plate stresses for the induction (left) and correction (right) for tested implants, viewed from the top. Implants are positioned on the right lateral aspect of the vertebral body. ....	123
Figure 5-1: Illustration of the methodological approach used to assess the biomechanical contributive effect of the ribcage in fusionless surgery. The arrows indicate the location of the simulated implants. ....	125
Figure 5-2: Growth plate stress distributions at the apical vertebra for the induced deformity, viewed from the top. Solid lines correspond to model including the ribcage. A, L, R, and P refer to Anterior, Left, Right, and Posterior respectively. Implants are positioned on the right lateral aspect of the vertebral body. ....	127
Figure 5-3: Growth plate stress distributions at the apical vertebra for deformity correction, viewed from the top. Solid lines correspond to model including the ribcage. A, L, R, and P refer to Anterior, Left, Right, and Posterior respectively. Implants are positioned on the right lateral aspect of the vertebral body. ....	128
Figure 5-4: Cobb angle progression for the induced (left) and corrected (right) deformities. Solid lines correspond to model including the ribcage. Negative values indicate a right convex curve. ....	129

Figure 5-5: Apical vertebral wedging progression for the induced (left) and corrected (right) deformities. Solid lines correspond to model including the ribcage. Negative values indicate wedged vertebrae with shorter vertebral body height to the left. ....	129
Figure A-1: Biology of the growth feedback loop.....	173
Figure B-1 : Current theories of the etiology of scoliosis.....	174
Figure C-1: Schematic of the procedure for biplanar spinal 3D reconstruction.....	178
Figure C-2: Calibration vest and belt for explicit calibration .....	180
Figure D-1: A) Illustration showing extruded regions of interest (Shaded boxes). B) Calcein marker frontlines. C) Hypertrophic columnar and chondrocyte heights. ....	182
Figure E-1: Custom sling design (Left) and actual prototype (Right) .....	185
Figure E-2: Sagittal instrumented region angles for all pigs in the dual-epiphyseal trial .....	186

## LIST OF SYMBOLS AND ABBREVIATIONS

3D	Three Dimensional
AIS	Adolescent idiopathic scoliosis
AVBS	Anterior vertebral body stapling
AVBT	Anterior vertebral body tethering
BW	Body Weight
CAD	Computer-aided design
EMG	Electromyography
EOS	Early onset scoliosis
FEA	Finite element analysis
FEM	Finite element model
pFEM	Porcine finite element model
hFEM	Human finite element model
Hz	Hertz: unit of frequency
<i>in silico</i>	Experiment performed via computer simulation
<i>in situ</i>	Experiment performed in an artificial environment out of organism
<i>in vivo</i>	Experiment performed in living organisms
MEF	Modèle par éléments finis
mg	Milligram
ml	Millilitre
mm	Millimetre
MPa	Mega Pascal ( $\text{kg/m.s}^2$ )
Mx, My, Mz	Moment in x, y, and z in the Cartesian coordinate system
N	Netwons ( $\text{kg.m/s}^2$ )

ng	Nanogram
OPN	Osteopontin
Pa	Pascals ( $\text{kg/m.s}^2$ )
ROM	Range of motion
SIA	Scoliose Idiopathique de l'adolescent
SMA	Shape memory alloy
SS	Stainless steel
Ux, Uy, Uz	Translation in x, y, and z in the Cartesian coordinate system
wrt	With respect to
$\sigma$	Mechanical stress ( $\text{kg/m.s}^2$ )
$\varepsilon$	Mechanical strain
$\Sigma$	Sum of



## LIST OF APPENDICES

APPENDIX A – Skeletal growth feedback loop .....	172
APPENDIX B – Scoliosis etiology .....	174
APPENDIX C – Three dimensional reconstruction of the spine .....	178
APPENDIX D – Histomorphometric observations .....	182
APPENDIX E – Custom sling for standardized radiographs .....	184

## INTRODUCTION

Scoliosis is a complex three dimensional deformity of the spine requiring treatment for progressive cases. The gold standard in treating this disease revolves around spinal bracing of moderate curves while complex instrumentation accompanied by segmental spinal arthrodesis tackles severe cases. The effectiveness of bracing in halting curve progression is still questionable; yet, it remains a mainstream treatment for progressive moderate curves. Spinal instrumentation continues to be amongst the vastly invasive and costly surgeries as it relies on re-aligning the spine with pedicle screws, hooks, and rods accompanied by segmental spinal fusion, invasively reducing spinal mobility. The drawbacks of these conventional treatments set the frameworks for extensive research and development to explore alternative approaches.

Recent interest has shifted towards minimally invasive fusionless adolescent idiopathic scoliosis treatment strategies that harness residual vertebral growth in an attempt to regain normal growth locally and realign the spine globally. By increasing compressive loading on the growth plates on the convex side of the scoliotic curvature, growth can be retarded as stated by the Hueter-Volkman principle. As such, fusionless devices aim at reshaping wedged vertebrae to their normal geometries and, over time, realign the spine while maintaining segmental mobility and axial vertebral growth without resorting to invasive surgery. Over the past decade, several investigations have attempted fusionless scoliosis correction, clinically, using anterior vertebral body tethering or stapling on the convex side of curves. Although promising, the temporal influence of current treatments is still halted by the insufficient solid long-term clinical outcomes. Furthermore, the influence of current clinically approved devices on the intervertebral disc is still question to the speculative long-term effectiveness of these new techniques.

To address these shortcoming and to improve upon the current understanding of the biomechanics of fusionless instrumentation precursory to human clinical applications, animal trials are the foremost *in vivo* testing platforms for new concepts that endeavor to achieve global three-dimensional correction of an otherwise complex deformity. Although a widely effective method for fusionless implants design assessment and long-term growth modulating action, experimental trials can be time and cost consuming, spanning

up to 1 year follow-up with implants often bridging the intervertebral disc, compromising its health over time as speculated by multiple reports. To better evaluate and understand the behavior of these new devices, numerical methods can be utilized in a controlled environment to accelerate the design optimization process, reducing unnecessary experimental procedures for final product *in vivo* testing. Yet, a detailed literature review revealed the lack of a large animal numerical model integrating epiphyseal growth dynamics and programmed growth modulation capable of simulating experimental fusionless surgery and the long-term impact of novel growth sparring-devices. Such model would further facilitate knowledge transfer from experimental trials to human applications.

The overall objective of this doctoral project was to develop, test, and verify a new large animal finite element model, namely porcine FEM including the ribcage and integrated epiphyseal growth dynamics, for the assessment of fusionless implants before proceeding to complex animal experiments. The model was then used to design an improved fusionless implant without compromising the health of the intervertebral disc by acting locally without bridging the intervertebral space, as was shown previously with a device depicting a similar prong design. Additionally, the developed model was exploited to evaluate differences between two mainstream fusionless implant testing strategies, namely the inverse and 2-step approaches, and evaluate the biomechanical contribution of the ribcage in fusionless surgery. To attain the main goal of this study, human and porcine spinal anatomies were reviewed and compared. Furthermore, spinal biomechanics, scoliosis deformity, fusionless treatments, and the various numerical models and techniques in scoliosis research were critically reviewed.

Following an extensive literature review (Chapter 1), the main research hypotheses were outlined along with the appropriate objectives to answer these research questions (Chapter 2, Figure 2-1). Two journal articles were generated following this doctoral project (Chapter 3, Chapter 4) with two other unpublished studies detailed in section 4.3 and Chapter 5 of this dissertation. Finally, the last two chapters summarize a general discussion and a conclusion ending with perspectives and future work. An appendix was included to summarize secondary preliminary observations for future projects.

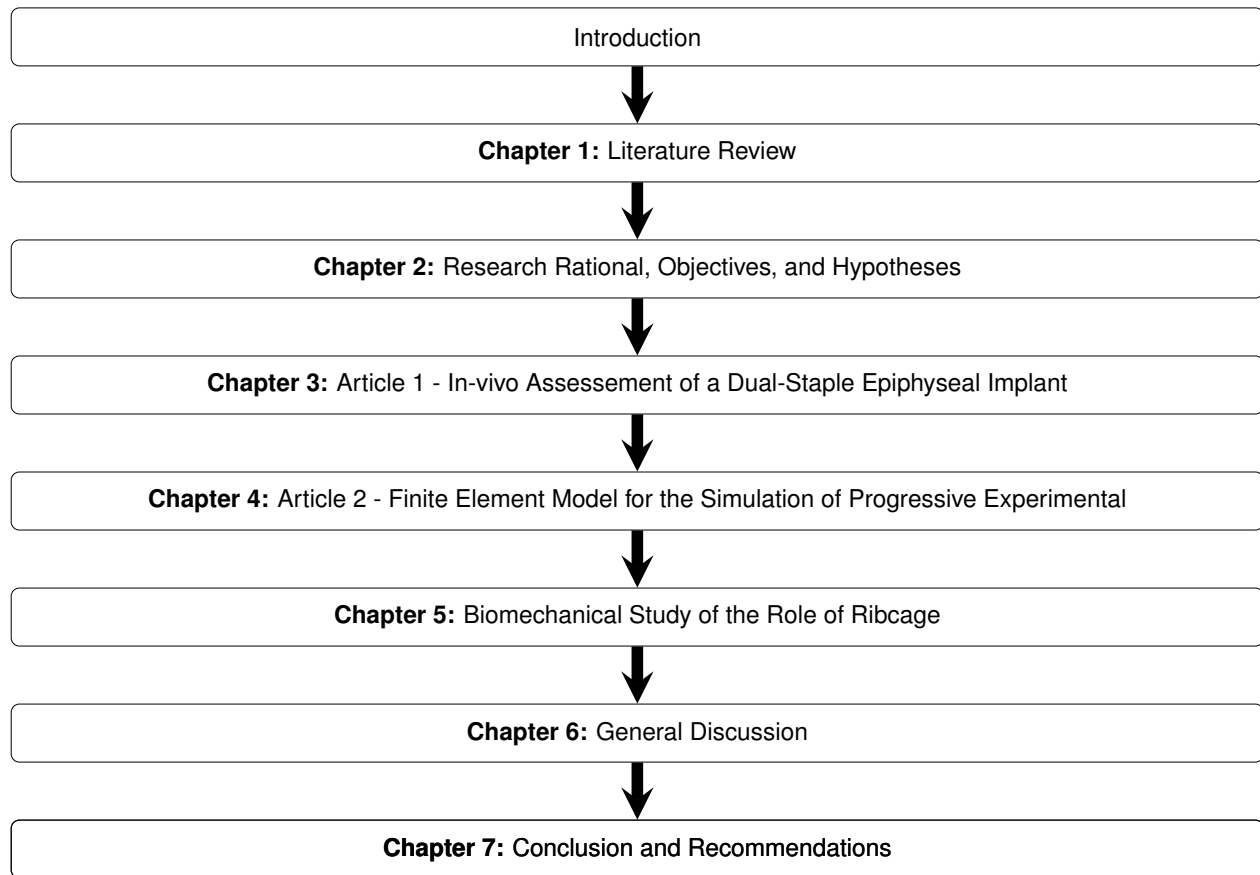


Figure 0-1 : Outline of the thesis

## CHAPTER 1 LITERATURE REVIEW

### 1.1 Anatomy of the Human Spine

The spinal column, like any other part of the musculo-skeletal system, forms the structural support for the body. Its distinct shape is outlined in all three anatomical planes, providing a complex system that houses and protects the spinal cord and the internal organs. This unique shape offers flexibility in all major spinal configurations and motion while incorporating muscle attachment sites for overall stability, load transfer, and resistance to the upper body weight. The spine is a complex system comprised of different elements working in conjunction, offering it its global biomechanical behavior. To understand this behavior, a description of the functional anatomy is imperative.

The proximal portion is the foremost region of the spine and defines the cervical spine composed of seven vertebrae designated as C1-C7 (Figure 1-1). In the sagittal plane, the cervical vertebrae shape an arch convex anteriorly and denoted the cervical lordosis.

The next region of the spine is denoted as the thoracic spine composed of the twelve vertebrae (T1-T12). The ribcage is attached to the thoracic spine at the costal joints and allows the articulation of each rib head with respect to the vertebrae. The thoracic vertebrae form a posteriorly convex curvature in the lateral plane, also known as kyphosis, and is defined from T1 to T12.

The final portion is defined by three regions: the lumbar spine, the sacrum, and the coccyx. The lumbar section consists of 5 vertebrae (L1-L5) and forms a lordotic curve in the sagittal plane, much like the cervical region, ending in a kyphotic curve at the sacrum and coccyx. The latter two regions are composed of fused vertebrae (S1-S5 and Co1-Co4)

In addition, the spine encompasses the intervertebral discs and spinal ligaments. These structures define the intervertebral lateral angular profiles and, along with a group of muscles, serve as support for the vertebrae and stability mechanism for the entire spine.

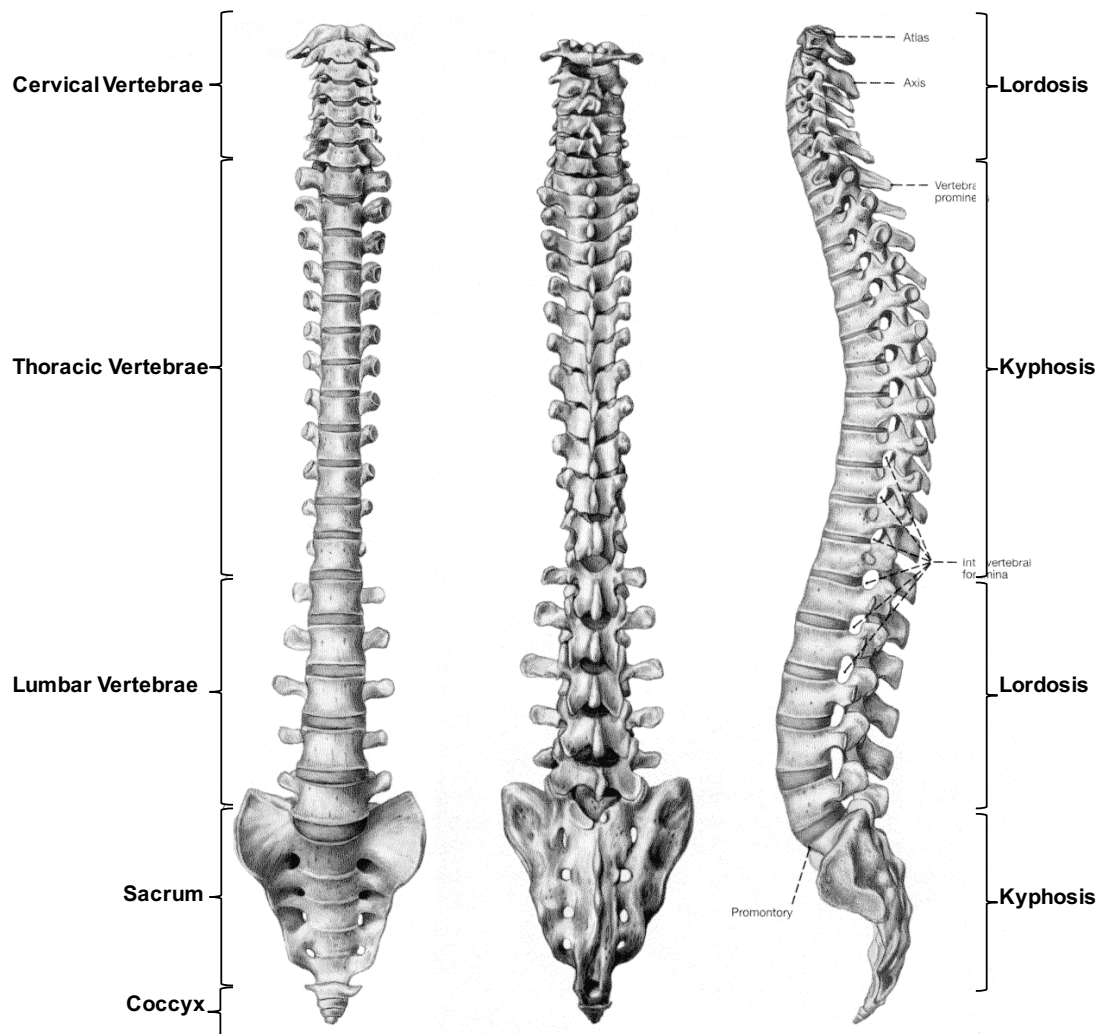


Figure 1-1 Spinal column. From left to right: Antero-Posterior, Postero-Anterior, and Lateral views (Wikimedia commons)

### 1.1.1 Vertebrae

The vertebrae shaping the spine share the same structural anatomy with differences lying within their specific morphology identified in each spinal region. Particular exclusions are held for the atlas and axis as they form the direct transition and connection from the cranium to the remainder of the spine. Each vertebra consists of two main structures (Figure 1-2). The body forms the anterior portion and the arch shapes the posterior structures. The latter is formed of two pedicles, two laminae, and seven processes: two transverse, one spinal, and four articular processes. Confined from both sides by the

pedicles, the spinal canal is formed by the space between the body and the arch. It is circular in shape gradually changing to triangular towards the lumbar region [1].

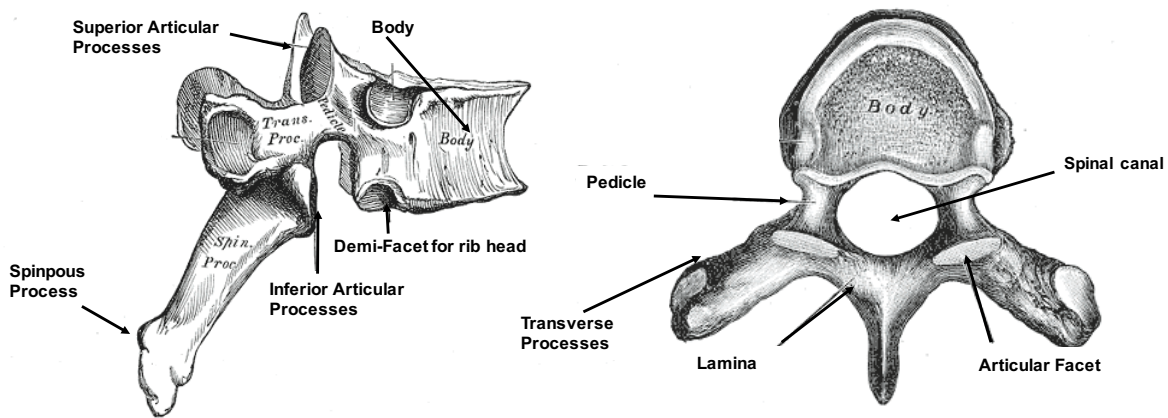


Figure 1-2: Thoracic Vertebrae depicting the body and posterior bony structures (Left: Lateral View, Right: Top View) (Modified from [2])

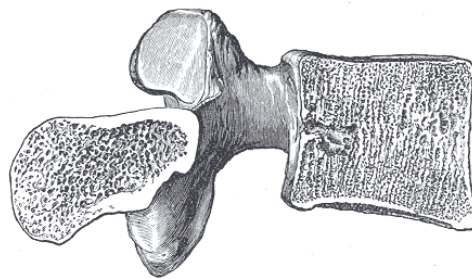


Figure 1-3: Cross-sectional view of a lumbar spine illustrating the cortical shell and cancellous bone interior (Adopted from [2])

The vertebral body forms the largest portion of the vertebra. It is relatively cylindrical in shape with an elliptical cross-section. Its upper and lower surfaces are flat and thick, and provide attachment sites for the intervertebral discs. Viewed from the frontal plane, the body is concave on both sides. It is composed of cancellous bone surrounded by a thin layer of cortical bone of approximately 0.64 mm thickness [3] (Figure 1-3). The cancellous bone, or trabecular bone, is formed of trabeculae oriented ipsi-directional to the main loading vector. Particular to the thoracic vertebrae, the body includes left and right costo-vertebral demi-facets, with the exception of T1, T9, T10, T11, and T12 bodies which possess full facets. Demi-facets are located proximally and distally forming whole facets with adjacent vertebrae permitting full articulation with the corresponding rib head.

The pedicles are thick and short processes projected posteriorly on either sides of the upper part of body. Superiorly and inferiorly, they are curved and form upper and lower notches, which form the intervertebral foramina with adjacent vertebrae. The laminae are posterior projections from the pedicles directed medially, which fuse to form the vertebral foramen from which the spinal process is projected posteriorly. There are two superior and two inferior articular processes with articular surfaces coated with cartilage serving as articular joints with the upper and lower neighboring vertebrae. The transverse processes stem bi-laterally and provide articulation surfaces for the costo-transverse joints in the thoracic region.

### 1.1.2 Intervertebral discs

The intervertebral discs (IVD), also known as the intervertebral fibrocartilages, are composed of two parts: the *annulus fibrosus* (AF) and the *nucleus pulposus* (NP). The IVD is the largest avascular structure of the human body, acts as the load bearing spinal component, and play a role in the spine flexibility and mobility between adjacent segments (functional segments). The IVDs occupy 20-33% of total spine height [4] with varying heights between spinal regions. The thicker anterior aspect provides the cervical and lumbar regions their respective lordotic curvatures [2].

The *nucleus pulposus* is formed of a fine fibrous matrix offering it a soft, gelatinous texture [2] (Nachemson 1960). It is enclosed by the AF and vertebral endplates. The *annulus fibrosus* is a well organized structure with 15 to 25 layers of parallel collagen fibers, also called lamellae, interconnected by a network of elastic fibers [2], [5] and progressively decreasing thicknesses from the inner to the outer annulus. In each lamella, the fibers are oriented at a 30° to 65° angle with the endplates, alternating directions between layers as shown in Figure 1-4. Composed of 70-90% water, proteoglycans, and a network of collagen, the NP exhibits hydrostatic behavior with near incompressibility in a complex interaction with the AF and the vertebral endplates. Briefly, under axial compression, the hydrostatic nucleus forces itself towards the more resistant fibers of the annulus, which stretch due to this increasing pressure, providing a resistive response similar to a “spring-damper” behavior [2], [4], [6] (Figure 1-4). Thus, one of the primary roles of the fibers is to withstand tensile stress under complex loading. The nucleus occupies 30% to 50% of the



cross-sectional area of the IVD [4] and is located slightly posteriorly relative to the entire disc. Being avascular, nutrients are transported to the disc by diffusion through the pores within the upper/lower cartilaginous endplates [7] and by fluid flow mechanisms from the surrounding metabolic solutions [8]. The outer third portion of the annulus is innervated [9], giving rise to low back pain in degenerated discs. Adams *et al.* and Jenson argue that the inherent differences between the anterior and posterior annulus fibrosus explain the predominant subjection of the lumbar region to elevated mechanical stresses [6], [10], [11].

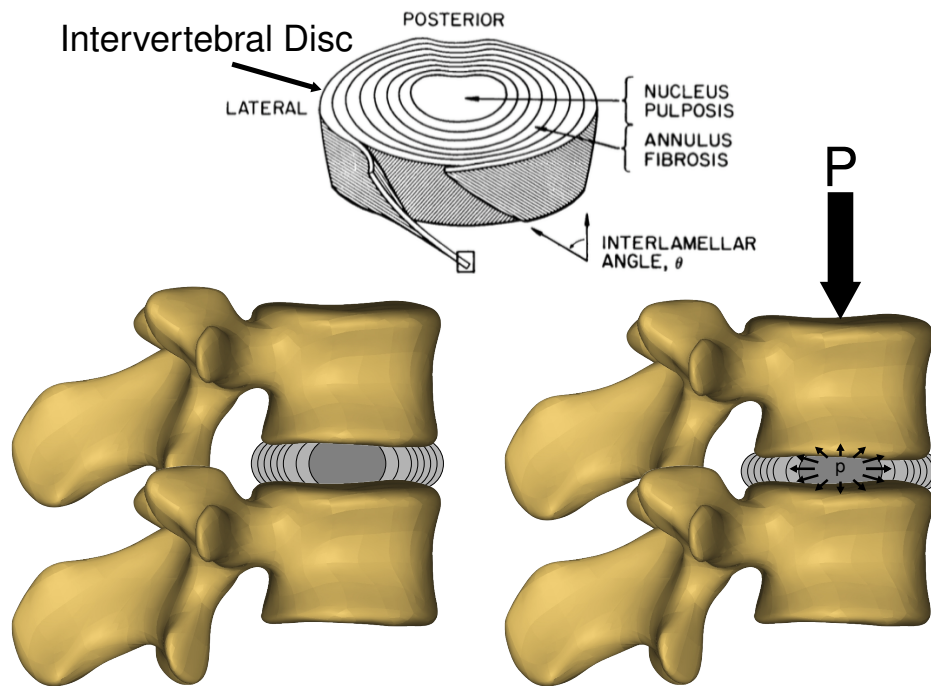


Figure 1-4: The intervertebral disc depicting the nucleus pulposus and annulus fibrosis (top). The lamellated structure of the annulus is shown with intermittent fibres orientation between layers allowing a spring-damper response as the disc is compressed by physiological loading as the nucleus forces itself on the annular lamellae (lower-right figure) (Modified from [5]).

### 1.1.3 Ligaments

Numerous ligaments are found along the spinal column and ribcage (ref. Section 1.1.4) due to their important role in stabilizing the spine when subjected to extensive ranges of motion. Their hyperelastic non-linear behaviour offers an exponential tensional resistance when spinal motion exceeds the neutral (normal) loading regime, as an additional

protection, due to the intrinsic sturdy connectivity of their main component collagen type I fibers. Much like the intervertebral discs, the ligaments acquire their nutrients from the surrounding fluids by diffusion as they lack vascular channels. As such, in cases of unforeseen injuries, ligaments require substantial time for recovery, when the latter is achievable.

Within the spinal column (excluding the ribcage), seven majors ligaments are identified as shown in Figure 1-5: 1- Anterior Longitudinal Ligament, 2- Posterior longitudinal ligament, 3- Ligamentum Flava, 4- Interspinous ligament, 5- Supraspinous ligament, and 6- Capsular ligament which links adjacent articular processes (superior articular process from subjacent vertebra and inferior articular process from superjacent vertebra) via the articular joint. The seventh ligament bundle (intertransverse ligament) spans between the transverse processes of adjacent vertebrae.

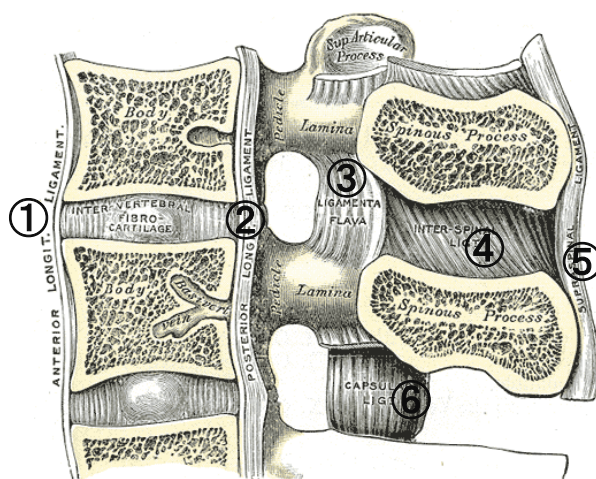


Figure 1-5: Six major spinal ligaments. The intertransverse ligament is not shown; it spans between the transverse processes of adjacent vertebrae (Modified from [2])

### 1.1.4 Ribcage

The ribcage provides stability to the thoracic spine by increasing its stiffness in flexion, extension, left/right lateral bending, and axial rotation. This inherent resistive response is a combined action of the different anatomical structures within the ribcage construct formed of 12 pairs of ribs, costal cartilage, the sternum, and the intercostal ligaments (Figure 1-6). As previously mentioned, the rib head articulates at the vertebral body facets

of adjacent vertebrae with the exception of T1 and T9 to T12 which have full facets, forming the costovertebral joint encapsulated in fibrous connective tissues. The first 7 ribs, namely sternal ribs, are connected to the sternum via the costal cartilage while the 8<sup>th</sup> to 10<sup>th</sup> ribs are asternal and do not directly attach to the sternum. The last 2 ribs are designated as floating with no intercostal cartilage. The ribs also articulate with the vertebrae at the costotransverse joint, which presents itself as facets on the transverse processes of thoracic vertebrae. Finally, intercostal ligaments assure a network of connective fibrous tissue between adjacent ribs.

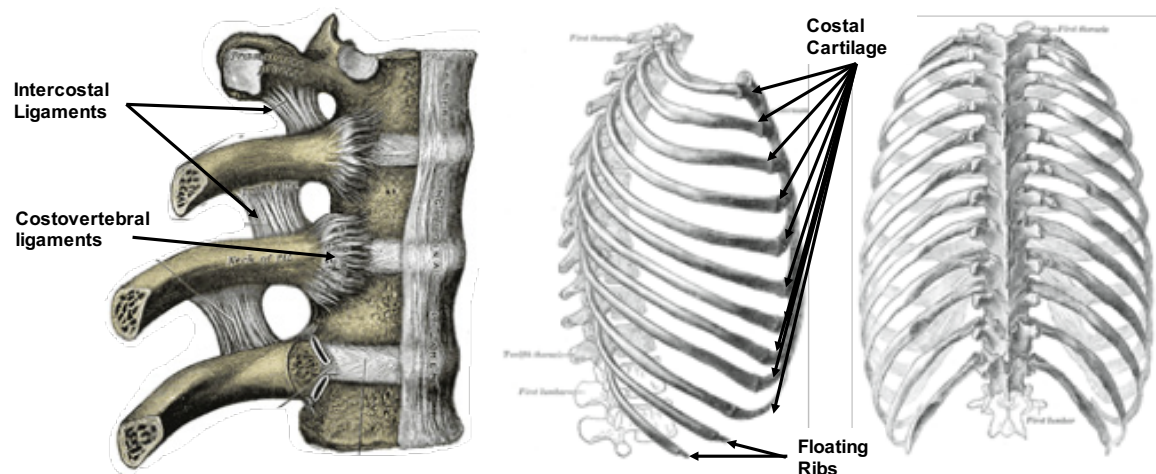


Figure 1-6: The Ribcage and intercostal ligaments (Modified from [2])

### 1.1.5 Porcine Spine and Thorax Anatomy

The porcine spine and thorax, like humans, is composed of vertebrae, intervertebral discs, ligaments, ribs, costal cartilage, and the sternum. Nonetheless, differences lie within anatomical and morphological aspects of the spine and thorax. Swine spines typically consist of 15 to 16 thoracic and 6 lumbar vertebrae, which share similar anatomical structures to humans. More specifically, a vertebral body defines the main structure (0.45 mm cortical thickness [12]) along with posterior elements (pedicles, laminae, articular facets, and spinous and transverse processes) (Figure 1-7).

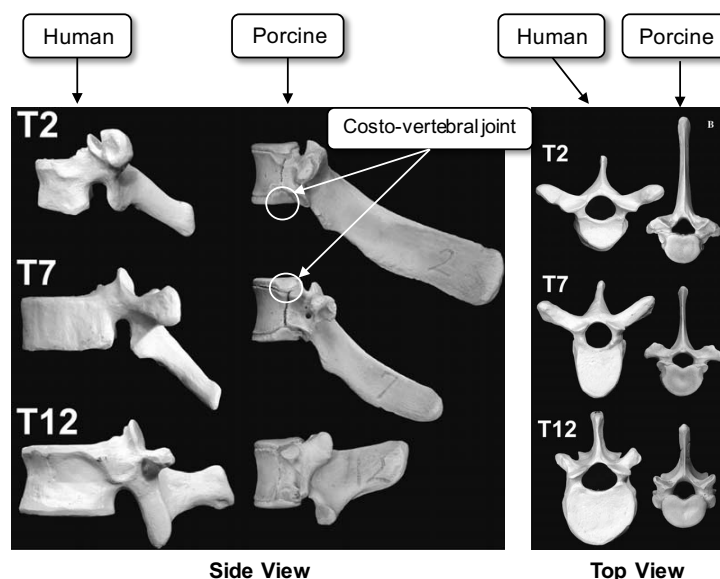


Figure 1-7: Difference between swine and human thoracic vertebrae (Modified from [13])

Table 1-1: Anatomical differences between humans and pigs

Human	Pig
<b>17 Vertebrae</b> <ul style="list-style-type: none"> <li>• 12 Thoracic (T1-T12)</li> <li>• 5 Lumbar (L1-L5)</li> </ul>	<b>21 Vertebrae</b> <ul style="list-style-type: none"> <li>• 15 Thoracic (T1-T15)</li> <li>• 6 Lumbar (L1-L6)</li> </ul>
<b>12 Ribs</b> <ul style="list-style-type: none"> <li>• 7 sternal</li> <li>• 2 asternal, 2 floating</li> </ul>	<b>14 Ribs</b> <ul style="list-style-type: none"> <li>• 8 sternal</li> <li>• 7 asternal</li> </ul>
<b>Sagittal Profile</b> <ul style="list-style-type: none"> <li>• 20°- 45° kyphosis</li> <li>• 30°- 50° lordosis</li> </ul>	<b>Sagittal Profile</b> <ul style="list-style-type: none"> <li>• 30° kyphosis</li> <li>• 8° lordosis</li> </ul>

Yet, anatomical differences lie within thoracic vertebrae. The latter articulate with the ribs, like in humans, at the costo-transverse and costo-vertebral joints. In swine, unlike humans, the costo-vertebral joints consist of two demi-facets. This pattern is consistent along the thoracic region (with the exception of T15, which only features a superior demi-facet) such that the rib head articulates at the intervertebral disc level from T1 to T15 (rib 1 articulates with C7-T1 in swine). The porcine ribcage consists of 14 pairs of ribs where the first 7 are joint to the sternum via costal cartilage (sternal ribs). The last 7 ribs are asternal and articulate with the preceding ribs via the costal cartilage (Figure 1-8), with no floating ribs. Similar to humans, the rib articulates at the costotransverse joint with the

same numbered vertebra from T1-T8, with the absence of the latter between T9-T15. The pig thorax is more oval in shape when viewed cranio-caudally.

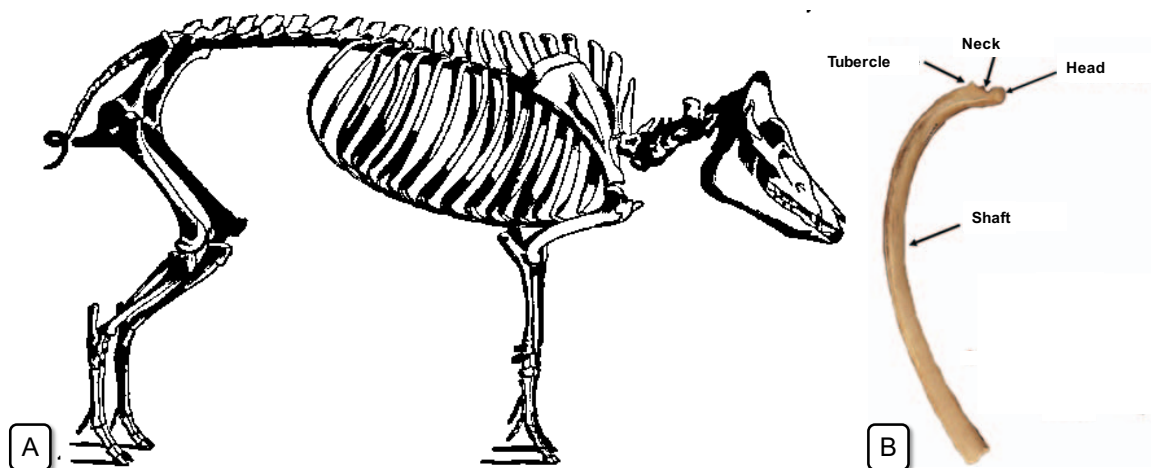


Figure 1-8: Skeleton of a pig showing the ribcage. 14 pairs of ribs articulate from T1 to T15  
(Modified from [14] and [15])

Table 1-2: Differences between the porcine and human ribcage anatomy

	PORCINE	HUMAN
<b>Geometry</b>	Oval (14 pairs of ribs)	Cuboid (12 pairs of ribs)
<b>Rib orientation</b>	Protrude ventrally planar to vertebral local coord sys	Protrude anteriorly and caudally
<b>Costo-vertebral joint</b>	Consistently at IVD, articulating w\ lower & upper vertebrae	IVD level except at T1, T9-T12
<b>Costochondral junction</b>	R1-R14 (no floating ribs)	R1-R10
<b>Range of Motion</b>	No data with ribcage, larger in all rotational directions (without)	Ribcage decreases range of motion
<b>Rigidity</b>	No data with ribcage, smaller in all rotational directions (without)	Ribcage increases spinal stiffness in flexion, extension, lateral bending, and axial rotation
<b>Costo-transverse joint</b>	Detached from T9-T15 to accommodate changing facet joints orientation	Attached at all levels

A striking difference between human and swine vertebrae is the presence of a second ossification layer (a.k.a. subchondral bone) in the latter in all spinal regions. Subchondral bone is located between the intervertebral disc and the vertebral body and forms a second layer of bone, similar to the epiphysis in the human femur (Figure 1-9). The biomechanical role of this ossification layer is unclear; however, functionally, it acts as a nutrient diffusion

barrier between the vertebral body and growth plate whilst its damage may lead to degenerative changes in the disc [16], [17].

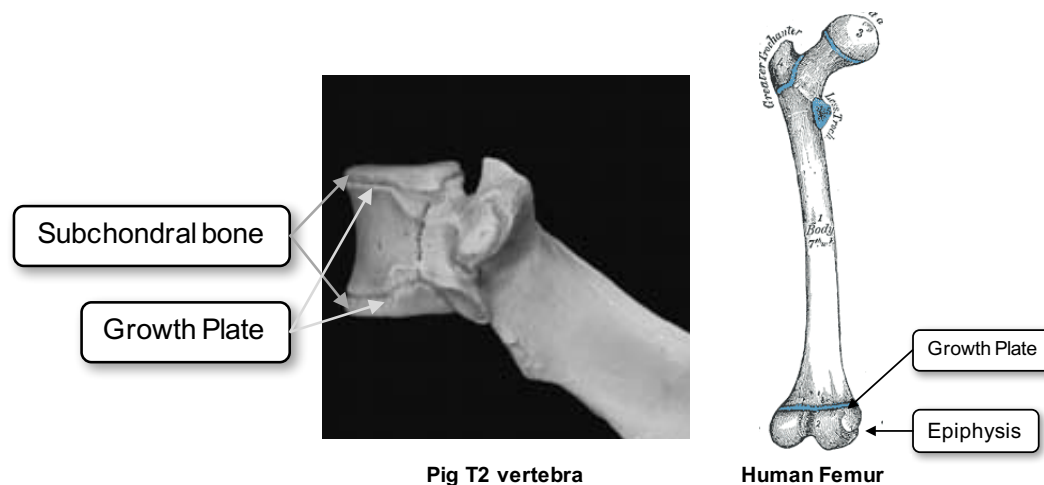


Figure 1-9: Porcine T2 (left) showing the subchondral bone and growth plate, similar to the human epiphysis in long bones (right) (Modified from [13] and [2])

The intervertebral disc anatomy resembles that of human. It is composed of a nucleus pulposus and annulus fibrosus with NP/IVD ratio ranging between 23-43% [18], [19]. Type I and II collagen can be found in the AF with type I in the outermost AF and Type II within the inner most AF and varying proportions in between. Conversely, the nucleus contains type II collagen exclusively [20]. A similar trend is observed within the human IVD; however, type I and II AF collagen proportions are higher compared to swine. Additionally, the nucleus water content is similar to humans with similar mechanical behaviour and creep response under axial loading [21]. Porcine IVDs exhibit age related degenerative changes manifested as a reduction in its function to absorb and distribute external loads and with fibrous tissue formation within the outer edge of the NP [18], similar to humans [18], [22].

Morphologically, it is difficult to obtain a direct comparison between immature porcine vertebrae and adolescent human vertebrae, in part, due to the limited availability of young human spines. Nevertheless, several investigations have compared pig spines (of varying age) to mature human spines, with variable outcomes linked to the swine breeds and age [13], [23], [24]. In a recent analysis, Busscher *et al.* [24] compared the morphology of 4 months old domestic swine ( $n = 6$ ), commonly used in orthopaedic research, with adult

human spines (n = 6, range: 55-84 years old). The porcine vertebral body height (VBH) increased from T1 to L6 (similarly to humans); however, the increase in VBH was smaller in pigs with vertebral body heights comparable in the upper thoracic region (T1-T12). Porcine VBH were more comparable to adolescents before their growth spurt [24]. Similarly, the upper and lower endplates width and depth (UEW, UED, LEW, LED) increased caudally, with the latter more constant along the spine, defining an elliptically shaped endplate. The cross-sectional areas increased by 25% in pigs vs 195% in humans [13]. Thus, vertebral bodies are shorter and narrower with respect to the human spine [13], [24]. Pedicles span the entirety of the vertebral body height and their height is slightly larger than humans with similar widths along the thoracic spine [13], [24]. The facets are oriented similarly to humans in the upper thoracic region (T1-T9), with a sudden transition at T9-T10 junction equivalent to the human thoracolumbar T12-L1 transition. The intervertebral disc height increases relatively slowly caudally in the pig spine and is consistently smaller than its human equivalent at each segmental level [13], [23], [24].

Globally, the pig presents a kyphosis and a lordosis. The extent of these is much lower than what is expected in humans; however, obtaining true measurements in animals maybe be challenging due to animal positioning under anesthesia. As muscular contribution is virtually eliminated, the lateral profile does not depict the actual shape expected when the animal is ambulatory. Furthermore, a relative profile measurements from excised spines may be changed due to the dissection of soft tissue and absence of muscle tone [24].

The anatomical resemblance between swine and human vertebrae has attracted many investigations to use these animal models for orthopaedic implant *in-* and *ex-vivo* testing. Notwithstanding, morphological differences, specifically the intervertebral disc space, should be accounted for when transferring results to clinical applications. Furthermore, swine typically present higher bone mineral density [25]; thus, interpreting fracture testing and implants pullout results should be meticulously analyzed by acknowledging inherent differences between humans and pigs. The use of animals, pigs included, in orthopaedic research relating to spinal treatment will be covered in-depth in Section 1.4.3.3.



## 1.2 Biomechanics of the Spine

Spinal biomechanics encompasses several aspects including spinal loading, spinal range of motion, and the interaction between the different spinal structures to achieve these functional behaviors. Following the preceding overview of spinal descriptive anatomy, the following sections will address the functional description of the latter structures involved in the various aspects of spinal biomechanics.

### 1.2.1 Spinal Loads

Spinal loading is a complex interaction between various stabilizing muscles and soft-tissues as a means to counteract the moments created by gravitational loads. It is generally accepted that the spine is mainly loaded along the vertebral axial direction with approx. 92% of loads distributed along the anterior and posterior regions of the intervertebral discs [26]. Using a custom-designed pressure sensitive needle, Nachemson *et al.* [27] found *in vivo* intradiscal pressures reaching  $\sim 0.87\text{MPa}$ , indicating the importance of the IVD as a load bearing and transmission medium between spinal segments. The mechanism by which the disc achieves such resistance can be directly related to its inherent functional anatomy depicted as a spring-damper mechanism (Figure 1-4). Combining this ingenious biological mechanism with the structural strength of the vertebral body, the spine can endure compression of  $\sim 2\text{KN}$  at C7 and  $\sim 8.5\text{KN}$  at L4 [4]. Linders *et al.* [28] observed a linear correlation between the applied load and the vertebral cortical shell strain measurements, indicating the vertebral body's important contribution to resisting loads at the vertebral body level, with 45% of the load sharing [29], [30]. Discal L3-L4 pressures can reach up to 3 times standing measurements as posture changes (Figure 1-10) [31], with pressures increasing relatively more than the applied load due to annulus fibrosus tensile resistance, reaching 4-5 times the applied force and posing a risky site for spinal injury. Further risk factors extend to loading history, aging, and genetic inheritance, affecting the strength of spinal tissues, and hence, its load bearing capacity.



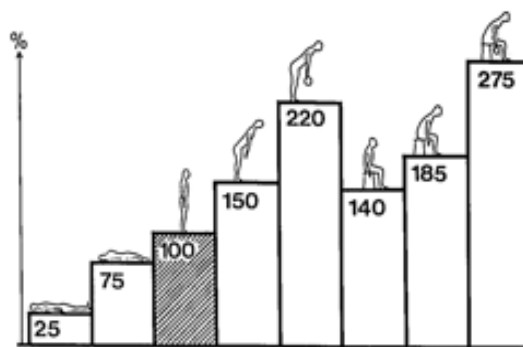


Figure 1-10: L3-L4 intradiscal pressure variation as a function of posture when compared to standing (Modified from [31])

Load allocations (gravity and muscle forces) along the spine is difficult to quantify due to limitations in measuring forces generated by the spinal stabilizer muscles. Uneducated assumptions in a complex mechanical equilibrium may render a complex problem more inconsistent. However, several researchers have attempted to quantify these loads by defining or relating segmental load ratios as a function of body weight (BW) [32], [33]. More specifically, Schultz *et al.* [32] have established an approximate correlation between BW and spinal segmental level based on a developed model linked to intradiscal pressures and myoelectric measurement. As such, 14% body weight load was allocated to T1 with segmental 2.6% BW incremental increases up to L5 (Figure 1-11). Such loading strategy was adopted by Villemure *et al.* [34] in a finite element model to simulate progressive scoliosis deformities in adolescent idiopathic scoliosis. In a more refined model including the ribcage and abdominal and skin (soft) tissues, Clin *et al.* [35] integrated Schultz load model application whereas equivalent loads were applied with a sagittal offset to account for segmental centers of mass. Moreover, these numerical models lacked the appropriate spinal muscle force vectors. Investigations by Patwardhan's team demonstrated that the spine consistently buckled under compressive vertical forces (akin to gravity) 10 times lower than the physiological loads (~1000N) withstood by the spine [36]. Buckling was due to the absence of the stabilizing effects of spinal muscles. A concept of "Follower Load" was then postulated, where loads are applied tangential to the spinal curvature, attempting to minimize the effect of shear and bending. Patwardhan, by applying a follower load using a system of guides and wires, concluded that the stability and load-carrying capacity of the lumbar spine increased [37]

under loads reaching 1200N. However, the study was limited to the lumbar spine, and the load path was fixed, where it was hypothesized it should remain near the segmental center of rotation. Other limitations of this approach is its pure compressive aspect (eliminating shear loading) disagreeing with current understanding of the asymmetrical vertebral stresses associated with scoliotic deformities [38]. Nonetheless, follower loading was applied by Dreischarf *et al.* [39], using a finite element model and locating the optimal follower load path posterior to the vertebral bodies showed its stabilizing effect as the total ROM was less sensitive to the follower load application points. Yet, ongoing computational investigations attempt to capture the realistic behavior of the spine under upper body loads and intervertebral stress distribution [40]–[42].

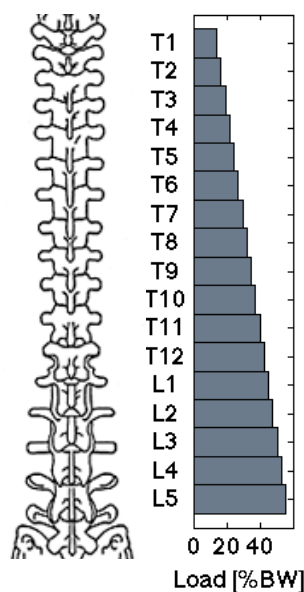


Figure 1-11: Graphical representation of the correlation between body weight and spinal segmental loading as developed by [32]

Although current understanding of spinal loading is limited for human cases, investigating quadrupedal spinal loading poses an ambiguous avenue to current research aiming at experimental animal trials involving spinal implants. In quadrupeds, gravitational loads are ventrally directed. Dorsal and ventral muscle forces (Figure 1-12b) act concurrently to stabilize the spine in the lateral profile to maintain the natural curvatures, the absence of which would “flatten” the vertebral column.

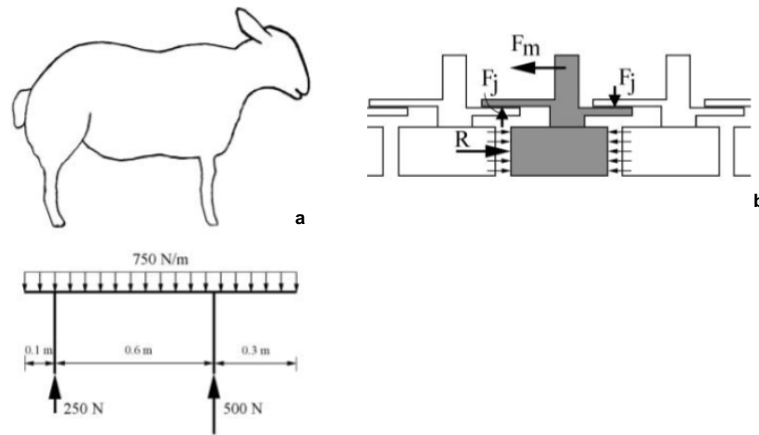


Figure 1-12: a) Ventrally directed gravitational force vectors in quadrupeds, b) Dorsal and Ventral muscle co-activation to stabilize the spine in the sagittal plane (Modified from [43])

As such, the resultant load is directed in the longitudinal axis of the vertebral body, mainly axially compressing the vertebra, analogous to human spines. Such occurrence is not unrealistic given the morphological similarities between ovine, porcine, bovine, and human vertebrae [1] suggesting that, functionally, the latter have adopted shapes to withstand similar loading environments. To further add, quadrupedal vertebral bodies exhibit trabeculae oriented longitudinally further demonstrating load vector orientation as trabeculae are normally aligned in the major loading direction (Wolff's law) [43]. Subtle differences may arise in the shear vector at segmental level, especially at the thoracolumbar junction. In humans, the resultant shear force is directed posteriorly while it is anteriorly oriented in quadrupeds. This, in part, is due to the change in resultant force from gravity due to the natural sagittal (kyphosis/lordosis) differences between both species with an acute transition between kyphosis and lordosis presenting itself at the T12-L1 levels (human).

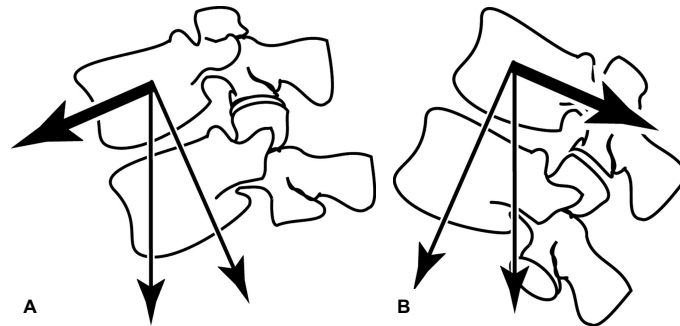


Figure 1-13: Shear vector direction in the loaded quadruped and primates (A) and human (B) spines (Modified from [44])

It is speculated that spinal loads are higher in quadrupeds vs humans as higher forces are required to maintain the inherent sagittal shape of an otherwise horizontal spine, similar to a suspension bridge [43], [45]. Using stress sensors implanted in the annuli of midthoracic discs, swine *in vivo* measured pressures were 0.56, 0.63, and 0.55 MPa for sitting, standing, and walking, respectively [46]. Thus, physiological compressive stresses within pig spines ranged to values similar to humans [46], which may be explained by the smaller endplate surface area in pigs subjected to higher spinal loads. Nevertheless, *in vivo* intervertebral disc or growth plate stresses are scarce within the literature.

### 1.2.2 Spinal Motion

Spinal motion is the product of the interaction between the various spinal structures manifested as relative rotations and translations of each vertebral level. At a multisegmental level (2 or more vertebrae and their enclosed intervertebral discs), rotations correspond to flexion (flex) and extension (ext), right and left lateral bending (LB), and right and left axial rotations (AR). On this note, translations correspond to the anterior and posterior, medial and lateral, and axial translations with respect to adjacent segments. Figure 1-14 provides an illustrative depiction of the notions of translation and rotation within the context of the spinal functional unit.

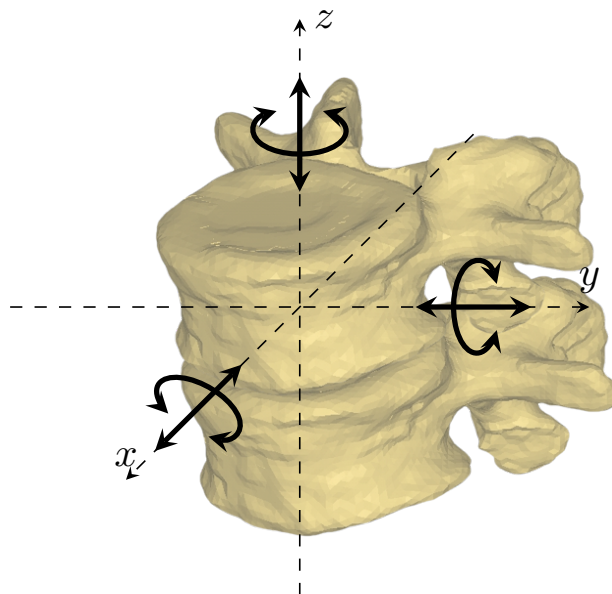


Figure 1-14: Vertebral translations and rotations. Along the x-axis: antero-posterior translation and lateral left/right bending, along y-axis: medio-lateral translation and Flex./Ext., and along z-axis: proximo-distal translation and axial rotation.

Figure 1-15 shows a graphical representation of the ranges of motion (ROM) of the different spinal segments from C0-C1 to L5-S1 in Flex./Ext., Lateral Bending, and Axial Rotation. The ROM in Flex./Ext. increases in the cephalocaudal direction (from C0-C1 to L5-S1). Conversely, axial rotation decreases in the cephalocaudal direction. Such differences arise from the anatomical orientation of the vertebral zygapophyseal joints where, in the thoracic region, the superior facets are directed posteriorly, slightly superiorly, and slightly laterally while the inferior facets are directed anteriorly, slightly inferiorly, and slightly medially (Figure 1-16). Such disposition increases resistance to extension, while allowing for flexion and axial rotation. In the lumbar region, the superior facets are concave in shape and directed medially, and oriented vertically. The inferior facets are directed laterally and oriented vertically (Figure 1-16). This anatomical setup allows for flexion and extension, while blocking axial rotation. Overall, the ROM in flexion is marginally higher than extension due to the specific orientation of these facets. Lateral bending shows relatively small changes as compared to Flex./Ext. and axial rotation along the spine.

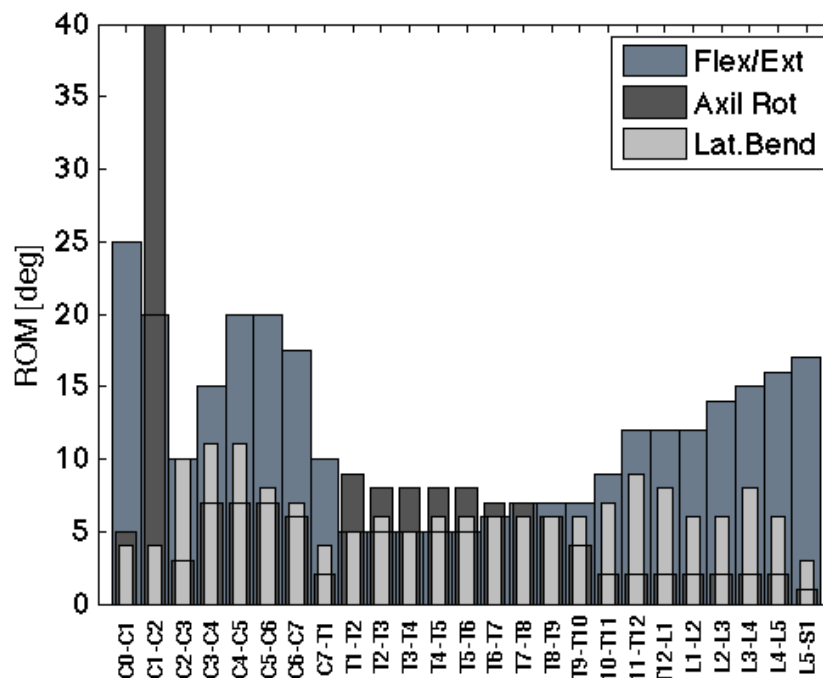


Figure 1-15: Segmental flexion/extension, lateral bending, and axial rotation along the human spine (obtained and modified on 01-03-2016 from <http://wings.buffalo.edu/academic/departement/eng/mae/courses/417-517/Orthopaedic%20Biomechanics/Lecture%2012.pdf>)

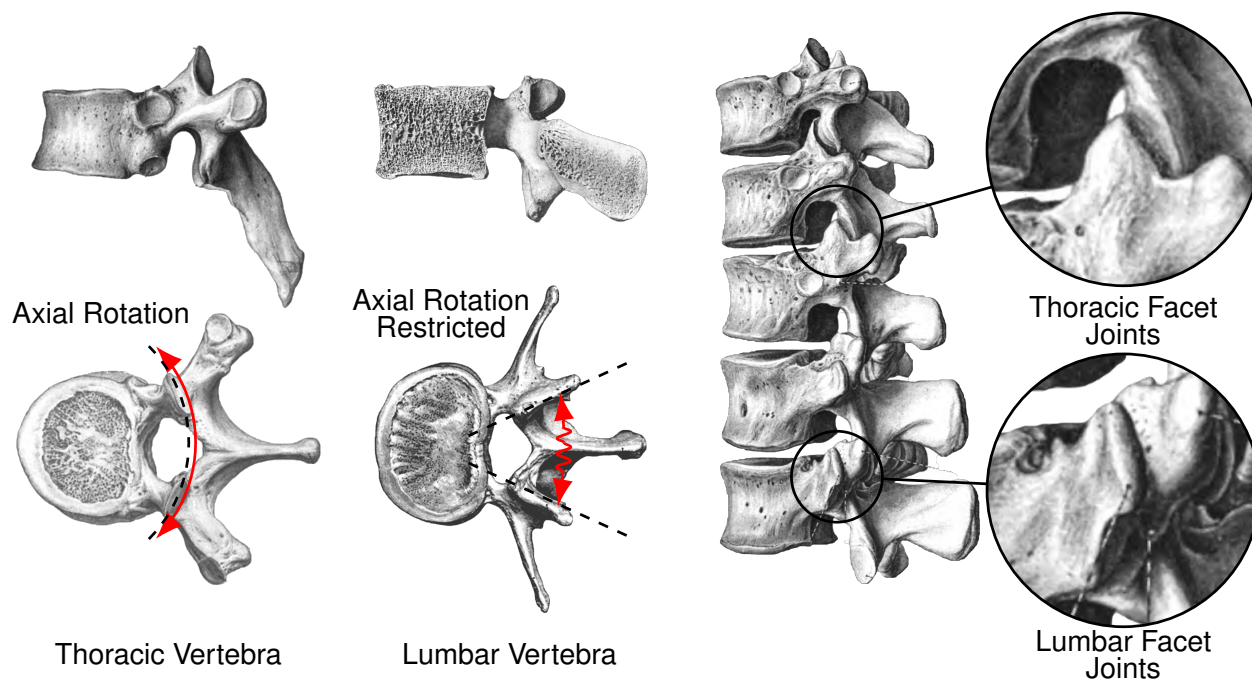


Figure 1-16: Facet joint orientation in the thoracic and lumbar regions and their functional contribution to axial rotation

Several investigations have demonstrated that removal of posterior elements and disruption of their corresponding spinal ligaments increased ROM in Flex./Ext., AR, and LB [11], [47]–[50]. Flexion ROM alterations correlated with intraspinous/supraspinous ligaments, and ligamentum flavum injuries. Extension ROM correlated with anterior ligament and pedicle injuries; AR correlated with anterior disc injury, anterior endplate injury, and capsular ligament injuries; LB correlated with posterior disc and endplate injuries, indicating the respective roles of these elements in the ROM of motion in flex/ext, LB, and AR.

The ribcage provides further stability to the thoracic spine by increasing its stiffness in all three physiological rotations. Using a canine spine ((T5-T9) with corresponding ribs and sternum), Oda *et al.* [51] showed that removal of the posterior elements increased ROM in Flex/Ext, removal of the 7<sup>th</sup> costo-vertebral joints increased ROM in AR and LB, and destruction of the ribcage increased the neutral zone (NZ) in AR and LB. Large NZ is an indicator of spinal instability [4] as movement within this zone necessitates minimal muscular activity. Further, Yao 2011 [52] tested 4 female thoracic spines with ribcage and concluded that resection of the costo-vertebral joint increased vertebral displacement. These results accentuated the importance of the ribcage in stabilizing the thoracic spine, which was further demonstrated by the works of Brasiliense *et al.* [53] demonstrating 78% increase in thoracic stability with an intact thorax. Works of Busscher [49] were focused on the segmental ROM of the upper and lower thoracic, and lumbar spines with 3 cm of ribs remaining in an attempt to emulate the ribcage stabilizing effect. However, his works do not account for the important contribution of the intercostal, costochondral, and sternum interactions [51]–[53]. Thus, his ROM results reflected White and Panjabi's [4] ROM of the ligamentous spine.

Spinal motion, in its complexity, presents coupled motion in all 6 degrees of freedom (DoF), also termed off-axis motion. Globally, lateral bending causes the cervical and upper thoracic spinous processes to rotate towards the opposite direction, mid-thoracic region shows little to no rotation, lower thoracic and lumbar present rotations in the same direction (Figure 1-17). Coupled motion is a product of the length of the spine, with increasing coupled motion with segment length [54], the type of motion, and the region of the spine [47]. Rotations are also coupled with translations. Flexion results in an upwards

axial translation, in the lumbar region, but this coupling is less pronounced in the thoracic region. Extension is followed by downwards axial translation in the thoracic and lumbar regions. Axial rotation results in lateral bending in the same direction (thoracic and lumbar), and flexion and axial translation in the lumbar region (mainly due to the configuration of the lumbar facet joints and the tendency of the annulus fibers to reorient vertically). Lateral bending caused little coupled motion, except for rotation. Results are from experiments on 3 unit segments (T11-L1) and do not reflect the complete behavior of the whole spine. However, they present a comprehensive perspective of motion coupling within the spine. These complex behaviors should be accounted for when testing new spinal implants, experimental spinal stability testing, and simulations involving elaborate loading.

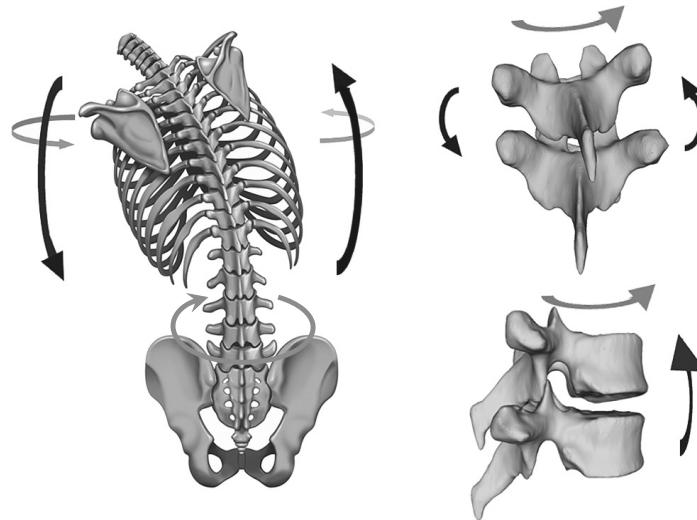


Figure 1-17: Coupled spinal motion (Modified from [55])

When compared to humans, porcine spine range of motion was typically comparable in the lower thoracic and lumbar regions [56]. The overall biomechanical behavior was similar with trends showing higher flexion vs extension, and symmetrical left/right lateral bending and left/right axial rotation ranges of motions. Largest flexion/extension ROM was in the lower thoracic and lumbar region. Axial ROM were larger in the upper and midthoracic region while lateral bending was largest in the cervical region. These tendencies were also observed in human spinal regions [4] and are partly due to the functional orientation of the facets joints and the spinal ligaments in both species. Similar



absolute ranges of motion were shown between the lower thoracic and lumbar regions between humans and pigs. Notably, the ribcage was not included in these analyses and, thus, neither its biomechanical contribution. Although comparable, porcine ROM were compared to published human data subjected to different rotational moments. In the swine study,  $\pm 1.0$  Nm (C1-C2),  $\pm 2.5$  Nm (cervical region), and  $\pm 7.5$  Nm (thoracic and lumbar regions) were applied to the tested functional units.

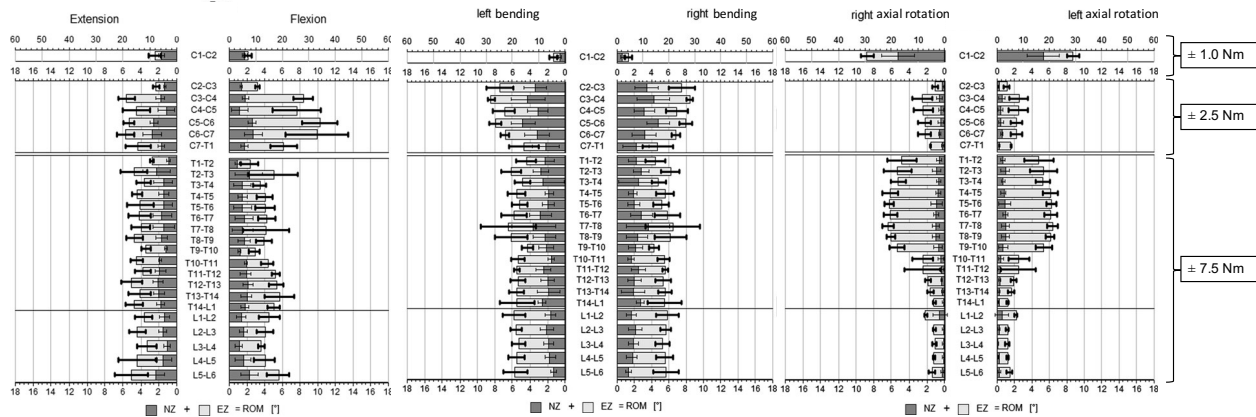


Figure 1-18: Porcine spine segmental range of motion for the cervical, thoracic, and lumbar regions (Modified from [56])

In another study, controlled moments (2 Nm) were applied to multisegmental specimens (4 vertebrae and 3 IVDs) from the upper, mid, lower thoracic, and lumbar regions of porcine (~4 months old) and human (55-84 years) spines. Data from the middle IVD and adjacent vertebrae (representative of physiological unrestrained motion segment) was collected after 3 preloading cycles. The results showed, although not significant, that range of motion and neutral zone were generally more prominent in porcine vs human segments [50]. However, after removal of the posterior elements, ranges of motion were similar at the lower thoracic and lumbar regions, which may be partly due to the differences in facet orientation within these regions as the facet change orientation abruptly more cranially in pigs. The aforementioned results reflect, arguably, a more realistic comparison between species as standardized loads were applied.

Data is unavailable to explain the role of the ribcage in the pig spine. However, as previously mentioned, Oda *et al.* [51] showed the important contribution of the ribcage to spinal stability in a canine experimental test. Dogs have a similar ribcage form factor as

pigs [14]; thus, the behaviour of the porcine ribcage under biomechanical loads and mechanical testing can be hypothesized to reflect a similar response, with the ribcage increasing stability in the thoracic region.

## **1.3 Physiology of Bone Tissue**

### **1.3.1 Composition of bone and cartilage tissue**

Bone is a connective tissue composed mainly of cells embedded in an extracellular matrix. It serves as mechanical support and organ protection, mineral reserve, constant source of bone tissue remodeling, and production of blood cells from the enclosed bone marrow. The extracellular matrix is formed of three constituents: collagen fibers, minerals, and a fundamental substance. Due to their elastic properties, the collagen fibers offer bone its resistance to mechanical loading while the fundamental substance serves as a medium for the fibers. Mainly composed of hydroxyapatite and calcium carbonate, the minerals form the inorganic fraction of the extracellular matrix and provide bone with its rigidity and hardness.

Bone cells include osteoblasts, osteoclasts, and osteocytes. Osteoblasts are involved in the apposition of the extracellular matrix and play an important role in bone modelling and remodelling. Osteocytes are “old” osteoblasts. They lack the capacity to differentiate and synthesize bone tissue. Furthermore, they are involved in the maintenance of the extracellular matrix. Osteoclasts, multinuclear cells, are involved in the resorption of bone. They are also highly migratory along the span of bone tissue. Osteocytes interconnect with bone lining cells and form the first line of action in bone remodelling by coordinating the spatial and temporal recruitment of bone forming and resorbing cells [57]–[59].

### Compact Bone & Spongy (Cancellous Bone)

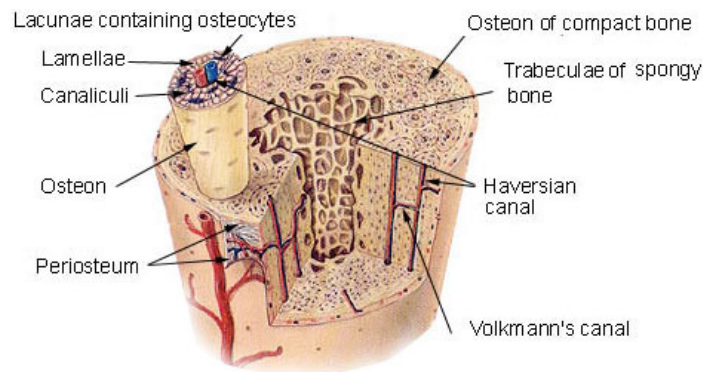


Figure 1-19: Macroscopic composition of bone (Obtained from:

<http://www.training.seer.cancer.gov/anatomy/skeletal/tissue.html> on 08/01/2016)

Macroscopically, bone is mainly composed of cortical and cancellous bone. Both structures are formed of lamellar bone, which, in turns, is formed of organized parallel layers of collagen fibers. In cortical bone, these fibers alternate directions from layer to layer forming a concentric shell surrounding the enclosed cancellous bone. On the other hand, the lamellae form trabecular structures of diverse sizes in cancellous bone. Osteons are formed by 20 concentric lamellae with up to 7 rings of osteocytes in osteons walls. Capillaries run through the centers of the osteons, known as Harvasian canals, to supply the required nutrients. A fibrous layer, namely the periosteum, surrounds bone except at cartilaginous sites such as in articulations.

### 1.3.2 Epiphyseal Growth Plate

The epiphyseal growth plate is where longitudinal bone growth occurs via layered bone deposition. In humans, the growth plate is situated between the intervertebral disc and the vertebral body at the proximal and distal extremities. The growth plate is avascular, for the exception of its boundary with the metaphysis of the vertebral body whose vascular anatomical purpose will be widely covered in Section 1.3.3. The growth plate is divided into 3 zones (Figure 1-20) [60]. The reserve zone is composed of idle chondrocytes with very low proliferative rate, namely why this zone is also referred to as the resting zone with a high extracellular matrix (ECM) to chondrocyte ratio [61]. The ECM is mainly composed of collagens (primarily type II), proteoglycans, and non-collagenous proteins.

The proliferative zone is composed of flattened chondrocytes, organized into columns and ready to divide. In the mature (lower) proliferative zone, chondrocytes have already undergone division and are stacked into columns separated by the ECM, ready for hypertrophy. In the hypertrophic zone, chondrocytes are found enlarged and organized into columns with an increase in enzyme activity/synthesis promoting secretion of type X collagen [60] (only found in the growth plate). In the lower hypertrophic zone, chondrocytes undergo apoptosis after secreting a highly specialized matrix promoting cartilage calcification sites for bone formation via the osteoblasts in the vascular invasion zone (Figure 1-20).

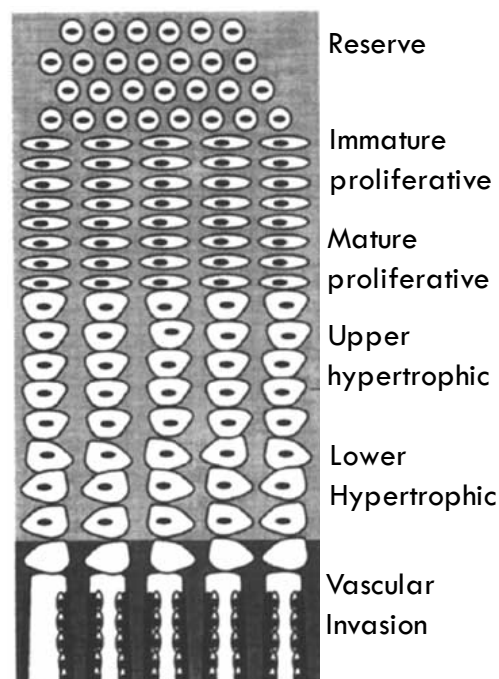


Figure 1-20: Vertebral epiphyseal growth plate and its zonal divisions: the reserve, proliferative, and hypertrophic zones (obtained from <http://www.nzdl.org/gsd/collect/ccgi/archives/HASHee86.dir/p133.jpg> on 03-01-2016)

### 1.3.3 Bone Growth

Normal bone growth is defined by two processes: endochondral ossification (ossification centers: OC) and appositional growth (bone surface growth). Endochondral growth is responsible for longitudinal bone growth. Peripheral (transverse) bone growth is achieved through endoconjunctive development by means of intramembranous ossification at the

periosteum. Figure 1-21 gives an illustrative representation of both growth processes and their respective growth direction. More specifically, the spinous and articular processes ossification centers (1) are involved in the posterior element growth and are typically closed by age 12 [62]. The neurocentral cartilage (2), also known as the neurocentral junction, exhibits a bilateral growth pattern contributing to pedicular growth and well as parts of the posterior vertebral body wall at the junction site and undergoes full ossification and closure by 12 years of age [62]. The superior and inferior growth plates contribute to longitudinal vertebral growth similar to long bone growth at the epiphyses. The epiphyseal growth plate is fully closed at maturity. Appositional, a.k.a. peripheral, bone growth is achieved through intramembranous ossification via the actions of osteoclasts, osteoblasts, and osteocytes at the periosteum [61]. Apposition persists throughout life through the process of modelling and remodeling. This section will focus on endochondral longitudinal growth.

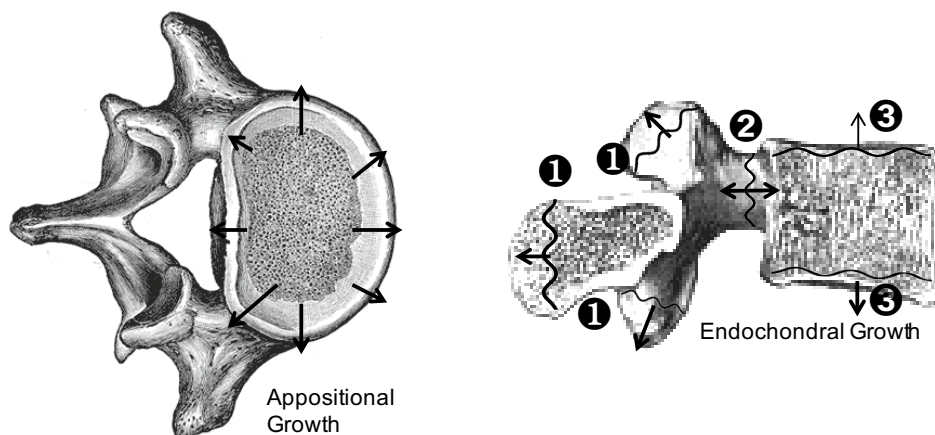


Figure 1-21: Appositional (Left) and endochondral (right) growth. Arrows indicate growth direction and wavy lines illustrate ossification centers (Modified from [4])

Endochondral growth is a complex process involving chondrocytes proliferation and differentiation, hypertrophy, matrix mineralization, and chondrocyte apoptosis. Each individual process is regulated by systemic hormones, locally produced growth factors, and gene expression. These regulatory activities are involved in a complex metabolic loop spanning beyond the scope of this thesis; however, a brief description warrants appreciation to the elaborate growth feedback signaling loop (APPENDIX A).

The growth of the disc is ambiguous at most and it is believed to occur as a by-product of ECM matrix synthesis and cell division. The works of Stokes [65] concluded that vertebral growth predominates IVD growth with the latter contributing to virtually zero growth by the age of 12.

Spinal growth changes over time and occurs in three phases. By the age of 5, sitting height occupies 66% of its final height with 30 cm of residual growth. There is little growth in sitting height (2 cm) during the second phase (5-10y). The third phase corresponds to puberty with diverging patterns between girls (11y) and boys (13y) where remaining sitting height increases by 12 cm (boys) and 13 cm (girls). Particular to puberty, an accelerated growth phase (11-13 bone age, girls, 13-15 bone age, boys) is marked by lower limb growth arrest with 4.5 cm in sitting height residual gain until maturity [66], [67]. The epiphysis ossifies at bone maturity and fuses to the metaphysis.

As will be detailed in further sections, it is imperative to identify the peak growth phase when attempting to treat pediatric spinal disorders. Clinicians rely on anatomic landmark to estimate remaining or the onset of peak growth. Risser sign [68] forms the predominate indicator with Risser 0 to 1 indicating peak growth onset has not begun with little to no remaining growth for Risser 1-5. Other anatomic indicators relies on the Sauvegrain method which assesses the elbow growth plate as it closes before the onset of peak growth [66], [69]. The Greulich-Pyle method relies on an atlas of hand and wrist radiographs of males and females until maturity with corresponding traits correlated to actual age. The method is relatively fast; however, its application to genetically diverse patients may induce variations in actual bone age identification [70]. Notably, the Tanner and Whitehouse method [70] relies on the evaluation of 20 regions of interest within the epiphyseal growth plates of the fingers. The method is accurate, though time-consuming.

Moreover, the ribs include growth plates responsible for its development and expansion. The cage volume is 6% at birth, 30% by 5y, 50% by 10, and 100% at skeletal maturity. Although at 30% volume at the age of 5, it occupies 66% of its final height [67].

Porcine growth plates are devised similarly to humans with a reserve, proliferative, and hypertrophic zone [71]–[73], exhibiting the same functional characteristics as human growth plates. Additionally, growth response to invoked stresses follows similar trends

[74] (Section 1.3.4). Although pig growth is not as well documented as humans, these animals display an accelerated and reduced growth phases. In more detail, porcine daily growth is accelerated between the age 1 to 4 months and sees a reduction afterwards to a full arrest after 12 months age [75] (Figure 1-22). Quoted in numbers, Landrace pigs (typically explored in spinal research) grow at a rate of 0.4cm/vertebrae between 3-6 months of age, thereby reduced to 0.5cm over the next 5 months [76]. Conversely, no available documentation described the growth of the porcine ribcage.

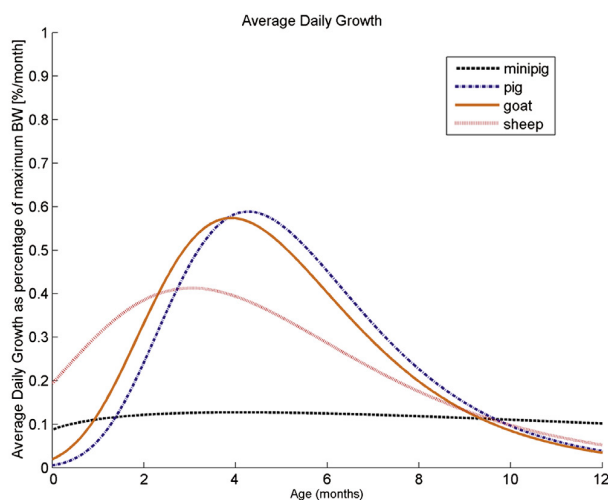


Figure 1-22: Pig growth as a function of age (Adopted from [75])

### 1.3.4 Growth Modulation

Many of the factors governing bone growth play an inherent role in bone growth modulation. These factors include: Parathyroid hormone-related peptide, Indian hedgehog, transforming growth factor- $\beta$ . Other factors, such as insulin-like growth factor, Vitamin D, and vascular endothelial growth factor (VEGF, role still unidentified), are also involved in growth rate regulation. Factors tampering growth rate also include hormonal abnormalities, toxic agents, and growth plate injuries. Maturation of chondrocytes is also identified by physical and biochemical changes occurring in the temporal and spatial patterns imposed on these cells. These changes invoke growth rate alteration through principles of mechanotransduction. Otherwise said, mechanical loading alters GP growth rate. Mechanotransduction pathways postulations include membranous mechanoreceptors, specific mechanotransduction membrane proteins, molecular

pathways, ion channels, growth factors and systemic hormones [59]. In the context of this thesis, focus will be attributed to mechanical growth modulation.

Mechanical growth alteration is described by the Heuter-Volkmann principle [77]. As postulated, growth can be retarded by increasing compression or accelerated by reducing compression forces with respect to normal physiological loading. The principle has been explored in several experimental settings in an attempt to find a mathematical correlation between growth rate and imposed forces with compression, distraction, torsion, and shear loading environments [74], [78]–[85]. Findings from these investigations support the Heuter-Volkmann principle; however, growth plate and rate responses vary with loading strategies. Under controlled torsional loading, Moreland observed that shear forces altered epiphyseal plate columnar orientation without affecting cellular thickness or growth rate [86]. Their results agreed with earlier experimental findings by Arkins [85] suggesting columnar reorientation was a repercussion of mechanical torsion on an otherwise soft growth plate. The extensive research by Stokes *et al.* has demonstrated a strong correlation between applied loads and growth patterns. With a custom apparatus, asymmetrical loads were applied on rat tails with resultant asymmetrical growth patterns suggesting growth retardation which was then reversed by reversing load application, indicative of unimpaired growth. Growth rate variations were associated with alterations in growth plate zonal and chondrocyte heights reflected as a reduction in cellular enlargement in the hypertrophic zone. Other factors included the number of proliferative cells, proliferation rate, and matrix synthesis [64], [81], [84]. Moreover, tensile loads resulted in less growth modulation than compressive forces [74] (Figure 1-23) with complication including premature GP closure under tensile loads [78]. Stokes's findings were then translated into a well-established empirical relationship correlating growth rate with growth plate stress modifications.

$$G = G_m [1 + \beta(\sigma - \sigma_m)] \quad (1)$$



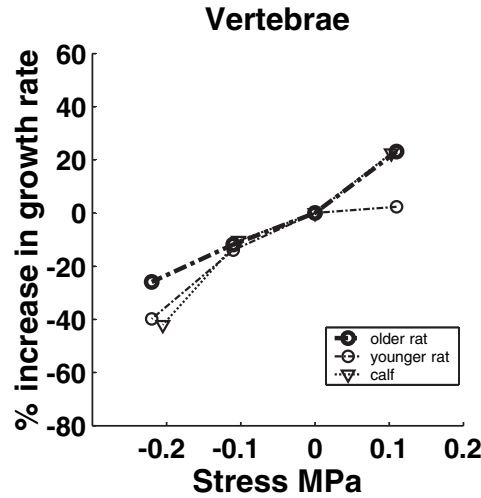


Figure 1-23: Growth rate alterations as a function of applied load on vertebral growth plates of various species (Modified from [74])

In equation (1),  $G$  is the actual growth and  $G_m$  corresponds to normal (unaltered) growth rate, both of which are expressed in mm/year.  $\sigma$  and  $\sigma_m$  represent actual and normal physiological compressive stresses in MPa.  $\beta$  is the growth sensitivity factor ( $\text{MPa}^{-1}$ ). Data leading to this empirical correlation indicate its consistent appropriateness regardless of species or growth plate location (vertebra vs long bone), suggesting it can be transferred to investigate growth responses in human applications or large quadrupeds. Specific changes to  $\beta$  may be required as the sensitivity of vertebral versus tibial to applied stress may vary between 0.4 and 2.4  $\text{MPa}^{-1}$  [74]. Moreover, discrepancies in distraction loading were noted suggesting the numerical relation may be most reliable for compressive applications to award interspecies transfer.

Other studies have investigated the effects of dynamic versus static compressive loading on growth resumption and GP histomorphometric alterations. Ohashi *et al.* have shown that growth is recovered one week after dynamic axial load removal on growing rat ulnae [83]. Valteau *et al.* assessed the effect of controlled dynamic versus static compression and concluded dynamic average stress resulted in similar growth rate modulation than static regimes with dynamic loads reflecting less detrimental changes to the GP [84]. In recent *in vivo* analyses, Ménard *et al.* have shown growth reduction by increasing the frequency or the amplitude of dynamic compression without histomorphometric changes to the epiphyseal growth plates of rat tails. However, changing the frequency and

amplitude concomitantly altered growth plate integrity [87]. Furthermore, static compression affected the structural integrity of the intervertebral disc indicating dynamic compression favour disc health preservation [88] with removal of both static and dynamic loads re-establishing growth, indicating a phenomenon of “catch-up” growth [89]. Nonetheless, evidence of force threshold below which bone growth would not be stimulated is yet to be elucidated [61] with prospective applications of dynamic *in vivo* load for human application yet to be fully elaborated.

Other numerical correlations have been postulated for the growth plate response to external stimuli. Carter’s model related octahedral stresses to promoting endochondral ossification while hydrostatic stresses to promoting preservation of cartilaginous tissue. The model is limited as the growth direction is not accounted for, with underestimation of growth modulation under compression loads [90]. The model also considers multi-axial loading, which was previously shown not to affect the growth response with torsional (off-axis) loads. Otherwise, Frost suggested that growth modulation was a function of chondral growth force response curve, which indicates a threshold should be exceeded for compressive loading to retard growth (Figure 1-24) [91]. Frost’s chondral growth factor response curve (CGFRC) suggests that compressive forces could lead to accelerated growth (similar to distraction forces) until a loading threshold is reached, beyond which growth is decelerated. In a recent preliminary numerical model, it was shown that the lumbar growth follows the CGFRC rather than Hueter-Volkmann principle as the later only explains progressive growth modulation and does not account for unresponsive or auto-corrective situations [92]. However, the study requires further *in vivo* analyses to establish the threshold load for growth response.

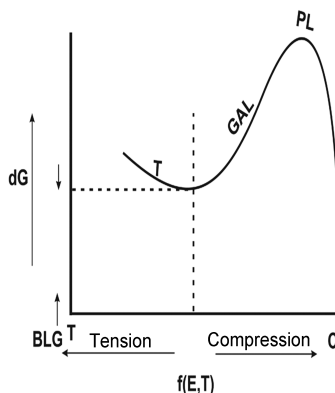


Figure 1-24: Chondral growth force response curve (Modified from [92])

## 1.4 Scoliosis

Scoliosis is a complex disease that manifests itself in the coronal, sagittal, and transverse anatomical planes, which can be differentiated into several types depending on the nature of its etiology. Congenital and idiopathic scoliosis are most common incidences. Neuromuscular scoliosis and neurofibromatosis are other occurrences; however, they represent a small fraction of the observable characteristics of this spinal musculoskeletal condition. Idiopathic scoliosis (IS) affects 80% of the 2-3% scoliotic occurrences in the population [93]–[97]. Adolescent idiopathic scoliosis (AIS) affects 70-80% of IS patients [93], [96], [97] with its etiology still to be elucidated.

Several geometric parameters characterize scoliosis's severity. One of the most prominent measured indices is the Cobb angle, which is used to determine the angle of the spinal curvature at its inflection points (Figure 1-25). The method was originally developed by Cobb [98] to identify guidelines for scoliosis classification using radiographic films. Advancement in spinal 3D reconstruction techniques have shed new insights onto the three dimensional aspect of the deformity requiring further identification of new measurement indices to help surgeons better target treatment strategies [99], [100]. In a recent prospective study, Nault *et al.* have identified 3D parameters differentiating between progressive and non-progressive curve for similar age and Cobb angles [101]. Likewise, by analysing the “Plane of maximum curvature (PMC)” (the maximum 3D plane within the points of inflection of the curvature), 3D structural differences were evidenced between patients presenting similar 2D Cobb angles [102], further emphasizing the

importance of analysing the multidimensional aspect of the complex structural and morphological changes in scoliotic spines.

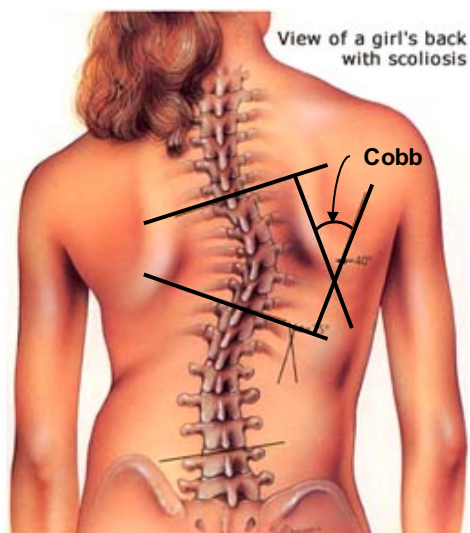


Figure 1-25: Scoliosis viewed from the back and Cobb angle measurement (Modified from: <http://www.kwikfit4u.com/wp-content/uploads/2014/07/scoliosis.jpg> on 02/10/2015)

With the inherent three dimensional nature, it becomes evident to evaluate the axial rotation of segmental vertebrae. Wever *et al.* have shown a distinct rotation of the apical vertebrae with vertebral bodies oriented towards the convexity of the deformity [99]. This peculiar aspect of the deformity explains the presence of the rib hump (Figure 1-26) resulting in self-image acceptance hurdles in adolescents, leading to reduced lung capacity in progressive severe deformities [67].

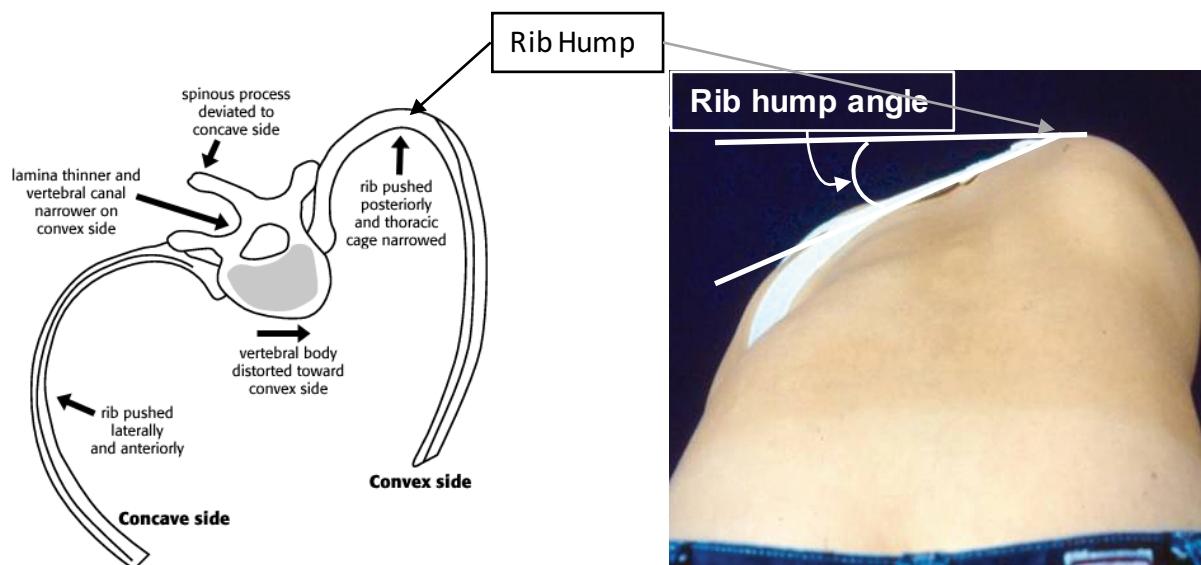


Figure 1-26: Transvers view of the trunk illustrating the differences between normal and scoliotic spines (<http://rad.washington.edu/about-us/academic-sections/musculoskeletal-radiology/teaching-materials/online-musculoskeletal-radiology-book/scoliosis/> on 01/03/2016 (Left) and [96] (Right))

### 1.4.1 Scoliosis pathogenesis and pathomechanism

Scoliosis pathomechanism was proposed through different concurrent theories. Progression risk factor can be summarized as: curve patterns, severity of the curvature at peak growth (11-13y girls, 13-15 boys), Risser sign (indicator of skeletal maturity), progression history, and gender.

The spine exhibits an inherent dorsal shear load at the thoracolumbar junction (Figure 1-12) contributing to the rotational instability created by the inactivation of the facet joints. Adding to the inherent pre-existing vertebral rotation (to the right) in humans, these shear loads shift the mechanical environment to a state of unbalance [44], [128]. More specifically, this rotational instability results in asymmetrical loading in all three anatomical planes. The excess loads on the neurocentral cartilage causes asymmetrical growth patterns between the left and right pedicles (Hueter-Volkman principle). *In vivo* trials on immature pigs have shown that disruption of the neurocentral joints using unilateral pedicle screws resulted in consistent scoliosis-like deformity [129], [130]. Though, FEM resulted in contradictory outcomes implying differential pedicle growth alone in

adolescents does not produce vertebral wedging nor scoliosis [131]. As the neurocentral joint fuses by the age of 10 (before adolescence and the onset of peak growth) and the inconsistent results as to the role of this junction in deformity progression, these findings do not necessarily confirm scoliosis pathomechanism theories but rather a pedicle remodelling phenomenon, referred to as “bone drift” [128] secondary to the deformity. Nault *et al.* have shown that relative differences in apical vertebral rotation and plane of maximum deformity were present between progressive and non-progressive AIS, with progressive patients more hypokyphotic [101]. Differences in shear loads may occur between kyphotic and hypokyphotic curves, further relating to the underlying role of shear loads on the progressive nature of this deformity.

The correlation between spinal growth and the progression of scoliosis is strongly dependent on the extent of the initial curve [95]. The associated growth plate stresses on a normal spine (0.8-0.9 MPa [31]) were found to differ from those of a deformed spine. In the latter, growth plate stress differences (0.7 MPa, convex, 1.3MPa, concave) were found when the spine was subjected to 1010N, 2 mm laterally offset compressive load [38]. As such, normal growth is disrupted (Hueter-Volkman principle) resulting in a wedged vertebrae locally, and a deformed spine globally, in turn, increasing asymmetrical load in a “vicious cycle” [77] (Figure 1-27). Symptomatic vertebrae are normally wedged in the coronal plane suggesting either an IVD adaptation in the sagittal plane or load asymmetry absence in that plane [100]. Growth modulation and the “vicious cycle” explain the risk of progression at peak growth with greater growth modulation for larger curves [65]. A retrospective study on 56 patients followed for 5 years indicated that 31.5° Cobb at peak growth velocity is a predictor for eventual corrective surgery [132]. Asymmetrical loads explain theories involving dorsal shear force instability, relative anterior spinal overgrowth, and repetitive asymmetrical muscle activity and gravitational forces, where a combination of these concepts, in conjunction with growth modulation, reflect pathomechanisms purely of mechanical source. However, these concepts do not discern between progressive and non-progressive curves. Moreover, the principle of Hueter-Volmann disregards the contribution of the IVD in scoliosis progression. It was noted the latter, as a soft tissue ending its natural growth before the onset of peak growth, adapts to load variations within a curved spine, taking a wedged form similar to vertebrae [133]. In a recent study,

Schlösser *et al.* have shown the important contribution of the IVD in the three dimensional deformity of the spine further emphasizing the adaptive nature of this soft joint [134]. However, extensive research is required to further understand the interplay between the intervertebral disc, vertebral growth, and scoliosis progression.

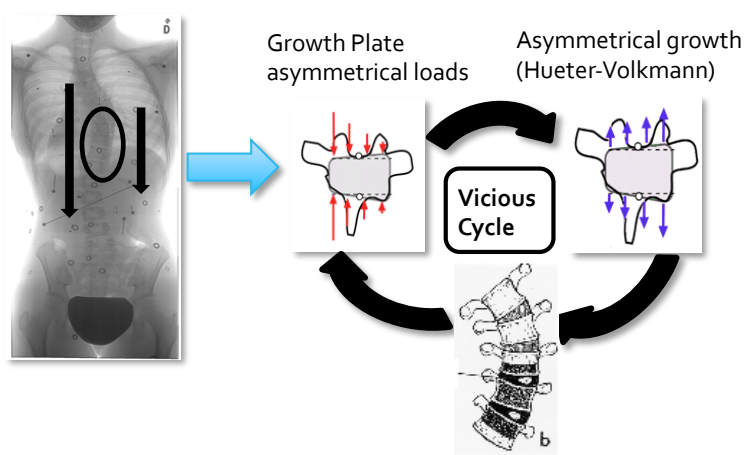


Figure 1-27: Vicious cycle for scoliosis progression pathomechanism

With the complex biomechanical contributors to the progressive nature of this disease, it is imperative to bare in mind the implications for treatment strategies aiming at correcting morphological changes within the spine and further the development of novel corrective strategies.

### 1.4.2 Treatment

Treating scoliosis is dependent on the type of the disease, the degree of maturity of bone, and the Cobb angle [93]–[95], [135]. Table 1 summarizes scoliosis treatment strategies evaluated by the Cobb angle method. For small curves, clinicians routinely monitor the deformity for signs of progression. For moderate curves, bracing is recommended (Figure 1-28) whereas for severe curves, invasive spinal surgery is required to limit the evolution of the curve severity.

Table 1-3: Conventional scoliosis treatment strategies

Cobb Angle	Treatment
$\dots \leq 20^\circ$	No treatment, routine followups
$20^\circ \leq \dots \leq 40^\circ$	Bracing (orthotics)
$\dots \geq 40^\circ$	Surgery: rods, screws, and hook system

Orthotics are recommended as a means to halt the progressive nature of the deformity before skeletal maturity. In the past decade, investigators focused on evaluating the effect of bracing on halting or even correcting scoliosis. More specifically, bracing was shown to be successful at preventing curve progression [135]–[139] with success rate correlating with wearing time [135]. Patients are required to wear their brace for 23h/day posing issues with compliance, quality of life, and self-image. Reduced curve progression and reduced referral to surgery were observed for more compliant patients [140]. In a recent study, Negrini *et al.* have shown that, despite the brace’s positive outcome in preventing curve progression, quality of life was unchanged during the treatment phase [138]. Using a self-appearance questionnaire, Misterska *et al.* concluded that wearing time correlated significantly with body shape perception with psychological impairment more prominent for late adolescent patients [141]. In a review, it was outlined that brace treatment is recommended for AIS patients presenting curves between  $25^\circ$ -  $35^\circ$  with effectiveness in larger curves ( $35^\circ$ - $45^\circ$ ) strongly related to wear time [142]. Nonetheless, these orthotics manage to reduce the progression of the deformity in favor of delaying the onset of surgical intervention [135], [136], [140]. Although effective in stopping curve progression, current braces are not personalized to patients’ three dimensional geometries. Recent investigations focus on integrating finite element modeling to explore optimal orthotics designs with minimal materials and skin surface contact [143]–[147]. Via these numerical tools, braces can be personalized, design parameters can be tested such as strap tension, padding locations and thickness, positions of opening, and among other parameters suited to maximize patient’s comfort and 3D correction. Aubin *et al.* showed that a “NewBrace”, designed and optimized to the patient’s spine and torso geometries using CAD and FEM, was more effective than a standard brace with 32% less contact surface [147]. These promising results encourage the merger between numerical modeling and clinical applications of orthotics.



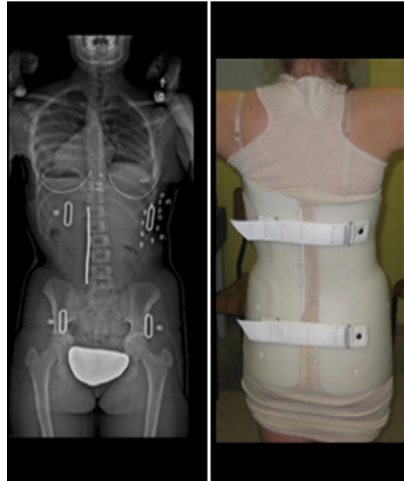


Figure 1-28: Patient treated with a standard brace (Modified from [146])

For progressive severe curves, the conventional approach to halting curve progression and correcting the deformity relies on spinal instrumentation and fusion. The spine is realigned via a system of metal rods, pedicle screws and hooks, invasively reducing spinal mobility. Here, spinal fusion involves joining multiple vertebral segments to form a solid bone structure, also referred to as segmental spinal arthrodesis. Surgery is typically performed after skeletal maturity. However, if a curve presents progressive signs which may pose complications before the intervention, surgeons operate by arresting anterior spinal growth to prevent anterior overgrowth (the crank shaft phenomenon) [148], [149]. This complex procedure involves various instrumentation choices (rod type and diameter, levels to instruments, etc...). Aubin *et al.* have reported that, for the same case, instrumentation strategies differed between surgeons depending on their personal preferences, correction goals, amongst other factors [150]. Moreover, the general aim is to realign the spine with minimal post-operative complications. Despite the common use of the procedure for large curves, it is an invasive and costly approach [151].

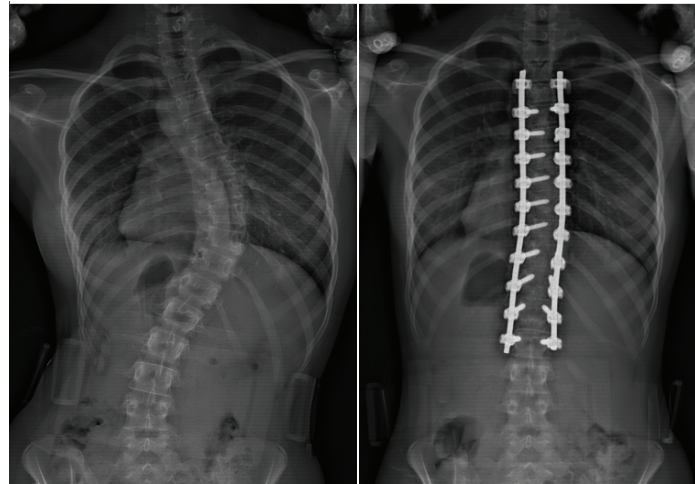


Figure 1-29: Before (left) and after (right) radiograph examples of spinal instrumentation

### 1.4.3 Fusionless devices

Recent interest has shifted towards minimally invasive fusionless AIS treatment strategies that harness residual vertebral growth. As previously mentioned, growth can be manipulated by changing the loading on the vertebral growth plate (Hueter-Volkman principle). As such, fusionless devices attempt to reshape wedged vertebrae to their normal geometries, over time, and realign the spine while maintaining segmental mobility [152] without resorting to invasive surgery [153] (Figure 1-30).

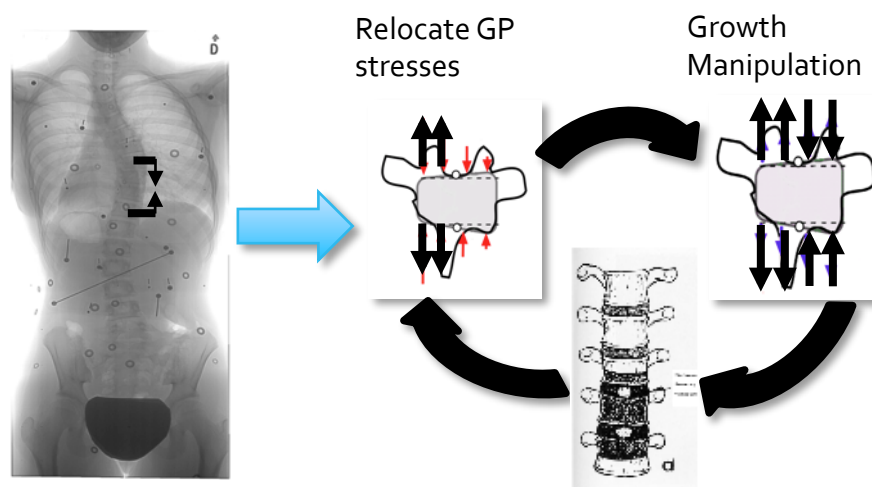


Figure 1-30: Compression-based fusionless implant's cycle of deformity correction

Different techniques exist depending on their mode of action: compression, distraction, or guided [154], all of which attempt to modulate vertebral growth by imposing differential

concave-convex growth. Fusionless surgery is suitable for patients with remaining growth, and was suggested as an alternative to non-compliance to bracing. Fusionless techniques differ according to their objective; these can be used to delay fusion for early onset scoliosis, to avoid pulmonary failure, to treat moderate progressive curves, or avoid degeneration of segments above and below fused vertebrae. The following sections will provide an overview/critic of the common compression, distraction, and guided fusionless implants used to treat scoliosis in humans.

#### **1.4.3.1 Distraction-based and Guided-based**

Presently, growing rods (GR) and VEPTR (Vertical expandable prosthetic titanium rib) constitute the widely applied distraction-based methods. GR was based on the original Harrington growing rod technique [155], which consisted of inserting an expandable rod on the concave portion of the deformed spine. The technique was then developed to include a dual growing rod construct placed subcutaneously or intramuscularly via hooks and screws [156]. Typically, the procedure is performed for early onset scoliosis (EOS) and congenital scoliosis to avoid short trunk height following fusion of curves greater than 60°. GR is invasive as it requires periodic lengthening (approx. every 6 months) until fusion is performed at skeletal maturity with complications including laminae breakage, screw pull-out, implant breakage, and infections [156]–[159]. VEPTRs originally aimed at treating thoracic insufficiency but the technique is currently used to correct spinal deformity in EOS. The construct requires lengthening every 6 months, increasing surgical complications [105], [156], [159], [160]. An emerging magnetic construct based on transcutaneous distractions via a magnetic field is gaining popularity [161]. Current case studies are limited; however, preliminary outcomes indicate less psychological impact to patients and parents, fewer distraction surgical procedures, and improved quality of life. Yet, complication rates outweigh the benefits afforded by the construct [159].

Guided-based techniques rely on spinal growth to passively expand or lengthen the construct using sliding rods. Two promising approaches are clinically employed. The Shilla technique consists of dual rods, with fusion at the apex and non-locking screws at the end vertebrae. As the patient grows, the rods slide at the extremities, guiding the spine [162]. The second technique relies on the modern Luque trolley system [163] consisting

of 4 rods (2 on each side of the spine) fixed at the end vertebrae while connecting via guide wires within the instrumented region allowing the spine to grow whilst the rod slide respectively. Both guided-based techniques are promising as they do not require periodic surgical lengthening interventions.

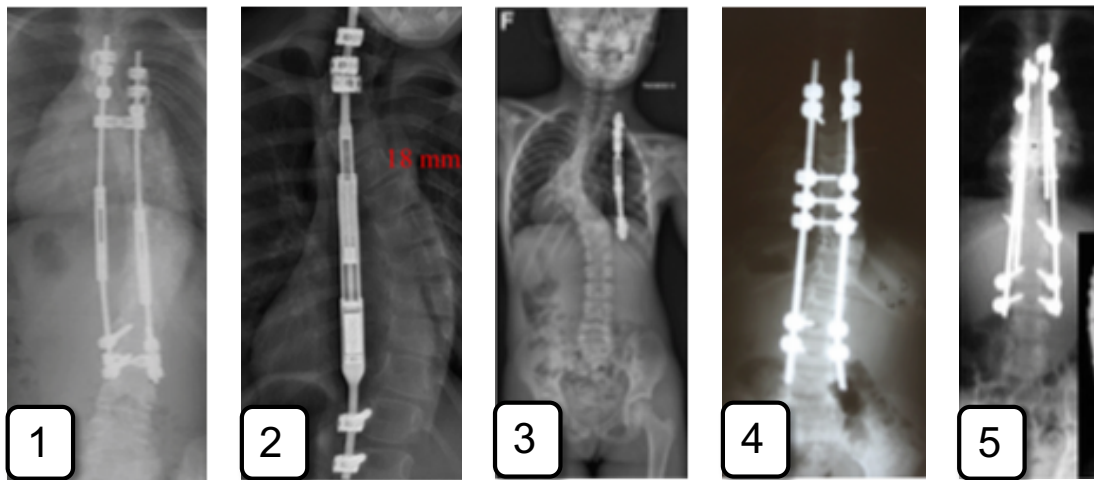


Figure 1-31: Radiographic examples of: 1- Growing rods, 2- Magnetic growing rod, 3- VEPTR, 4- Shilla, 5- modern Luque trolley (1 to 4 modified from [159], 5 modified from [163])

An internal growing rod system was recently tested on 3 female AIS patients with curves between  $43^{\circ}$ - $53^{\circ}$  and Risser 1-4. The construct consists of a growing rod affixed at the concavity of the apical region (Figure 1-32) and is elongated via prescribed physical exercise due to an internal ratchet system [164]. The preliminary clinical application showed promising curve correction ( $45^{\circ} \pm 8^{\circ}$  to  $28^{\circ} \pm 8^{\circ}$ ); yet, results were hindered by the small sample size and patients past growth peak.

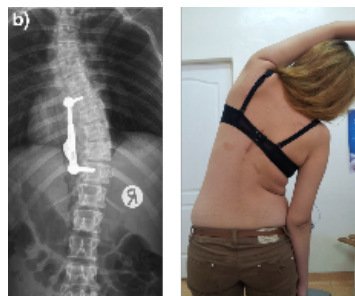


Figure 1-32: ApiFix system (left) insert on the concavity of the apical region. Daily exercise for system elongation via a ratchet system (Modified from [164])

Thus far, distraction and guided-based techniques remain the foremost recommendation for EOS [159], [162] with application in AIS. To take full advantage of the pubertal growth spurt, compression-based implants are currently used in a clinical context to treat AIS.

#### 1.4.3.2 Compression-based

Some of the early clinical applications of compression-based implants date back to the works of Smith *et al.* where curve progression at the instrumentation site was arrested in 3 patients with compensatory curve development at uninstrumented regions [165]. The authors speculated that, had they increased the number of instrumented vertebrae, a better control over the curvature, even correction, might have been achieved. However, limited knowledge related to this emerging technique resulted in poor correction outcomes. Using shape memory alloy (SMA) staples (Figure 1-33), which clamp into the vertebral bodies at body temperature increasing compressive stresses on the growth plate, Betz *et al.* have shown a success rate of 79% for thoracic curves and 87% for lumbar curves with 84% kyphosis and 87% lordosis of their normal range [152], [153]. The clinical trials aided at establishing guidelines to the treatment of AIS using this technique, although the success threshold was relatively generous ( $>10^\circ$  correction). The authors recommended instrumenting progressive curves  $<45^\circ$  with sufficient remaining growth (Risser 0-1).

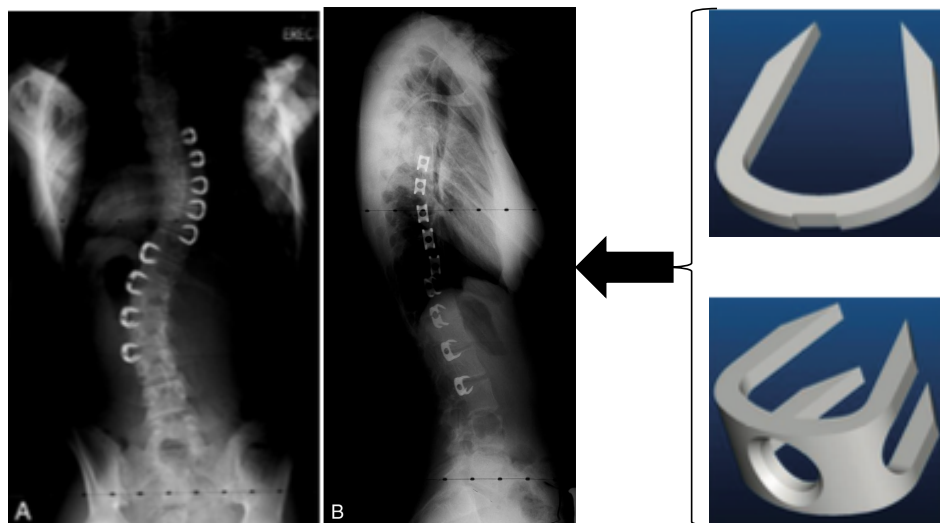


Figure 1-33: Shape memory alloy staples clinical example (Modified from [152], [153])

Another promising fusionless technique relies on vertebral body tethering (VBT, Figure 1-34), which consists of inserting custom vertebral body screws on the convex side interconnected with a tightened polyethylene ligament. The construct compresses the growth plate, similar to SMA staples, with the added benefit of flexibility [166]. Early applications were demonstrated on a single case (8y boy, T6-T12 tethering) corrected from 40° to 6° Cobb after 4 years of growth [167]. Although the study reported remarkable coronal correction and control over the sagittal plane, it was limited to one reported outcome. Recent clinical investigations demonstrated well-established findings using VBT of curves generally below 45° [168]. VBT was performed on 11 skeletally immature patients aging  $12.3y \pm 1.6y$  with  $44.2^\circ \pm 9.0^\circ$  and  $25.5^\circ \pm 8.7^\circ$  coronal thoracic and lumbar curves respectively. In this small cohort, coronal curves were corrected by 70% and 71% respectively over 2 years follow-up with axial rotation correction ( $12.4^\circ \pm 3.3^\circ$  to  $6.9^\circ \pm 3.4^\circ$ ). Furthermore, the techniques demonstrated promising control of kyphosis and lordosis with little to no neurological, infectious, or hardware complications. More importantly, this recent clinical trial established preliminary guidelines for VBT treatment strategies aimed at curves between 35° and 60° (flexible to <30°) with sufficient remaining growth (Risser  $\leq 1$ ). Peculiar outcomes indicated possible overcorrection via VBT requiring additional intervention for tether relaxing. Although promising, the temporal influence of current clinical treatments on the IVD health is halted by the insufficient solid long-term clinical outcomes. Experimental testing of current compression-based fusionless devices revealed changes in disc viable cell density and reduced vascularization of the endplates, which may lead to disc degradation [166], [169]. Also, earlier experience with stapling postulated that increasing compression on the intervertebral discs may increase the risk of spontaneous spinal arthrodesis [152]. Thus, caution in targeting curves with respect to their progressive nature as well as residual growth becomes utmost challenging, speculative of further long-term assessment on larger cohort and, perhaps, combined with numerical modeling, would establish specific clinical assessment and surgical guidelines for optimal correction [170], [171].



Figure 1-34: Vertebral body tether: Postero-Anterior view (left), lateral view (right) (Modified from [168])

Compression fusionless implants, by the nature of their design and mechanical action, act on the vertebral bodies. Thus, designing and inserting these devices should naturally avoid vascular and soft tissue damage. At present, VEPTRs, growing rods, magnetic growing rods, and the SHILLA technique have been approved by the FDA. Other devices, such as vertebral body tethering, vertebral body stapling, and the Luque trolley technique are used off-label in a clinical setup. Over the years, several attempts at assessing the biomechanical, *in vivo*, and corrective potential of new devices have been pursued in an experimental set-up. To fully appreciate the extent of the work leading to current (and future) successful clinical applications, an overview of the experimental endeavors is warranted.

#### 1.4.3.3 Experimental fusionless assessment

Fusionless devices are experimentally tested via two approaches. The first relies on inducing a deformity in an otherwise normal spine (inverse approach) based upon the premise that, if the device induces local and global spinal changes, it can, theoretically, correct an existing deformity. The second, a 2-step approach, is based on using the investigated device to correct an already induced deformity (

Table 1-4). As scoliosis is exclusive to humans [172], several investigators have ventured to develop *in vivo* porcine [173]–[175], ovine [176], and caprine [130], [177] scoliosis

models best mimicking the three dimensional aspect of idiopathic scoliosis. Some of the early applications of compression-based implants date back to the works of Nachlas and Borden [178] with successful creation of a deformity on normal canine spines instrumented with a 3 level staple. Subsequently, the authors attempted correcting the deformed spine by inserting staples on the curve convexity and noted minor curve correction with creation of compensatory curves at non-instrumented levels. These early attempts were based on rudimentary understanding of the growth modulation process, let alone, its application on spinal corrective treatment; however, they set the framework for future development. Braun *et al.* ventured to understand the biomechanics of two early implant designs, namely SMA and bone anchor ligaments. Their well-established finding, many of which set the basis for current clinical applications, have demonstrated the different mechanisms by which these implant designs act and the corrective potential linked to their application. By attempting to correct a deformed goat model, the authors concluded that SMA staples can correct moderate curves with bone anchor ligaments achieving a better correction [179], [180]. Further attempts using a custom staple (Figure 1-35) endoscopically implanted on the right lateral aspect between T6 and T12 of immature pigs have successfully induced a coronal deformity ( $16.4^{\circ} \pm 5.4^{\circ}$ ) by passively restraining growth [181]. However, the device, aiming at correcting the frontal plane, resulted in variable effects on the sagittal plane. Although its growth modulation was extensively documented [46], the implant was shown to reduce normal dynamic loading on the disc [71] due to its inherent rigid design [182].

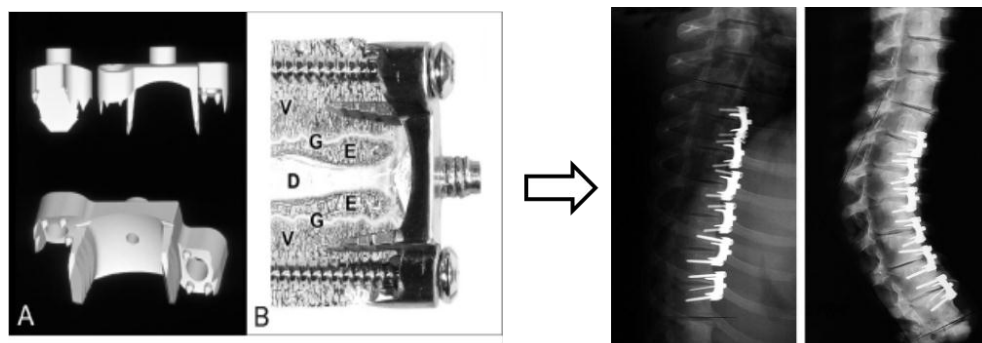


Figure 1-35: Custom stainless steel staple and bone screw fixation (Modified from [181])

Newton *et al.* have further pursued a different compression-based approach relying on segmental anterior spinal tethering. The implant design works akin to bone anchor



ligaments relying on anterior vertebral body lateral compression through segmental cable tensioning. Attempts on bovine thoracic vertebrae were successful at manipulating growth by unilaterally compressing an otherwise normal spine [183] (Figure 1-36). The authors reported screw pullout with adverse increase in the sagittal profile. It was hypothesized that the rigidity of the stainless steel cables, along with the rapid growth of bovine vertebrae, resulted in excessive tensile loads leading to screw pullout, further demonstrated by a lower failure rate using a two cable setup [183]. Later, using a polyethylene cable on immature pig vertebrae, the authors successfully induced a coronal deformity ( $30^{\circ} \pm 13^{\circ}$  after 12 months growth) with wedged instrumented vertebrae and intact bone-screw interface as evidenced by histological assessment [184]. Interestingly, reversed IVD wedging (discs wedged opposite to vertebrae) was noticed over the growth period and no disc degeneration was observed. The authors further explored the effect of pre-tensioning and concluded that the latter created an immediate deformity (intra-operative) compared to non-tensioned; however, coronal and sagittal angles, and vertebral wedging were similar after 12 months growth, with no signs of disc degeneration [185]. Similar spinal motion was also noticed between non- and pre-tensioned groups suggesting cable tension was dissipated within the intervertebral disc as a consequence of long-term vertebral growth and growth restraint. These extensive animal trials have shown promising results as to the corrective and, to a certain extent, motion preservation potential of SMA staples and anterior vertebral body tethering, which explains their current clinical application in adolescent idiopathic scoliosis.

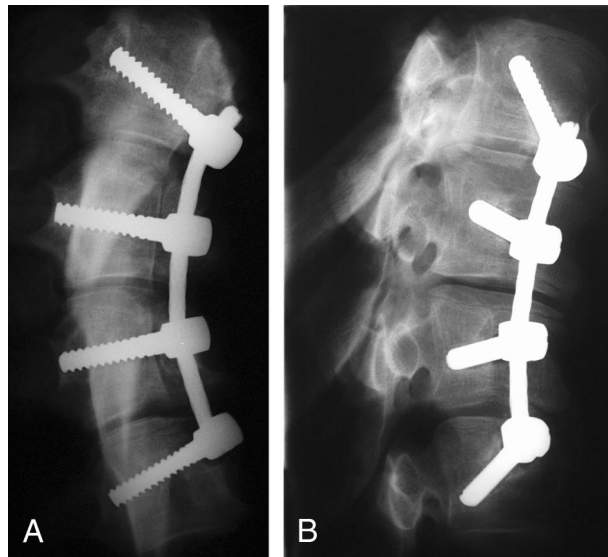


Figure 1-36: Bovine thoracic vertebral stainless steel cable tethering (Modified from [183])

Despite their promising outcomes, the above implants bridge the intervertebral gap and predominantly compress the IVD to achieve the desired growth modulation. A growing concern is linked to the long-term influence on the intervertebral disc health due to increased segmental compressive stresses and relatively reduced spinal motion [166], [185], [186]. On a rabbit model, Hee *et al.* demonstrated that compressed discs resulted in reduced disc height with degenerative signs, reduced cell and extracellular matrix synthesis, reduced vascular channel volume, and showed signs of ossified endplates [187]. By reversing the load (applying distraction), cell and ECM synthesis, and vascular volume increased but ossified endplates remained, suggesting morphological alteration to the disc may be regained after load removal. Similarly, SMA stapling and anterior body tethering were shown to decrease disc cell density with increased apoptosis by inducing a deformity via these implants on immature goats [166]. These findings were consistent with observed AIS human apical discs, which may indicate these metabolic changes are secondary to the progressive curve creation. Conversely, Upasani *et al.* have found metabolic changes quantified by lower IVD water content and height following 6 months anterior VBT with no early degenerative signs [188]. Demirkiran *et al.* found similar disc morphologies between instrumented and control animals following repeated distractions indicative of preserved disc health for spine under fusionless instrumentation [186]. Hence, these histomorphometric results suggest disc compression (vs distraction) may

adversely alter disc histology. Yet, current disc health analyses are conducted on healthy discs with metabolic changes maybe occurring secondary to the implant insertion. Thus, such *in vivo* conditions do not depict the actual scenario perceived in AIS treatment where discs are inherently subjected to an unnatural mechanical loading environment.

With this rising concern, new endeavors were sought to achieve vertebral growth modulation without bridging the intervertebral disc space. Early attempts were performed by Schmid *et al.* using a intravertebral hemi-staple on 4 rat caudal vertebrae ( $n = 11$ ). Briefly, the device consisted of a prong located between the growth plate and the disc and attached to the vertebral body wall, without spanning the IVD space (Figure 1-37). The authors demonstrated the growth modulating potential of this novel device by inducing  $30^\circ \pm 6^\circ$  and  $10^\circ \pm 3^\circ$  mean maximum Cobb and vertebral wedging respectively with 69% unaltered discs [189]. However, the unassuming size of the implant challenged insertion within the limited space provided by rat tails. The device was later upsized to adapt larger porcine thoracic vertebral morphologies and was shown to induce  $6.5^\circ \pm 3.5^\circ$  and  $4.1^\circ \pm 3.6^\circ$  Cobb and vertebral wedging [190], respectively, with no adverse effects on disc when consistently placing the device (over three months growth) [191]. Though preliminary, this promising approach warrants further in-depth development to further optimize such minimally invasive implant.

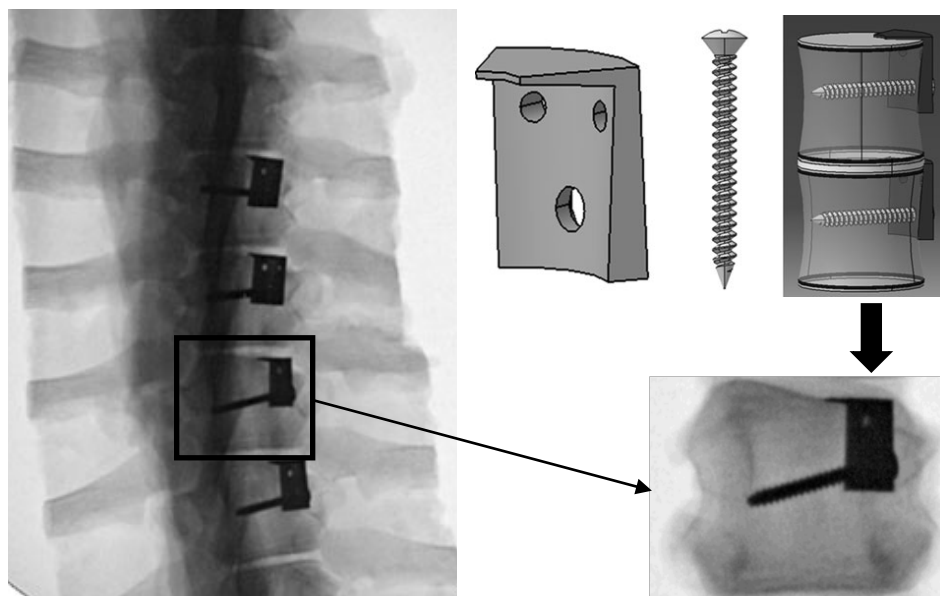


Figure 1-37: Hemi-staple design. Fluoroscopy images of excised thoracic spine after 3-months curve induction on immature pigs (Modified from [190])

Table 1-4: Summary of experimental fusionless implant testing and development of animal scoliosis models

Animal	Reference	Technique	Results, Comments, Prospective
<b>Dog</b>	Nachlas 1951 [178]	Deformity induction using unilateral staple spanning 2 lumbar IVD units and Contralateral stapling for correction	Induction and corrections successful with creation of compensatory curve. Some implant loosening and breakage observed. First attempt at spinal stapling to control growth.
<b>Rabbit</b>	Smith 1987 [192]	Tethering thoracic spine (T4-T10) into asymmetric lordosis	Progressive structural scoliosis with localized spinal cord damage. Limited sagittal plane deformity control.
<b>Cow</b>	Newton 2005 [183]	Vertebral bicortical screws T6-T9: ① 1 screw/vert + 1 cable, ② 2 screws/vert + 2 cable	① Variable instrument fixation and inconsistent curve creation as opposed to ②. Suggesting more stable construct with dual stainless steel cables and screws. Poor sagittal control.
<b>Goat</b>	Braun 2003 [177]	Posterior asym. rigid and flexible tethering with conv. rib resection & conc. rib tether.	Scoliosis induced with rigid and flexible tether, large lordosis creation with latter.

<b>Goat</b>	Braun 2005-2006 [179], [180]	SMA staples for curve correction.	Curve correction possible, for moderate curves, with SMA staples, better correction with bone anchor ligament.
<b>Pig</b>	Wall 2005 [181]	Rigid staple hemiepiphysiodesis with screw fixation	Curve creation (8 weeks), little screw loosening. Sagittal profile varied with progressive kyphosis. Custom staple & screw fixation minimized implant failure.
<b>Pig</b>	Newton 2008 [184]	Anterior bone anchor screws + tether	Curve creation with opposite disc wedging, with no sagittal profile changes. IVD intact. Device may be used to correct, without impeding IVD health.
<b>Pig</b>	Schwab 2009 [173]	Unilateral posterior ligamentous tether, 8 segments, ipsilateral 5 level rib tethering	Lordoscoliotic curve creation with large post-op curve due to numerous instrumented levels. Cannot predict residual curve creation after tether removal. Could be used as scoliosis model for implant testing.
<b>Pig</b>	Odent 2009 [174]	Posterior laterally offset tether	Created structural scoliosis model with apparent chest wall deformity. Could be used as a scoliosis model for implant testing.
<b>Goat</b>	Zhang 2009 [130]	Posterior pre-bent rod with contralateral rib resections	Scoliosis like curve creation with vertebral wedging, trunk deformity and axial rotation. No curve progression after rod removal with persistent growth shown in histology. Could be used as a scoliosis model for implant testing.
<b>Pig</b>	Newton 2011 [185]	Anterior bone anchor screws + tether	Tested tether pre-tensioning did not alter long term curve creation.
<b>Pig</b>	Newton 2011 [193]	SMA square cross-section rods: single or dual, locked or unlocked	Coronal deformity created. No difference between single and dual, with unlocked tending to higher deformity. Endplate fracture in 85% of cases due to high SMA force. Better kyphosis control in single vs dual rod. Square cross-section may be used for axial rotation correction.
<b>Pig</b>	Patel 2010 [194]	Anterior bone anchor screws + tether	Curve corrected with no change in the sagittal plane.
<b>Pig</b>	Carreau 2012 [73]	2 SMA staples in mid-thoracic region	Small deformity created. Not enough staples for large deformity. Signs of GP closure.
<b>Pig</b>	Driscoll 2012 [190]	Hemi-staple (localized to upper growth plate) without spanning IVD	Small curve creation. IVD health conserved when implant positioned over the growth plate. Sagittal plane conserved with evidence of inverse disc wedging.
<b>Pig</b>	Moal 2013 [76]	Anterior correction via a custom tether targeting 3D correction	Removal of inducing tether does not stop vertebral growth. Custom tether reduced coronal deformity and re-established normal sagittal plane. Apical axial rotation and vertebral wedging corrected.

<b>Sheep</b>	Burke 2014 [176]	Posterior laminae + ipsi-lateral rib tethering + contralateral rib resection	Ovine scoliosis model developed. First attempt shows coronal deformity outweighed by sagittal deformity with highest deformity in growth peak period. Rotational deformity evident. Maybe used to assess fusionless devices with specific modification to inducing technique
<b>Sheep</b>	Burke 2014 [195]	Hinged lateral implant	Aimed to correction coronal and axial deformity with no adverse changes to sagittal plane. Shown to induce deformity while corrective potential outweighed by stiff induced deformity and counteraction of rib tethering. Promising preliminary trial for 3D spinal deformity correction.
<b>Pig</b>	Liu 2015 [196]	Posterior pedicles screw tethering	Coronal and sagittal deformity induced. First trial at posterior pedicular tethering for fusionless correction. Sagittal deformity lordotic in nature, outweighing the aim at re-establishing kyphosis in scoliotic deformity. Early metabolic signs of disc immobilization.

As previously explained, scoliosis is a three dimensional deformity; thus, an ideal fusionless device is one capable of addressing corrections in all three anatomical planes. The presented devices thus far act, predominantly, on a single anatomical plane, mainly the coronal plane with varying effects on the sagittal profile. More specifically, coupled effects of the current implants resulted in either variable [181] or unchanged [184], [190], [194] sagittal plane deformity with rotational deformity correction scarce or as a side-effect [188]. A recent investigation explored a new hybrid anterior tethering system, which was tested *in vivo* on immature porcine spine with an already induced deformity via Schwab's *et al.* [173] porcine spine model. The study explored two groups with progressive deformities: untreated (inducing tether released, n=5) and treated (correction via custom anterior tether, n=5) (Figure 1-38). After 20 weeks of growth, the newly designed tether succeeded at correcting the otherwise progressive coronal, sagittal, and rotational deformities [76]. Another interesting implant relied on a hinged mechanism which, as the spine grows, corrected the coronal and transverse planes while preserving sagittal plane (Figure 1-39). The authors were successful at inducing a deformity on normal sheep spines with no change in the transverse or sagittal planes since the implant's hinge design corrects rotational deformities unidirectionally. In other terms, a normal spine does not present rotational malformation, and thus, none exist to correct. Conversely, they also

attempted correcting an already induced deformity via this new implant with no success as its corrective potential was outweighed by the increased spinal and ribcage stiffness following the inducing procedure involving posterior laminae tethering combined with ipsi-lateral rib tethering and contra-lateral rib resection [195]. The authors hypothesized that the rib tether (un-extracted following the inducing phase), along with morphological spinal changes, contributed to spine stiffening.

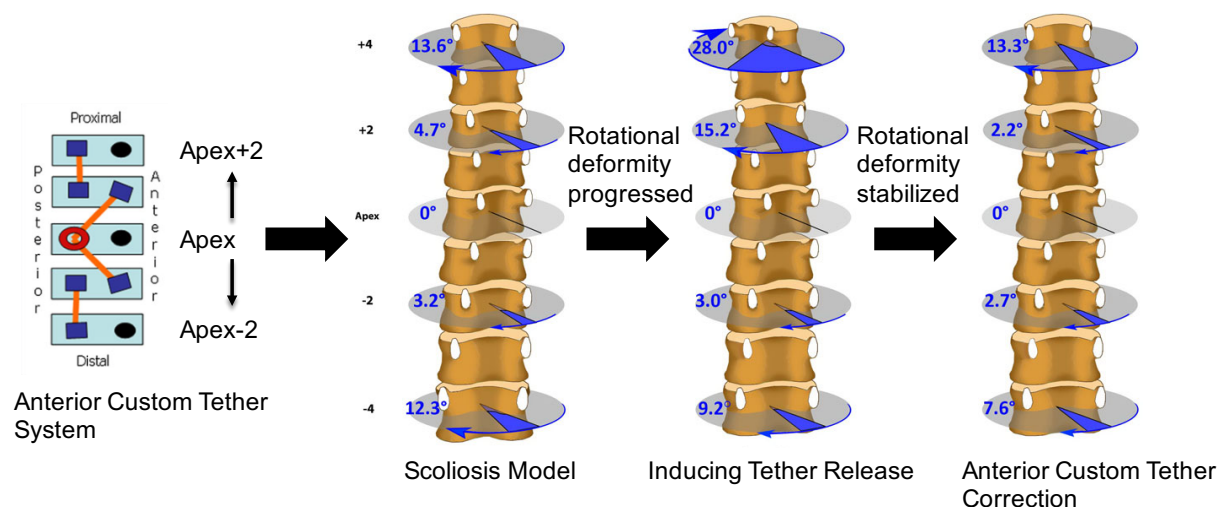


Figure 1-38: Hybrid anterior tether aiming at correcting rotational deformity (Modified from [76])

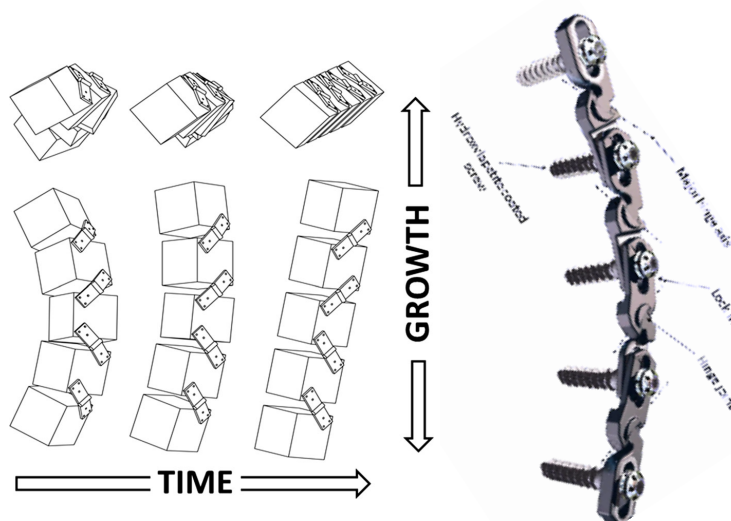


Figure 1-39: Hinged implant design aiming at correcting all three anatomical planes as the spine grows (Modified from [195])

Although animal trials support the hypothesis that new implants are best tested in similar conditions as their human application, i.e. idiopathic-like *in vivo* animal trials, to date, both the inverse and the 2-step approach remain widely applied experimentally. Yet, the 2-step approach is quite expensive and extensive as it requires two surgical interventions (induction + correction) each of which can span lengthy time-frames and affect spinal biomechanics. Additionally, the presented experimentally tested implants exhibit several shortcomings innate to their specific designs as they act differently on each respective anatomical plane or bridge the intervertebral disc space. Currently, no long-term (more than 1 year follow-up) has been explored experimentally to assess the real lifelong influence on disc health. Additionally, animal trials allow the study of the potency of new implants in shorter periods of time (e.g. pigs grow approx. 1.1 mm/vertebra/month [75], [76], [190], [197] while adolescents during growth spurt grow 1 mm/vertebra/year [66]). Finally, current experimental *in vivo* trials typically aim at assessing the efficacy, functional application, long-term growth manipulation, and device/bone interface integrity. Preliminary in their nature, these trials evaluate new implant concepts to confirm growth modulation in an *in vivo* environment prior to assessing biocompatibility restrictions. To date, Wall *et al.* rigid custom staple is the sole device currently approved by the FDA amongst those presented in

Table 1-4. Future applications of these devices would aim at reducing, even eliminating, possible toxicity imposed by a foreign object introduced in living tissue to further meet FDA and ISO 13845 requirements for medical devices. However, biocompatibility is beyond the scope of this thesis work but warrants further in-depth evaluation to ensure safe application of experimentally tested devices when transferred clinically. Nevertheless, *in vivo* trials can be time-consuming when exploring a spectrum of implant designs and transfer the new knowledge to human cases.

## 1.5 Biomechanical Modeling of the Scoliotic Spine

As previously stated, finite element modeling demonstrated its practical application in spinal biomechanical investigations. These numerical tools have been explored to simulate complex biomechanical spinal behaviour, bone remodelling, spinal disorder pathomechanism theories, disc degeneration, amongst other. Nevertheless, modeling



strategies should be handled by acknowledging their limits and simplified assumptions. With the wide range of its applicability, focus will be attributed to investigations applied to scoliotic spines with attention to finite element modeling.

Typically, FEM geometries can be parametric or personalized. The former involves a set of parameters describing geometric characteristics such as spinal global shape, local vertebral morphology, which in turn, are translated into nodal coordinates used to build the model. Advantages of such modeling techniques are reflected by the simplicity of adapting geometric parameters to build distinctive models, scaled geometries, or representing generalized deformed spines. Conversely, personalized models reflect the actual geometry of the patient obtained via 3D reconstruction techniques.

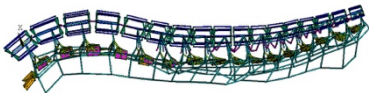
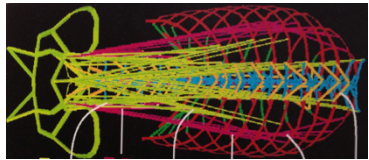
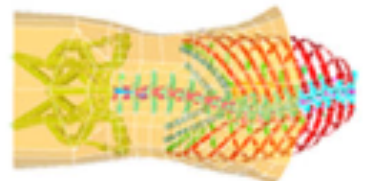
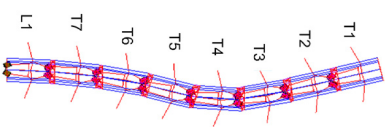
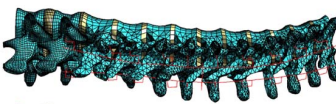

### **1.5.1 Finite Element Modeling**

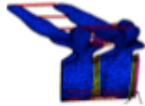

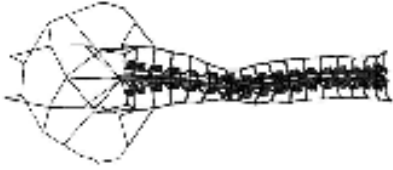
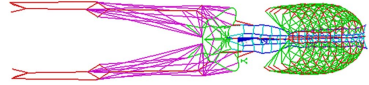
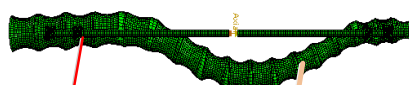
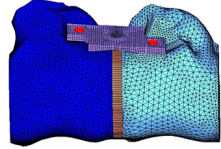
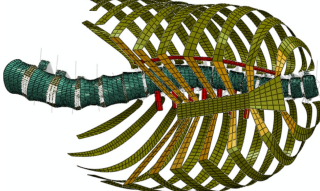
Finite element models offer alternative tools to simulate various functional parameters to address inherent limits imposed by experimental testing (reproducibility and variability). Thus, design, experimental, and morphological parameters can be modified and tested in a reproducible manner. Moreover, FEM provides internal stress and strain analysis difficult, sometimes unfeasible, to obtain in vivo or in-vitro.

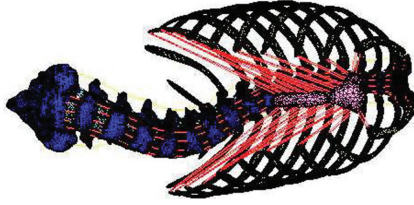
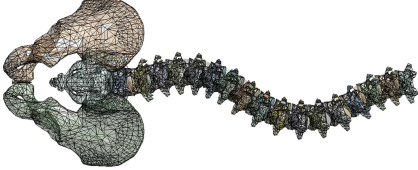

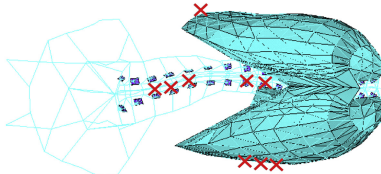
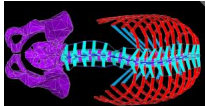
One should consider each model's limitations at the cost of the destined application. Simulation processing time versus level of details required are certain restrictions justifying the use of specific modeling techniques as opposed to others. Results interpretation in FEM is equaled by the quality of the model and the appropriateness of its application. Detailed vertebrae and intervertebral discs models (solid elements) allow for detailed regional stress/strain calculation in vertebral cortical and cancellous bone, growth plates, and IVD. Beam-based models can be used to obtain qualitative and quantitative stress analysis, emphasizing the overall model's biomechanical behavior rather than details within the different spinal elements. FEM are simplifications of the behavior of an actual physical element, which emphasizes the chosen assumptions in the modeling techniques and the interpretation of the results accordingly. These assumptions may be linked to adopted mechanical properties, mesh size and density, boundary conditions, and applied loads.

Focus will directed towards current models involved in the study of scoliosis and treatment strategies over the past decade. The following table summarizes the description of current models and their application.

Table 1-5: Summary of current finite elements models in scoliosis research

Model	Description	Application
 Villemure 2002 [34]	T1-L5. Beam elements. Patient specific biplanar reconst.. Post. elem. + facets + ligs. Growth modulation programmed.	Explore scoliosis pathomechanism. Explore effect mech. load alteration on curve progression. Influence of pedicle growth asymmetry on curve progression
 Huynh 2006, 2007 [125], [131]	T1-S1. Beam elements. Patient specific biplanar reconst. Post. elem. + facets + ligs. Rib cage, sacrum. Spinal muscles. Growth modulation programmed.	Simulate curve progression due to erector muscles impairment.
 Clin 2007, 2011 [35], [143]	T1-S1. Beam elements. Patient specific biplanar reconst. Post. elem. + facets + ligs. Rib cage, sacrum, abdominal tissue solid elem.	Compare & optimize brace design for scoliosis correction. Evaluate gravity application methods on spinal loads and brace treatment
 Lafortune 2007 [217]	Chicken T1-T7, L1 spine. Beam elements. Post. elem.+facets+ligs. Growth modulation programmed.	Simulate curve progression following asym. spinal load (moment) replicating curve progression in pinealectomized chicken.
 Rohlmann 2008 [210]	T3-L2, rigid vertebrae, Linear elastic, NP incomp., AF hyperelastic Neo-Hookean, Ligament spring elem. CT scan reconst.	Simulate immediate impact of different posterior instrumentation, pedicle screws, and instrumentation variants.
 Lalonde 2008, 2009 [206], [207]	T1-L5. Patient specific biplanar reconst, Cort., cancellous, no post. elem, GP 3 zones, AF+fibers, hyperelast. NP incomp., Apophyseal ring.	Simulate curve correction during lat. decubitus positioning in surgery. Simulate the immediate corrective effects of vertebral SMA stapling.

 <p>Lin 2009 [205]</p>	<p>T7-T8 CT reconst, GP divided in 3 zones. Growth modulation programmed. Linear elastic mech. prop.</p>	<p>Evaluate difference between 2 growth modulation strategies and new energy based growth model under combination of tension, compression, &amp; shear loads.</p>
 <p>Driscoll 2009, 2011, Shi 2011 [42], [126], [127]</p>	<p>T1-L5. Patient specific with parameterization potential. cort., cancellous, no post. elem, GP 3 zones, Linear elastic NP+AF. Growth modulation programmed.</p>	<p>Investigate concave-convex prop. biases in curve progression. Compare corrective effect of ≠ fusionless implant techniques. Investigate abnormal anterior growth in AIS progression.</p>
 <p>Drevelle 2010 [120]</p>	<p>T1-S1, Pelvis, vertebrae rigid beam, facets, ligament spring elem, pelvis stiff beams, IVD as beam, personalized IVD props., growth sims 15% vertebral height lengthening.</p>	<p>Simulate curve progression patterns and pathomechanism hypothesis.</p>
 <p>Driscoll C 2012 [208], [209]</p>	<p>T1-S1. Beam elements. Patient specific biplanar reconst. Post. elem. + facets + ligs. Rib cage, sacrum, lower limbs.</p>	<p>Study the effects of lower limbs position on spinal geometry during surgery.</p>
 <p>Abolaeha 2012 [212]</p>	<p>T1-L5. Parametric. cort., cancellous, no post. elem, GP 3 zones, Linear elastic NP+AF. Growth modulation programmed.</p>	<p>Simulate the long-term correction of a Harrington-like growing rod instr. with periodic 6-month lengthening.</p>
 <p>Kumar 2012 [218]</p>	<p>T7-T8 functional unit, CT reconstr. Growth plate and growth dynamics.</p>	<p>Simulate custom staple prestress influence on longitudinal growth. Compare predictive simulation to experimental results.</p>
 <p>Little 2013 [211]</p>	<p>T1-L5. Solid Elements. Patient specific, CT reconstruction. Post. elem. + facets + ligs: beam and spring elements. Rib cage shell elements.</p>	<p>Simulate anterior rod and screws scoliosis curvature correction.</p>

 <p>Zhang 2013 [216]</p>	<p>T1-S1, Pelvis, CT reconstruction, NP + AF, no grav. and muscles, Rib cage. Solid elements, cartilage beam elem.</p>	<p>Simulate different surgical correction approaches prior to intervention.</p>
 <p>Driscoll 2013 [215]</p>	<p>T1-S1, Pelvis. Solid linear elem. Patient specific geom., NP+AF, spinal ligament spring elem. Rigid vertebrae.</p>	<p>Simulate different posterior instr. correction strategies with two screws head designs.</p>
 <p>Agarwal 2015 [213]</p>	<p>T1-S1, generalized juvenile model Cobb 35°. Cort. cancellous, post. elem, NP, AF hyperelastic, Ligament spring elem., GP and growth modulation.</p>	<p>Simulate the long-term correction of a Harrington-like growing rod instr. with different distraction forces and distraction intervals</p>
 <p>Vergari 2015 [214]</p>	<p>T1-S1. Beam elements. Patient specific. Post. elem.+facets+ligs. Rib cage, sacrum, abdominal tissue. Intercostal Membrane elastic shell. Patient specific rib and costal cartilage prop. Gravitational and muscles forces excluded.</p>	<p>Simulate curvature treatment via orthotics.</p>
 <p>Clin 2015 [170]</p>	<p>T1-S1, Pelvis, Patient Specific reconst., Post. elem.+ ligs, ribcage, growth plates and growth modulation</p>	<p>Simulate fusionless implant correction and insertion variants.</p>

Applications of these models can be grouped into 2 main avenues: Immediate and long-term impact simulations.

Lalonde *et al.* [206], [207] developed a detailed T1-L5 FEM of the anterior aspect of the vertebra, including the epiphyseal plates and spinal ligaments. The model allowed to simulate the immediate deformity correction and determine growth plate stresses following insertion of shape memory alloy staples and simulate intra-operative lateral decubitus patient positioning and compare spinal shapes indices to patients' data. Clin *et al.* [35], [143] built upon Aubin's model [219] a personalized beam element based thoracolumbar FEM including the vertebrae, ribcage, pelvis, major spinal ligaments, and

abdominal soft tissue. The model served to test the immediate spinal corrections following spinal bracing, design and optimize orthotics, as well as test different gravitational load application methods. Similarly, Vergari *et al.* [214] added personalized ribcage properties and intercostal membrane to simulate the impact of brace treatment. Driscoll *et al.* [208], [209] added to the Clin's model by incorporating the lower limbs to evaluate the effect of intra-operative limb positioning on spinal geometry changes. Rohlmann *et al.* [210] developed a detailed volumetric T3-L1 model based on CT scans, including the major spinal ligaments, and aimed at simulating the immediate impact of different posterior instrumentation variations on spinal correction and vertebral loads. Little *et al.* [211] proposed a personalized detailed hybrid model of the thoracolumbar spine, including the ribcage, to simulate curve correction following anterior instrumentation strategies. Driscoll *et al.* [215] developed a simplified FEM of the thoracolumbar spine and pelvis, excluding the ribcage, to simulate surgical maneuvers involved in various posterior spinal instrumentation. Similarly, Zhang *et al.* [216] developed a detailed FEM with inclusion of the ribcage and aimed at simulating various surgical correction approaches to determine the optimal intervention.

Other FEMs integrated growth dynamics to simulate the long-term effects of growth-sparing implants and curve progression patterns. Villemure [34] constructed a thoracolumbar patient specific FEM using beam and spring elements to represent vertebrae and ligaments, respectively. Growth modulation was programmed according to the Hueter-Volkman principle with the model serving to simulate different curve progression patterns, followed by other investigators [120]. Appending the ribcage and spinal erector muscles to the previous model, Huynh [125], [131] tested the impact of differential neurocentral junction growth and erector muscle impairment on curve progression. Lin *et al.* [205] generated a detailed T7-T8 functional unit volumetric model integrating the growth plates and growth dynamics and evaluated differences between two growth modulation theories under various loading patterns. To complement Hui's model, Driscoll [42], [126], [127] included growth dynamics on a parametric thoracolumbar FEM of the anterior spine to simulate curve progression following concave/convex mechanical properties bias, assess fusionless implant long-term correction, and compare model progression to patient specific data. Other parametric models included growth

dynamics to simulate curve correction following Harrington-like growing rods [212] and evaluate the effects of distraction forces and lengthening intervals [213]. Using a FEM, Stokes *et al.* [220] integrated 11% asymmetrical concave/convex rib growth to test hypothesis of scoliosis initiation indicating asym. rib growth resulted in axial rotation and curve progression similar to adolescent scoliosis. Carrier *et al.* [221] investigated rib shortening or lengthening as alternative corrective procedures for AIS with results indicating reduced vertebral wedging and Cobb angle with deterioration of apical rotation and rib hump. These models highlighted the important contribution of the ribcage; yet, no attempt at assessing the biomechanical contribution of the latter in fusionless surgery has been previously attempted.

Nevertheless, these models reflected human juvenile or adolescent spinal geometries while current growth-sparing devices continue to be tested, experimentally, on animal equivalents. Computational animal models integrating growth dynamics to simulate curve progression patterns and fusionless implants are scarce. Lafortune *et al.* [217] developed a simplistic chicken thoracic spine FEM simulating induced scoliotic-like deformation following asymmetrical loads to emulate curve progression following pinealectomy. Odent *et al.* [222] predicted the intraoperative deformity creation via various ligament tethering configurations using a 2D FEM of 11 porcine thoracic vertebral bodies and intervertebral discs (IVD). The model used human mechanical properties and lacked growth dynamics to predict long-term deformity prediction and was primarily devised to test expected generalized immediate deformities. Kumar *et al.* [218] developed a porcine T7-T8 functional unit FEM including growth dynamics to compare simulated a custom implant growth restraint. Yet, the model did not capture the complete spinal biomechanical behavior in fusionless implant and focused on a single implant design. Thus, a review of the literature does not reveal any attempts at developing a complete porcine spine thoracolumbar FEM integrating growth dynamics, the ribcage, and major spinal ligaments for the simulation of immediate intra-operative spinal manipulations, progressive scoliosis, long-term curve induction or correction, and fusionless implant analyses.

## CHAPTER 2 RESEARCH RATIONAL, OBJECTIVES, AND HYPOTHESES

The prevailing conventional surgical scoliosis treatment relies on re-aligning the spine with instrumentation accompanied by segmental spinal fusion, invasively reducing spinal mobility. Over the past two decades, fusionless growth-sparing implants have undergone extensive investigations with increasing understanding of their biomechanical response on the spine. With recent clinical applications demonstrating the promising potential of these growth harnessing implants, more prominently in the form of vertebral body tethering, increasing interest have materialized their future application, future development and improvement. Despite encouraging short-term spinal corrections, a solid design platform is required to assess the biomechanical, short- and, more specifically, long-term impact of new emerging implant designs. Animal trials have been extensively explored to assess new fusionless implant concepts, design parameters, and *in vivo* response precursory to human clinical applications.

Nevertheless, experimental animal trials can be time-consuming as various implant concepts are required before transferring the acquired knowledge to human applications. Thus, an alternative, numerical testing platform is required to test implants prior to *in vivo* trials and facilitate knowledge transfer. While current implants predominantly compress the intervertebral disc and bridge the intervertebral space increasing the risk of long-term disc degeneration, insufficient long-term *in vivo* evidence hinder the full assessment of the disc health following prolonged segmental compression in both experimental and clinical fusionless applications. A new localized hemi-staple was proposed to solve segmental compression complications; yet, its mono-epiphyseal application limits fully harnessing the growth of vertebral body.

Moreover, experimental spinal growth-sparing research relies on either inverse approach or 2-step approach. Although spinal loading differs between a normal and deformed spine, both approaches are still widely utilized. However, the impact of the tested device may differ depending on the selected approach. Theoretically, these implants should be tested in similar spinal conditions as scoliosis.

Finally, the stabilizing role of the ribcage was highlighted in earlier sections. However, its role in fusionless surgery is not fully understood and the unassuming size of newly developed implants should account for the biomechanical contribution of the ribcage.

To address the underlying shortcomings, the overall objective was to develop, verify, and exploit a distinctive porcine spine finite element model for the simulation of progressive experimental scoliosis, and design and validate a new dual-epiphyseal growth modulating implant.

To fulfill the general objective, specific sub-objectives were devised as follows:

Objective 1: Develop a porcine spine finite element model, integrating porcine adapted growth dynamics and ribcage.

Objective 2: Develop, test, and validate dual-staple implant on immature pigs.

Objective 3: Exploit the developed FEM to:

- i. Evaluate the difference between inducing vs correcting an induced deformity via equivalent fusionless implants.
- ii. Examine of the role of the ribcage in fusionless spinal surgery.

These specific objectives stemmed from seeking answers to the following research hypotheses:

H1: A thoracolumbar porcine spine finite element model, including epiphyseal growth dynamics, can represent the appropriate biomechanical behaviour and growth modulating effect of fusionless implants with simulated Cobb angle within 5°, vertebral wedging within 2°, and vertebral rotation within 3°.

H2: Modulating the growth of the superior and inferior epiphyseal plates, simultaneously via a local implant without bridging the intervertebral disc space, can increase, by at least two folds, progressive Cobb angle and vertebral wedging compared to single growth plate alteration.



H3: The growth modulating impact of fusionless implants is less prominent via the 2-step versus the inverse experimental approaches for Cobb angle and vertebral wedging manipulations.

H4: The biomechanical contribution of the ribcage is manifested by an increase in thoracic rigidity leading to a reduction in the impact of fusionless implants following a change in growth plate stress distribution.

To highlight the methodological approach undertaken to address the proposed research hypotheses (Figure 2-1), this thesis was devised into 7 chapters. Chapter 1 & 2 covered a detailed literature review focused on limitations of current fusionless experimental testing methodology leading to the above proposed hypotheses and related objectives. As such, Chapter 3 presents an improved dual-epiphyseal implant, its *in silico*, *in situ*, and *in vivo* testing procedures devised to address hypothesis 2. Moreover,  $\mu$ -CT results arising from the *in vivo* trials are presented in Section 3.3. Chapter 4 presents a porcine spine finite element model, including epiphyseal growth dynamics and the ribcage, developed as per objective 1 to explore hypothesis 1. An investigational study is also detailed to address hypothesis 3 as highlighted in objective 3.i (Chapter 4, Section 4.3). Chapter 5 highlights an investigational simulated study to fulfill objective 3.ii and address hypothesis 4. Finally, the outcomes of this doctoral thesis are discussed comprehensively in Chapter 6 followed by a conclusion and future perspectives (Chapter 7).

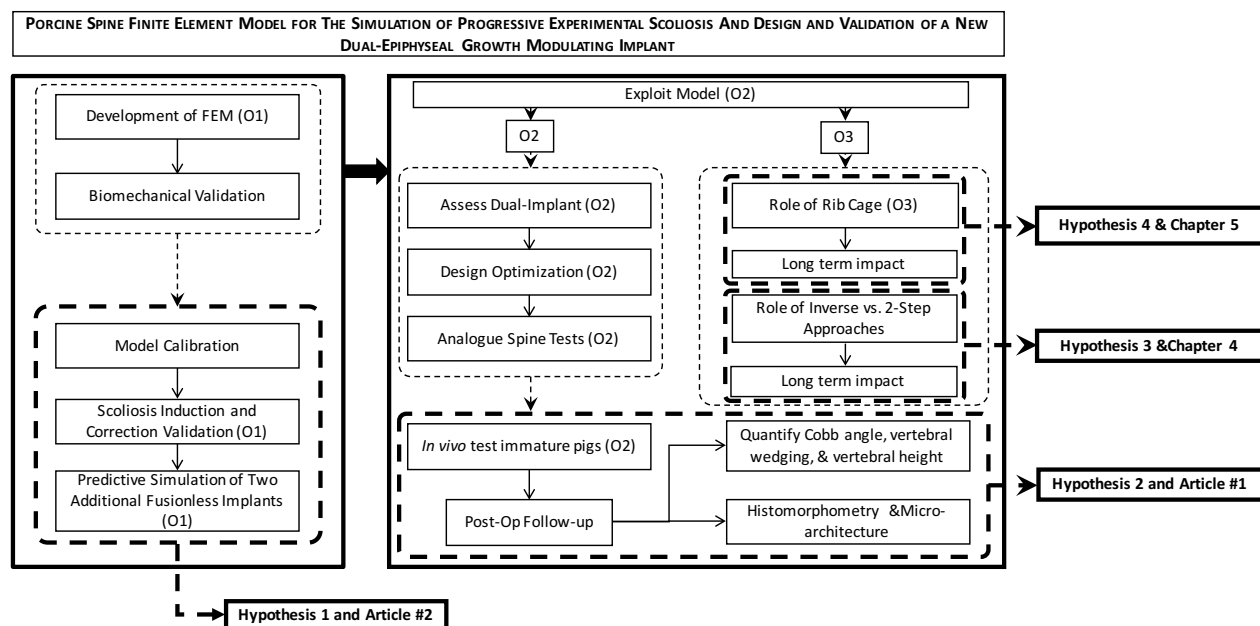


Figure 2-1: Methodology diagram and related manuscripts and chapters

## CHAPTER 3     *IN VIVO* ASSESSEMENT OF A DUAL-EPIPHYSEAL IMPLANT

### 3.1 Presentation of the Dual-Epiphyseal implant

A rising concern is linked to the intervertebral disc health following prolonged segmental compression both experimentally and clinically. A localized hemi-staple was proposed to solve segmental compression by acting locally on the growth plate without bridging the intervertebral space. Yet, its mono-epiphyseal application limits fully harnessing the growth of vertebral body. A localized device, a dual-epiphyseal staple, acting on both growth plates simultaneously without bridging the intervertebral disc space was proposed.

The design of the dual-epiphyseal implant was built and improved upon a previous implant, namely, the hemi-staple (Figure 1-37, [190]). Similarly, preserving spinal motion encourages nutrient transfer to the intervertebral disc, ensuring longevity. Although to date long-term IVD health assessment are scarce, histomorphometric analyses of hemi-staple trials showed preserved disc health whilst the implant adequately positioned between the growth plate and intervertebral disc. Although promising, the hemi-staple acted on a single growth plate by passively restraining growth and is yet to harness the full growth potential of the vertebral body. Additionally, the implant is entirely passive where the applied force on the epiphysis cannot be controlled. One can argue that, by exploiting both growth plates, the long-term performance of the implant would be improved, if not, doubled. Nevertheless, vertebrae inherently exhibit differing geometries, both linked to various wedging magnitudes (scoliosis) and increasing heights craniocaudally. The desired response was to locally act on both the proximal and distal growth plates concurrently without crossing the disc space. The proposed revised design offers both the capabilities of adapting to different vertebral body geometries as well as controlling the applied load.

Thus, specific design requirements were to be met. The device would act locally on both epiphyseal plates, provide adjustable height intra-operatively, avoid major spinal arteries, and maintain segmental mobility. An additional design feature was the ability to, not only provide passive restraint, but also provide an active restraint via controlled loading to achieve pre-determined growth modulation without growth arrest. By using the previously

described growth modulation equation (Equation 1), growth can be determined as a function of applied load and, thus, predicting the expected/desired correction. An important aspect was to minimize surgical steps when inserting the implant. Figure 3-1 illustrates the initial concept and the evolution of the desired correction over time. To accomplish local growth modulation, a prong design, similar to the hemi-staple, was sought out and would be inserted proximally and distally. As height adjustment was required, a two components design was proposed: top and bottom components which slide respectively.

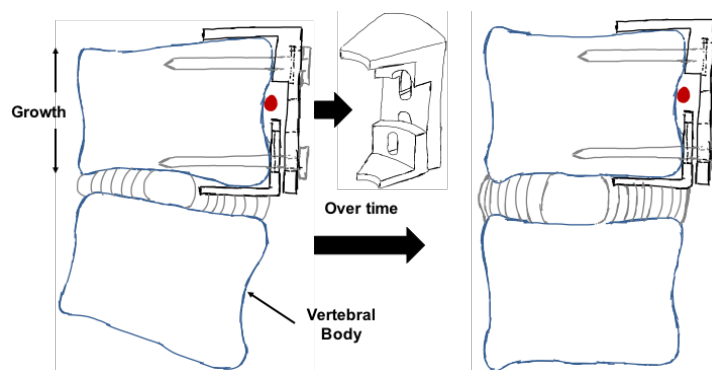


Figure 3-1: Concept Dual-Epiphyseal implant: Growth modulation over time. Superior vertebral wedging corrected.

The initial concept was focused around achieving two modes of application: Fixed and Force-Controlled. Fixed mode is aimed at attaining ipsi-lateral growth arrest while Force-Controlled modulated growth for the desired growth rate. Figure 3-2 illustrates the preliminary top and bottom implant slots for screw insertion and the various screws positions for fixed, force-controlled, and height adjusted to large vertebra. The final manufactured slots are also presented and will be discussed in-depth.

#### Fixed mode setup:

To achieve this application, the screws are positioned as illustrated in Figure 3-2. The implant is placed on a custom holding tool and then inserted on the vertebra. The first screw is then inserted in the lower slot of the top implant component and through the slot of the bottom implant, which is then fastened for secure fixture. Screw concentricity and alignment is ensured by the holding tool. The second screw is then inserted through the second slot of the top implant component for final fixation. Following spinal growth, the

passive reaction forces created on the screws restrain growth. Two screws ensure adequate fixation and limit components relative displacements.

*Force-Controlled mode:*

The positioning steps are similar to the fixed mode setup; however, differences lie within the addition of an elastic or hyper-elastic ligament (thereafter named “ligament”), which provides the desired compressive forces. The implant is assembled per-op by inserting the ligament in the corresponding grooves featured on the top and bottom implant components. Similarly, the implant is inserted on the vertebral body with screws not fully fastened to allow relative translation and prevent restraint via locked screws. The ligament tension then modulates axial growth via choosing the appropriate ligament properties. Hyper-elastic ligaments are proposed since they exhibit relatively constant reaction loads over a large displacement scale (Figure 3-3); thus, loading remains consistent even following implant height adjustment (Figure 3-4). Growth modulation is then achieved as a function of the applied, controlled ligament tension.

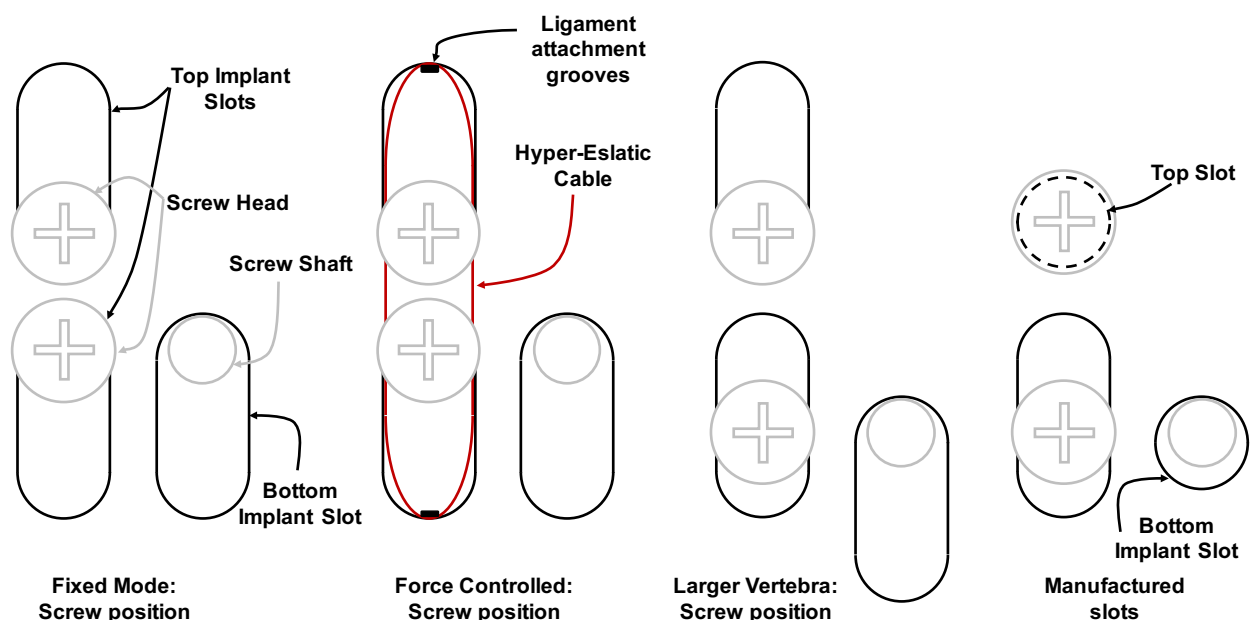


Figure 3-2: Top and lower implant slots and screw locations for different applications modes. Slots are depicted in Figure 3-1 for each of the implant components. Vertically stacked slots correspond to the top implant component and a single slot corresponds to the bottom implant component.

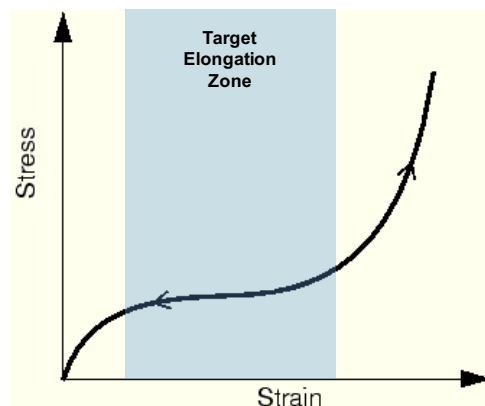


Figure 3-3: Hyperelastic material stress-strain curve. Target zone indicates hyperelastic ligament elongation zone for controlled/constant load (Modified from:

<http://abaqusdoc.ucalgary.ca/v6.9/books/gsa/default.htm?startat=ch10s06.html>).

Following several design iterations, it was then decided to pursue the Fixed Mode design with a slight design alteration to minimize machining time for this thesis's initial *in vivo* investigation (Figure 3-2: Manufactured slots). Briefly, a similar setup as fixed mode is applied with replacing the obround for the top implant and bottom implant by circular slots. Dual-epiphyseal growth modulation feasibility was formerly tested via numerical simulations on an adolescent scoliotic spine [170] and using the in-house developed porcine spine finite element model (presented subsequently in this thesis work) both of which integrated growth dynamics (Figure 3-4). Finally, prior to physical *in-situ* testing, the preliminary implant designs were 3D printed using a 10/1 scale to confirm feasibility of the holding tool and the initial expansion mechanism. Once satisfactory, one-to-one scaled implants were 3D printed and tested on equivalent Sawbones T7-T9 multi-segmental spinal unit. The final implant was then designed using CATIA V5R20 (Figure 3-5).

Surgical insertion is achieved via 4 steps. First, the implant is placed on a custom holding tool and its height is adjusted intra-operatively using a custom fitted T15 Torx head. The implant is then positioned on the vertebral body with gentle tapping insuring prongs are located between the growth plates and discs proximally and distally. The first screw is inserted via the custom holding tool to ensure concentric alignment. Finally, the holding tool is repositioned on the top implant guides for insertion of the second screw (Figure 3-5).

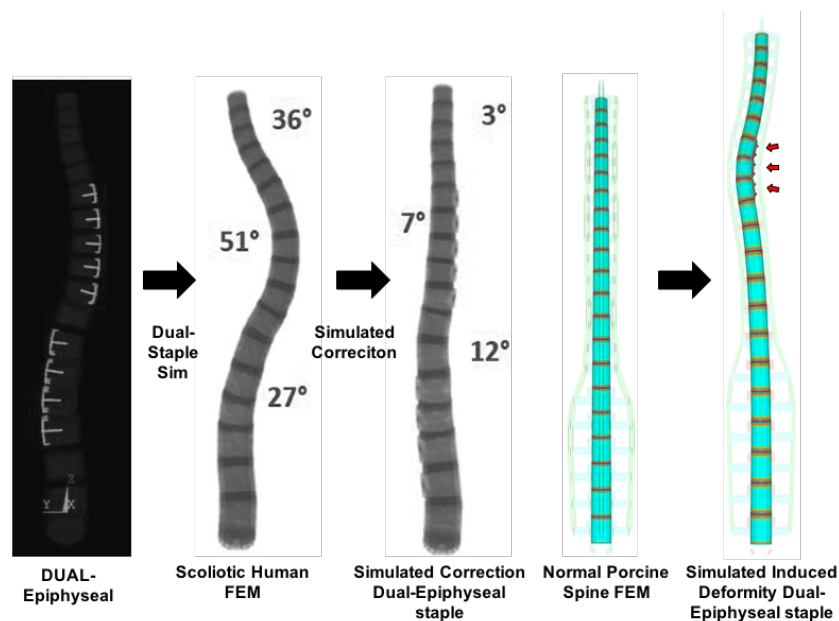


Figure 3-4: DUAL-Epiphyseal staple simulations on human and porcine FEMs. Potential correction in human and promising induction in pigs.

An additional advantage of the final implant design is the ability to insert the top or bottom components individually, should the need arise. More specifically, each component includes guides for the holding tool. Intra-operatively, if the surgeon deems the vertebra extremely deformed and cannot accommodate dual-epiphyseal insertion, one component can be inserted to obtain modulation similar to the current hemi-staple.

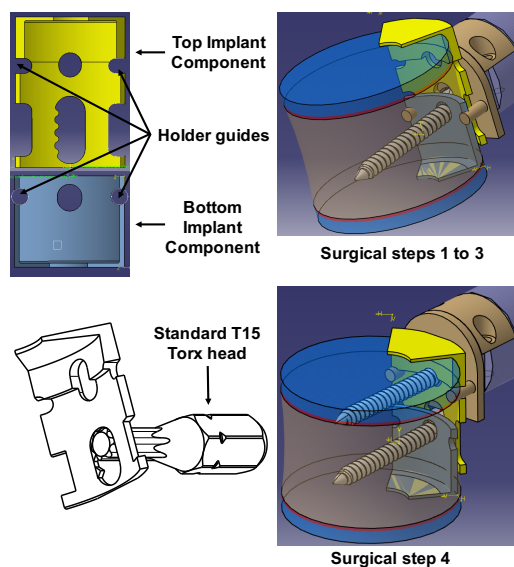


Figure 3-5: Final implant design and surgical steps.

The implant was then machined and tested on Sawbones vertebra to affirm the feasibility of the height expansion mechanism and ease of insertion between the disc and vertebral body. With satisfactory *in situ* results, *in vivo* trials were conducted on immature pigs and followed over 3 month growth (Section 3.2). Intra-operatively, the insertion site was guided via fluoroscopic imaging followed by implant height adjustment (Figure 3-6). This *in vivo* investigations constituted the subject of the first article as part of this thesis while the implant's design was submitted as a "Declaration of Invention" for Ecole Polytechnique's records.

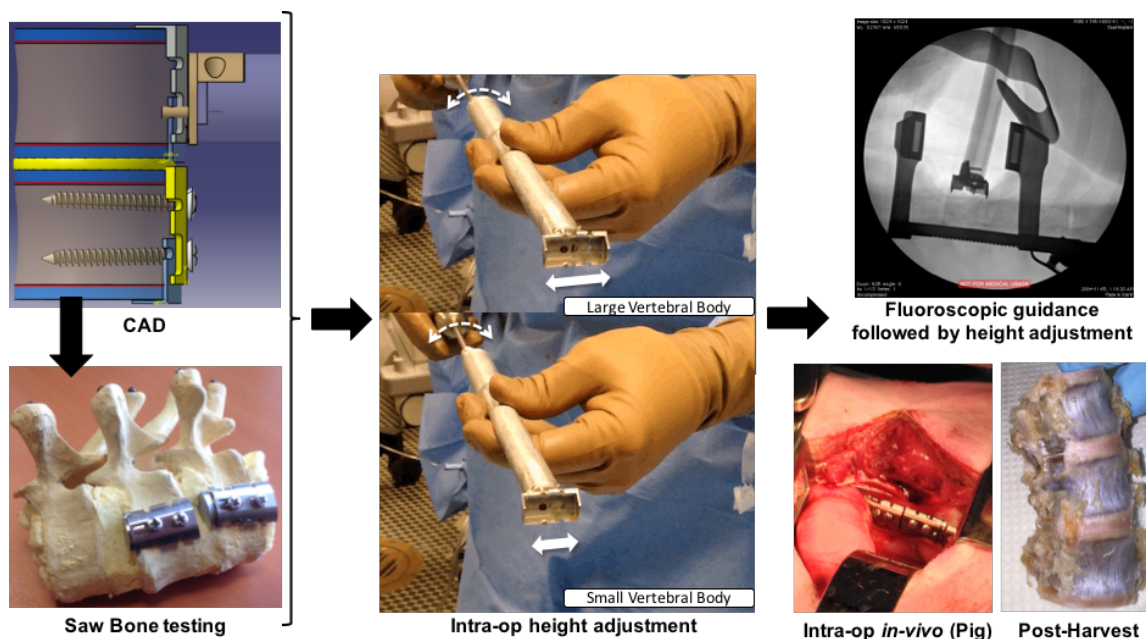


Figure 3-6: Concept to application. CAD design followed by Sawbones feasibility and *in vivo* trials



### **3.2 Article 1 : Local Epiphyseal Growth Modulation for the Early Treatment of Progressive Scoliosis: Experimental Validation Using A Porcine Model**

To test the previously described device, an *in vivo* study was conducted to assess global spinal modifications (deformity induction) over 3-month growth along with local vertebral alterations reflected by vertebral wedging and left/right height differences.

This *in vivo* study was reported in a paper submitted to the journal Spine on October 22, 2015 under the title “Local Epiphyseal Growth Modulation for the Early Treatment of Progressive Scoliosis: Experimental Validation Using A Porcine Model”, for which the contribution of the first author is considered as 85%. The manuscript was accepted for publication and was pre-published on February 8, 2016. Conclusions drawn allowed realization of objective 2 and exploring hypothesis 2.

# Local Epiphyseal Growth Modulation for the Early Treatment of Progressive Scoliosis: Experimental Validation Using A Porcine Model

Bahe Hachem<sup>1,2</sup> B.Eng., Carl-Eric Aubin<sup>1,2,3</sup> Ph.D. P.Eng., Stefan Parent<sup>2,3</sup> M.D. Ph.D

<sup>1</sup>*Dept. of Mechanical Engineering, Polytechnique Montreal, Montreal, Canada*

<sup>2</sup>*Research Center, Sainte-Justine University Hospital Center, Montreal, Canada*

<sup>3</sup>*Dept. of Surgery, Faculty of Medicine, Université de Montréal, Montreal, Canada*

Address for notification, correspondence and reprints:

Carl-Eric Aubin, Ph.D., P.Eng.

Full Professor

Polytechnique Research Chair in Orthopedic Engineering' & NSERC/Medtronic Industrial  
Research Chair in Spine Biomechanics

Polytechnique Montreal, Department of Mechanical Engineering

P.O. Box 6079, Station "Centre-ville", Montreal (Quebec), H3C 3A7 CANADA

E-mail: [carl-eric.aubin@polymtl.ca](mailto:carl-eric.aubin@polymtl.ca)

Phone: 1 (514) 340-4711 ext 2836; FAX: 1 (514) 340-5867

**Disclosure:** This study was funded by the Natural Sciences and Engineering Research Council of Canada (grant # 346145 - 11; Industrial Research Chair with Medtronic of Canada).

**Acknowledgement:** The authors would like to acknowledge the assistance of Dr Gabriel Gutman MD, Dr Aurélie Benoit PhD, Dr Irène Londono PhD, and Viviane Lalande MASc.

The device(s)/drug(s) that is/are the subject of this manuscript is/are not FDA-approved for this indication and is/are not commercially available in the United States.

## **Structured Abstract**

### **Study Design**

Experimental study of a localized device for the control of the vertebral growth using an immature porcine model.

### **Objective**

To experimentally evaluate a localized device acting on the epiphyseal growth plates without bridging the intervertebral disc of immature hybrid pigs over three months of growth.

### **Summary of background data**

Based on current published literature, fusionless devices offer promising scoliosis treatment alternatives to conventional spinal instrumentation and fusion in the growing spine. Current compression-based devices achieve growth modulation while also compressing the intervertebral discs, increasing the risk of long-term disc degeneration.

### **Methods**

An intravertebral staple acting on both the superior and inferior growth plates was inserted locally over T7-T9 of 7 healthy immature pigs. Four age-matched animals served as controls. Radiographs were acquired monthly to assess induced spinal curvature and vertebral wedging (inverse model). Global (spinal) and local (vertebral, discal) geometric changes were evaluated over 3-months follow-up. Final left/right vertebral height differences were also quantified.

### **Results**

The only postoperative complication observed was one pig that had a persistent deep infection and excluded from the study. No significant changes in spinal alignment were reported in control animals. Final induced Cobb angle was  $25.0^{\circ} \pm 4.2^{\circ}$  measured over T7-T9, with no observable sagittal profile modification. Highest vertebral wedging occurred at T9 with  $18.2^{\circ} \pm 2.7^{\circ}$ . Cumulative vertebral wedging over T7-T9 accounted for  $45.4^{\circ}$ , demonstrating evidence of reversed disc wedge phenomenon. Vertebral height was  $3.9 \pm 1.0$  mm shorter on the instrumented side suggesting full growth restraint. Local and regional induced deformities significantly differed from their control counterparts ( $p < 0.001$ ).

## Conclusion

In this animal model, the local epiphyseal device achieved significant localized growth modulation over as little as three instrumented levels, with explicit vertebral wedging exclusive of the intervertebral disc. By increasing the number of instrumented levels, one may achieve higher curvature control potentially providing a unique local correction method to correct spinal deformity without affecting the intervertebral disc.

## Keypoints:

- The explored local epiphyseal dual-staple achieved significant vertebral growth modulation evidenced by vertebral wedging ( $18^\circ$ ) over merely 3 instrumented vertebrae (cumulative vertebral wedging:  $45^\circ$ ) exclusive of the intervertebral disc.
- The induced vertebral wedging was compensated by reversed disc wedging, emphasis of the local vs global effect, which may be explained as a physiological response of a normally straight pig spine to maintain a forward looking gaze.
- The experimental results suggest that the explored device could be exploited for the correction of scoliotic spinal deformities via passive growth modulation without bridging the intervertebral disc space.

## Mini Abstract/ Précis:

A localized epiphyseal device acting on 3 vertebrae without crossing the discs was evaluated on 7 immature pigs over 3-months growth. Localized growth modulation ( $24.5^\circ$  Cobb angle) and explicit vertebral wedging ( $18.2^\circ$ ) were achieved, which may be potentially promising in the future for the correction of scoliosis in the growing spine.

### 3.2.1 Introduction

Scoliosis is a biomechanically complex three dimensional deformity of the spine, whose treatment is challenging, especially in young children. The gold standard in treating curves progressing beyond 40° relies on re-aligning the spine with instrumentation accompanied by segmental spinal arthrodesis (fusion), invasively reducing spinal mobility.

Recent interest has shifted towards minimally invasive fusionless scoliosis treatment strategies that harness residual vertebral growth. By increasing compressive loading on the growth plates, growth can be retarded (Hueter-Volkman principle [1]). As such, fusionless devices attempt to reshape wedged vertebrae to their normal geometries and, over time, realign the spine while maintaining segmental mobility [2] without resorting to invasive surgery [3]. Several investigations have attempted compression-based fusionless scoliosis correction in growing spines, clinically, using anterior vertebral body tethering [4] or stapling [2] on the convex side of curves generally below 45° [4] as larger curves require substantial initial intra-operative correction, increasing compression on the intervertebral discs (IVD) and the risk of spontaneous spinal arthrodesis [2]. Experimental testing of compression-based fusionless devices revealed changes in disc viable cell density and reduced vascularization of the endplates, which may lead to disc degradation [5]. Although promising, the temporal influence of current treatments on the IVD health is halted by the insufficient solid long-term clinical outcomes.

Fusionless growth modulating implants are explored via animal trials before translating findings to clinical applications. Braun et al. [6] reported successful correction of an otherwise induced deformity with implant efficacy halted by initial curve magnitude and staple loosening. Bylski-Austrow et al. [7] reported reduced growth ipsi-lateral to the implant using a rigid staple spanning the IVD space with reduced disc height and range of motion [8], with no consensus to the required range of motion for sustained IVD health. Newton et al. [9] used unilateral 4-level AT. Although no degeneration was observed in an otherwise compressed disc, the observations were limited to 12 months follow-up, which does not represent long-term clinical applications of the device. Liu et al. [10] focused on elastic posterior L1-L5 tethering on pigs resulting in local and global spinal deformity with changes in endplate epiphysis and reduced disc thickness. Burke et al. [11]

demonstrated the three-dimensional curve induction/correction potential of a novel construct in immature lambs with promising results and maintained spinal mobility in all three anatomical planes. Their proposed approach may reduce the risk of segmental symptomatic degenerative changes but further investigation is required for conclusive analysis.

As fusionless instrumentation approach intends to maintain intervertebral mobility, disc health is utmost important to consider. The above promising implants bridge the intervertebral gap and predominantly compress the IVD, increasing the risk of segmental disc degeneration and growth plate damage. Based on short-term literature, minimizing the compression on the disc is anticipated to have less long-term detrimental effects. To address this shortcoming, Driscoll et al. [12] implanted intravertebral hemi-staples, a device with a prong located between the growth plate and the disc and attached to the vertebral body wall, without spanning the IVD space. Reported data showed apparent localized vertebral wedging and evident instrumented Cobb angle with signs of disc health sustainability [12]. Yet, the proposed localized hemi-staple acted solely on the superior growth plate and did not harness the full vertebral growth potential. To address this issue, this study aimed at developing a localized implant acting simultaneously on the superior and inferior growth plates, maximizing growth modulation, while providing an expansion mechanism to intraoperatively accommodate various vertebral shapes and testing the proposed implant on immature pigs to assess local growth changes and global spinal deformity.

## **3.2.2 Material and Methods**

### **3.2.2.1 Implant-Functional Description**

The feasibility of the proposed implant, namely dual-staple, was first evaluated using in-house simulations on a porcine spine finite element model (FEM) and published simulations on a patient specific FEM [13]. The implant comprised of two portions: an upper and a lower piece (Figure 3-7). Each piece comprised a 0.5mm thick prong inserted between the IVD and the thin ossification site just above the growth plate (5mm approx. penetration)) and a body attached to the vertebral body wall. The latter included guides

for a custom holding tool and fixed using bone screws (25x2.8mm diameter). In this custom design, the upper piece slides via a custom expansion mechanism with the lower piece secured to the holder allowing for intra-operative height adjustment and prong re-positioning for various thoracic/lumbar vertebral morphologies (Fig. 1). Stainless steel 316L (UNS S31603) was used for the dual-staple and bone screws.

### **3.2.2.2 Surgical Procedure**

Eleven 11-week-old hybrid female pigs (Landrace/Yorkshire, 25-35Kg) were allowed to acclimatize for 1 week after arrival. Animals were randomly assigned into two groups: 7 instrumented and 4 controls, with group sizes determined using a power of 0.8 and a significance of 0.05. The study was approved by our Hospital Institutional Committee for Animal Care in Research and our University Ethical Committee. Pre-operatively, animals were sedated by intramuscular injection of atropine (0.04 mg/kg), azaperone (4 mg/kg), and ketamine (25 mg/kg). Propofol (1.66 mg/kg) and buprenorphine (0.02 mg/kg) were injected intravenously prior to intubating with a 6.5mm endotracheal tube. Anaesthesia was maintained by automatic ventilation (oxygen and 1-3% Isoflurane). Heart rate and blood pressure were tracked via a monitor connected to the tip of the ear or tongue. Surgery was performed under a sterile environment in the left decubitus position with insertion site shaved and prepared with Proviiodine solution. Access to vertebrae T7-T9 was achieved via a right side thoracotomy between the seventh and eighth ribs. Fluoroscopic imaging allowed insertion site guidance with the dual-staple mounted on a custom-designed holding tool and device height was precisely adjusted via the custom expansion mechanism (Figure 3-7). Once satisfactory positioning was achieved, a screw was inserted to fix the lower implant portion. The holding tool was then repositioned on the top piece using guides and a second screw was inserted for final construct fixation (Figure 3-7). The implant design and insertion method were meticulously crafted to minimize surgical steps (4 total steps/vertebra).

Site closure was performed after T7-T9 device insertion in the instrumented group (Figure 3-8). All surgeries were performed by the same spine surgeon. A fentanyl patch (7.5 mg) and intramuscular injections of antibiotics (Excenel 3 mg/kg) were administered over 3-

days post-operative. Pigs were allowed to interact and socialize once recovery was confirmed prior to which they were kept in individual cages.

Follow-up proceeded  $85 \pm 2$  days (12 weeks) post-operative during which animals were housed locally for the first three weeks then transferred to a private facility for the remainder of the study. Monthly postero-anterior (PA) and lateral (LAT) radiographs were taken with the animals placed in prone position on a custom sling. While imitating the natural quadrupedal spinal configuration as closely as possible, this setup allowed for standardized acquisitions and reduced repositioning errors as the X-ray source moved between orthogonal views. Animals were then euthanized by inducing deep anaesthesia followed by a lethal injection of saturated potassium chloride.

### **3.2.2.3 Progressive Deformity Evaluation**

Relevant clinical indices were measured at each radiographic time-point to assess and quantify the temporal changes introduced by the device. Constrained Cobb and sagittal curve angles were measured between T7-T9 to assess global spinal alterations (angles between the upper endplate of the superior instrumented vertebra and the lower endplate of the inferior instrumented vertebra on both the coronal and sagittal views (Figure 3-8). Furthermore, coronal and sagittal vertebral wedging were measured at each level from T6 to T12. Similarly, coronal and sagittal intervertebral disc wedging was assessed from T6 to T12. Vertebral and intervertebral levels were selected to further assess the local changes at the instrumentation site (T7-T9), adjacent to instrumented levels, and off-instrumentation in both anatomical planes. Also, terminal left/right vertebral height differences were measured for instrumented vertebrae. Equivalent regional and local measurements were performed for control animals. Temporal measurements (Constrained Cobb and sagittal angles, vertebral wedging, and IVD wedging) and final vertebral height difference were compared between the instrumented and control group using Student's t-tests (significance level  $p < 0.05$ ).

Implants were verified for possible loosening/dislodgement. Additionally, relative segmental implant interaction, identified by implant contact between adjacent vertebrae, was verified as intervertebral spacing is limited in pigs [14]. Implant placement was



assessed at each radiograph and compared to previous images to confirm consistent prong placement between the growth plate and the IVD. Implant components (upper and lower) were observed over the follow-up period to confirm secure fixation with no relative displacement (upper with respect to lower component). The spines (T1-T15) were harvested immediately post-sacrifice to further verify both sustained mobility and no implant segmental obstruction. Manual left/right bending under fluoroscopic imaging identified vertebral motion to visually confirm sustained mobility. Finally, screws and implants were extracted for preliminary bone/screw interface assessment.

### **3.2.3 Results**

#### **3.2.3.1 Surgery and post-sacrifice examination**

Minimal blood loss occurred during surgery (<50 ml) and no immediate postoperative complications were observed. Average surgery time to install all three devices, including incision site opening and closure, was 32.5 min (standard deviation 8.2 min). The animals weighed  $29.1 \pm 7.4$  kg pre-op. The instrumented group underwent weight gain of  $2.6 \pm 1.3$  kg/week and showed no signs of reduced physical activity while controls gained  $3.0 \pm 1.8$  kg/week ( $p=0.14$ ). No animal was lost during the study period, but post-sacrifice examination revealed signs of deep infection in one animal, which was subsequently omitted from the study. Early signs of infection were observed in two cases, which were treated accordingly and recovered within the first week post-op. Two animals (including the omitted case) showed 2 fused ribs near the incision site only observed during dissection. No implant dislodgment was noticed from radiographs or at dissection. Conversely, some screws were easily removed for 3 cases with no evidenced implant loosening. No contact between adjacent implants was apparent in post-sacrifice imaging. Manual bending confirmed sustained mobility albeit minimal in this animal model (Figure 3-9).

#### **3.2.3.2 Analysis of postoperative regional indices**

Pre-sacrifice global angles showed the apparent effect of the dual-staple (Figure 3-10). In the coronal plane (Figure 3-11a), instrumented Cobb angle (between T7-T9) was  $25.0 \pm 4.2^\circ$  (range:  $20^\circ$ - $32^\circ$ ), while kyphosis was  $11.2 \pm 4.2^\circ$  (range:  $6^\circ$ - $17^\circ$ ) in the sagittal

plane. Differences between instrumented and controls were statistically significant for the Cobb angles ( $p < 0.0001$ ), but not for the sagittal angles ( $11.2 \pm 4.2^\circ$  vs  $6.5 \pm 2.2$ , instrumented vs controls).

### 3.2.3.3 Analysis of postoperative local indices

Induced coronal vertebral wedging was evident at the instrumented levels at every time-point, with the maximum value at T9 (final:  $18.2 \pm 2.7^\circ$ , range:  $15^\circ$ - $23^\circ$ ) (Figure 3-11b). Instrumented vertebral wedging was statistically different than controls at each time-point ( $p < 0.0001$ ). Cumulative 3-level vertebral wedging was greater than  $45^\circ$ . Non-instrumented vertebrae (T6, T11, and T12) showed no statistical differences with controls. Vertebral wedging in the sagittal plane was not significantly different from controls at each measured level.

No statistical difference was observed in the sagittal plane between both instrumented and control intervertebral disc wedging. Similarly, coronal plane IVD wedging for the controls and tested group did not differ between T10-T11 and T11-T12. Intervertebral disc wedging adjacent to the instrumented region (T6-T7 and T9-T10 IVD wedging) was  $-9 \pm 1.5^\circ$  and  $-8.7 \pm 3.7^\circ$ , respectively and was significantly different than control equivalents ( $p < 0.0001$ ). Furthermore, intervertebral disc wedging between instrumented vertebrae was statistically different than controls ( $p < 0.0001$ ). IVD wedging was most prominent at T8-T9 level for the 8w ( $-10.2 \pm 1.5^\circ$ ) and 12w ( $-11.2 \pm 2.6^\circ$ ) time-points (Figure 3-11c) but not statistically different when compared to the remaining instrumented levels for equivalent time-points.

Vertebral body height difference was most notable for the tested group. Instrumented vertebral concave/convex height difference was  $2.9 \pm 1.0$ mm,  $4.0 \pm 0.8$ mm, and  $3.9 \pm 1.0$ mm for T7, T8, and T9 respectively (vs.  $-0.1 \pm 0.26$ mm,  $0.1 \pm 0.28$ mm, and  $0.3 \pm 0.48$ mm, respectively for control animals).

## 3.2.4 Discussion

The dual-staple intravertebral device modulated growth with evidenced vertebral concave/convex height difference and coronal plane vertebral wedging towards the

instrumentation side with global deformity, exclusive of the intervertebral disc. The deformity was prominent within the instrumented region; yet, cumulative instrumented vertebral wedging ( $>45^\circ$ ) was greater than constrained Cobb angle. These differences are clear indications of the local versus the global effect of the implant designed to locally reshape the vertebral body to its normal morphology without compromising the intervertebral junction. The absence of wedging in the adjacent vertebrae further accentuates the local effect of the implant as constrained Cobb angle was measured between wedged vertebrae. The unaltered sagittal angle is explained by the lateral implant placement intended to act in the coronal plane exclusively, without affecting axial rotation as it requires bridging the intervertebral gap to exploit coupled vertebral motion. Inserting the implant antero-laterally would allow controlling the coronal and sagittal deformities; nonetheless, in vivo trials are required to establish an affirmation.

The explored device achieved significant cumulative vertebral wedging  $>45^\circ$  over only three levels; however, this prominent local deformity was compensated by IVD wedging in the opposite direction. Newton et al. [15] also observed reversed disc wedging when inducing a spinal deformity with an anterior tether. This phenomenon is not unheard of in experimental scoliosis induction surgery involving implants positioned on the vertebral bodies as they do not produce enough moment to counteract the physiological compensatory mechanism in quadrupeds. We believe quadrupeds tend to maintain a forward gaze as a natural head position enforcing a moment opposing an otherwise global deformity and engendering localized reversed disc wedging. The absence of the latter in other scoliosis inducing techniques can be attributed to the large moment arm produced when combined with ipsilateral rib tethering [16] or the implant's lateral offset [17]. Nonetheless, the presented device achieved substantial local deformity and perhaps its corrective potential would not be hindered by reversed disc wedging as discs are already wedged in the same direction as the vertebrae in human scoliotic spines [18,19]. Thus, the device would mostly act on reversing vertebral wedging with disc wedging eliminated as the spine realigns. Further corrective surgery is required to warrant conclusive confirmation.

The device achieved more than two times the vertebral wedging expected from a similar device [12], anteriorly tethered vertebrae [15], and posterior spinal tethering [20] on age-matched animal models. Sizable differences can be attributed to rigidly fixing the dual-staple with two screws, eliminating relative top/bottom implant motion allowing full local growth restraint. Landrace/Yorkshire hybrid pig vertebrae grow  $20\mu\text{m/day/growth plate}$  on average ( $3.4\text{ mm/vertebra/12weeks}$ ) equivalent to our measured vertebral height difference ( $4.0 \pm 0.8\text{ mm}$ ) indicative of adequate superior/inferior epiphyseal plate growth restraint. Unlike this study, Driscoll et al.'s hemi-staple [12] was fixed with one screw creating minimal hinge effect at the screw/implant interface, losing part of its restraining effect during the early stages of growth. Moreover, the explored dual-staple acted locally without transmitting loading through the intervertebral disc, contrary to vertebral tethering, and thus modulated vertebral growth through growth restraint, exclusively.

The prong was designed for insertion between the IVD and the upper/lower growth plates (or second ossification endplates for porcine vertebrae) posing a concern about its influence on the disc health. Histological evidence revealed sustained growth plate and disc health for similar prong designs when inserted directly above the endplate just below the disc [21]. In our study, the device was consistently positioned between the disc and the corresponding upper/lower endplates with no dislodgment/loosening. Moreover, the device's unassuming design simplifies surgical maneuvers and lowers implant misplacement risks since the custom expansion mechanism allows for real-time intra-operative implant height readjustment for varying vertebral shapes and realignment between the growth plates and discs. Furthermore, porcine vertebrae typically present a second ossification layer [22] granting easy identification of the IVD/vertebra interface. Humans lack this second ossification site. Clinically, one would require a more robust guiding technique using, perhaps, custom probes with micrometer resolution [23]. Further histological analysis is required to confirm sustained disc health.

The current study poses several limitations. Radiographs were acquired at two different housing sites; nonetheless, the same custom sling was used, ensuring standardized imaging as animals enlarge over time and reducing spinal shape changes by eliminating animal repositioning between PA and LAT views. Moreover, poor image quality limited

instrumented vertebral endplate visibility in the PA view due, but not limited to, the sternum obstruction and the implant signal attenuation. Measurements were consistently performed by the same operator based on detailed knowledge of porcine spine anatomy to reduce temporal measurements inconsistencies. Finally, fused ribs cases included the omitted animal (deep infection) and a case with a broken rib removed intra-operatively to eliminate complications. Controlled manual bending images confirmed maintained mobility, although minimal, indicating the negligible effect of these fused ribs. Perhaps a modified manual bending protocol would demonstrate a rather physiological intervertebral mobility.

### **3.2.5 Conclusion**

In this animal model, the explored local epiphyseal device achieved significant vertebral growth modulation over as little as three instrumented levels, with explicit vertebral wedging. Perhaps one may attain better curvature control by increasing the number of instrumented vertebrae over the apical region thus providing an efficient corrective method for spinal deformity excluding the intervertebral discs.

### **3.2.6 References**

- [1] Stokes IA, Spence H, Aronsson DD, et al. Mechanical modulation of vertebral body growth. Implications for scoliosis progression. *Spine (Phila Pa 1976)* 1996;21:1162–7.
- [2] Betz RR, Ranade A, Samdani AF, et al. Vertebral body stapling: a fusionless treatment option for a growing child with moderate idiopathic scoliosis. *Spine (Phila Pa 1976)* 2010;35:169–76.
- [3] Betz RR, Kim J, D'Andrea LP, et al. An innovative technique of vertebral body stapling for the treatment of patients with adolescent idiopathic scoliosis: a feasibility, safety, and utility study. *Spine (Phila Pa 1976)* 2003;28:S255–65.
- [4] Samdani AF, Ames RJ, Kimball JS, et al. Anterior Vertebral Body Tethering for Idiopathic Scoliosis: Two-Year Results. *Spine (Phila Pa 1976)* 2014;39 :1688-1693.

- [5] Hunt KJ, Braun JT, Christensen BA. The effect of two clinically relevant fusionless scoliosis implant strategies on the health of the intervertebral disc: analysis in an immature goat model. *Spine (Phila Pa 1976)* 2010;35:371–7.
- [6] Braun JT, Akyuz E, Udall H, et al. Three-dimensional analysis of 2 fusionless scoliosis treatments: a flexible ligament tether versus a rigid-shape memory alloy staple. *Spine (Phila Pa 1976)* 2006;31:262–8.
- [7] Bylski-Austrow DI, Wall EJ, Glos DL, et al. Spinal Hemiepiphysiodesis Decreases the Size of Vertebral Growth Plate Hypertrophic Zone and Cells. *J Bone Jt Surg* 2009;91:584–93.
- [8] Coombs MT, Glos DL, Wall EJ, et al. Biomechanics of spinal hemiepiphysiodesis for fusionless scoliosis treatment using titanium implant. *Spine (Phila Pa 1976)* 2013;38:E1454–60.
- [9] Newton PO, Farnsworth CL, Upasani V V, et al. Effects of intraoperative tensioning of an anterolateral spinal tether on spinal growth modulation in a porcine model. *Spine (Phila Pa 1976)* 2011;36:109–17.
- [10] Liu J, Li Z, Shen J, et al. Spinal growth modulation with posterior unilateral elastic tether in immature swine model. *Spine J* 2015;15:138–45.
- [11] Burke J, Vettorato E, Schöffmann G, et al. Modulation of spinal shape with growth following implantation of a novel surgical implant. *Eur Spine J* 2015;24:1522–32.
- [12] Driscoll M, Aubin CE, Moreau A, et al. Spinal growth modulation using a novel intravertebral epiphyseal device in an immature porcine model. *Eur Spine J* 2012;21:138–44.
- [13] Clin J, Aubin C-E, Parent S. Biomechanical simulation and analysis of scoliosis correction using a fusionless intravertebral epiphyseal device. *Spine (Phila Pa 1976)* 2015;40:369–76.
- [14] Busscher I, Ploegmakers JJW, Verkerke GJ, et al. Comparative anatomical dimensions of the complete human and porcine spine. *Eur Spine J* 2010;19:1104–14.

- [15] Newton PO, Upasani V V, Farnsworth CL, et al. Spinal Growth Modulation with Use of a Tether in an Immature Porcine Model. *J Bone Jt Surg* 2008;90:2695–706.
- [16] Schwab F, Patel A, Lafage V, et al. A porcine model for progressive thoracic scoliosis. *Spine (Phila Pa 1976)* 2009;34:E397–404.
- [17] Zheng X, Sun X, Qiu Y, et al. A porcine early-onset scoliosis model created using a posterior mini-invasive method: a pilot study. *J Spinal Disord Tech* 2014;27:E294–300.
- [18] Wever DJ, Veldhuizen AG, Klein JP, et al. A biomechanical analysis of the vertebral and rib deformities in structural scoliosis. *Eur Spine J* 1999;8:252–60.
- [19] Parent S, Labelle H, Skalli W, et al. Vertebral wedging characteristic changes in scoliotic spines. *Spine (Phila Pa 1976)* 2004;29:E455–62.
- [20] Moal B, Schwab F, Demakakos J, et al. The impact of a corrective tether on a scoliosis porcine model: a detailed 3D analysis with a 20 weeks follow-up. *Eur Spine J Off Publ Eur Spine Soc Eur Spinal Deform Soc Eur Sect Cerv Spine Res Soc* 2013;22:1800–9.
- [21] Driscoll M, Aubin CE, Moreau A, et al. Novel Hemi-staple for the Fusionless Correction of Pediatric Scoliosis: Influence on Intervertebral Discs and Growth Plates in a Porcine Model. *J Spinal Disord Tech* 2013.
- [22] Laffosse JM, Odent T, Accadbled F, et al. Micro-computed tomography evaluation of vertebral end-plate trabecular bone changes in a porcine asymmetric vertebral tether. *J Orthop Res* 2010;28:232–40.
- [23] Beaudette K, Strupler M, Benboujja F, et al. Optical coherence tomography for the identification of musculoskeletal structures of the spine: a pilot study. *Biomed Opt Express* 2012;3:533–42.

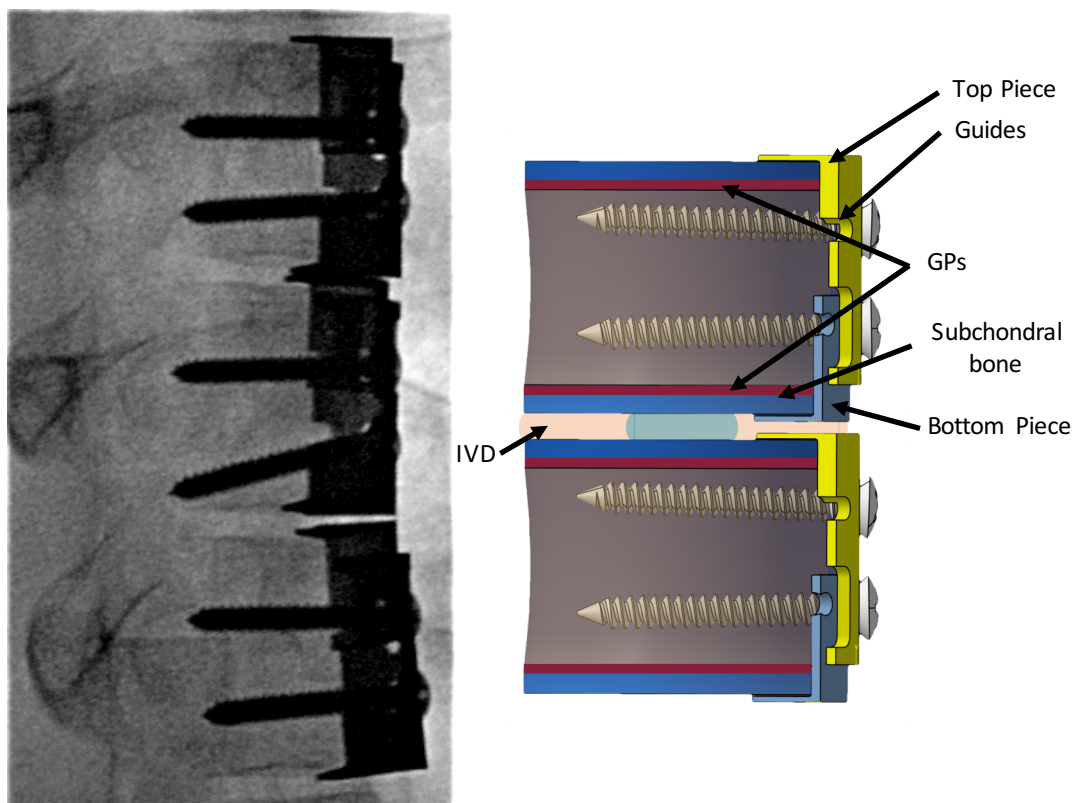


Figure 3-7: Intraoperative fluoroscopic image of dual-staple insertion site. The implant's height is adjusted intraoperatively while mounted on a custom tool. Two screws are used for implant fixation.



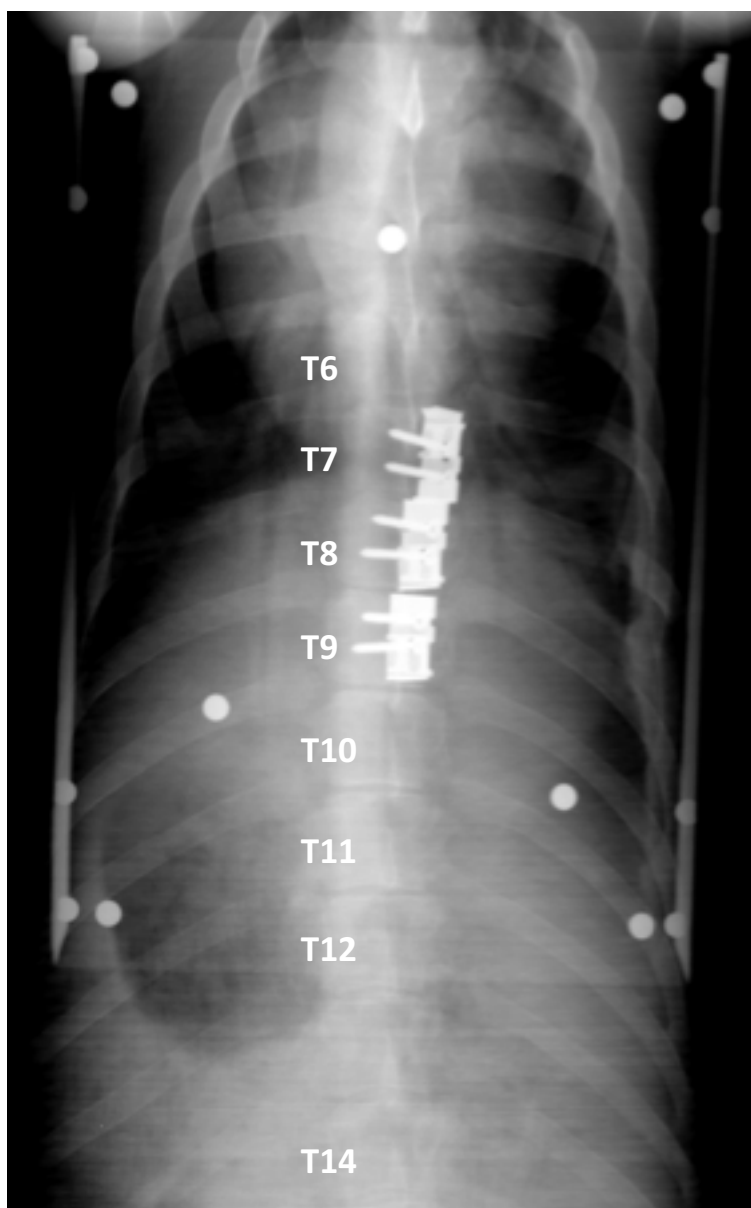


Figure 3-8: Postoperative postero-anterior radiograph showing implant positioning.

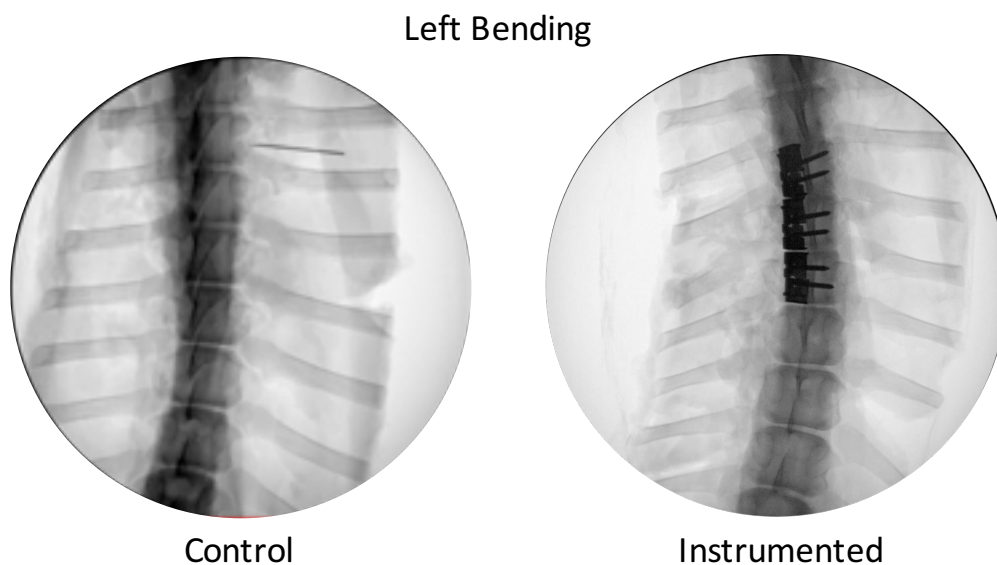


Figure 3-9: Example of manual left bending under fluoroscopic imaging showing sustained mobility in instrumented and off-instrumented regions when compared to control spines.

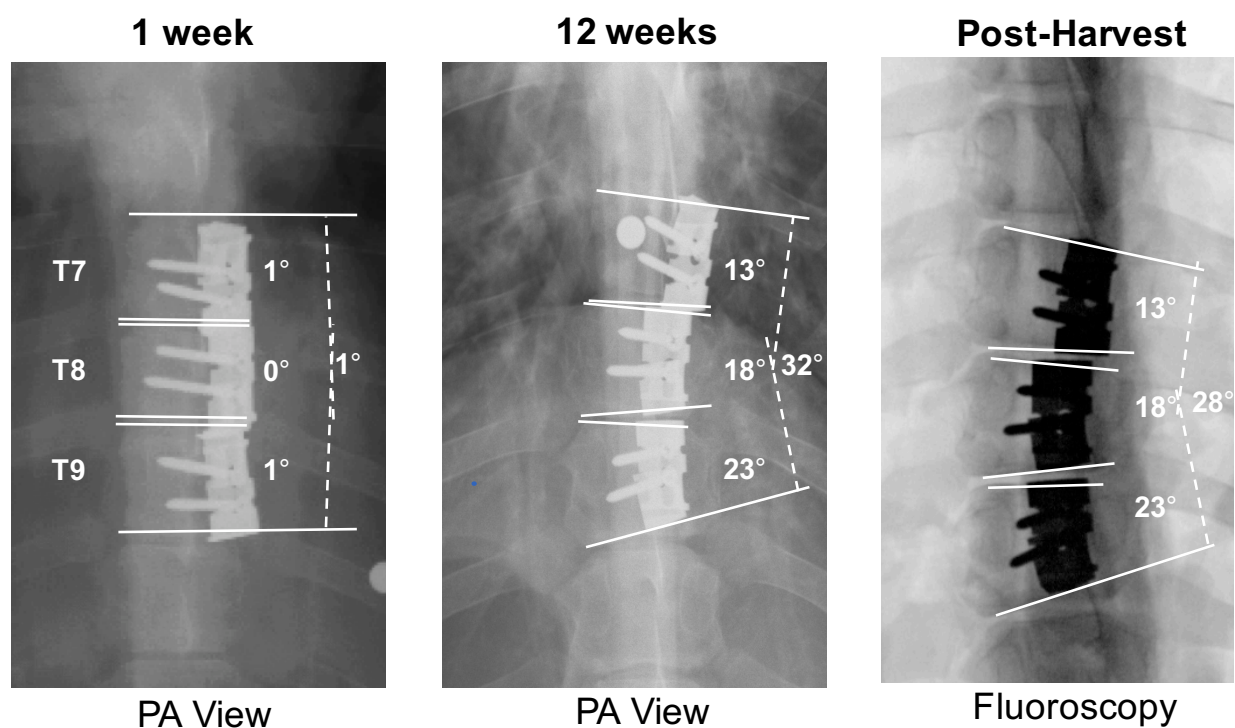


Figure 3-10: Close-up radiographs in the coronal view 1 and 12 weeks postoperative and fluoroscopic image of the excised deformed region at study completion. Progressive local and

global deformity are evidenced at 12 weeks and post-harvest (at 12 weeks) showing important vertebral coronal wedging at T7, T8, and T9.

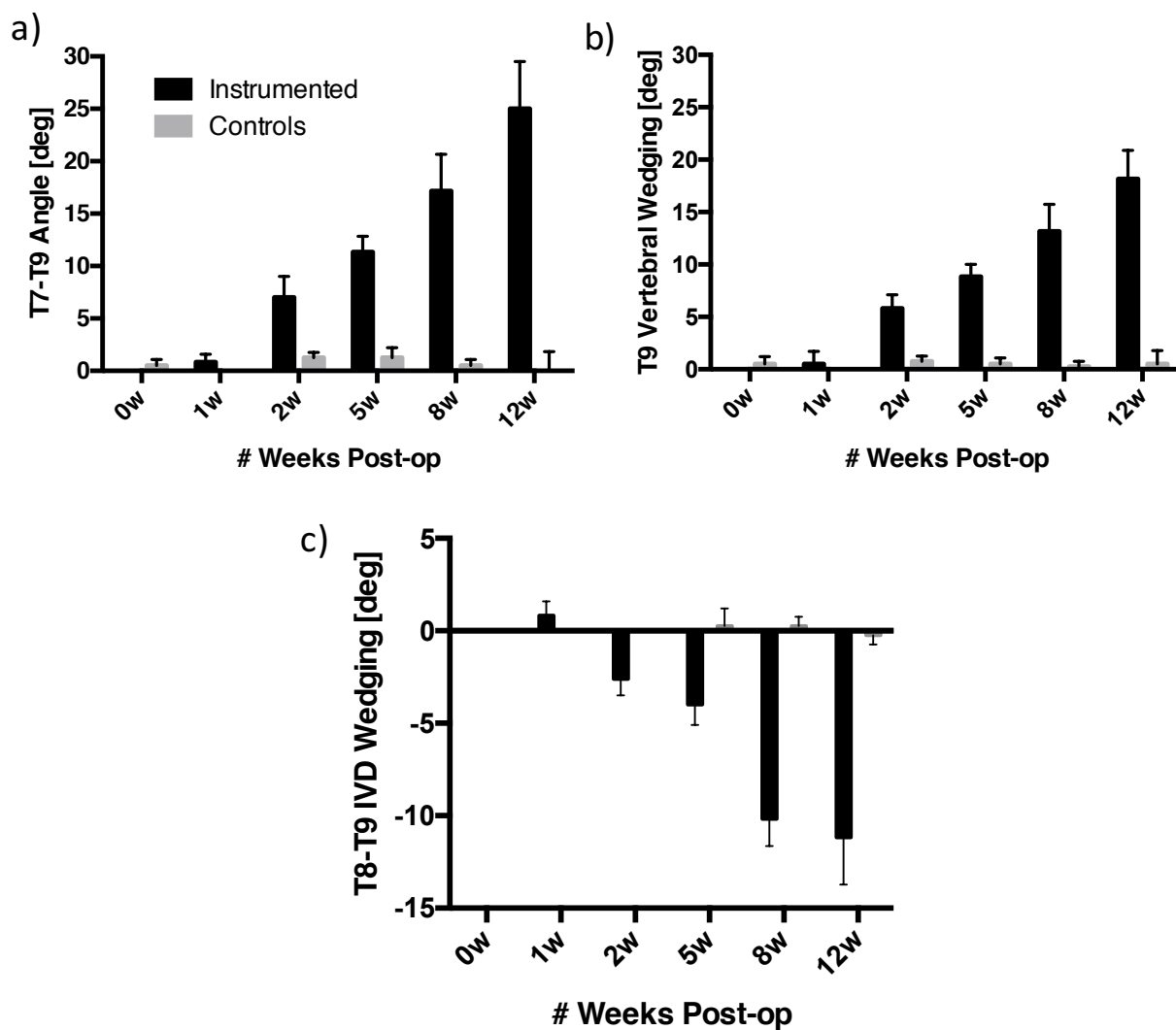


Figure 3-11: Instrumented vs. control temporal coronal T7-T9 regional (a) and T9 vertebral coronal wedging (b) coronal T8-T9 intervertebral disc wedging (c). Results presented as means  $\pm$  standard deviation.

### **3.3 Additional ex-vivo observations and prospective analyses of the instrumented vertebrae**

Following the *in vivo* trials performed jointly at Sainte-Justine hospital's animal facility and AccelLab Inc., animals were euthanized by inducing or maintaining deep anesthesia followed by a lethal injection of saturated potassium chloride (KCl, rapid IV bolus). Death was confirmed by auscultation. Animals were then subjected to an extensive necropsy with a detailed examination of the spine, the external body, and the thorax (including its contents). Any particular observations were documented with tissue harvested for sampling. The spine (C1-L6), including 3-5 cm left and right ribs, were harvested and immersion-fixed in neutral buffered formalin (NBF). Spines were cut in three sections (cervical, thoracic, and lumbar) before immersion due to the limited transport box sizes.

The spines were then dissected within 24h to minimize the effect of NBF on tissue fixation. Each spine was carefully dissected allowing the extraction of T7-T9 segments as well as T11-T12 from both instrumented and control animals. The former segment identified the instrumented (and control counterparts) levels while the latter were defined as internal controls, which were chosen to investigate the off-instrumented influence of the device. Segments were then used for two investigations (Figure 3-12). First, T7-T9 segments (controls and instrumented) were scanned via  $\mu$ -CT imaging to assess bone micro-architectural integrity and bone mineral density. Scans also served as critical indicators to investigate the performance of the implant as well as the implant's insertion site otherwise not easily distinguished via traditional radiographs. Second, T7-T9 and T11-T12 segments were then embedded in methylmethacrylate following a well-documented procedure for future histomorphometric analyses to quantify growth dynamics, growth plate height, hypertrophic zone and chondrocyte heights, and intervertebral disc integrity. Briefly, segments were soaked in 4% paraformaldehyde (PFA)/PBS with 3 solution changes over 7 days succeeded by dehydration in ethanol with 80%, 95%, and 100% concentration with 3 solution changes over 7 days. Twenty-four hours in 100% xylene (3 solution changes) resulted in complete specimen dehydration. Samples were then passed in 0%, 1%, and 3.8% MMA over 14 days before which they were embedded in 3.8% solution for final

polymerization. An abnormal heat diffusion interfered with normal polymerization and prompted re-initiation of the MMA embedding procedure over an additional 14 days.

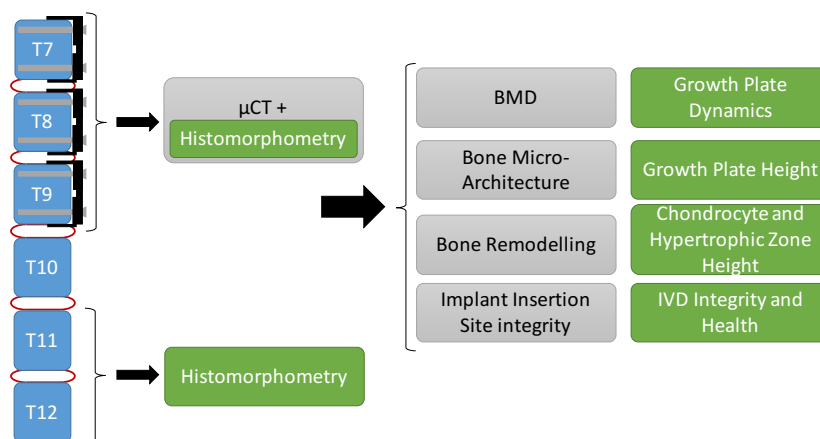


Figure 3-12: Illustration of excised segments and projected study allocation

### 3.3.1 μ-CT investigation

#### 3.3.1.1 Methods

Imaging was performed using a SkyScan 1176 μ-CT. The excised T7-T9 spinal segments, including IVDs, were wrapped in PBS-soaked gauze and placed on the scanner's bed. Each segment was scanned individually after removal of the posterior elements due to the limited scan diameter (68mm) using consistent parameters between samples (18 μm resolution, 90 kV, 278uA, 0.5 mm Aluminum filter, and 0.5° rotation step). Scans were typically completed within 45-60 min, each.

The rational for the acquired scans was to assess the bone micro-architecture integrity and bone mineral density. Bone micro-architecture is characterized using specific indices: the bone volume fraction ( $B_v/T_v$ ), specific bone surface ( $B_s/B_v$ ), trabecular number ( $T_bN$ ), trabecular thickness ( $T_bT_h$ ), trabecular separation ( $T_bS_p$ ), and connectivity density ( $C_{od}$ ). These parameters quantify bone quality and micro-architecture and are automatically calculated following post-processing of reconstructed CT slices and SkyScan's provided software. The reconstructed slices also allowed visualizing bone's integrity at implant and screw insertion site as conventional radiographs limit such observation and analyses.

### 3.3.1.2 Results

Here, a qualitative analysis is presented and further quantitative analysis will shape the framework of a future project. As such, Figure 3-13 shows mid-coronal CT slices for instrumented and control T7-T9 vertebrae. Figure 3-14 illustrates the mid-transverse slices for T7, T8, and T9 instrumented and control vertebrae.

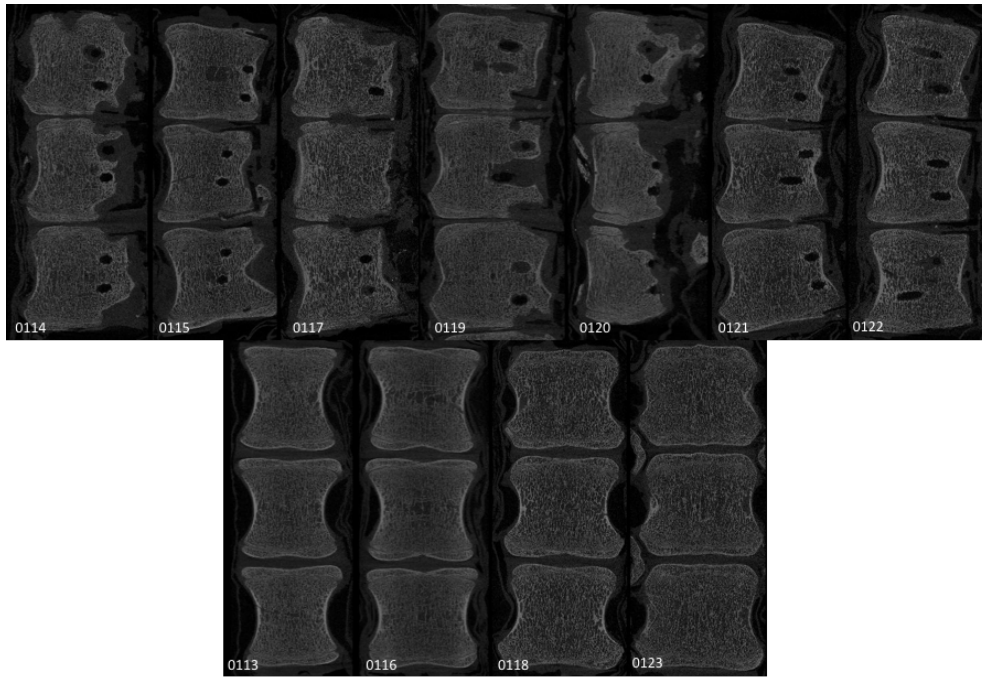


Figure 3-13: Mid-coronal CT slices. Top row shows instrumented T7-T9 vertebrae, and bottom row reflects control counterparts. Numbers identify animal tags.

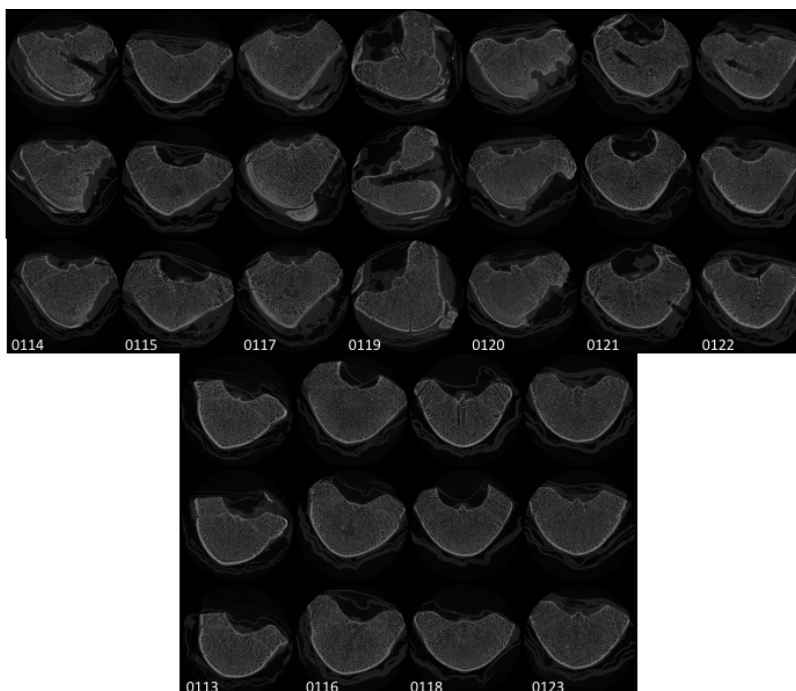


Figure 3-14: Mid-transverse CT slices. Top 3 rows correspond to instrumented T7, T8, and T9 while the bottom row corresponds to control counterparts. Numbers identify animal tags.

The following table summarizes the qualitative  $\mu$ CT and radiographic observations.

Table 3-1:  $\mu$ -CT qualitative observations

Pig #	Group	Qualitative Observations and Comments
0113	Control	No signs of vertebral deformity or malformation.
0114	Instrumented	No sagittal wedging, no signs of implant slippage. Evident coronal wedging. Screws penetrated spinal canal, Signs of bone loss and fibrous tissue formation around and over implant.
0115	Instrumented	No sagittal wedging, no signs of implant slippage. Evident coronal wedging. Screws penetrated spinal canal.
0116	Control	No signs of vertebral deformity or malformation.
0117	Instrumented	No sagittal wedging, no signs of implant slippage. Evident coronal wedging. Fibrous tissue formation around and over implant.
0118	Control	No signs of vertebral deformity or malformation.
0119	Instrumented	No sagittal wedging, no signs of implant slippage. Evident coronal wedging. Significant bone loss due to deep tissue infection evident during dissection. Case omitted from study.

<b>0120</b>	Instrumented	No sagittal wedging, no signs of implant slippage. Evident coronal wedging. Fibrous tissue formation around and above implant. Signs of bone loss.
<b>0121</b>	Instrumented	No sagittal wedging, no signs of implant slippage. Evident coronal wedging. Best implant placement. Minor fibrous tissue formation.
<b>1022</b>	Instrumented	No sagittal wedging, no signs of implant slippage. Evident coronal wedging. No fibrous tissue formation.
<b>0123</b>	Control	No signs of vertebral deformity or malformation.

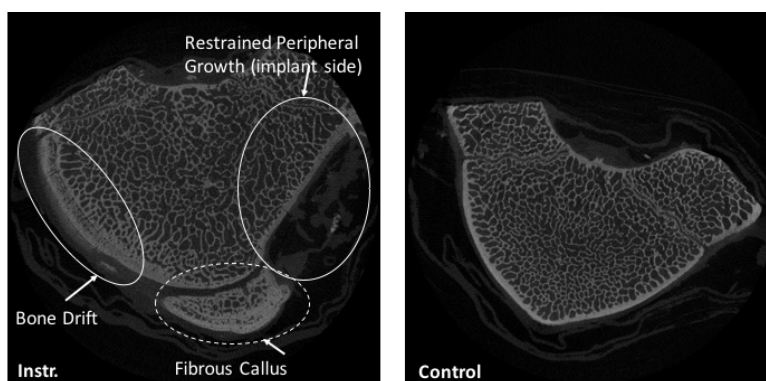


Figure 3-15: Instrumented vs. Control transverse CT cuts showing possible signs of restrained bone growth, bone drift phenomenon, and fibrous callus formation.

### 3.3.1.3 Discussion

Qualitatively, three phenomena can be observed from transverse CT cuts (Figure 3-15). First, peripheral (appositional) growth appears as ongoing. The cortical shell is flattened ipsi-lateral to instrumentation site with tendencies of shaping to the implant's periphery when compared to control vertebrae. The device restrained peripheral growth as it was fixed on the vertebral body wall. Transverse vertebral growth is not well documented within the literature which limited direct comparison with similar device circumferential profiles sheathing the vertebral body wall [181], [190] or bone anchor screws [184], [223]. Nevertheless, adolescent human vertebrae seize peripheral growth between 10-12y age [66]; thus, clinical applications will not be hindered by vertebral transverse growth.

Furthermore, a fibrous callus was found in two animals, one of which was omitted from the submitted manuscript due to discovering deep tissue infection at necropsy. The infection found its way to the vertebral bodies, consuming more than 1/3 of its volume as



evident in Figure 3-13 (animal 0119). In the second case (animal 0120), the source of the formation was unknown. It may have been due to intra-operative tissue injury or a response to prolonged (1 week) antibiotic exposure. Other sources may be linked to a broken rib during intra-operative manipulations. In both cases, its presence was undetected via conventional radiographs but was evident during dissection. Yet, manual left and right bending of the excised spine showed maintained spinal mobility under fluoroscopic imaging.

Finally, bone drift was observed in 4/6 animals contra-lateral to instrumentation side which may have been due to bone remodelling. More specifically, the implant's construct may have stress-shielded the vertebral body, and perhaps re-allocated loading to the un-instrumented side, increasing appositional bone formation. However, qualitatively, the cortical shell thickness at instrumentation side was similar to control animals contradicting possible stress shielding pending quantitative measurements. A separate explanation may be linked to the animals physiological response. In our submitted investigation, reversed disc wedging was evidenced and it was speculated as a compensatory response of animals, opposing an otherwise unnatural imposed spinal deformity. A closer look at the transverse  $\mu$ CT slices with this bone drift example further explains such compensatory *in vivo* response as the contra-lateral side exhibited an excess loading following animals re-straightening their spines. An interesting approach would require testing the device to correct deformed animal spines and observe bone drift occurrence.

These qualitative observations show the macro-structural changes due to the implant; however, as explained, many of these changes may have been secondary to injury. The second phase was to analyze the micro-architecture of the vertebral body trabecular bone. The framework for this study was initiated within this thesis. To analyse the bone mineral density, a reference model was used to calibrate the density range curve. As such, pig and human phantoms (250 and 750 mg/cc) were scanned using the same parameters as the control and instrumented vertebrae. Phantoms allow calibrating a linear BMD curve as a function of the Hounsfield unit (HU). Pig phantoms were chosen as they best describe the expected range of densities for our investigation. Micro-architectural parameters and BMD will be used to quantify the quality of bone in regions of interest and compare results to control animals.

## CHAPTER 4     FINITE ELEMENT MODEL FOR THE SIMULATION OF PROGRESSIVE EXPERIMENTAL SCOLIOSIS

### 4.1 Framework of the second article

Animal models have been extensively explored to establish progressive *in vivo* scoliosis models and evaluate the intra-operative, post-operative, and long-term effect of new, state-of-the-art fusionless implants (Section 1.4.3.3, Table 1-3). However, current experimental testing strategies can be time and cost-consuming as they require follow-up over several months for each implant design iterations. This study aimed at developing and validating a novel porcine spine finite element model as an alternative platform to simulate progressive experimental scoliosis and fusionless implants. A well-established experimental porcine scoliosis model and deformity correction were simulated and compared to published results. Two additional fusionless implants were simulated via the inverse approach and the induced deformities were compared to reported data.

The results of the performed simulations were submitted to European Spine Journal on March 10 2016, under the title “Porcine Spine Finite Element Model: A Complementary Tool to Experimental Scoliosis Fusionless Instrumentation”, for which the contribution of the first author is considered as 85%. Conclusions drawn allowed realization of objective 1 and exploring hypothesis 1.

## **4.2 Article 2: Porcine Spine Finite Element Model: A Complementary Tool to Experimental Scoliosis Fusionless Instrumentation**

### **Porcine Spine Finite Element Model: A Complementary Tool to Experimental Scoliosis Fusionless Instrumentation**

Bahe Hachem<sup>1,2</sup>, Carl-Eric Aubin<sup>1,2,3</sup>, Stefan Parent<sup>2,3</sup>

<sup>1</sup>*Dept. of Mechanical Engineering, Polytechnique Montreal, Montreal, Canada*

<sup>2</sup>*Research Center, Sainte-Justine University Hospital Center, Montreal, Canada*

<sup>3</sup>*Dept. of Surgery, Faculty of Medicine, Université de Montréal, Montreal, Canada*

Address for notification, correspondence and reprints:

Carl-Eric Aubin, Ph.D., P.Eng.

Full Professor

Canada Research Chair in Orthopedic Engineering' & NSERC-Medtronic Industrial  
Research Chair in Spine Biomechanics

Polytechnique Montreal, Department of Mechanical Engineering

P.O. Box 6079, Station "Centre-ville", Montreal (Quebec), H3C 3A7 Canada

E-mail: [carl-eric.aubin@polymtl.ca](mailto:carl-eric.aubin@polymtl.ca)

Phone: 1 (514) 340-4711 ext 2836; FAX: 1 (514) 340-5867

**Acknowledgements** This study was funded by the Natural Sciences and Engineering Research Council of Canada (grant # 3-6145 - 11; Industrial Research Chair with Medtronic of Canada).

#### **ABSTRACT**

**Purpose:** Developing fusionless devices to treat pediatric scoliosis necessitates lengthy and expensive animal trials. The objective was to develop and validate a porcine spine numerical model as an alternative platform to assess fusionless devices.

**Methods:** A parametric finite element model (FEM) of an osseoligamentous porcine spine and ribcage, including the epiphyseal growth plates, was developed. A follower type load replicated physiological and gravitational loads. Vertebral growth and its modulation were programmed based on the Hueter-Volkman principle, stipulating growth reduction/promotion due to increased/reduced compressive stresses. Scoliosis induction via a posterior tether and 5-level rib tethering was simulated over 10 weeks along with its subsequent correction via a contralateral anterior custom tether (20 weeks). Scoliosis induction was also simulated using two experimentally-tested compression-based fusionless implants (hemi & rigid staples) over 12 & 8 weeks growth, respectively. Resulting simulated Cobb and sagittal angles, and apical vertebral wedging and left/right height alterations were compared to reported studies.

**Results:** Simulated induced Cobb and vertebral wedging were 48.4° and 7.6° and corrected to 21° and 5.4°, respectively, with the contralateral anterior tether. Apical rotation (15.6°) was corrected to 7.4°. With the hemi and rigid staples, Cobb angle was 11.2° and 11.8°, respectively, with 3.7° and 2.0° vertebral wedging. Sagittal plane was within published range. Convex/concave side vertebral height difference was 3.1mm with the induction posterior tether and reduced to 2.3mm with the contralateral anterior tether, with 1.4mm and 0.8mm for the hemi and rigid staples, respectively.

**Conclusions:** The FEM represented growth-restraining effects and growth modulation with Cobb and vertebral wedging within 0.6° and 1.9° of experimental animal results, while it was within 5° and 2° for the two simulated staples. Ultimately, the model would serve as a time and cost-effective tool to assess the biomechanics and long-term effect of compression-based fusionless devices prior to animal trials, assisting the transfer towards treating scoliosis in the growing spine.

**Keywords:** *Scoliosis, Growth Modulation, Finite Element Model, Fusionless Implant, Experimental Scoliosis*

#### 4.2.1 Introduction

While the etiology of scoliosis, a three-dimensional spinal deformity, is yet to be elucidated, the pathomechanism of this disease is linked to alterations in normal spinal

loading governed by the Hueter-Volkman principle [1]. As such, asymmetrical spinal forces cause disruptions in the otherwise normal vertebral growth supported by the clinical presence of vertebral wedging within scoliotic spines [2]. Bracing and corrective spinal fusion prevail as prominent conventional treatments with the latter halting curve progression using instrumentation to fuse the spine. Despite its appealing outcomes, instrumentation and fusion is invasive and impairs spinal mobility.

Recent investigations have explored minimally invasive growth-sparing devices that promote differential concave-convex growth modulation and, over time, locally reverse vertebral wedging and globally correct or arrest the spinal deformity. Clinical investigations demonstrated well-established findings using vertebral body stapling [3] and tethering [4]; yet, a solid design platform is required to further explore and assess the short- and long-term effects of the wide designs of current and future fusionless approaches.

By inducing (inverse approach) or correcting a deformity, animal models have been explored for fusionless implant concept testing, design parameter assessment, and validation prior to human clinical trials. Most prominent are immature swine for their comparable vertebral dimensions to adolescents [5], similar biomechanical behavior, and rapid growth rate [6], allowing the study of the potency of new implants in shorter periods of time (pigs grow approx. 1.1 mm/vertebra/month [7, 8] while adolescents during growth spurt grow 1 mm/vertebra/year [9]). Nevertheless, experimental trials can be time-consuming when exploring a spectrum of implant designs and transfer the new knowledge to human cases.

By integrating growth dynamics, finite elements models (FEM) were previously demonstrated as alternative numerical tools simulating and hypothesizing scoliosis pathomechanism theories [10, 11], curve progression [12], and long-term effects of fusionless devices [13]. Current models reflected human adolescent spinal geometries with limited attempts on animal models. Lafortune et al. [14] developed a chicken thoracic spine FEM simulating induced scoliotic-like deformation following pinealectomy. Kumar et al. [15] developed a porcine T7-T8 functional spine unit FEM including growth modulation and implant pre-stress with preliminary simulations in-line with previously reported histomorphometric results; however, the model did not capture the complete spinal

biomechanical behavior in fusionless implant surgery. Thus, no attempt to develop a porcine thoracolumbar FEM integrating growth dynamics for curve induction/correction has been documented.

To address the underlying shortcomings, the objective was to develop, test, and verify a distinctive porcine spine finite element model by integrating biomechanical and growth responses, and simulating the long-term growth modulating action of different compression-based fusionless devices and comparing the deformity to published experimental data.

#### **4.2.2 Methods**

A parametric finite element model was developed using published morphometric data of a porcine spine [5] and ribcage (in-house measurements). Vertebral bodies were modeled with hexahedral elements depicting cancellous bone and 0.45mm thick cortical bone [16]. The posterior bony structures, ribs, sternum, and costal cartilage were modeled as 3D elastic beams while tension-only springs captured the non-linear behavior of the ligaments [10], with cross-sectional areas reflecting porcine specific anatomical measurements (Figure 4-1). Facet segmental orientation and location were assessed from  $\mu$ -CT and CT imaging from three 2-months old fresh Landrace/Yorkshire pig spines using a custom algorithm (MATLAB 2013a, MathWorks Inc., Natick, Massachusetts). Surface-to-surface contact pairs and shell elements represented their behavior. Facet interlocking mechanism at T10-T11 vertebral level [17] was also accounted for similarly to the T12-L1 facets transition in human spines.

The IVD was divided into the nucleus pulposus (30% cross-sectional area following findings ranging between 23%-43% for age-matched pigs [18]) and the annulus fibrosus. The growth plate was represented by 3 zones as previously explored [11]: the stress sensitive zone, the newly formed bone zone (NFB) where ossification occurred, and a transition zone joining the soft growth plate and the underlying cortical and cancellous bone. Zonal height ratios were adopted [19] with overall height obtained from in-house histomorphometric measurements of un-instrumented pig growth plates. A 2mm layer of subchondral bone, specific to pigs, was also modeled between the growth plate and the

IVD. The initial configuration reflected a normal spine with no apparent deformity. Thus, the coronal profile was straight with 30° kyphosis and 8° lordosis in the sagittal plane [5].

Vertebral body cortical [20] and cancellous bone [18] mechanical properties were obtained from the literature. Otherwise, the nucleus pulposus, annulus fibrosus, and the seven major spinal ligaments properties were calibrated using published ranges of motion and spinal flexibility testing [21]. The subchondral bone layer was assigned cancellous bone properties following structural similarities observed from  $\mu$ -CT scans and the lack of documented data. The ribs, sternum, costal cartilage, intercostal ligaments and posterior bony structures were assigned similar properties as human FEM [13] with the ribcage shape reflecting a porcine anatomy. Table 4-1 summarizes all linear elastic mechanical properties.

A follower-type load, representing force vectors tangential to the spinal curvature, approximated the stabilizing action of muscle forces [22] with cumulative magnitude accounting for 60% body weight. In quadrupeds, the major spinal loads are directed axially [23] counteracting the ventrally directed gravitational pull, further demonstrated by similar trabecular orientation between human and pig vertebral bodies. The model was immobilized at L5 while blocking T1 from translating in the transverse direction, emulating a forward gazing animal.

Growth was simulated via a previously validated iterative process (Figure 4-2) [12] relating axial vertebral growth rate to the variation between the actual ( $\sigma$ ) and normal physiological stresses ( $\sigma_m$ ). Briefly, the iterative algorithm was initiated with spinal loading from which an emulated growth response was computed as a function of growth plate sensitive zone stresses ( $\sigma$ ) followed by model geometry update where relevant clinical indices were calculated at each iterative step (Figure 4-2). This growth correlation was formulated following in-vivo trials suggesting its interspecies transfer with specific sensitivity factor ( $\beta$ ) adjustments (range 0.4-2.4 MPa<sup>-1</sup>) [1]. To calibrate the growth parameter ( $\beta$ ), scoliosis induction was simulated to match Schwab's induction data [24] for the first 6 weeks of growth. Baseline growth rate ( $G_m$ ) and  $\beta$  were then adjusted to 0.154 (age: 12-20 weeks) and 0.14 mm/week/GP (beyond 20 weeks) (GP: Growth Plate), and 0.6 MPa<sup>-1</sup>, respectively, matching pigs' natural accelerated growth aged between 3-5 months and

reduced beyond 5 months [6, 8]. In-house normal growth rate measurements indicated a  $20 \mu\text{m/day/GP}$  (i.e.  $0.14 \text{ mm/day/GP}$ ), in-line with reported porcine thoracic growth gain of  $0.4 \text{ cm/vertebra}$  (age: 12-22 weeks) and  $0.5 \text{ cm/vertebra}$  (age: 22-42 weeks) [8] and the Gm integrated in our model.

The growth behavior was validated using multiple approaches. First, scoliosis induction via the well-established Porcine Scoliosis Model (PSM) [24] was simulated. In brief, a posterior spinal tether (8-10 levels) and 5-level ribs tethering initiated an immediate and long-term deformity response. Cobb angle (intra-op and temporal) and vertebral wedging were evaluated after 10 weeks of growth. Then, additional 20-week correction via a contralateral anterior tether (PSM deformity correction) was simulated [8]. Independently, two compression-based fusionless devices were also simulated. First, a localized epiphyseal staple, namely hemi-staple, was modelled between T5-T8 vertebrae and consisted of a flat prong inserted between the growth plate and the IVD with the device's body fixed to the vertebral wall [7, 13]. Second, Wall's et al. [25] rigid staple, which spans the intervertebral space, was simulated between T6-T12. Growth modulation was simulated over the reported study periods (3 & 2 months, respectively). Constrained Cobb angle (instrumented levels), vertebral wedging, and vertebral left-right height differences (VHD) outlined the compared indices, when available. Modeling and analyses were performed using ANSYS v15 (Ansys Inc., Canonsburg, PA, USA).

### 4.2.3 Results

Figures 4-3a and 4-3b show the progression of the induced deformity for the PSM and correction via the anterior tether. Global and local coronal indices are illustrated. Simulated immediate coronal curve was  $23.2^\circ$  after tether settlement and progressed to  $48.4^\circ$  following 10 weeks growth simulations with  $7.6^\circ$  apical vertebral wedging. Simulated immediate post-operative Cobb was corrected to  $35.9^\circ$  and reduced to  $21.4^\circ$  after 20 weeks growth with  $5.4^\circ$  apical vertebral wedging. Simulated axial rotation progressed to  $15.6^\circ$  and was corrected to  $7.4^\circ$ , as expected from the corrective tether design [8]. Concave/convex vertebral height difference was  $3.1\text{mm}$  and was corrected to  $2.3\text{mm}$ .

The growth modulating effect of the additionally simulated fusionless devices was evidenced by the presence of local vertebral wedging and global coronal deformity. The



final Cobb angle and vertebral wedging are illustrated in (Figure 4-4) for both implants. Apical vertebral wedging was  $3.7^\circ$  and  $2.0^\circ$  for the simulated implants, respectively. Constrained Cobb angle was  $11.2^\circ$  and  $11.8^\circ$ , respectively at simulation end. Concave/convex height differences at the apical vertebra were 1.4mm and 0.8mm for the hemi-staple and rigid staple. Vertebral height was lowest at the instrumentation side for all instrumented levels demonstrating computed growth restraint at these sites. Contrarily, the sagittal profile remained unchanged over the simulated period with no apparent sagittal vertebral wedging.

#### **4.2.4 Discussion**

A porcine spine FEM was developed and verified as a platform for the assessment of the initial and long-term effects of spinal fusionless implants. Scoliosis induction via a posterior and 5-level rib tethering was simulated as well as the growth modulating effect of two compression-based implants with evidenced global and local deformities.

The model reproduced the scoliosis inducing procedure reported by Schwab et al. [24]. The intraoperative spinal manipulations and posterior and rib tether insertion were simulated with immediate Cobb angle ( $23.5^\circ$ ), which was within reported post-operative angles ( $24.5^\circ \pm 7.4^\circ$ ). Over 30 weeks of growth, the model was capable of reproducing the Cobb angle to within less than  $0.6^\circ$  (induced:  $48.4^\circ$  vs  $49^\circ$ , corrected:  $21.4^\circ$  vs  $21^\circ$ ) and vertebral wedging to less than  $1.9^\circ$  (induced:  $7.6^\circ$  vs  $7.6^\circ$ , corrected:  $5.4^\circ$  vs  $7.3^\circ$ ), similarly for vertebral height differences (induced: 3.1mm vs  $3.2 \pm 3.5$ mm, corrected: 2.3mm vs  $4.4 \pm 1.8$ mm). The apical vertebral rotation corroborated between simulated and experimental values (induced:  $15.6^\circ$  vs  $17.2^\circ$ , corrected:  $7.4^\circ$  vs  $10.3^\circ$ , with the latter approximated from reported data [8]). The simulated apical vertebral wedging was within the reported experimental variability ( $\pm 3.2^\circ$ ); however, VBH was lower. These differences may be explained by the placement of the simulated custom anterior tether. The latter is a specific interconnecting ligament setup aiming at correcting rotational deformity [8]. The authors provide no indication as to the exact in-vivo placement of the implant, which can vary between animals; thus differences with the simulated values can be deemed admissible. The reproduced sagittal profile was within the published range; however, the large experimental variability ( $5^\circ$ - $36^\circ$ ) during experimental positioning of the animals and

tether intra-operative tensioning limits a direct comparison. The simulations suggest the model can reproduce scoliosis induction techniques while acknowledging sagittal profile limits due to non-standardized animal manipulations during the X-ray acquisitions. Likewise, the deformed model can be used to assess the corrective potential of compression-based fusionless devices extrapolated for future treatment of scoliosis in the growing spine.

The model overestimated coronal deformity for the hemi-staple ( $11.2^\circ$  vs.  $6.5^\circ \pm 3.5^\circ$ , range:  $3-12^\circ$ ), and underestimated the rigid staple's deformity ( $11.8^\circ$  vs  $16.4^\circ \pm 5.4^\circ$ ). The sagittal profile showed no variation with respect to its normal counterpart as expected from the lateral placement of the simulated implants, restricting their effect to the coronal plane. Simulated apical vertebral wedging and concave/convex height difference corroborated with reported values (hemi-staple:  $3.7^\circ$  vs.  $4.1^\circ \pm 3.6^\circ$  and  $1.4\text{mm}$  vs  $1.2 \pm 1.4\text{mm}$ , rigid staple:  $2^\circ$  vs.  $2^\circ \pm 0.46^\circ$  [26]). Driscoll et al. [7] presented a greater cumulative hemi-staple vertebral wedging than constrained coronal Cobb angle evidence of reversed IVD wedge (opposite to vertebrae). Induced scoliosis may act differently, disrupting normal growth and resulting in reversed IVD wedging as an in-vivo compensatory mechanism in quadrupeds tending to maintain a forward looking gaze (a phenomenon further reported in curve induction experiments [27]). The developed model is unable to predict such a physiological response, which can explain discrepancies in the coronal instrumented Cobb (hemi-staple). The model also assumes ideal antero-lateral implant placement with prongs located adjacent to the intervertebral disc, which was not consistently reproduced experimentally [7]. Yet, differences in constrained Cobb angle still fall within  $5^\circ$  errors expected from measured radiograph [28]. Vertebral height measures are not available for the rigid staple, limiting a direct comparison. Also, the authors report discs wedged in the same direction as vertebrae [25] with our model showing similar IVD wedging arising from temporal segmental compression as a passive impact of the implant. Notwithstanding, vertebral wedging and height differences corroborated with reported values indicative of successful implementation of the growth model for a porcine spine.

The growth parameters were calibrated within the range of normal reported physiological rates [7, 8]. Moreover, the stress sensitivity factor ( $\beta = 0.6 \text{ MPa}^{-1}$ ) complied with different published animal species stress sensitivity factors ( $0.4-2.4 \text{ MPa}^{-1}$ ) [1]. Growth parameters

were further verified by simulating the growth of un-instrumented pig spines over equivalent growth phases. The normal coronal and sagittal temporal profiles were reproduced, which also confirms the plausibility of the applied follower load method (unpublished in-house data).

The outcomes of this computational model should be interpreted by recognizing the inherent limitations. The applied follower load method was chosen following several load application trials as the biomechanics of quadruped spines is not fully understood. To verify load application, normal growth plate stresses (0.8 MPa) were computed and corroborated with reported in-vivo intervertebral disc loads for standing pigs [30]. Nonetheless, localized growth plate stress profiles are not easily quantified experimentally, emphasizing the added potential of the model. Moreover, vertebral morphological data are inconsistent within published studies [5, 17] deriving from the multitude of swine breeds in biomechanical investigations. Morphological data were averaged over common porcine breeds for our model. Variations also extend to mechanical properties with values either taken from the literature, calibrated using custom algorithms, or estimated to reported human FEM. Vertebral body peripheral growth and neurocentral junction (NCJ) were omitted. Several investigations using human FEM [10] and porcine NCJ disruption [29] showed inconsistent results as to the role of the NCJ in spinal deformity. To the authors' knowledge, there are no published data for peripheral growth. Epiphyseal growth modulation and growth patterns may hold true whether or not peripheral growth was accounted for as growth rate correlates with the difference between a deformed and otherwise normal spine. Moreover, human vertebral peripheral and NCJ growth is halted prior to adolescence [9] facilitating the transfer of gained knowledge to clinical applications. The ribcage was modeled, but its growth was omitted in our simulations. Pilot simulations have shown the stabilizing role of the ribcage in stiffening the thoracic spine. Further exploratory simulations would elucidate its role in fusionless surgery. Nonetheless, the FEM reproduced experimental fusionless growth modulation as reported in published studies within the bounds of the identified limits and further coupling with standardized experimental observations is required to validate the model's behaviour under different implant configurations.

The developed model is a unique porcine spine and ribcage FEM integrating epiphyseal growth dynamics. The model demonstrated its potential to reproduce the growth restraining effect of two compression-based implants and scoliosis induction via a well-established porcine scoliosis model. Simulations with additional implant designs would further improve this tool as a complementary platform to further explore and provide initial implant design optimization before proceeding to long surgeries and to help bridge the knowledge transfer to clinical applications.

#### 4.2.5 References

1. Stokes IA, Aronsson DD, Dimock AN, et al. (2006) Endochondral growth in growth plates of three species at two anatomical locations modulated by mechanical compression and tension. *J Orthop Res* 24:1327–1334.
2. Parent S, Labelle H, Skalli W, de Guise J (2004) Vertebral wedging characteristic changes in scoliotic spines. *Spine (Phila Pa 1976)* 29:E455–62.
3. Betz RR, Ranade A, Samdani AF, et al. (2010) Vertebral body stapling: a fusionless treatment option for a growing child with moderate idiopathic scoliosis. *Spine (Phila Pa 1976)* 35:169–176.
4. Samdani AF, Ames RJ, Kimball JS, et al. (2014) Anterior Vertebral Body Tethering for Idiopathic Scoliosis: Two-Year Results. *Spine (Phila. Pa. 1976)*.
5. Busscher I, Ploegmakers JJW, Verkerke GJ, Veldhuizen AG (2010) Comparative anatomical dimensions of the complete human and porcine spine. *Eur Spine J* 19:1104–1114.
6. Roth AK, Bogie R, Jacobs E, et al. (2013) Large animal models in fusionless scoliosis correction research: a literature review. *Spine J* 13:675–688.
7. Driscoll M, Aubin CE, Moreau A, et al. (2012) Spinal growth modulation using a novel intravertebral epiphyseal device in an immature porcine model. *Eur Spine J* 21:138–144.

8. Moal B, Schwab F, Demakakos J, et al. (2013) The impact of a corrective tether on a scoliosis porcine model: a detailed 3D analysis with a 20 weeks follow-up. *Eur spine J Off Publ Eur Spine Soc Eur Spinal Deform Soc Eur Sect Cerv Spine Res Soc* 22:1800–1809.
9. Dimeglio A (2001) Growth in pediatric orthopaedics. *J Pediatr Orthop* 21:549–555.
10. Huynh A-M, Aubin C-E, Rajwani T, et al. (2006) Pedicle growth asymmetry as a cause of adolescent idiopathic scoliosis: a biomechanical study. *Eur Spine J* 16:523–529.
11. Driscoll M, Aubin C-E, Moreau A, et al. (2009) The role of spinal concave-convex biases in the progression of idiopathic scoliosis. *Eur Spine J* 18:180–187.
12. Shi L, Wang D, Driscoll M, et al. (2011) Biomechanical analysis and modeling of different vertebral growth patterns in adolescent idiopathic scoliosis and healthy subjects. *Scoliosis* 6:11.
13. Clin J, Aubin C-E, Parent S (2015) Biomechanical simulation and analysis of scoliosis correction using a fusionless intravertebral epiphyseal device. *Spine (Phila Pa 1976)* 40:369–376.
14. Lafortune P, Aubin C-éric, Boulanger H, et al. (2007) Biomechanical simulations of the scoliotic deformation process in the pinealectomized chicken: a preliminary study. *Scoliosis* 2:16.
15. Kumar B, Bylski-Austrow DI, Liu Y (2012) Finite element model of spinal hemiepiphysiodesis: effect of contact conditions, initial conditions, and growth. *Stud Heal Technol Inf* 176:99–103.
16. Akahoshi S, Sakai A, Arita S, et al. (2005) Modulation of bone turnover by alfacalcidol and/or alendronate does not prevent glucocorticoid-induced osteoporosis in growing minipig. *J Bone Miner Metab* 23:341–350.
17. Bozkus H, Crawford NR, Chamberlain RH, et al. (2005) Comparative anatomy of the porcine and human thoracic spines with reference to thoracoscopic surgical techniques. *Surg Endosc* 19:1652–1665.

18. Ryan G, Pandit A, Apatsidis D (2008) Stress distribution in the intervertebral disc correlates with strength distribution in subdiscal trabecular bone in the porcine lumbar spine. *Clin Biomech* 23:859–869.
19. Sergerie K, Lacoursière M-O, Lévesque M, Villemure I (2009) Mechanical properties of the porcine growth plate and its three zones from unconfined compression tests. *J Biomech* 42:510–516.
20. Kato N, Koshino T, Saito T, Takeuchi R (1998) Estimation of Young's modulus in swine cortical bone using quantitative computed tomography. *Bull Hosp Jt Dis* 57:183–186.
21. Gillespie KA, Dickey JP (2004) Biomechanical role of lumbar spine ligaments in flexion and extension: determination using a parallel linkage robot and a porcine model. *Spine (Phila Pa 1976)* 29:1208–1216.
22. Patwardhan AG, Meade KP, Lee B (2001) A frontal plane model of the lumbar spine subjected to a follower load: implications for the role of muscles. *J Biomech Eng* 123:212–217.
23. Smit TH (2002) The use of a quadruped as an in vivo model for the study of the spine - biomechanical considerations. *Eur Spine J* 11:137–144.
24. Schwab F, Patel A, Lafage V, Farcy JP (2009) A porcine model for progressive thoracic scoliosis. *Spine (Phila Pa 1976)* 34:E397–404.
25. Wall EJ, Bylski-Austrow DI, Kolata RJ, Crawford AH (2005) Endoscopic mechanical spinal hemiepiphysiodesis modifies spine growth. *Spine (Phila Pa 1976)* 30:1148–1153.
26. Glos DL, Boehm LA, Jain V V, et al. (2011) Coronal Plane Displacement Gradient Precedes Vertebral Growth Modification Using Titanium Spinal Hemiepiphyseal Implant. *Orthop. Res. Soc. Annu. Meet.*
27. Newton PO, Upasani V V, Farnsworth CL, et al. (2008) Spinal Growth Modulation with Use of a Tether in an Immature Porcine Model. *J Bone Jt Surg* 90:2695–2706.
28. Pruijs JEH, Hageman M a PE, Keessen W, et al. (1994) Variation in Cobb angle measurements in scoliosis. *Skeletal Radiol* 23:517–520.

29. Beguiristain JL, De Salis J, Oriaifo A, Canadell J (1980) Experimental scoliosis by epiphyseodesis in pigs. *Int Orthop* 3:317–321.

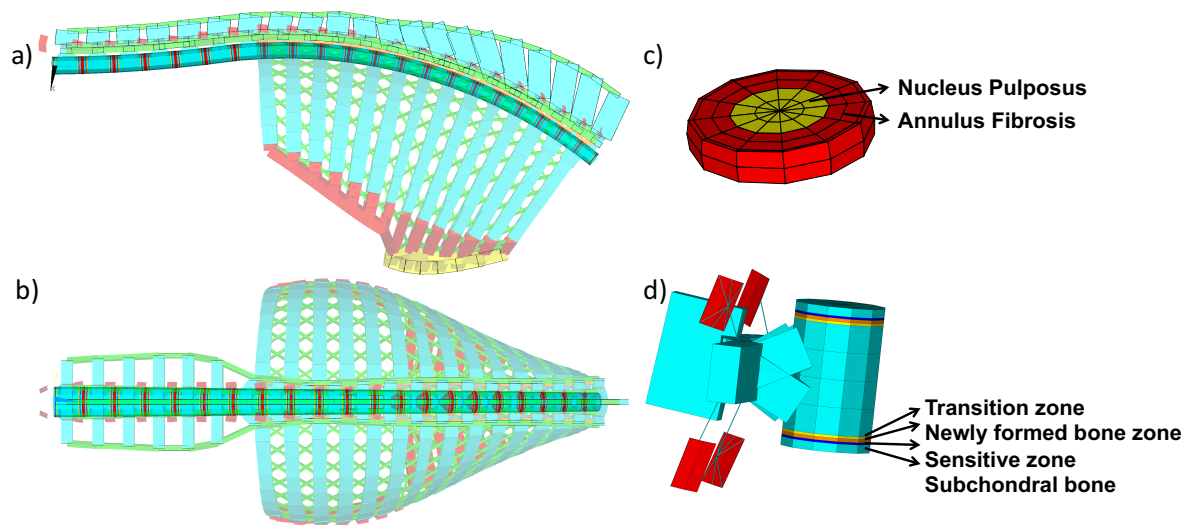


Figure 4-1: Parametric porcine spine model featuring the vertebral bodies (T1-T15, L1-L6). a) Lateral and b) posterior-anterior views c) Intervertebral disc nucleus pulposus and annulus fibrosis. D) L6 vertebra and growth plate zonal details.

Table 4-1: Reported and calibrated mechanical properties attributed to the different spinal anatomical structures

Anatomical Structure	Young's Modulus (MPa)	Poisson's Ratio	Element Type
Cortical Bone	14000	0.34	Solid Hexahedron
Cancellous Bone	500	0.3	Solid Hexahedron
Subchondral Bone	500	0.3	Solid Hexahedron
Sensitive Zone	11	0.24	Solid Hexahedron
Newly Formed Bone Zone	100	0.3	Solid Hexahedron
Transition Zone	300	0.3	Solid Hexahedron
Nucleus Pulposus	1	0.499	Solid Hexahedron
Annulus Fibrosis	10	0.45	Solid Hexahedron
Spinal Ligaments	1-250	0.3	Tension-Only Springs
Pedicles	14000	0.3	Beam
Transverse, Spinous, and Articular Processes	1000-9000	0.3	Beam
Ribs	5000	0.1	Beam
Sternum	1000	0.2	Beam
Costal Cartilages	250	0.3	Beam

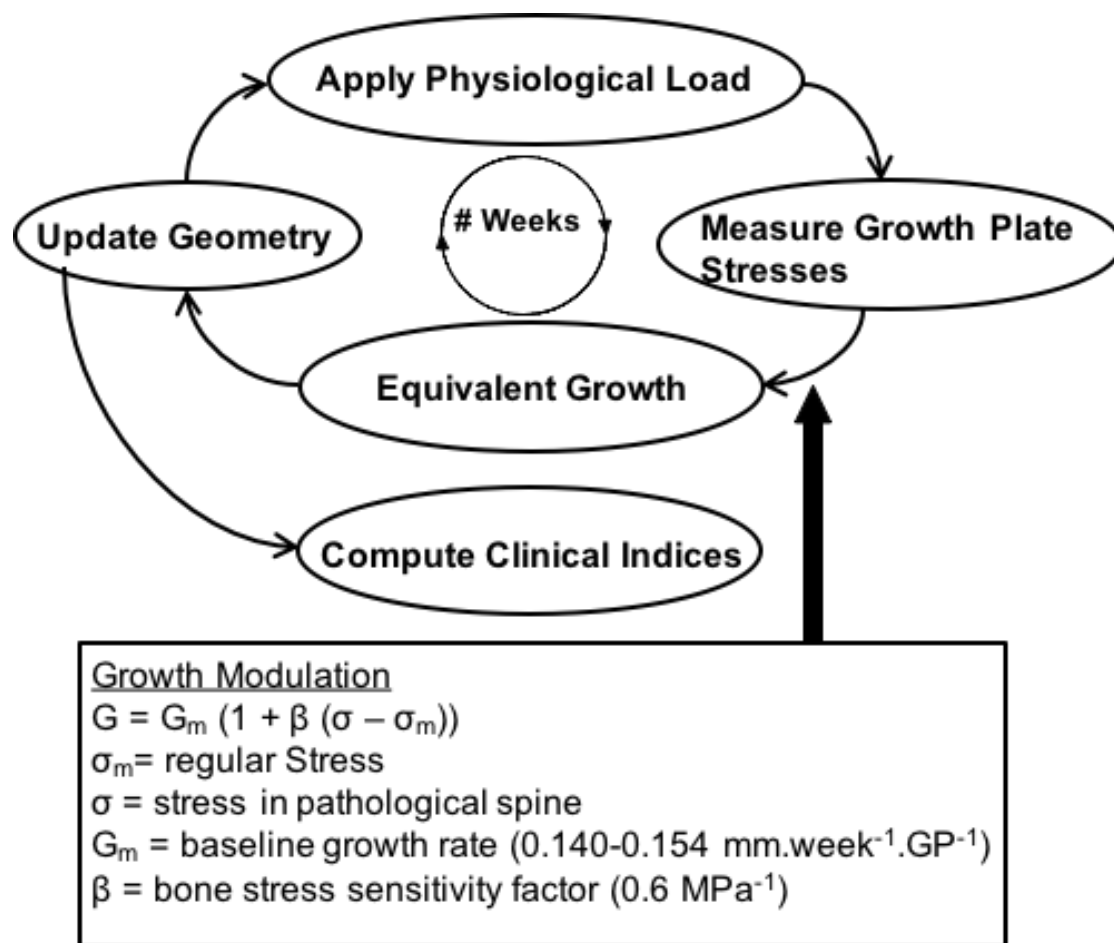


Figure 4-2: Growth model algorithm. Growth plate stresses are computed after physiological load application. An equivalent growth is the calculated as a function of stress differential. The model's geometry is then updated for clinical indices identification.



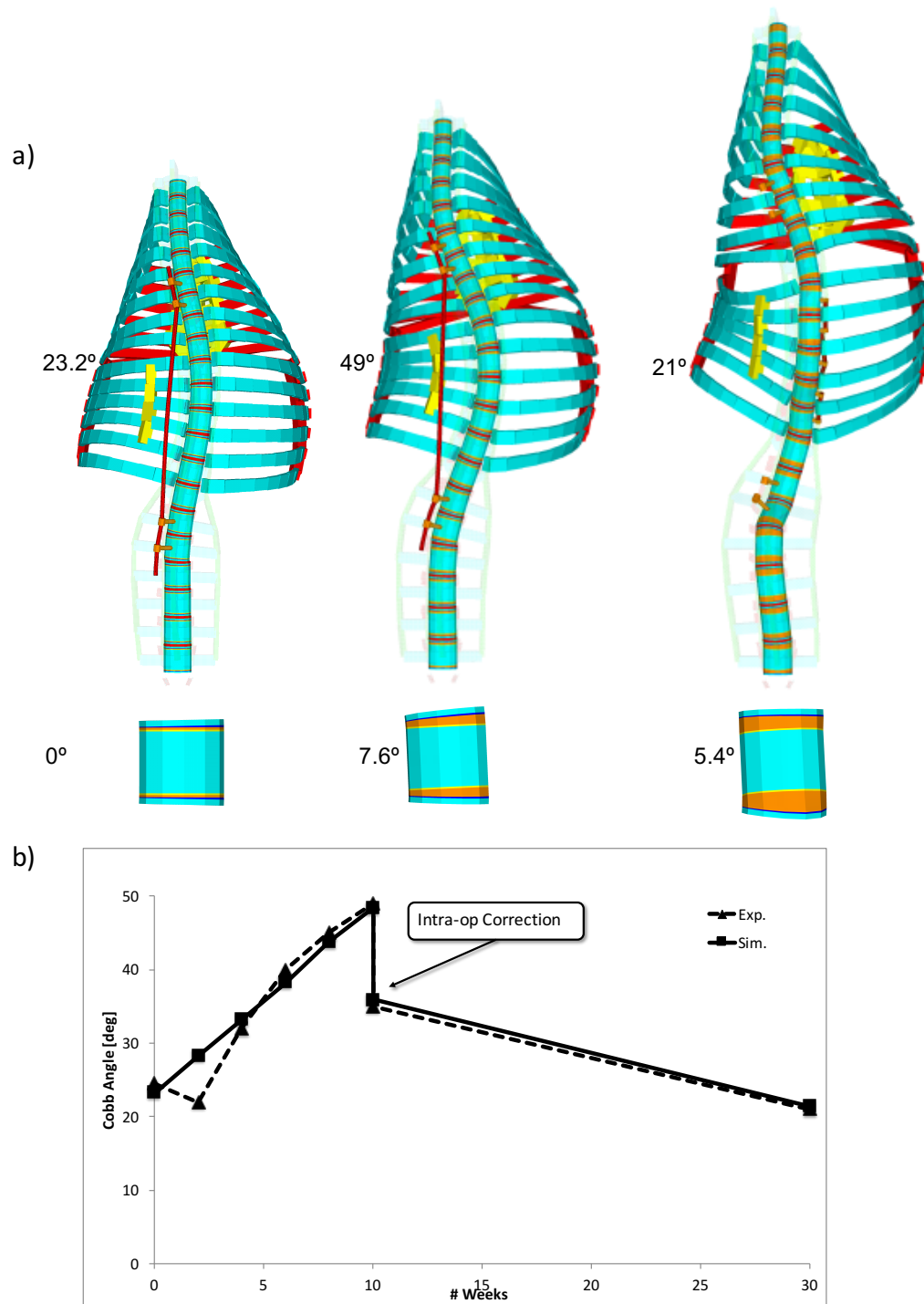


Figure 4-3: Simulated intraoperative posterior and rib tether insertion deformity induction and anterior curve correction (a). The above models (global and apical thoracic vertebra) are at 0w, 10w induction, and 20w after correction. Intercostal ligaments not shown

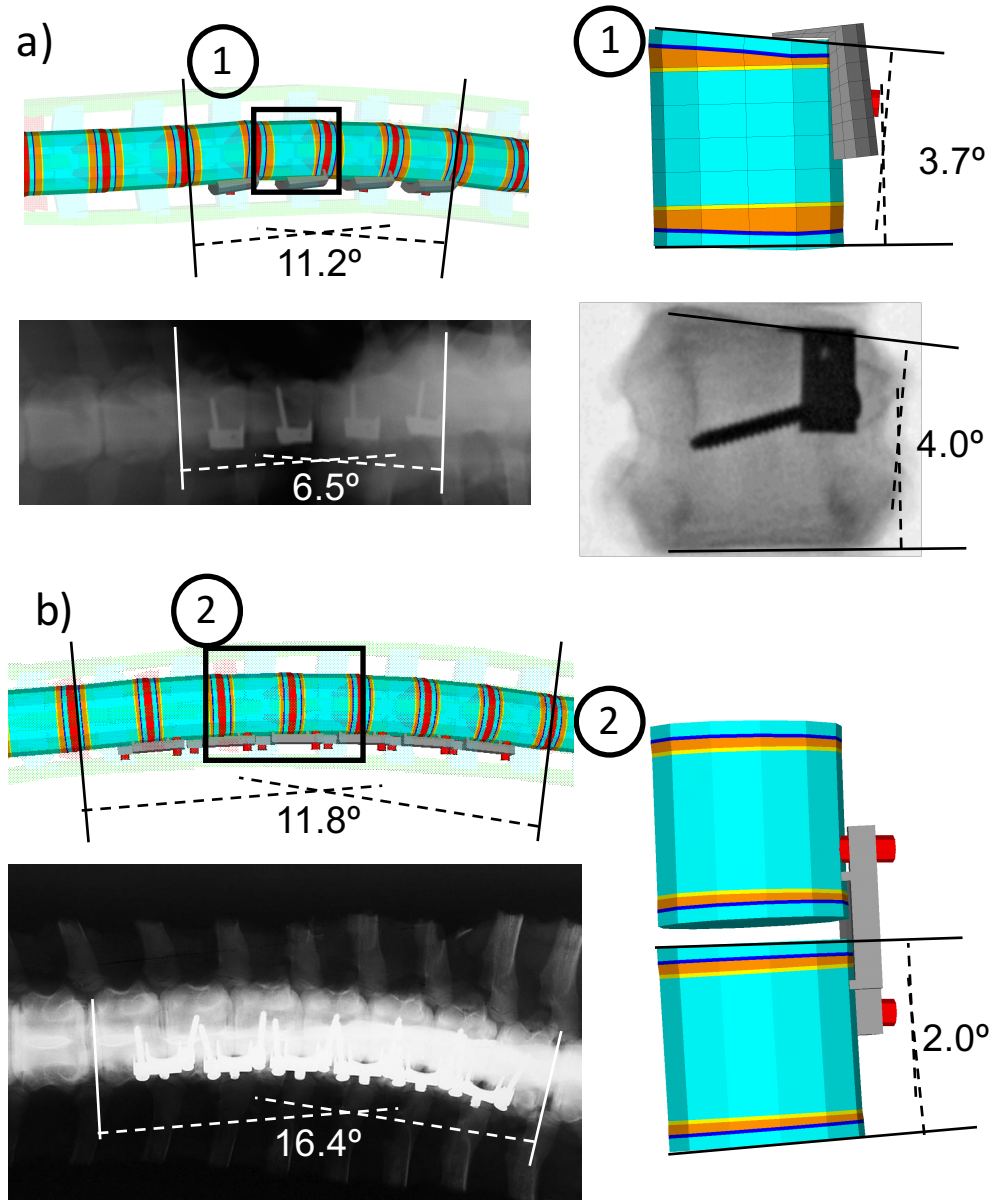


Figure 4-4: Cobb angle and vertebral wedging for the hemi-staple (a) [190] and rigid staple (b) [181]. Comparison between simulated and experimental data showing global and local simulated deformity after 3 months (hemi-staple) and 2 months (rigid staple) of growth

### 4.3 Additional Details: Model's Calibration and Verification/Validation

The model's growth parameter calibration, its verification and validation, and its predictive capabilities were performed in accordance to the ASME V&V-40 (Verification and Validation of computational modelling for medical devices). As such, several steps were undertaken to meet these requirement as outlined by (Figure 4-5).

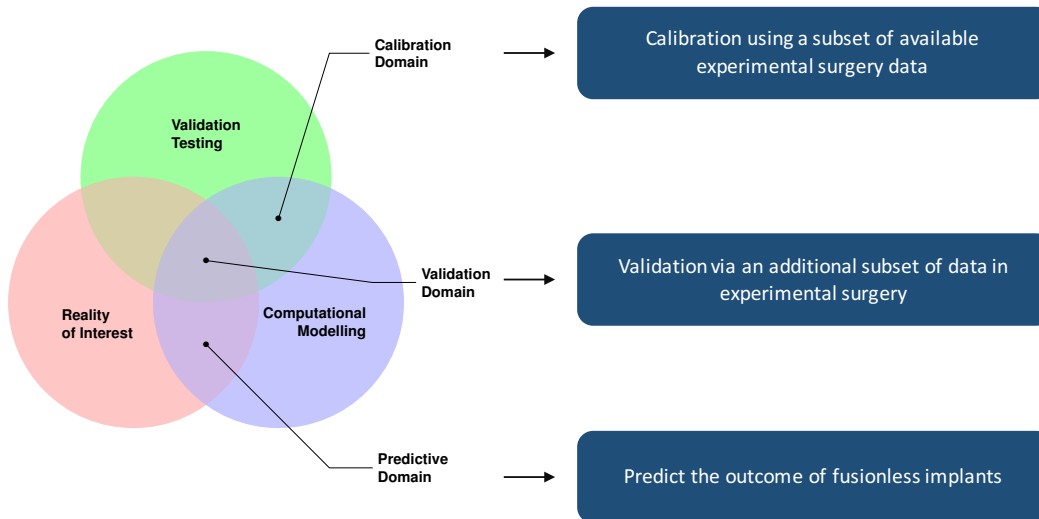


Figure 4-5: Porcine spine finite element model calibration, verification/validation, and predictive assessment as per ASME V&V-40 standards

To calibrate the model's growth parameters ( $\beta$  and  $G_m$ , Eq.(1), Figure 4-2), Schwab *et al.* *in vivo* porcine scoliosis model (PSM) was simulated. More specifically, scoliosis induction was simulated to match the first 6 weeks of curve creation. Briefly, a posterior spinal tether (8-10 levels) and 5-level ipsi-lateral ribs tethering initiated an immediate and long-term deformity response. Growth & growth modulation were simulated via a previously validated iterative process (Figure 4-2) [34] relating axial vertebral growth rate to the variation between the actual ( $\sigma$ ) and normal physiological stresses ( $\sigma_m$ ) (Section 4.2.2). This growth correlation was formulated following in-vivo trials suggesting its interspecies transfer with specific sensitivity factor ( $\beta$ ) adjustments [74].

Baseline growth rate ( $G_m$ ) and  $\beta$  were then adjusted until the model matched reported experimental data for Cobb angle and vertebral wedging. As such, the calibrated baseline growth rate was adjusted to 0.154 mm/week/GP (age: 12-20 weeks) and 0.14

mm/week/GP (beyond 20 weeks) (GP: Growth Plate). Growth rates were chosen to account for accelerated and decelerated growth phases reported in pigs (Figure 1-22). Calibrated baseline growth rates were comparable to reported data [76] and to in-house growth rate measurement on normal pig spines. The stress sensitivity factor  $\beta$  was adjusted to  $0.6 \text{ MPa}^{-1}$  and was consistent with expected published data (range  $0.4\text{-}2.4 \text{ MPa}^{-1}$ ) [74].

To validate the model's behaviour and the adjusted growth parameters, the remainder of the PSM's induction phase was simulated (up to 10 weeks). Temporal Cobb angle and vertebral wedging were evaluated after 10 weeks of growth and compared to the PSM data. An additional validation step involved simulating 20-week correction of the PSM via a contralateral custom anterior tether [76]. Final simulated Cobb angle and vertebral wedging were then compared to reported data for validity and shown to be within  $1^\circ$  Cobb,  $2^\circ$  vertebral wedging, and  $3^\circ$  axial rotation.

Finally, the model's predictive capability was examined by simulating two compression-based fusionless devices via the inverse approach. First, a localized epiphyseal staple, namely hemi-staple, was modelled between T5-T8 vertebrae [190] (Figure 1-37). Second, Wall's et al. [181] rigid staple, which spans the intervertebral space, was simulated between T6-T12. Growth modulation was simulated over the reported study periods (3 & 2 months, for the hemi- and rigid staples, respectively). Constrained Cobb angle (instrumented levels), vertebral wedging, and vertebral left-right height differences (VHD) outlined the compared indices. Simulated results to within  $5^\circ$ ,  $2^\circ$ , 20% Cobb angle and vertebral wedging confirmed the predictive capability of the developed model.

The pFEM's calibration, verification/validation, and predictive outcomes highlighted the core of the second article as part of this thesis work (Section 4.2) by respecting the ASME V&V-40 guidelines.

## 4.4 Inverse vs 2-Step Experimental Approaches: A Numerical Investigation

### 4.4.1 Introduction

Although animal trials support the hypothesis that new implants are best tested in similar conditions as their human application, i.e. idiopathic-like *in vivo* animal trials, to date, both the inverse and the 2-step approach remain widely applied experimentally. With several investigators venturing to develop *in vivo* scoliosis models, both exploratory avenues are promising and have demonstrated well-established results indicating new fusionless implants can engender changes to both a normal and a deformed spine. Morphological changes in the disc and the vertebra [166], stiffening of the spine following an artificial surgical inducing procedure which may involve concave rib tethering or convex rib resection [179], [180], [195], and differential concave/convex loading due to an existing spinal curvature are absent in a normal spine. Thus, it has been speculated that the growth modulation imposed by the newly tested implants are over estimated when evaluated on a normal spine via the inverse approach. Yet, the 2-step approach is quite extensive and long as it requires two surgical interventions (induction + correction) each of which spanning lengthy time-frames.

### 4.4.2 Methodology

The developed porcine spine FEM was exploited to test hypothesis 3 and evaluate the differences between the inverse and the 2-step strategies. As such, four implants were tested as described in Figure 4-6 and resulting spinal global and local changes were evaluated.

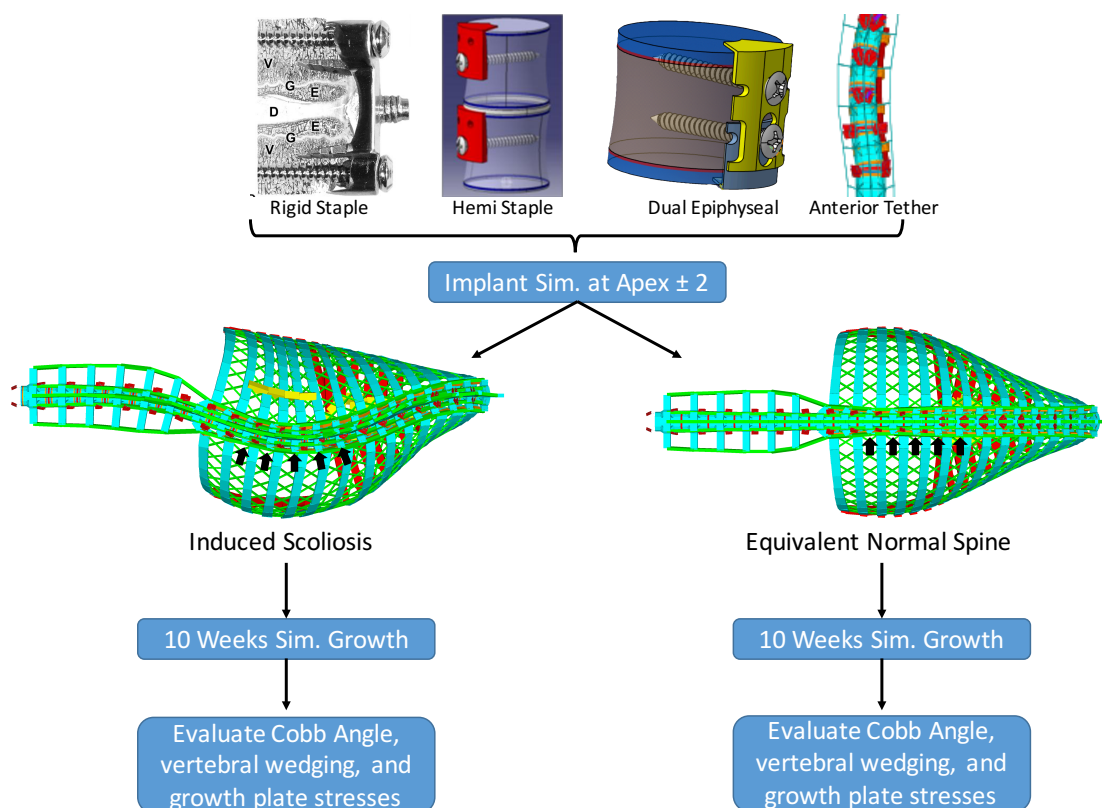


Figure 4-6: Diagram showing methodology for comparative simulation between Correction versus induction using 4 implants simulated at the apex  $\pm 2$ . The arrows indicate the location of the simulated implants.

To test the proposed hypothesis, simulations were conducted using two separate models. The first consisted of the porcine scoliosis model (PSM) as described in the submitted manuscript (ref. section 4.2) and the literature review (

Table 1-4) while the second reflected an equivalent normal model. More specifically, the PSM corresponded to simulating induced idiopathic-like scoliosis in an otherwise 12 weeks old normal spine using a unilateral posterior tether spanning from T6-T7 to L1-L2 (8 instrumented levels) with ipsi-lateral 5-level rib tethering. Scoliosis was induced over 6 weeks of growth to  $\sim 35^\circ$  coronal deformity followed by removal of the inducing tether. Similarly, a 12 weeks old normal spine growth was simulated over 6 weeks to reflect an age-matched spine and reflected a normal equivalent spine for the inverse approach simulations. Following the initial 6 weeks of simulated growth, four implants were modeled at the apex  $\pm 2$  levels as illustrated by the black arrows in Figure 4-6. Likewise, the implants were modeled on the age-matched normal spine at equivalent vertebral levels

(inverse approach). Implants were thus simulated at the right lateral aspect of the vertebral bodies for both models, which corresponded to the convexity of the deformed spine for the 2-step and concavity of the induced deformity (inverse approach). The simulated devices consisted of the rigid staple, hemi-staple, dual-epiphyseal staple, and anterior tether. These implants were chosen for their local action (hemi- and dual-epiphyseal staples) and those that spanning the intervertebral disc space (rigid-staple and anterior tether). Typically, anterior tethers are implanted via segmental tensioning between each vertebral level. However, given the passive growth modulating impact of the other three simulated implants, a fair comparison was conducted by simulating the tether snug tight with no initial pre-tension. Thus, the passive action of the tether was simulated and compared to the passive action of the remainder implants.

Growth was then computed over an additional 10 weeks for both models. Additionally, curve progression over 10 weeks (or growth excluding implants) was simulated for both models and served as reference geometries. Thus, a total of 10 simulations were conducted.

Using a previously validated iterative growth algorithm [34], [42], [90], [170], physiological loads were applied via the follower load method as described in *Section 4.2*. An empirically established growth modulation equation [74] was used to determine equivalent growth as a function of calculated growth plate stresses (ref. *Section 1.3.4*). The model was then updated to its new geometry where spinal shape indices were calculated at each iterative step.

Simulations were then compared between similar implants for inducing versus correcting an existing deformity as relative measures of correction or induction. Furthermore, the corrective potential was contrasted between each tested implant to outline their inherent differences. Curve progression of un-instrumented spines outlined the expected progression without corrective or inducing interventions. Constrained Cobb angle at the apex  $\pm 2$  levels, apical vertebral wedging, and growth plate stresses outlined the comparison framework. Growth plate stress profiles were also computed at different regions: Anterior (A), Anterior Left (AL), Left (L), Posterior Left (PL), Posterior (P), Posterior Right (PR), Right (AR), and Anterior Left (AL) (Figure 4-10).

### 4.4.3 Results

Figure 4-7A illustrates the absolute correction while Figure 4-7B points to the absolute inducing effect of each simulated implant. Following the porcine scoliosis model, the induced scoliosis deformity was  $32.6^{\circ}$  calculated between the apex  $\pm 2$  levels. The final Cobb angle was least corrected by the hemi-staple ( $32.6^{\circ}$  to  $29.2^{\circ}$ ) followed by the rigid staple ( $27.9^{\circ}$ ), the anterior tether ( $16.0^{\circ}$ ), then the dual-epiphyseal staple ( $12.7^{\circ}$ ) while the un-instrumented curve progressed to  $40.4^{\circ}$ . Conversely, the final induced Cobb angle was least for the rigid staple ( $7.1^{\circ}$ ) followed by the hemi-staple ( $10.3^{\circ}$ ), the anterior tether ( $22.5^{\circ}$ ), then the dual-epiphyseal staple ( $23.9^{\circ}$ ) while the un-instrumented curve progressed with no deformity.



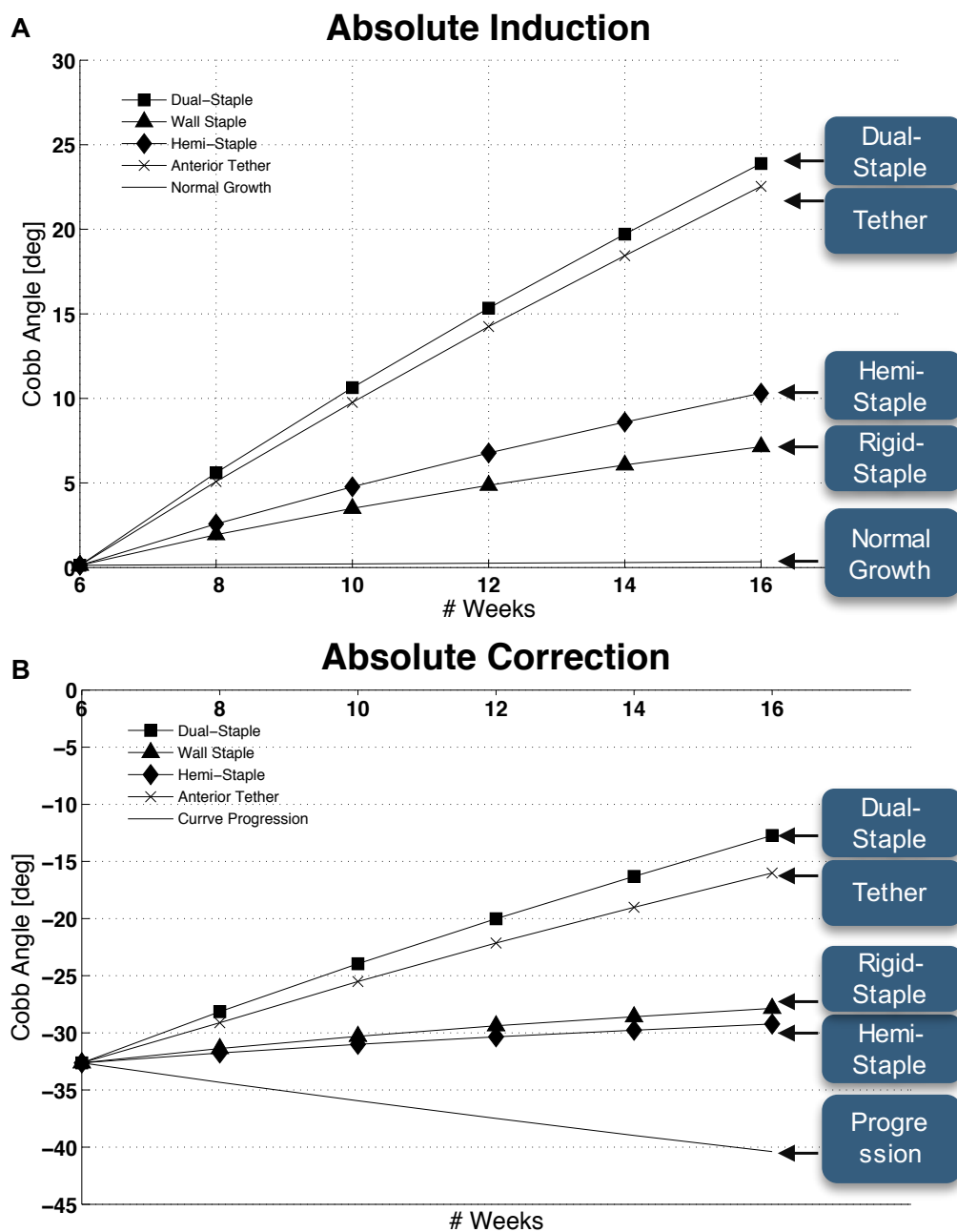


Figure 4-7: Absolute correction and induction of the simulated implants and expected curve progression. Negative values indicate a right convex curve.

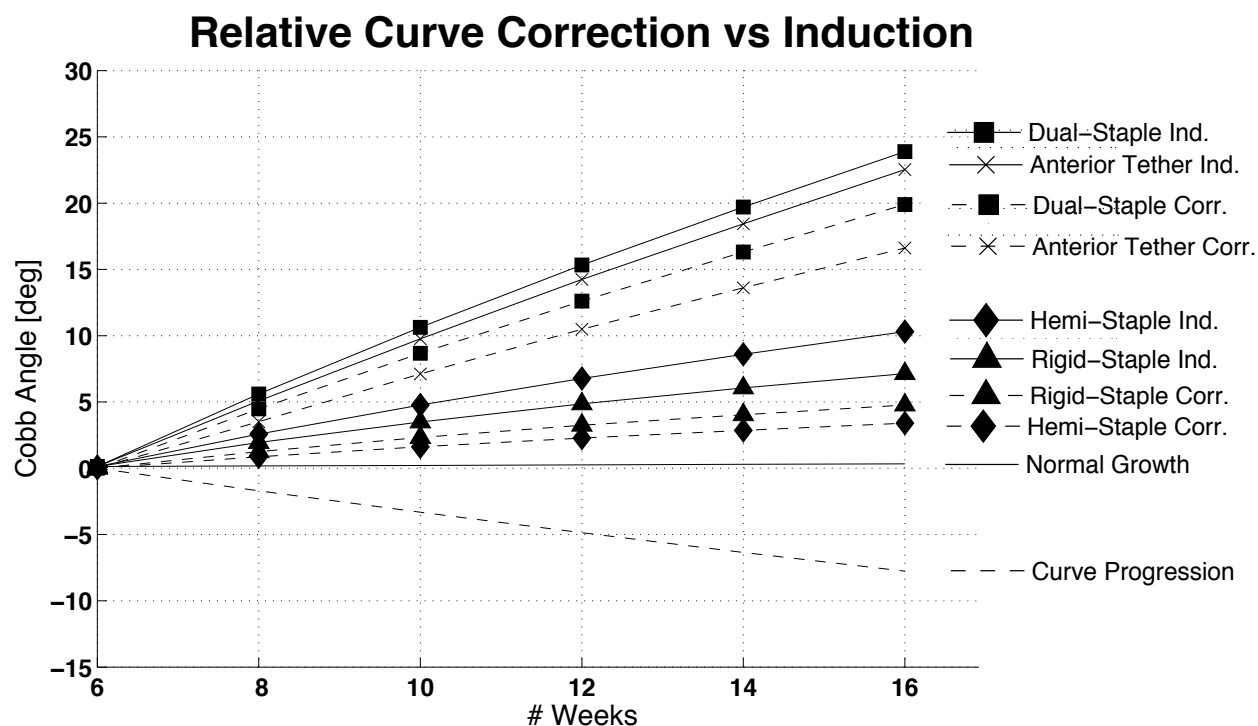


Figure 4-8: Relative curve evolution for correction and induction. Angles are presented as delta change with respect to the initial deformity (Corr.) or non-instrumented spine (Ind.).

Figure 4-8 illustrates the relative curve evolution for each implant when tested under the inverse and the 2-step approach. Relative angles referred to the difference in correction or induction angles with respect to the initial angles prior to instrumentation. Differences are presented in absolute values to facilitate direct comparison between the inverse and 2-step approaches. The dual-staple corrected the initial curve by  $19.9^\circ$ , followed by the tether ( $16.6^\circ$ ), then the rigid ( $4.8^\circ$ ) and hemi-staple ( $3.4^\circ$ ) while the un-instrumented curve progressed by  $7.8^\circ$ . The graph also demonstrated, for each implant inclusively, the difference between their corrective and inducing effects, with the latter consistently more prominent.

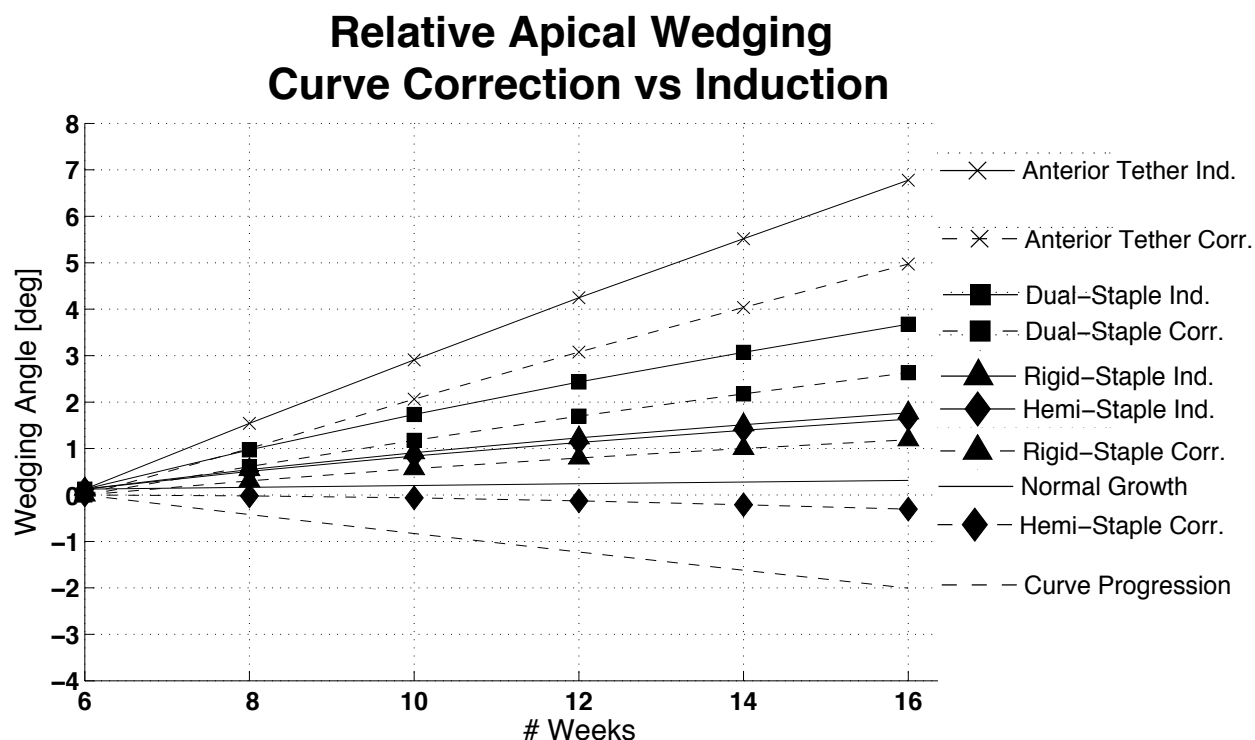


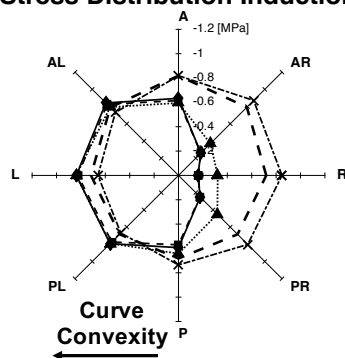
Figure 4-9: Relative apical vertebral wedging evolution for correction and induction.

Relative apical vertebral wedging is presented in Figure 4-9 for the induction and correction simulations, similarly to relative Cobb angles presented in Figure 4-8. The extent of induced apical vertebral wedging was consistently greater than corrected wedging for each simulated implant. In decreasing order, growth modulation was more prominent for the tether, the dual-staple, the hemi-staple, then the rigid staple.

Figure 4-10 illustrates the growth plate stresses at the apical vertebra for curve induction (left) and correction (right) simulations. All tested implants are presented as well as equivalent stresses from the un-instrumented spines. For induction simulations, growth plate convex stresses (opposite to instrumentation site) remained comparable to normal spinal stresses with minor differences. On the concave (instrumented region), growth plate stresses were shielded for all implants except the anterior tether with noticeable increase in compressive stress. For the correction simulations, growth plate stresses were shifted towards the concavity of the curvature opposite to instrumentation site. Stresses were similarly shielded at the instrumentation site except for the tether. The latter shifted

the stresses towards to convexity of the deformity as to slowly regain normal growth plate stresses.

### Stress Distribution Induction



### Stress Distribution Correction

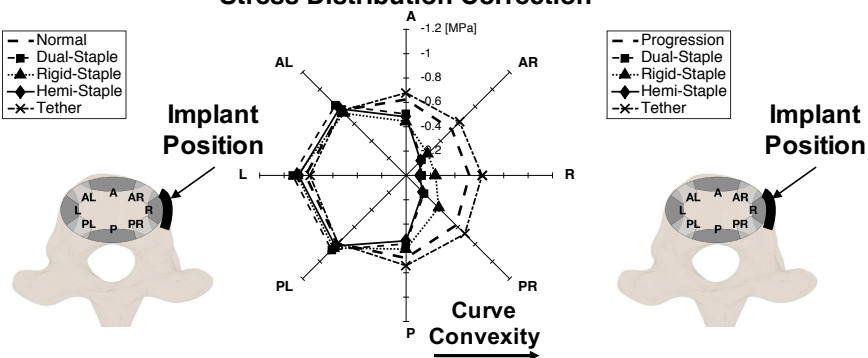


Figure 4-10: Apical growth plate stresses for the induction (left) and correction (right) for tested implants, viewed from the top. Implants are positioned on the right lateral aspect of the vertebral body.

Discussions and conclusions drawn from this investigational study are presented in the general discussion (Section Chapter 6) and conclusion (Chapter 7) of the current thesis.

## CHAPTER 5 BIOMECHANICAL STUDY OF THE ROLE OF RIBCAGE

### 5.1 Introduction

The ribcage contributes to the overall stability of the thoracic spine as previously explored in the “Literature Review” Section 1.2.2. By removing the ribcage, the stiffness of the thoracic spinal region reduced in flexion, extension, lateral bending, and axial rotation. Several investigators have developed scoliosis animal models via different inducing techniques combined with ribcage manipulations to increase the moment on the spine [173], [177] (Table 1-3). Numerical simulations confirmed the biomechanical contribution of the ribcage in successful brace treatment simulations. Furthermore, finite element simulations have indicated the important role of the ribcage in curve progression [220] or as possible scoliosis corrective approach via surgical resectioning [221]. Yet, the biomechanical contribution of the ribcage to the corrective outcomes of unassuming fusionless devices has not been documented. An investigational study was conducted using the developed pFEM for the realization of objective 3.ii and exploring hypothesis 4.

### 5.2 Methodology

The developed porcine spine finite element model (*Section 4.2*) was used to conduct an investigational analysis to assess the importance of accounting for the biomechanical impact of the ribcage in fusionless instrumentation simulations targeted for the correction of spinal deformities. The methodology employed is illustrated in Figure 5-1. Two fusionless implants, namely a Hemi-Staple and an Anterior Tether, were tested under the inverse and the 2-step approaches by including or excluding the ribcage over the simulated period. The implants were chosen to account for localized device designs and those spanning the intervertebral disc space.

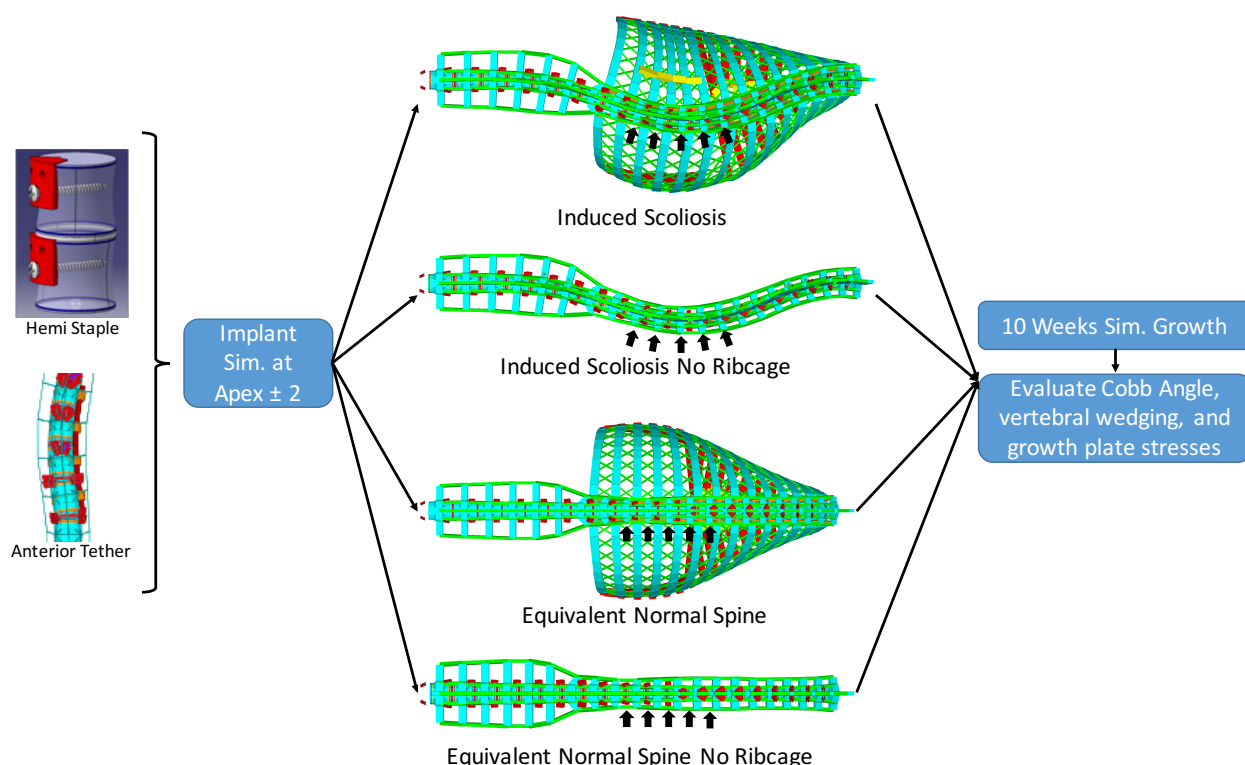


Figure 5-1: Illustration of the methodological approach used to assess the biomechanical contributive effect of the ribcage in fusionless surgery. The arrows indicate the location of the simulated implants.

The procedure consisted of modeling the two types of implants at the apex  $\pm 2$  levels on a deformed spine (2-step approach) and equivalent levels on a normal spine (inverse approach). Implants were thus simulated at the right lateral aspect of the vertebral bodies for each model, which corresponded to the convexity of the deformed spine for the 2-step. The inverse approach was also chosen to investigate the ribcage's stabilizer role under external implant action on a straight spine. Similar simulations were also conducted on equivalent spines by excluding the ribcage. Thus, 8 simulations were performed over 10 weeks of growth and growth modulation. Additionally, equivalent growth was simulated for un-instrumented deformed and matched normal spines cumulating to 12 overall simulations. Clinically, anterior tethers are inserted via segmental tensioning between each vertebral level. However, to conduct a fair comparison with the hemi-staple (passive action), the tether was simulated snug tight with no initial pre-tension. Thus, only its

passive action was considered. Although not representative of expected intra-operative applications of spinal anterior tethering, the chosen modeling procedure was assumed to be sufficient for a comparative investigation.

Each simulation was initiated by modeling the implants at the selected levels. Using the iterative process presented in *Sections 4.2* and *4.3*, physiological loads were applied via the follower load method from which growth plate stresses were evaluated and an equivalent growth modulation was calculated. The model was then updated to its new geometry to calculate important spinal indices at each iterative step.

Final apical vertebral growth plate stresses, apical vertebral wedging, and Cobb angle measured on the instrumented segment outlined the compared indices. Growth plate stress profiles were determined at different regions as explored in *Section 4.4.2* and Figure 4-10. Comparisons were performed between models including and lacking the ribcage for both the inverse and 2-step approaches separately to highlight differences, if any, and justify accounting for the ribcage's contribution in future fusionless implant designs and simulations and explain its biomechanical impact.

### 5.3 Results

Figure 5-2 depicts a graphical representation of the regional growth plate stress profiles at the apical vertebra for the induced deformity simulations. Stress profiles for each tested implants are presented for models including and excluding the ribcage. Normal growth stress profiles are similarly presented. Stress profiles were quasi-equivalent for normal spinal loading with or without the ribcage; however, the profile was shifted slightly anteriorly in the latter case. Stresses at the instrumentation side (R) showed signs of stress shielding for the hemi-staple and were consistently lower than the un-instrumented side (L). Differences lie on the un-instrumented side when the ribcage was included with stresses higher with its inclusion. Similar trends were observed on the un-instrumented side for the anterior tether. Contrarily, stresses at the instrumentation side were increased relative to normal spinal loading reaching values up to 0.82 MPa antero-laterally with the ribcage omitted (Figure 5-2).

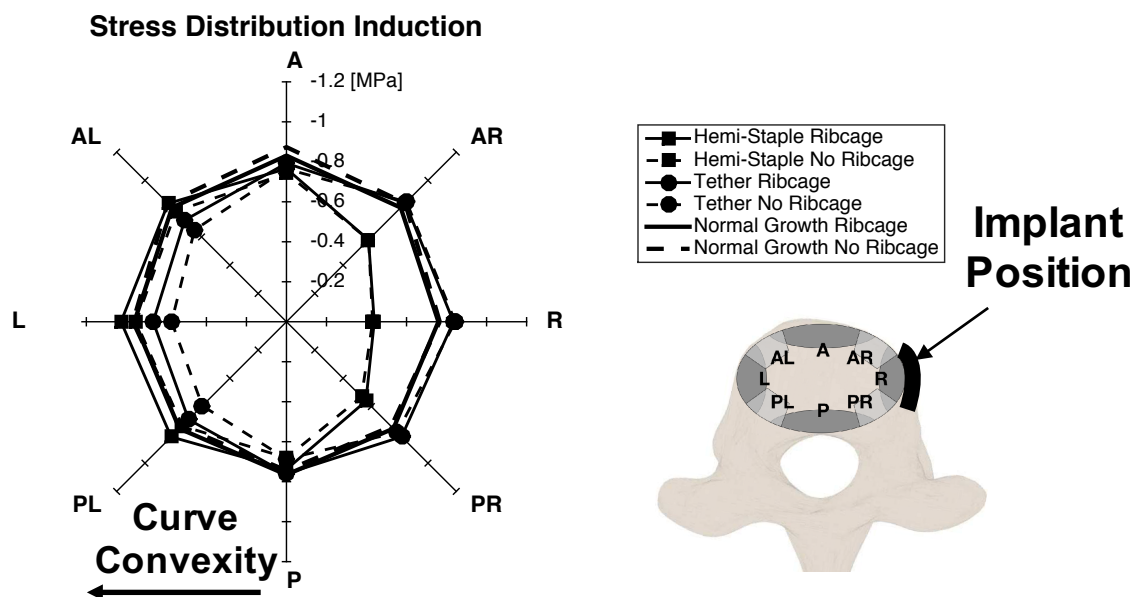


Figure 5-2: Growth plate stress distributions at the apical vertebra for the induced deformity, viewed from the top. Solid lines correspond to model including the ribcage. A, L, R, and P refer to Anterior, Left, Right, and Posterior respectively. Implants are positioned on the right lateral aspect of the vertebral body.

Figure 5-3 illustrates the regional growth plate stresses for deformity correction simulations. Curve progression (un-instrumented spine) stress profiles are shifted towards the concavity of the curvature following omission of the ribcage reaching 0.88 MPa stresses. Similar tendencies were observed for the hemi-staple and anterior tether.



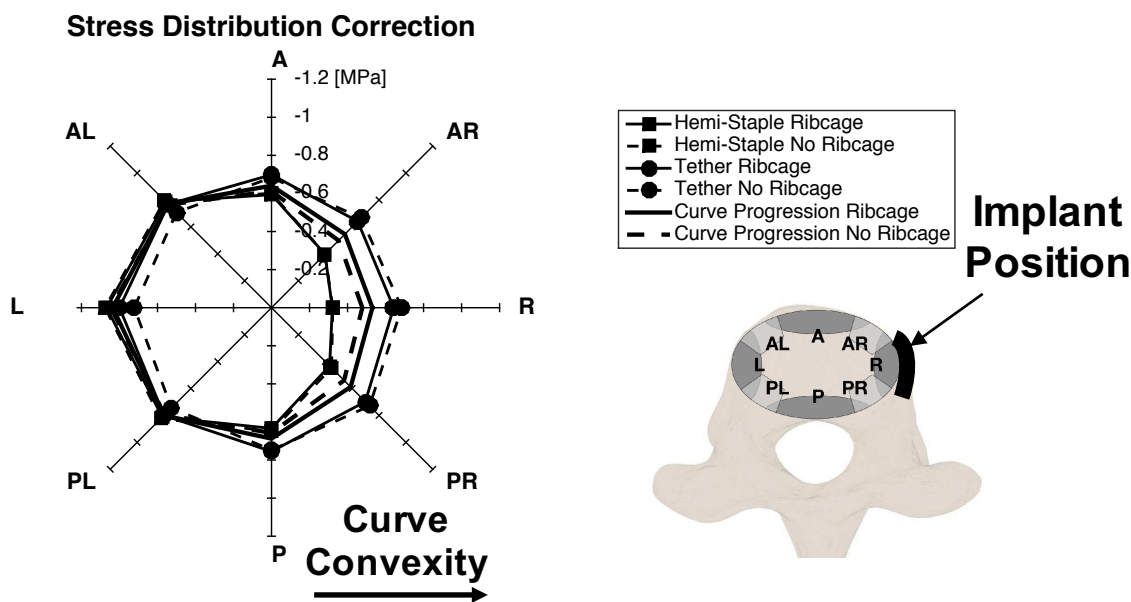


Figure 5-3: Growth plate stress distributions at the apical vertebra for deformity correction, viewed from the top. Solid lines correspond to model including the ribcage. A, L, R, and P refer to Anterior, Left, Right, and Posterior respectively. Implants are positioned on the right lateral aspect of the vertebral body.

Progressive Cobb angles are presented in Figure 5-4 for curve induction (left) and correction (right) simulations. Removal of the ribcage resulted in nearly doubling the induced curve for both the hemi-staple and anterior tether. However, normal growth was not affected by the ribcage presence with no apparent coronal deformity.

No differences were observed in the corrective potential of the hemi-staple with exclusion of the thorax. However, a higher correction was observed for the tether for simulations lacking the ribcage (final curves:  $-1^\circ$  vs  $-14^\circ$ ). In a similar manner, the curve progressed beyond  $-48^\circ$  vs  $-40^\circ$  with the thorax.

The tendencies were also echoed for apical vertebral wedging for both the induction and correction simulations for each implant, respectively. Vertebral wedging was corrected (or induced) with a difference of  $\sim 2^\circ$ . Removal of the ribcage resulted in a higher local growth modulation. Additionally, removal of the ribcage resulted in an overcorrection of apical vertebral wedging for the tether simulations ( $2^\circ$  vs  $-0.2^\circ$ ).

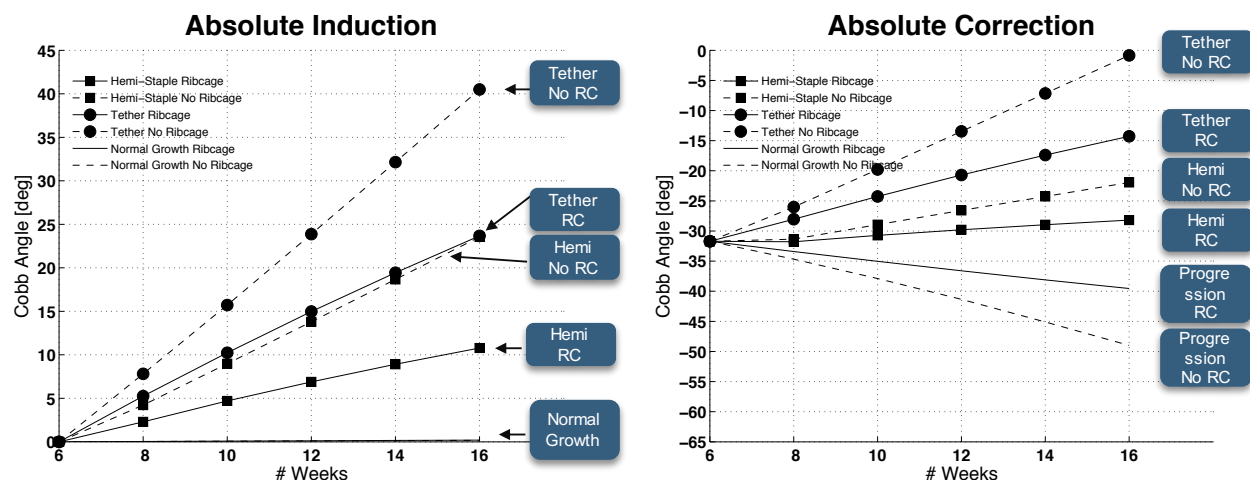


Figure 5-4: Cobb angle progression for the induced (left) and corrected (right) deformities. Solid lines correspond to model including the ribcage. Negative values indicate a right convex curve.

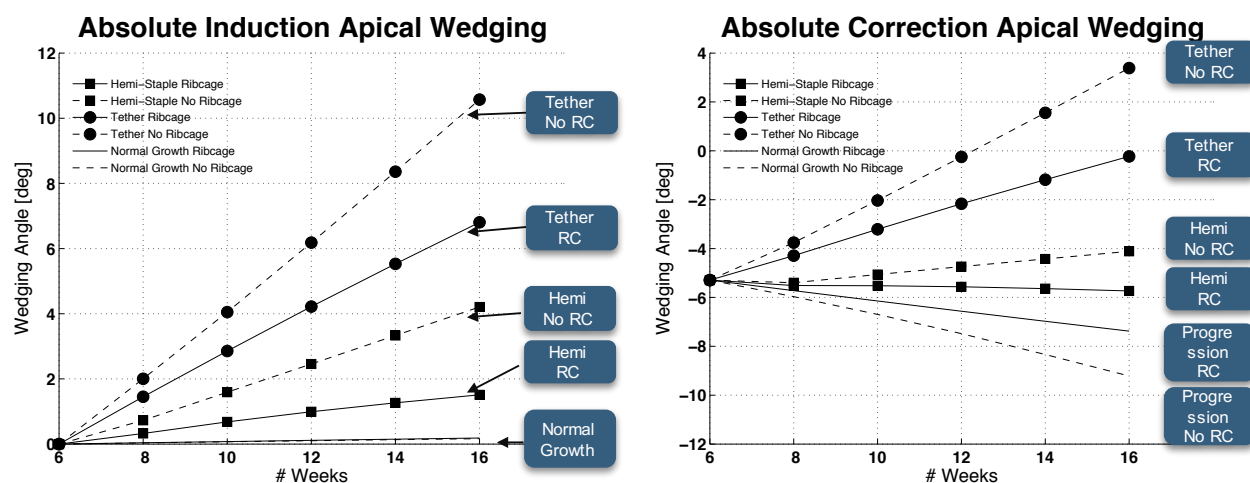


Figure 5-5: Apical vertebral wedging progression for the induced (left) and corrected (right) deformities. Solid lines correspond to model including the ribcage. Negative values indicate wedged vertebrae with shorter vertebral body height to the left.

Discussions and conclusions drawn from this investigational study are presented in the general discussion (Section Chapter 6) and conclusion (Chapter 7) of the current manuscript.

## CHAPTER 6 GENERAL DISCUSSION

*In vivo* animal trials have been explored to extensively assess emerging fusionless devices focused towards alternative treatment strategies to conventional surgical interventions with implant predominantly bridging the intervertebral disc space. New implants are typically tested via the inverse or 2-step approaches; however, a detailed review of current investigations highlighted the temporal and investment challenges linked to these time-consuming trials. To tackle these limitations, a porcine spine finite element model, including the ribcage, and dual-epiphyseal implant were developed. Current investigations predominantly test fusionless devices experimentally, with prior challenges previously re-iterated. The pFEM was distinctively developed as a novel approach that was never tested nor attempted prior to this thesis work. The model was shown to reproduce equivalent experimental data and allowed exploiting this tool to further test differences between the inverse and 2-step experimental approaches and identify the biomechanical contribution of the ribcage in fusionless experimental surgery. Moreover, the improved dual-epiphyseal staple's feasibility was originally tested using the pFEM and included a custom, state-of-the-art, expansion mechanism offering dimensional height adjustment intra-operatively to accommodate diverse vertebral morphologies.

The developed pFEM reproduced a progressive scoliosis model and its correction as well as the inducing effect of two fusionless implants (inverse approach), albeit not replicated reversed disc wedging for the latter. Simulated results were less than 1° Cobb, 2° vertebral wedging, and 3° axial rotation for progressive scoliosis and its correction and 5° Cobb, 2° wedge, and 3° rotation for the two tested implants. Progressive scoliosis model and correction simulations served as initial model verification and confirmation of applied boundary conditions and spinal loading. Speculations behind a larger induced Cobb angle for the simulated implants arose from an *in vivo* phenomenon addressed as reversed disc wedging where discs wedged opposite to the vertebrae for the hemi-staple. We believe these animals exhibit a physiological compensatory response tending to maintain a forwards looking gaze and counteracting an induced deformity in an otherwise normal spine. Perhaps including an intermediate simulation step may replicate this behaviour by applying moments on un-instrumented vertebrae. Thus, the model was able to reproduce progressive scoliosis creation via a renowned porcine scoliosis model, its correction via a

custom anterior tether, and the curve inducing effect of two fusionless implants within curve and vertebral wedging thresholds conforming and, therefore, confirming hypothesis 1.

Although a specific porcine experimental scoliosis model and fusionless implants were explored for our pFEM verification/validation, a more robust and complete confirmation of its predictive capability would include the simulation of current experimental approaches such as a posterior segmental pedicular tethering [196], anterior shape memory alloy staples [73], and Odent's porcine scoliosis model via posterior offset tethering [222]. Such complementary simulations would further shape the model's verification and validation as per ASME's V&V-40 recommendations for computation modelling of medical devices. Reproducing the aforementioned experimental outcomes would further demonstrate the complementary status of our developed model to current experimental surgeries and perhaps reducing the required surgical interventions for final pre-clinical *in vivo* device testing.

The developed porcine finite element model was parameterized to facilitate personalization for future development. More specifically, a review of current experimental trials on porcine spines typically report averaged measurements of spinal indices (Cobb, wedging, amongst other). Our simulations were compared to average data without accounting for individual measures due to scarcity. Ideally, personalizing the model's morphological parameters and comparing curve progression to individual experimental cases would further demonstrate the ability of case-by-case simulations. As it stands, the pFEM simulates expected averaged measurements and could be used to test for different implant designs, their overall growth restraining effects, and provide a prospective perception of expected outcomes.

A verified model set the framework for two investigational studies as part of this thesis work. The first consisted of assessing differences between the inverse and 2-step approaches commonly used in experimental fusionless surgery. The second involved evaluating the biomechanical contribution of the ribcage and its role in fusionless surgery. Differences between the inverse and 2-step approaches were evident in our investigational simulations. Each simulated implant consistently revealed a lesser

potential in correcting a deformity versus inducing a spinal curvature. Under the inverse approach, the implant retarded normal growth ipsi-lateral to their insertion site (Hueter-Volkman law). Thus, the vertebral body wedged accordingly resulting in a global spinal deformity with the curvature's concavity presenting itself on the implant's side. The comparative simulations showed that, for the inverse approach, an increased growth plate stress on the concave side (ipsi-lateral to implantation site) and reduced stresses contralateral were by-products of the created curve with increasing concave stresses rather aiding at inducing the deformity via the Hueter-Volkman principle (Figure 4-10). Conversely, under the 2-step approach, the implants were modeled on the convex portion of the curvature aiming at realigning the spine. The tested implants acted against the excessive concave (contralateral) stresses [38], explaining the differences between both approaches. Similar patterns were observed for the apical vertebral wedging with induced wedging consistently higher with the tested implant when compared to its corrective capacity. Arguably, the 2-step approach represented, more realistically, the intended clinical application of the implants as patients with scoliosis typically present excessive concave stresses. Thus, this comparative investigation revealed important differences between most commonly conducted experimental fusionless implant testing approaches with results suggesting the 2-step approach is best suited for fusionless implant evaluation. However, one must consider cost and time limitations involved in each selected approach as the latter requires an initial curve creation step via established animal scoliosis model induction techniques while ensuring sufficient remaining growth for fusionless implant correction. As stated in the literature review (Section 1.3.3), pig growth rate varies with age with an accelerated growth between 3-6 months of age and reduced afterwards. Such behaviour was included in our model, however, growth rate was assigned two constant values corresponding to the accelerated and decelerated phase, respectively. Future refinement may comprise of recording weekly growth rates and including the latter in the developed model. Nevertheless, the model offered an alternative testing platform for an investigation which would have otherwise required several months and animal subjects. However, by highlighting the main objectives of conducted investigations, results should be carefully interpreted before proceeding to clinical trials.

Although the performed simulations were intended to compare the inverse and the 2-step approaches, results can also be interpreted to evaluate disparities between each implant. Interestingly, simulations showed that the tether and dual-epiphyseal staple were equivalently successful at correcting the global aspect of the deformity with the tether correcting apical vertebral wedging to a higher extent. Wedging discrepancy was minimal ( $\sim 2^\circ$ ) and would probably not have been detected in *in vivo* radiographic imaging as the difference is below the  $4^\circ$  radiographic vertebral wedging errors [224]. A speculative source of such difference in Cobb angle may arise from the method by which these two implants modulated growth. The dual-staple acted on both the proximal and distal growth plates simultaneously without bridging the intervertebral gap for maintained mobility. Thus, growth was restricted just below the prongs while the remainder of the epiphyseal plate's growth is maintained. Conversely, the anterior tether connected adjacent vertebrae using special bone-anchor screws leaving two un-impacted growth plates (the superior and inferior GP of the first and last instrumented vertebrae, respectively) (Figure 4-6). As the spine grew, the tether restricted growth by transferring loads via the intervertebral disc, which were shown to be distributed differently over the growth plate when compared to the dual-staple (Figure 4-10). Globally, differences arose from non-modulated growth at un-instrumented extremities and such behaviour was also noted in pig spines subjected to anterior tethering [184].

The hemi and rigid staples affected deformity induction and correction comparably. The hemi-staple modulated one growth plate exclusively without spanning the intervertebral space, allowing for functional intervertebral motion. Conversely, the rigid staple bridged the intervertebral disc segment while being rigidly fixed between adjacent vertebrae, compressing the disc as the spine grows [71]. Similarly to the anterior tether, the superior and inferior growth plates of the first and last instrumented vertebrae, respectively, are un-affected by rigid staple instrumentation. Although both staples were consistent in creating a deformity on a normal spine, they merely constrained its progression on a deformed spine. Perhaps the stiff nature of the rigid staple reduced inter-segmental motion necessary for spinal realignment. Conversely, the hemi-staple merely contributed at modulating vertebral growth proximally without crossing the disc, and thus, the excess concave stresses (2-step approach) contributed to different distal growth plate

modulation, opposing the added correction imposed by the implant. In the inverse approach, this excess stress contributed to the progression of the induced deformity. The simulated corrective potential of the hemi-staple was inline with previous simulation on a human spine model showing prevention of deformity progression with limited correction [170].

The simulated tether correction was comparable to reported experimental spinal correction [194]; however, dual-epiphyseal, hemi- and rigid staple correction outcomes cannot be corroborated with experimental data given the lack thereof. Moreover, the inserted tether was not tensioned intra-operatively in the simulations. As the explored implants mainly acted passively, inserting an un-tensioned tether would produce a fair comparison. Inclusion of the tether intra-operative tensioning would, logically, show an improved correction simulation compared to the current value. However, Newton *et al.* [185] concluded that intra-operative tensioning did not alter long-term curve induction on an *in vivo* porcine model. Yet, strikingly, the dual-staple matched the global Cobb angle without spanning the vertebral space.

As previously discussed, reversed disc wedging, a common phenomenon for implants tested under the inverse approach [184], [190], was not accounted for in our simulations. The tested implants do not generate enough moment arm to overcome this physiological compensatory mechanism, which cannot be simulated with our current model. However, expecting such occurrence would even favor the 2-step approach as the discs are already wedged in the same direction as vertebrae in a deformed spine. Thus, the implant would mainly correct vertebral wedging while the discs are expected to wedge back to their normal angles once the spine realigns over time.

Thus, our simulations allowed realization of objective 3.ii and exploring hypothesis 3 and further demonstrated the model can be exploited to test different implant designs and verify whether fusionless implants should be tested using the inverse or the 2-step approach. Nonetheless, parallel *in vivo* trials for implants lacking available experimental data would further confirm if our correction simulations conform to expected outcomes. Further exploratory simulations involving specific design modification of a pre-selected implant, e.g. dual-staple, involving testing whether different materials, prong designs, or

insertion pre-stress would impact the overall performance of the implant. Doing so would confirm the ultimate intention behind developing our porcine finite element model as a fusionless implant design and optimization tool, minimizing the time and steps involved in experimental device testing.

In parallel, the model was explored to identify the biomechanical contribution of the ribcage in fusionless surgery. The simulations showed that, by omitting the ribcage, implant inducing and correcting effects were exaggerated mainly due to differences in stress distribution over the growth plate. More specifically, for the inverse approach, the loading profile was shifted towards the concavity of the deformity, reducing compression in the convexity and, thus, accelerating growth modulation in the latter and resulting in a greater deformity globally. The inverse approach results were comparable to published *in vivo* data for the hemi-staple [190] and anterior tether [184] with inclusion of the biomechanical contribution of the thorax. Although tether and hemi-staple animal trials were performed using 4 instrumented levels, 5 levels would arguably not reach coronal deformities as elevated as the ones computed by excluding the ribcage. Thus, the thorax contributed to the overall biomechanics of deformity creation and its inclusion in computational models produces results corroborating with experimental trials. The ribcage stabilizes the thoracic spine, increasing its stiffness in all anatomical rotational planes due to its functional role. The ribs articulate at the costo-vertebral and costo-transverse joints blocking excess movement and shielding the spine, especially in lateral bending which represents the closest mechanical behaviour in fusionless coronal deformities. Additionally, several reports have indicated rib fusion in scoliosis model creation presumably linked to rib manipulation intra-operatively or excessive deformation [173], [225]. The latter stiffens the instrumented region, hindering the correction potential of tested implants [195]. Fusionless devices acting on the vertebral bodies would require generating a large moment arm to successfully create a substantial deformity or correct an otherwise existing one. By excluding the thorax's functional influence, these tested implants are readily capable of inducing larger deformities to extents less likely to occur *in vivo*, thus corroborated by changes over the growth plate stresses as the spine becomes more flexible, bending it to a larger extent at the apex of the curvature. In turns, growth modulation is more apparent as observed by differences in apical vertebral



wedging (Figure 5-5), and thus, increasing the extent of created deformity. Notably, the ribcage was involved in the biomechanics of the thoracic spine, highlighting the importance of accounting for such a contribution.

Omission of the ribcage changed the biomechanics in the thoracic region. Current human spine numerical models simulating spinal growth and growth modulation exclude the ribcage [34], [126], [127]. Despite its omission, these models successfully reproduced un-instrumented curve progression patterns. In our porcine model, growth parameters and applied boundary conditions were equivalent between both investigated models. Perhaps modifications to the stress sensitivity factor and applied boundary conditions to account for the biomechanical influence of the ribcage may reproduce *in vivo* results following its omission. Nonetheless, this assumption was not tested and its future consideration may provide conclusive affirmation.

The reached growth plate stresses were higher on the concave portion of the deformity. Currently, investigations reporting measured porcine growth plate stresses are scarce restricting comparisons of the stress differences. Concave growth plate compressive stresses reaching 0.7 - 1.3MPa were found for adolescents with idiopathic scoliosis [38]. Unlike adolescents' body weight ranging from 30-40 Kg, pigs typically reach weights of 70-80 Kg. Along with smaller endplate cross-sectional areas [24], 0.8 MPa concave growth plate compressive stresses are arguably expected. In our simulations, body weight varied temporally to account for the increasing size of these animals unlike adolescents which typically show relatively constant weights. Nonetheless, a shift of more than 0.1 MPa was measured following omission of the thorax. Peripheral vertebral growth was also omitted. Perhaps considering this scarcely documented phenomenon would alter calculated growth plate stress distribution. However, given the comparative nature of this study, stress changes would remain relative between simulations and would not alter drawn conclusions.

Although the investigation was conducted on a porcine spinal anatomy, perhaps re-iteration of these simulations on a human adolescent spinal geometry model proposed by [42], [170] would elucidate whether such biomechanical contribution was animal specific. Porcine growth is accelerated, in shorter period of time, compared to humans, which may

sometime results in a “Xyphose” (hyper-kyphosis) phenomenon common in pigs. Perhaps this fast growth rate may, following spinal manipulation, alter the behaviour of the ribcage. Otherwise, perhaps modifying specific mechanical properties, such as discs or ligaments or both in the thoracic region, may account for the added rigidity from the ribcage for simulations lacking the latter. Similarly, additional degrees of freedom may also account for the added rigidity.

Nonetheless, this investigational study highlighted the important biomechanical contribution of the ribcage in fusionless surgery. The experimental and clinical implications forging from this investigational study lie within new implants involving ribcage manipulations. Thus, future implants, more specifically local implants incapable of producing enough immediate forces to counteract the added mechanical resistance of the ribcage, should be designed cautiously. Equivalently, experimental surgical interventions involving ribcage manipulations should account for these biomechanical limitations. Future simulations should account for the functional biomechanical contribution of the thorax when testing novel implants or scoliosis animal models involving ribcage surgical manipulations. Finally, this comparative study affirmed hypothesis 4 of this thesis work.

A promising research avenue would involve establishing a correlation between the porcine and human FEMs. The main objective of the pFEM was to assess and optimize implant designs prior to final experimental testing. The numerical nature of the developed model may be exploited to determine patterns of behaviour from these implants and their expected applications clinically. Notably, both the human and porcine FEMs may be exploited in conjunction to achieve final implant design. By understanding physiological differences between pigs and humans, knowledge transfer can be accelerated by devising specific correlations and expected implant design modifications.

The comparative investigations were conducted under various assumptions and limitations. Mechanical properties, more specifically the intervertebral disc and vertebral body, were assumed similar between the tested normal and deformed porcine spine finite element model. In a deformed spine, the intervertebral disc presents degenerative signs on the concave side of the curvature [226]. Using a finite element model of a right thoracic scoliotic spine, Driscoll *et al.* tested the effect of stiffer concave mechanical properties for

the disc and vertebral body and demonstrated a 37% increase in growth plate asymmetrical stresses and 5.9° Cobb angle difference when compared to a non-biased spine. Including such biases in our deformed model would, in fact, increase compressive concave stresses and reduce the simulated corrective effect of the tested implants. Although not tested, theoretically, outcomes of such simulation would further justify the need to test implants on a deformed spine as it more closely mimics the expected behaviour clinically. Moreover, the ribcage growth was omitted in our simulations. However, given the comparative nature of the inverse vs 2-step investigation, it was assumed that ribcage growth omission would not mitigate drawn conclusions, but rather omission of its mechanical contribution would, as explored in Chapter 5. The growth of the porcine thorax is not well documented in the literature, even so, its importance in experimental fusionless implant trials. Inclusion of the ribcage growth may provide a more realistic comparison but the overall biomechanical influence of the ribcage would, hypothetically, remain the same. Perhaps a well-documented porcine adaptive ribcage growth and its inclusion in the finite element model may provide more insights whether presented differences are corroborated for the assessed biomechanical thorax contribution. Moreover, the mechanical properties of the thorax were appropriated to human equivalents as no published data was available. The porcine thorax is relatively stiffer than its human equivalent, thus, it is expected that appropriate mechanical properties would further demonstrate even more substantial differences as the thoracic spine becomes stiffer leading to an even greater growth plate stress difference between both models.

A parallel stage of this thesis work was the development of a new dual-epiphyseal device for the treatment of progressive spinal deformities. The initial conceptual design of the proposed dual-staple was inspired by a previous implant, namely hemi-staple, whose purpose was to avoid spanning and compressing the intervertebral disc space to reduce risks of disc degeneration [227]. The hemi-staple was previously shown to preserve disc health whilst the prong is adequately positioned between the epiphyseal plate and the intervertebral disc [191]. As the hemi-staple's action is limited to one growth plate, the dual-epiphyseal implant's main purpose was to harness the growth of the superior and inferior epiphyseal plates simultaneously. The initial design was evaluated using a human

[170] and the porcine FEMs with results indicating the added advantage over the hemi-staple. These outcomes were re-iterated in this thesis's simulated comparative study. However, practical uses of the concept design were limited by its applicability to various vertebral morphologies. Thus, a custom expansion mechanism and holding tool were conceived allowing implant intra-operative height adjustment. The final implant design was then modeled under CATIA V5, machined, then tested on analogous saw bone vertebrae to confirm feasibility of the custom expansion mechanism, holding tool, and insertion method.

Following this *in situ* feasibility test, *in vivo trials* on immature pigs confirmed, via the inverse approach, the intended growth modulation achieved via this novel device (Section 3.2 and article 1). The experimental trials revealed the implant was capable of achieving local vertebral wedging reaching  $18^\circ$  with no evidence of implant dislodgment or loosening. Interestingly, cumulative vertebral wedging amounted to  $>45^\circ$  with  $24^\circ$  Cobb angle, a clear indication of reversed disc wedging as a compensatory physiological response, as previously discussed and in-line with previous hemi-staple [190] and anterior tether [184] findings. Nonetheless, the promising outcomes of the current *in vivo* trial may be outweighed by excessive concave stresses had the implant been tested under the 2-step approach. As previously demonstrated in our investigational simulations, the corrective influence of the dual-epiphyseal staple was less prominent than its inducing effect, yet with apparent curvature correction. A complementary study should be conducted on already deformed pig spines to conclusively demonstrate the expected *in vivo* correction using this novel implant and further determine the type and extent of curvatures the dual-epiphyseal device is best tailored to correct.

The dual-epiphyseal staple succeeded at creating more than twice the growth modulating effect than the hemi-staple and confirmed hypothesis 2. More specifically, the new device was fixed using 2 screws (upper and lower screws) locally. This fixation method ensured a rigid attachment, and thus, eliminating relative motion between the implant pieces. Pig vertebrae typically grow 3.4 mm over 12 weeks, which corroborates with  $4.0 \pm 0.8\text{mm}$  vertebral height differences measured experimentally and confirming full vertebral growth restraint. Unlike the dual-epiphyseal device, the hemi-staple trials indicated relative, but small, hinge effect as vertebrae grow due to its mono-screw fixation. Furthermore, as per

previous recommendations, the new device's prong was thinner than its predecessor to ensure localized targeting of the IVD/vertebra interface (IVD/subchondral bone interface in pigs). Such design modification, along with the surgeon's experience, resulted in consistent device insertion. In some cases, specially at the proximal vertebrae with limited insertion space, prongs seemed to penetrate the disc under fluoroscopic imaging but did not hinder the outcomes of this study as no visible damage was observed. Additionally, although the selected screws ensured adequate osteointegration, future screws with large pitch size should be used, as per the operating surgeon's recommendations.

Moreover, current long-term reports indicating disc health degradation following maintained compression are unavailable. However, short-term investigations have revealed changes in viable cell density, reduced vascularization within the endplates, and increased IVD cellular apoptosis [166], [169]. The authors speculated that these alterations may lead to disc degeneration resulting from long-term compression with unavailable data to support such claims. In our investigation, animals were followed for 3 months, which, arguably, does not support claims of mitigated disc health degradation. A future histological and histomorphometric assessment is required to confirm the IVD's structural integrity and reiterate the added benefit of the localized action of the developed implant versus those that span and compress the disc.

The conducted *in vivo* trials aimed at assessing the efficacy and functional application of the dual-epiphyseal staple. As such, the device's effectiveness was confirmed with results indicating concrete vertebral wedging and spinal deformity. Functionally, the device's implantation was proven effortless with successful intra-operative height adjustment and screw insertion. However, the device's biocompatibility was not assessed in this investigation. An important aspect to consider revolves around a possible tissue reaction following insertion of a foreign object into an *in vivo* environment. Stainless steel was chosen for both the implant and the screws to mitigate these concerns as it was previously shown as a biocompatible metal. Notwithstanding, the chosen stainless steel grade may not meet medical grade levels; thus, future investigations may require the use of better suited materials to reduce risks of inflammatory or immune reactions as per FDA and ISO13845 standards. Nonetheless, blood plasma samples were acquired monthly during

our animal trial follow-ups and frozen at  $-80^{\circ}\text{C}$  in anticipation of cytotoxic or inflammatory/immune responses analyses.

Moreover, the device was designed to also act as a force-controlled local implant (Section 3.1), yet, this functionality was not tested in our trials. A decision was made to omit machining details required to insert a hyper-elastic ligament between implant pieces to minimize costs for this first animal trial. Theoretically, the device may be targeted for smaller progressive scoliotic curves by pre-calculating the force required to achieve the desired growth modulation aimed at re-establishing a normal vertebral morphology. The force-controlled approach should be simulated using the developed pFEM to assess its feasibility before initial *in vivo* trials, thus granting localized force-controlled growth modulation without spanning the disc. Additionally, the device was conceived to be inserted, independently, on each growth plate should the need arise. This characteristic was tested on Sawbone vertebrae but our experimental trials did not require such resort.

Furthermore, the dual-epiphyseal staple was conceived to act locally without imposing mechanical compression on segmental motion segments. Theoretically, spinal mobility should be maintained. Preliminary manual bending of the excised spines showed maintained mobility, yet, admittedly, difficult to distinguish on fluoroscopic imaging. The spines were harvested, embedded in neutral buffer formalin (NFB), then transported to CHU Sainte-Justine for assessment. Although exposure to NFB was limited to less than 24 hours, the solution is a tissue fixative and may result in stiffening the spinal segment. Future bending should be conducted prior to fixating in NFB, ideally with animals sedated, to confirm maintained mobility.

Fibrous tissue formation over the implant region was noticed during dissection. Although not identifiable via radiographic PA nor LAT images, the tissue formation was evident after  $\mu$ -CT scans. The tissue resembled callus formed at bone healing sites following fracture [58]. Similar tissue deposition was observed with the hemi-staple experiments with no macroscopic changes to vertebral bone morphology. Nonetheless, instrumented vertebrae (and their normal counterparts) were scanned using a  $\mu$ -CT for future analysis of bone architecture at implant site. Furthermore, scanned samples were then fixed in MMA for future histological analysis to assess growth rate, growth plate and intervertebral

disc health, as well as signs of tissue degradation and fibrous tissue formation at implant prong insertion sites.

Although no detailed analysis of  $\mu$ -CT scans was performed in this thesis work, preliminary observations revealed pig vertebral peripheral growth was not halted. The outer vertebral wall shaped itself to the implant's geometry, indicating the vertebral body grew onto the implant. This suggests that pig peripheral growth, at the age they were experimented on, was still present. The scans were acquired after sacrifice; thus, the temporal aspect of this peripheral growth cannot be documented, nevertheless, determine whether it was still ongoing at extraction time point. Nonetheless, this phenomenon should be accounted for when testing new implants on pigs and interpret the experimental outcomes in the light of this bone behaviour as humans vertebral body peripheral growth is seized at 10-12y of age [66]. A temporal documentation of peripheral growth via 3D CT reconstruction can be established and perhaps included in the model.

Micro-CT imaging additionally revealed signs of bone loss at implant insertion sites. These may have occurred secondary to tissue injury following surgery or stress shielding under the implant prong. Shielding could have resulted from rigidly fixing the implant, locally. Thus, segmental loads transmitted from adjacent vertebrae would be resisted, locally, by the higher stiffness of the implant compared to bone, and thus, shielding bone around the implantation site. Such occurrence was noted with calculated growth plate stresses in our comparative simulations. Further bone quality and architecture, and histological analyses would elucidate the origin of observed bone loss.

## CHAPTER 7 CONCLUSION AND RECOMMENDATIONS

This thesis aimed at developing a novel porcine spine finite element model as an alternative testing platform to better understand the mechanisms by which new implants correct spinal deformities prior to proceeding towards experimental trials and transfer the acquired knowledge to human applications. Additional work led to the development of a new dual-epiphyseal implant addressing short-comings of currently and commonly tested devices.

The new pFEM readily demonstrated its ability to reproduce experimental results either for scoliosis-like curve induction models, correcting such induced deformity, or replicating implant growth modulation via the inverse approach. The pFEM development and verification phase replicated expected outcomes within hypothesized thresholds for Cobb angle, vertebral wedging, and axial rotation. Additional simulations with different experimentally tested implants and their design modifications would further verify and validate the pFEM as an alternative fusionless implant design optimization platform prior to final *in vivo* trials and transferring collected understanding to clinical applications.

The developed pFEM was further explored to assess differences between commonly used experimental fusionless implant testing approaches. Comparative simulations confirmed differences between the inverse and the 2-step approaches with the former exaggerating expected growth modulation from newly conceived implants. The simulated devices further demonstrated that, for the same instrumented levels, deformity correction is outweighed by the excessive concave growth plate stresses. It was highlighted that new implants should be tested under the 2-step approach to better understand their expected biomechanical and growth manipulation correction as it best mimics the expected corrective outcome when transposed to human clinical trials.

Comparative simulations also demonstrated an affirmative potential of the developed pFEM in outlining differences between implant designs. The conducted simulations revealed shortcomings between implants and their mode of application, an investigation which would have required substantial investment to achieve prior to venturing into experimental testing.



The biomechanical contribution of the ribcage in fusionless surgery was further highlighted via the pFEM. Simulations showed that, by excluding the ribcage, growth plate stresses were shifted towards the concavity of the deformity due to the reduced stiffness in the thoracic region. The ribcage's role in stabilizing the spine was further demonstrated. The investigational study underlined the importance of including the ribcage in future simulations. Moreover, new implants should account for the thorax's biomechanical input, specially if those intend to manipulate the ribs and directly impact the global aspect of the spine.

A new dual-epiphyseal device with a cutting-edge expansion mechanism demonstrated its ability to manipulate vertebral growth via the inverse approach. The device achieved substantial vertebral wedging and global deformity, which was outweighed by reversed disc wedging. Experimental trials via the 2-step approach are advised to further affirm the device can achieve local and global deformity correction, as was highlighted using the pFEM. Additionally, future analyses are required to confirm preservation of disc health and bone quality.

The conceived implant offered promising results that can be explored for the early treatment of progressive deformities in the growing spine. The device did not affect vertebral rotation, thus, clinical applications are tailored for curves exhibiting modest rotations. Supplementary experimental trials with a larger number of animals and protocol modification to include the 2-step approach would further affirm the added benefit of the device in a clinical setup.

Although detailed  $\mu$ -CT and histological analyses were not performed, data will be transferred to a new Master's project. Bone micro-architectural parameters and bone mineral density analyses will be used to quantify regional bone variations possibly caused by the implant. Scans may also be used to describe the three dimensional shape and variation of the growth plate by detecting empty spaces between the body and subchondral bone on sequential sagittal  $\mu$ CT scans. Histomorphometric analyses will allow quantifying growth rate and growth modulation, growth plate zonal characteristics, and intervertebral disc health.

The state-of-the-art porcine spine finite element model was readily capable of reproducing expected experimental *in vivo*. The model can be further explored to conceive and verify new implants before resorting for cumbersome experimental trials to facilitate knowledge transfer to concrete clinical applications. Furthermore, theories regarding uncertainties or differences between treatment or experimental approaches can be tested and evaluated. Finally, the dual-staple animal trials demonstrated a promising potential to correct spinal deformities in the growing spine without bridging and compressing the intervertebral disc space, thus promoting sustained long-term disc health and spinal mobility.

## BIBLIOGRAPHY

- [1] S.-R. Sheng, X.-Y. Wang, H.-Z. Xu, G.-Q. Zhu, and Y.-F. Zhou, "Anatomy of large animal spines and its comparison to the human spine: a systematic review," *Eur. Spine J.*, vol. 19, no. 1, pp. 46–56, 2009.
- [2] H. Gray and W. H. Lewis, *Anatomy of the human body*. Lea & Febiger, 1918.
- [3] W. T. Edwards, Y. Zheng, L. A. Ferrara, and H. A. Yuan, "Structural features and thickness of the vertebral cortex in the thoracolumbar spine.," *Spine (Phila. Pa. 1976)*., vol. 26, pp. 218–225, 2001.
- [4] A. A. White and M. M. Panjabi, *Clinical biomechanics of the spine*. Lippincott, 1990.
- [5] J. J. Cassidy, A. Hiltner, and E. Baer, "Hierarchical structure of the intervertebral disc.," *Connect. Tissue Res.*, vol. 23, no. 1, pp. 75–88, 1989.
- [6] G. M. Jensen, "Biomechanics of the lumbar intervertebral disk: a review.," *Phys. Ther.*, vol. 60, no. 6, pp. 765–773, 1980.
- [7] M. Törner and S. Holm, "Studies of the lumbar vertebral end-plate region in the pig.," *Ups. J. Med. Sci.*, vol. 90, no. 3, pp. 243–258, 1985.
- [8] D. W. McMillan, G. Garbutt, and M. A. Adams, "Effect of sustained loading on the water content of intervertebral discs: implications for disc metabolism," *Ann. Rheum. Dis.*, vol. 55, no. 12, pp. 880–887, 1996.
- [9] S.-H. Lee, R. Derby, Y. Chen, K. S. Seo, and M. J. Kim, "In vitro measurement of pressure in intervertebral discs and annulus fibrosus with and without annular tears during discography," *Spine J.*, vol. 4, no. 6, pp. 614–618, 2004.
- [10] M. A. Adams, D. S. McNally, and P. Dolan, "'Stress' distributions inside intervertebral discs. The effects of age and degeneration," *J Bone Jt. Surg Br*, vol. 78, no. 6, pp. 965–972, 1996.
- [11] A. M. Kaigle, S. H. Holm, and T. H. Hansson, "1997 Volvo Award winner in biomechanical studies. Kinematic behavior of the porcine lumbar spine: a chronic lesion model," *Spine (Phila Pa 1976)*, vol. 22, no. 24, pp. 2796–2806, 1997.

- [12] S. Akahoshi, A. Sakai, S. Arita, S. Ikeda, Y. Morishita, H. Tsutsumi, M. Ito, A. Shiraishi, and T. Nakamura, "Modulation of bone turnover by alfacalcidol and/or alendronate does not prevent glucocorticoid-induced osteoporosis in growing minipig," *J. Bone Miner. Metab.*, vol. 23, no. 5, pp. 341–350, 2005.
- [13] H. Bozkus, N. R. Crawford, R. H. Chamberlain, T. D. Valenzuela, A. Espinoza, Z. Yüksel, and C. A. Dickman, "Comparative anatomy of the porcine and human thoracic spines with reference to thoracoscopic surgical techniques," *Surg. Endosc.*, vol. 19, no. 12, pp. 1652–1665, 2005.
- [14] A. Chauveau, S. Arloing, and G. Fleming, *The comparative anatomy of the domesticated animals*. New York : Appleton, 1908.
- [15] R. Michael Akers and D. Michael Denbow, *Anatomy and Physiology of Domestic Animals*, 2nd Editio. Wiley-Blackwell, 2013.
- [16] G. Cinotti, C. Della Rocca, S. Romeo, F. Vittur, R. Toffanin, and G. Trasimeni, "Degenerative changes of porcine intervertebral disc induced by vertebral endplate injuries.," *Spine (Phila. Pa. 1976)*., vol. 30, no. 2, pp. 174–180, 2005.
- [17] J.-M. Laffosse, F. Accadbled, F. Molinier, N. Bonneville, J. S. de Gauzy, and P. Swider, "Correlations between effective permeability and marrow contact channels surface of vertebral endplates.," *J. Orthop. Res.*, vol. 28, no. 9, pp. 1229–34, 2010.
- [18] C. Park, Y. J. Kim, C.-S. Lee, K. An, H. J. Shin, C. H. Lee, C. H. Kim, and J.-W. Shin, "An in vitro animal study of the biomechanical responses of annulus fibrosus with aging.," *Spine (Phila. Pa. 1976)*., vol. 30, no. 10, pp. E259–65, 2005.
- [19] G. Ryan, A. Pandit, and D. Apatsidis, "Stress distribution in the intervertebral disc correlates with strength distribution in subdiscal trabecular bone in the porcine lumbar spine," *Clin. Biomech.*, vol. 23, no. 7, pp. 859–869, 2008.
- [20] D. R. Eyre and H. Muir, "Types I and II collagens in intervertebral disc. Interchanging radial distributions in annulus fibrosus.," *Biochem. J.*, vol. 157, no. 1, pp. 267–270, 1976.
- [21] J. C. Beckstein, S. Sen, T. P. Schaer, E. J. Vresilovic, and D. M. Elliott, "Comparison

- of animal discs used in disc research to human lumbar disc: axial compression mechanics and glycosaminoglycan content.," *Spine (Phila. Pa. 1976)*., vol. 33, no. 6, pp. E166–E173, 2008.
- [22] F. Wang, F. Cai, R. Shi, X.-H. Wang, and X.-T. Wu, "Aging and age related stresses: a senescence mechanism of intervertebral disc degeneration.," *Osteoarthritis Cartilage*, Oct. 2015.
  - [23] R. Dath, A. Ebinesan, K. Porter, and A. Miles, "Anatomical measurements of porcine lumbar vertebrae," *Clin. Biomech.*, vol. 22, no. 5, pp. 607–613, 2007.
  - [24] I. Busscher, J. J. W. Ploegmakers, G. J. Verkerke, and A. G. Veldhuizen, "Comparative anatomical dimensions of the complete human and porcine spine," *Eur. Spine J.*, vol. 19, no. 7, pp. 1104–1114, 2010.
  - [25] J. Aerssens, S. Boonen, G. Lowet, and J. Dequeker, "Interspecies differences in bone composition, density, and quality: potential implications for in vivo bone research," *Endocrinology*, vol. 139, no. 2, pp. 663–670, 1998.
  - [26] M. A. Adams and P. Dolan, "Spine biomechanics," *J. Biomech.*, vol. 38, no. 10, pp. 1972–1983, 2005.
  - [27] A. Nachemson and J. M. Morris, "In Vivo Measurements of Intradiscal Pressure. Discometry, a Method for the Determination of Pressure in the Lower Lumbar Discs," *J Bone Jt. Surg Am*, vol. 46, pp. 1077–1092, 1964.
  - [28] D. R. Linders and D. J. Nuckley, "Deduction of Spinal Loading from Vertebral Body Surface Strain Measurements," *Exp. Mech.*, vol. 47, no. 3, pp. 303–310, 2007.
  - [29] K. D. Cao, M. J. Grimm, and K. H. Yang, "Load sharing within a human lumbar vertebral body using the finite element method.," *Spine (Phila. Pa. 1976)*., vol. 26, no. 12, pp. E253–E260, 2001.
  - [30] S. K. Eswaran, A. Gupta, M. F. Adams, and T. M. Keaveny, "Cortical and trabecular load sharing in the human vertebral body.," *J. Bone Miner. Res.*, vol. 21, no. 2, pp. 307–314, 2006.
  - [31] A. L. Nachemson, "The Lumbar Spine An Orthopaedic Challenge," *Spine*, vol. 1,

- no. 1. pp. 59–71, 1976.
- [32] A. Schultz, G. Andersson, R. Ortengren, K. Haderspeck, and A. Nachemson, “Loads on the lumbar spine. Validation of a biomechanical analysis by measurements of intradiscal pressures and myoelectric signals.,” *J. Bone Joint Surg. Am.*, vol. 64, pp. 713–720, 1982.
  - [33] S. Iyer, B. a. Christiansen, B. J. Roberts, M. J. Valentine, R. K. Manoharan, and M. L. Bouxsein, “A biomechanical model for estimating loads on thoracic and lumbar vertebrae,” *Clin. Biomech.*, vol. 25, no. 9, pp. 853–858, 2010.
  - [34] I. Villemure, C. E. Aubina, J. Dansereau, and H. Labelle, “Simulation of Progressive Deformities in Adolescent Idiopathic Scoliosis Using a Biomechanical Model Integrating Vertebral Growth Modulation,” *J. Biomech. Eng.*, vol. 124, no. 6, p. 784, 2002.
  - [35] J. Clin, C. É. Aubin, N. Lalonde, S. Parent, and H. Labelle, “A new method to include the gravitational forces in a finite element model of the scoliotic spine,” *Med. Biol. Eng. Comput.*, vol. 49, no. 8, pp. 967–977, 2011.
  - [36] A. G. Patwardhan, R. M. Havey, K. P. Meade, B. Lee, and B. Dunlap, “A follower load increases the load-carrying capacity of the lumbar spine in compression,” *Spine (Phila Pa 1976)*, vol. 24, no. 10, pp. 1003–1009, 1999.
  - [37] A. Rohlmann, S. Neller, L. Claes, G. Bergmann, and H. J. Wilke, “Influence of a follower load on intradiscal pressure and intersegmental rotation of the lumbar spine.,” *Spine (Phila. Pa. 1976)*., vol. 26, no. 24, pp. E557–E561, 2001.
  - [38] I. A. F. Stokes, R. G. Burwell, and P. H. Dangerfield, “Biomechanical spinal growth modulation and progressive adolescent scoliosis--a test of the ‘vicious cycle’ pathogenetic hypothesis: summary of an electronic focus group debate of the IBSE.,” *Scoliosis*, vol. 1, p. 16, 2006.
  - [39] M. Dreischarf, T. Zander, G. Bergmann, and A. Rohlmann, “A non-optimized follower load path may cause considerable intervertebral rotations,” *J. Biomech.*, vol. 43, no. 13, pp. 2625–2628, 2010.

- [40] A. Rohlmann, T. Zander, M. Rao, and G. Bergmann, "Applying a follower load delivers realistic results for simulating standing.," *J. Biomech.*, vol. 42, no. 10, pp. 1520–6, 2009.
- [41] A. Rohlmann, T. Zander, M. Rao, and G. Bergmann, "Realistic loading conditions for upper body bending," *J Biomech*, vol. 42, no. 7, pp. 884–890, 2009.
- [42] M. Driscoll, C.-E. Aubin, A. Moreau, I. Villemure, and S. Parent, "The role of spinal concave-convex biases in the progression of idiopathic scoliosis," *Eur. Spine J.*, vol. 18, no. 2, pp. 180–187, 2009.
- [43] T. H. Smit, "The use of a quadruped as an in vivo model for the study of the spine - biomechanical considerations," *Eur. Spine J.*, vol. 11, no. 2, pp. 137–144, 2002.
- [44] J.-W. M. Kouwenhoven and R. M. Castelein, "The pathogenesis of adolescent idiopathic scoliosis: review of the literature.," *Spine (Phila. Pa. 1976)*., vol. 33, no. 26, pp. 2898–908, 2008.
- [45] M. Alini, S. M. Eisenstein, K. Ito, C. Little, A. A. Kettler, K. Masuda, J. Melrose, J. Ralphs, I. Stokes, and H. J. Wilke, "Are animal models useful for studying human disc disorders/degeneration?," *Eur. Spine J.*, vol. 17, no. 1, pp. 2–19, 2007.
- [46] D. I. Bylski-Austrow, D. L. Glos, F. E. Sauser, V. V Jain, E. J. Wall, and A. H. Crawford, "In vivo dynamic compressive stresses in the disc annulus: a pilot study of bilateral differences due to hemiepiphyseal implant in a quadruped model," *Spine (Phila. Pa. 1976)*., vol. 37, no. 16, pp. E949–956, Jul. 2012.
- [47] T. R. Oxland, M. M. Panjabi, E. P. Southern, and J. S. Duranceau, "An anatomic basis for spinal instability: a porcine trauma model.," *J. Orthop. Res.*, vol. 9, no. 3, pp. 452–62, 1991.
- [48] K. A. Gillespie and J. P. Dickey, "Biomechanical role of lumbar spine ligaments in flexion and extension: determination using a parallel linkage robot and a porcine model," *Spine (Phila Pa 1976)*, vol. 29, no. 11, pp. 1208–1216, 2004.
- [49] I. Busscher, J. H. van Dieen, I. Kingma, A. J. van der Veen, G. J. Verkerke, and A. G. Veldhuizen, "Biomechanical characteristics of different regions of the human

- spine: an in vitro study on multilevel spinal segments,” *Spine (Phila Pa 1976)*, vol. 34, no. 26, pp. 2858–2864, 2009.
- [50] I. Busscher, A. J. van der Veen, J. H. van Dieen, I. Kingma, G. J. Verkerke, and A. G. Veldhuizen, “In vitro biomechanical characteristics of the spine: a comparison between human and porcine spinal segments,” *Spine (Phila Pa 1976)*, vol. 35, no. 2, pp. E35–42, 2010.
  - [51] I. Oda, K. Abumi, D. Lu, Y. Shono, and K. Kaneda, “Biomechanical role of the posterior elements, costovertebral joints, and rib cage in the stability of the thoracic spine,” *Spine (Phila Pa 1976)*, vol. 21, no. 12, pp. 1423–1429, 1996.
  - [52] X. Yao, T. J. Blount, N. Suzuki, L. K. Brown, C. J. van der Walt, T. Baldini, E. M. Lindley, V. V Patel, and E. L. Burger, “A biomechanical study on the effects of rib head release on thoracic spinal motion,” *Eur Spine J*, 2011.
  - [53] L. B. C. Brasiliense, B. C. R. Lazaro, P. M. Reyes, S. Dogan, N. Theodore, and N. R. Crawford, “Biomechanical contribution of the rib cage to thoracic stability.,” *Spine (Phila. Pa. 1976).*, vol. 36, no. 26, pp. E1686–93, 2011.
  - [54] J. T. Lysack, J. P. Dickey, G. a. Dumas, and D. Yen, “A continuous pure moment loading apparatus for biomechanical testing of multi-segment spine specimens,” *J. Biomech.*, vol. 33, pp. 765–770, 2000.
  - [55] T. Fujimori, M. Iwasaki, Y. Nagamoto, Y. Matsuo, T. Ishii, T. Sugiura, M. Kashii, T. Murase, K. Sugamoto, and H. Yoshikawa, “Kinematics of the thoracic spine in trunk lateral bending: In vivo three-dimensional analysis,” *Spine J.*, vol. 14, no. 9, pp. 1991–1999, 2014.
  - [56] H.-J. Wilke, J. Geppert, and A. Kienle, “Biomechanical in vitro evaluation of the complete porcine spine in comparison with data of the human spine.,” *Eur. Spine J.*, vol. 20, no. 11, pp. 1859–68, 2011.
  - [57] R. Huiskes, R. Ruimerman, G. H. van Lenthe, and J. D. Janssen, “Effects of mechanical forces on maintenance and adaptation of form in trabecular bone.,” *Nature*, vol. 405, no. 6787, pp. 704–706, 2000.



- [58] D. W. Sommerfeldt and C. T. Rubin, "Biology of bone and how it orchestrates the form and function of the skeleton.," *Eur. Spine J.*, vol. 10 Suppl 2, pp. S86–95, 2001.
- [59] C. Huang and R. Ogawa, "Mechanotransduction in bone repair and regeneration," *FASEB J.*, vol. 24, pp. 3625–3632, 2010.
- [60] R. T. Ballock and R. J. O'Keefe, "The biology of the growth plate.," *J. Bone Joint Surg. Am.*, vol. 85-A, no. 4, pp. 715–26, 2003.
- [61] I. Villemure and I. A. F. Stokes, "Growth plate mechanics and mechanobiology. A survey of present understanding," *J. Biomech.*, vol. 42, no. 12, pp. 1793–1803, 2009.
- [62] A. Yamazaki, D. E. Mason, and P. A. Caro, "Age of closure of the neurocentral cartilage in the thoracic spine.," *J Pediatr Orthop*, vol. 18, no. 2, pp. 168–172, 1998.
- [63] R. Marino, "Growth plate biology: new insights.," *Curr. Opin. Endocrinol. Diabetes. Obes.*, vol. 18, no. 1, pp. 9–13, 2011.
- [64] I. A. Stokes, P. L. Mente, J. C. Iatridis, C. E. Farnum, and D. D. Aronsson, "Enlargement of growth plate chondrocytes modulated by sustained mechanical loading," *J Bone Jt. Surg Am*, vol. 84-A, no. 10, pp. 1842–1848, 2002.
- [65] I. A. F. Stokes and L. Windisch, "Vertebral height growth predominates over intervertebral disc height growth in adolescents with scoliosis.," *Spine (Phila. Pa. 1976).*, vol. 31, no. 14, pp. 1600–1604, 2006.
- [66] A. Dimeglio, "Growth in pediatric orthopaedics," *J Pediatr Orthop*, vol. 21, no. 4, pp. 549–555, 2001.
- [67] A. Dimeglio and F. Canavese, "The growing spine: how spinal deformities influence normal spine and thoracic cage growth," *Eur Spine J*, vol. 21, no. 1, pp. 64–70, 2012.
- [68] R. A. Brand, "50 Years Ago in CORR: The Iliac Apophysis: An Invaluable Sign in the Management of Scoliosis Joseph C. Risser MD CORR 1958;11:111–119," *Clin. Orthop. Relat. Res.*, vol. 466, no. 6, pp. 1516–1517, 2008.
- [69] A. Diméglio, Y. P. Charles, J.-P. Daures, V. de Rosa, and B. Kaboré, "Accuracy of

- the Sauvegrain method in determining skeletal age during puberty.," *J. Bone Joint Surg. Am.*, vol. 87, no. 8, pp. 1689–1696, 2005.
- [70] A. Manzoor Mughal, N. Hassan, and A. Ahmed, "Bone age assessment methods: a critical review.," *Pakistan J. Med. Sci.*, vol. 30, no. 1, pp. 211–5, 2014.
- [71] D. I. Bylski-Austrow, E. J. Wall, D. L. Glos, E. T. Ballard, A. Montgomery, and A. H. Crawford, "Spinal Hemiepiphysiodesis Decreases the Size of Vertebral Growth Plate Hypertrophic Zone and Cells," *J. Bone Jt. Surg.*, vol. 91, no. 3, pp. 584–593, 2009.
- [72] K. Sergerie, M.-O. Lacoursière, M. Lévesque, and I. Villemure, "Mechanical properties of the porcine growth plate and its three zones from unconfined compression tests," *J. Biomech.*, vol. 42, no. 4, pp. 510–516, 2009.
- [73] J. H. Carreau, C. L. Farnsworth, D. A. Glaser, J. D. Doan, T. Bastrom, N. Bryan, and P. O. Newton, "The modulation of spinal growth with nitinol intervertebral stapling in an established swine model," *J. Child. Orthop.*, vol. 6, no. 3, pp. 241–253, 2012.
- [74] I. A. Stokes, D. D. Aronsson, A. N. Dimock, V. Cortright, and S. Beck, "Endochondral growth in growth plates of three species at two anatomical locations modulated by mechanical compression and tension," *J Orthop Res*, vol. 24, no. 6, pp. 1327–1334, 2006.
- [75] A. K. Roth, R. Bogie, E. Jacobs, J. J. Arts, and L. W. van Rhijn, "Large animal models in fusionless scoliosis correction research: a literature review," *Spine J*, vol. 13, no. 6, pp. 675–688, Jun. 2013.
- [76] B. Moal, F. Schwab, J. Demakakos, R. Lafage, P. Riviere, A. Patel, and V. Lafage, "The impact of a corrective tether on a scoliosis porcine model: a detailed 3D analysis with a 20 weeks follow-up.," *Eur. spine J. Off. Publ. Eur. Spine Soc. Eur. Spinal Deform. Soc. Eur. Sect. Cerv. Spine Res. Soc.*, vol. 22, no. 8, pp. 1800–1809, Aug. 2013.
- [77] I. A. Stokes, H. Spence, D. D. Aronsson, and N. Kilmer, "Mechanical modulation of vertebral body growth. Implications for scoliosis progression," *Spine (Phila Pa*

- 1976), vol. 21, no. 10, pp. 1162–1167, 1996.
- [78] J. Peltonen, I. Alitalo, E. Karaharju, and H. Helio, “Distraction of the growth plate. Experiments in pigs and sheep,” *Acta Orthop Scand*, vol. 55, no. 3, pp. 359–362, 1984.
  - [79] D. D. Aronsson, I. A. Stokes, J. Rosovsky, and H. Spence, “Mechanical modulation of calf tail vertebral growth: implications for scoliosis progression,” *J Spinal Disord*, vol. 12, no. 2, pp. 141–146, 1999.
  - [80] I. A. Stokes, J. Gwadera, A. Dimock, and D. D. Aronsson, “Mechanical modulation of vertebral and tibial growth: diurnal versus full-time loading,” *Stud Heal. Technol Inf.*, vol. 91, pp. 97–100, 2002.
  - [81] I. A. Stokes, “Mechanical effects on skeletal growth,” *J Musculoskelet Neuronal Interact*, vol. 2, no. 3, pp. 277–280, 2002.
  - [82] I. A. Stokes, J. Gwadera, A. Dimock, C. E. Farnum, and D. D. Aronsson, “Modulation of vertebral and tibial growth by compression loading: diurnal versus full-time loading,” *J. Orthop. Res.*, vol. 23, no. 1, pp. 188–95, 2005.
  - [83] N. Ohashi, A. G. Robling, D. B. Burr, and C. H. Turner, “The effects of dynamic axial loading on the rat growth plate,” *J. Bone Miner. Res.*, vol. 17, no. 2, pp. 284–292, 2002.
  - [84] B. Valteau, G. Grimard, I. Londono, F. Moldovan, and I. Villemure, “In vivo dynamic bone growth modulation is less detrimental but as effective as static growth modulation,” *Bone*, vol. 49, no. 5, pp. 996–1004, 2011.
  - [85] A. M. Arkin and J. F. Katz, “The effects of pressure on epiphyseal growth; the mechanism of plasticity of growing bone,” *J Bone Jt. Surg Am*, vol. 38-A, no. 5, pp. 1056–1076, 1956.
  - [86] M. S. Moreland, “Morphological effects of torsion applied to growing bone. An in vivo study in rabbits,” *J. Bone Joint Surg. Br.*, vol. 62-B, no. 2, pp. 230–237, May 1980.
  - [87] A.-L. Ménard, G. Grimard, B. Valteau, I. Londono, F. Moldovan, and I. Villemure, “In

- vivo dynamic loading reduces bone growth without histomorphometric changes of the growth plate.," *J. Orthop. Res.*, vol. 32, no. 9, pp. 1129–36, 2014.
- [88] A.-L. Menard, G. Grimard, E. Massol, I. Londono, F. Moldovan, and I. Villemure, "Static and dynamic compression application and removal on the intervertebral discs of growing rats.," *J. Orthop. Res.*, Jul. 2015.
  - [89] A.-L. Menard, G. Grimard, I. Londono, F. Beaudry, P. Vachon, F. Moldovan, and I. Villemure, "Bone growth resumption following in vivo static and dynamic compression removals on rats.," *Bone*, vol. 81, pp. 662–668, Sep. 2015.
  - [90] H. Lin, C.-éric Aubin, S. Parent, and I. Villemure, "Mechanobiological bone growth: comparative analysis of two biomechanical modeling approaches," *Med. Biol. Eng. Comput.*, vol. 47, no. 4, pp. 357–366, 2008.
  - [91] H. M. Frost, "Skeletal structural adaptations to mechanical usage (SATMU): 3. The hyaline cartilage modeling problem.," *Anat. Rec.*, vol. 226, no. 4, pp. 423–432, Apr. 1990.
  - [92] S. Rajasekaran, R. N. Natarajan, J. N. Babu, P. R. M. Kanna, A. P. Shetty, and G. B. J. Andersson, "Lumbar Vertebral Growth Is Governed by 'Chondral Growth Force Response Curve' Rather Than 'Hueter-Volkmann Law,'" *Spine (Phila. Pa. 1976)*., vol. 36, no. 22, pp. E1435–E1445, 2011.
  - [93] W. Burgoyne, "The management of scoliosis," *Curr. Paediatr.*, vol. 11, no. 5, pp. 323–331, 2001.
  - [94] R. A. Dickson and P. Deacon, "Spinal growth," *J Bone Jt. Surg Br*, vol. 69, no. 5, pp. 690–692, 1987.
  - [95] M. Ylikoski, "Spinal growth and progression of adolescent idiopathic scoliosis," *Eur Spine J*, vol. 1, no. 4, pp. 236–239, 1993.
  - [96] J. A. Janicki and B. Alman, "Scoliosis: Review of diagnosis and treatment," *Paediatr Child Heal.*, vol. 12, no. 9, pp. 771–776, 2007.
  - [97] G. Glancy, "Advances in Idiopathic Scoliosis in Children and Adolescents," *Adv. Pediatr.*, vol. 54, no. 1, pp. 55–66, 2007.

- [98] J. R. Cobb, "Outline for the study of scoliosis," *Am Acad Orthop Surg Instr. Lect*, vol. 5, pp. 261–275, 1948.
- [99] D. J. Wever, A. G. Veldhuizen, J. P. Klein, P. J. Webb, G. Nijenbanning, J. C. Cool, and J. R. v Horn, "A biomechanical analysis of the vertebral and rib deformities in structural scoliosis," *Eur Spine J*, vol. 8, no. 4, pp. 252–260, 1999.
- [100] S. Parent, H. Labelle, W. Skalli, and J. de Guise, "Vertebral wedging characteristic changes in scoliotic spines," *Spine (Phila Pa 1976)*, vol. 29, no. 20, pp. E455–62, 2004.
- [101] M.-L. Nault, J.-M. Mac-Thiong, M. Roy-Beaudry, I. Turgeon, J. Deguise, H. Labelle, and S. Parent, "Three-dimensional spinal morphology can differentiate between progressive and nonprogressive patients with adolescent idiopathic scoliosis at the initial presentation: a prospective study.," *Spine (Phila. Pa. 1976)*., vol. 39, no. 10, pp. E601–6, 2014.
- [102] A. P. Sangole, C.-E. Aubin, H. Labelle, I. A. F. Stokes, L. G. Lenke, R. Jackson, and P. Newton, "Three-dimensional classification of thoracic scoliotic curves.," *Spine (Phila Pa 1976)*, vol. 34, no. 1, pp. 91–99, 2009.
- [103] W. J. Wang, H. Y. Yeung, W. C.-W. Chu, N. L.-S. Tang, K. M. Lee, Y. Qiu, R. G. Burwell, and J. C. Y. Cheng, "Top theories for the etiopathogenesis of adolescent idiopathic scoliosis.," *J. Pediatr. Orthop.*, vol. 31, no. 1 Suppl, pp. S14–S27, 2011.
- [104] S. Parent, P. O. Newton, and D. R. Wenger, "Adolescent idiopathic scoliosis: etiology, anatomy, natural history, and bracing," *Instr Course Lect*, vol. 54, pp. 529–536, 2005.
- [105] S. A. Patten, P. Margaritte-jeannin, J. Bernard, E. Alix, A. Labalme, A. Besson, S. L. Girard, K. Fendri, N. Fraisse, B. Biot, C. Poizat, A. Campan-Fournier, K. Abelin-Genevois, V. Cunin, C. Zaouter, M. Liao, R. Lamy, G. Lesca, R. Menassa, C. Marcaillou, M. Letexier, D. Sanlaville, J. Berard, G. A. Rouleau, F. Clerget-Darpoux, P. Drapeau, F. Moldovan, and P. Edery, "Functional variants of POC5 identified in patients with idiopathic scoliosis," *J. Clin. Invest.*, vol. 2, no. 3, pp. 3–7, 2015.
- [106] L. Xu, S. Huang, X. Qin, S. Mao, J. Qiao, B.-P. Qian, Y. Qiu, and Z. Zhu,

- "Investigation of the 53 Markers in a DNA-Based Prognostic Test Revealing New Predisposition Genes for Adolescent Idiopathic Scoliosis.," *Spine (Phila. Pa. 1976)*., vol. 40, no. 14, pp. 1086–1091, Jul. 2015.
- [107] M. Machida, J. Dubousset, Y. Imamura, T. Iwaya, T. Yamada, and J. Kimura, "An experimental study in chickens for the pathogenesis of idiopathic scoliosis.," *Spine (Phila Pa 1976)*, vol. 18, no. 12, pp. 1609–1615, 1993.
- [108] M. Machida, I. Murai, Y. Miyashita, J. Dubousset, T. Yamada, and J. Kimura, "Pathogenesis of idiopathic scoliosis. Experimental study in rats.," *Spine (Phila. Pa. 1976)*., vol. 24, no. 19, pp. 1985–1989, 1999.
- [109] K. M. Cheung, T. Wang, A. M. Poon, A. Carl, B. Tranmer, Y. Hu, K. D. Luk, and J. C. Leong, "The effect of pinealectomy on scoliosis development in young nonhuman primates," *Spine (Phila. Pa. 1976)*., vol. 30, no. 18, pp. 2009–2013, 2005.
- [110] M. Gene, C. Wai, W. William, W. Jun, Y. Annie, P. Yee, W. J. Ho, N. T. Bun, L. T. Ping, L. Simon, K. Man, N. Bobby, K. Wah, W. C. Chiu, Q. Yong, C. Jack, and C. Yiu, "A Review of Pinealectomy-Induced Melatonin-Deficient Animal Models for the Study of Etiopathogenesis of Adolescent Idiopathic Scoliosis," *Int. J. Mol. Sci.*, no. July, pp. 16484–16499, 2014.
- [111] W. W.-J. Wang, G. C.-W. Man, J. H. Wong, T.-B. Ng, K.-M. Lee, B. K.-W. Ng, H.-Y. Yeung, Y. Qiu, and J. C.-Y. Cheng, "Abnormal response of the proliferation and differentiation of growth plate chondrocytes to melatonin in adolescent idiopathic scoliosis.," *Int. J. Mol. Sci.*, vol. 15, no. 9, pp. 17100–14, 2014.
- [112] A. Moreau, D. S. Wang, S. Forget, B. Azeddine, D. Angeloni, F. Fraschini, H. Labelle, B. Poitras, C.-H. Rivard, and G. Grimard, "Melatonin signaling dysfunction in adolescent idiopathic scoliosis.," *Spine (Phila. Pa. 1976)*., vol. 29, no. 16, pp. 1772–1781, 2004.
- [113] M. Girardo, N. Bettini, E. Dema, and S. Cervellati, "The role of melatonin in the pathogenesis of adolescent idiopathic scoliosis (AIS)," *Eur. Spine J.*, vol. 20, no. SUPPL. 1, pp. 68–74, 2011.
- [114] T. T. Goultidis, K. A. Papavasiliou, A. S. Petropoulos, A. Philippopoulos, and G. A.

- Kapetanios, "Higher levels of melatonin in early stages of adolescent idiopathic scoliosis: toward a new scenario.," *J. Pediatr. Orthop.*, vol. 34, no. 8, pp. 768–773, Dec. 2014.
- [115] E. Acaroglu, I. Akel, A. Alanay, M. Yazici, and R. Marcucio, "Comparison of the melatonin and calmodulin in paravertebral muscle and platelets of patients with or without adolescent idiopathic scoliosis.," *Spine (Phila. Pa. 1976)*., vol. 34, no. 18, pp. E659–63, 2009.
- [116] T. Lowe, D. Lawellin, D. Smith, C. Price, T. Maher, A. Merola, and M. O'Brien, "Platelet calmodulin levels in adolescent idiopathic scoliosis: do the levels correlate with curve progression and severity?.,," *Spine (Phila. Pa. 1976)*., vol. 27, no. 7, pp. 768–775, 2002.
- [117] A. H. Hawasli, T. E. Hullar, and I. G. Dorward, "Idiopathic scoliosis and the vestibular system.," *Eur. Spine J.*, vol. 24, no. 2, pp. 227–33, 2015.
- [118] J. R. Pincott and L. F. Taffs, "Experimental scoliosis in primates: a neurological cause," *J. Bone Joint Surg. Br.*, vol. 64, no. 4, pp. 503–507, 1982.
- [119] X. Guo, W. W. Chau, Y. L. Chan, and J. C. Y. Cheng, "Relative anterior spinal overgrowth in adolescent idiopathic scoliosis. Results of disproportionate endochondral-membranous bone growth.," *J. Bone Joint Surg. Br.*, vol. 85, no. 7, pp. 1026–1031, 2003.
- [120] X. Drevelle, Y. Lafon, E. Ebermeyer, I. Courtois, J. Dubousset, and W. Skalli, "Analysis of Idiopathic Scoliosis Progression by Using Numerical Simulation," *Spine (Phila. Pa. 1976)*., vol. 35, no. 10, pp. 407–412, 2010.
- [121] B. Pourabbas Tahvildari, M.-A. Erfani, H. Nouraei, and M. Sadeghian, "Evaluation of bone mineral status in adolescent idiopathic scoliosis.," *Clin. Orthop. Surg.*, vol. 6, no. 2, pp. 180–184, Jun. 2014.
- [122] W. S. Yu, K. Y. Chan, F. W. P. Yu, B. K. W. Ng, K. M. Lee, L. Qin, T. P. Lam, and J. C. Y. Cheng, "Bone structural and mechanical indices in Adolescent Idiopathic Scoliosis evaluated by high-resolution peripheral quantitative computed tomography (HR-pQCT)," *Bone*, vol. 61, pp. 109–115, 2014.

- [123] K. Ishida, Y. Aota, N. Mitsugi, M. Kono, T. Higashi, T. Kawai, K. Yamada, T. Niimura, K. Kaneko, H. Tanabe, Y. Ito, T. Katsuhata, and T. Saito, "Relationship between bone density and bone metabolism in adolescent idiopathic scoliosis.," *Scoliosis*, vol. 10, p. 19, 2015.
- [124] I. Villemure, C. E. Aubin, J. Dansereau, and H. Labelle, "Biomechanical simulations of the spine deformation process in adolescent idiopathic scoliosis from different pathogenesis hypotheses," *Eur. Spine J.*, vol. 13, no. 1, pp. 83–90, 2004.
- [125] A. Huynh, C. Aubin, P. Mathieu, and H. Labelle, "Simulation of progressive spinal deformities in Duchenne muscular dystrophy using a biomechanical model integrating muscles and vertebral growth modulation," *Clin. Biomech.*, vol. 22, no. 4, pp. 392–399, 2007.
- [126] M. Driscoll, C. E. Aubin, A. Moreau, and S. Parent, "Biomechanical comparison of fusionless growth modulation corrective techniques in pediatric scoliosis," *Med Biol Eng Comput*, vol. 49, no. 12, pp. 1437–1445, 2011.
- [127] L. Shi, D. Wang, M. Driscoll, I. Villemure, W. C. Chu, J. C. Cheng, and C. E. Aubin, "Biomechanical analysis and modeling of different vertebral growth patterns in adolescent idiopathic scoliosis and healthy subjects," *Scoliosis*, vol. 6, p. 11, 2011.
- [128] R. M. Castelein, J. H. Van Dieën, and T. H. Smit, "The role of dorsal shear forces in the pathogenesis of adolescent idiopathic scoliosis - A hypothesis," *Med. Hypotheses*, vol. 65, no. 3, pp. 501–508, 2005.
- [129] J. L. Beguiristain, J. De Salis, A. Oriaifo, and J. Canadell, "Experimental scoliosis by epiphysiodesis in pigs," *Int Orthop*, vol. 3, no. 4, pp. 317–321, 1980.
- [130] Y.-G. Zhang, G.-Q. Zheng, X.-S. Zhang, and Y. Wang, "Scoliosis model created by pedicle screw tethering in immature goats: the feasibility, reliability, and complications.," *Spine (Phila. Pa. 1976)*, vol. 34, no. 21, pp. 2305–2310, 2009.
- [131] A.-M. Huynh, C.-E. Aubin, T. Rajwani, K. M. Bagnall, and I. Villemure, "Pedicule growth asymmetry as a cause of adolescent idiopathic scoliosis: a biomechanical study," *Eur. Spine J.*, vol. 16, no. 4, pp. 523–529, 2006.



- [132] M. Chazono, T. Tanaka, K. Marumo, K. Kono, and N. Suzuki, "Significance of peak height velocity as a predictive factor for curve progression in patients with idiopathic scoliosis.," *Scoliosis*, vol. 10, no. Suppl 2, p. S5, 2015.
- [133] R. E. Will, I. A. Stokes, X. Qiu, M. R. Walker, and J. O. Sanders, "Cobb angle progression in adolescent scoliosis begins at the intervertebral disc.," *Spine (Phila. Pa. 1976)*, vol. 34, no. 25, pp. 2782–2786, Dec. 2009.
- [134] T. P. C. Schlösser, M. van Stralen, R. C. Brink, W. C. W. Chu, T.-P. Lam, K. L. Vincken, R. M. Castelein, and J. C. Y. Cheng, "Three-dimensional characterization of torsion and asymmetry of the intervertebral discs versus vertebral bodies in adolescent idiopathic scoliosis.," *Spine (Phila. Pa. 1976)*, vol. 39, no. 19, pp. E1159–66, 2014.
- [135] S. L. Weinstein, L. A. Dolan, J. G. Wright, and M. B. Dobbs, "Effects of bracing in adolescents with idiopathic scoliosis.," *N. Engl. J. Med.*, vol. 369, no. 16, pp. 1512–1521, Oct. 2013.
- [136] J. O. Sanders, P. O. Newton, R. H. Browne, D. E. Katz, J. G. Birch, and J. A. Herring, "Bracing for idiopathic scoliosis: how many patients require treatment to prevent one surgery?," *J. Bone Joint Surg. Am.*, vol. 96, no. 8, pp. 649–653, Apr. 2014.
- [137] M. Lusini, S. Donzelli, S. Minnella, F. Zaina, and S. Negrini, "Brace treatment is effective in idiopathic scoliosis over 45 degrees: an observational prospective cohort controlled study.," *Spine J.*, vol. 14, no. 9, pp. 1951–1956, Sep. 2014.
- [138] S. Negrini, S. Minozzi, J. Bettany-Saltikov, N. Chockalingam, T. B. Grivas, T. Kotwicki, T. Maruyama, M. Romano, and F. Zaina, "Braces for idiopathic scoliosis in adolescents.," *Cochrane database Syst. Rev.*, vol. 6, p. CD006850, 2015.
- [139] S. Donzelli, F. Zaina, M. Lusini, S. Minnella, and S. Negrini, "In favour of the definition 'adolescents with idiopathic scoliosis': juvenile and adolescent idiopathic scoliosis braced after ten years of age, do not show different end results. SOSORT award winner 2014.," *Scoliosis*, vol. 9, p. 7, 2014.
- [140] A. G. Aulisa, M. Giordano, F. Falciglia, E. Marzetti, A. Poscia, and V. Guzzanti, "Correlation between compliance and brace treatment in juvenile and adolescent

- idiopathic scoliosis: SOSORT 2014 award winner.,” *Scoliosis*, vol. 9, p. 6, 2014.
- [141] E. Misterska, M. Glowacki, K. Adamczyk, and R. Jankowski, “Patients’ and Parents’ Perceptions of Appearance in Scoliosis Treated with a Brace: A Cross-Sectional Analysis,” *J. Child Fam. Stud.*, vol. 23, no. 7, pp. 1163–1171, 2013.
- [142] T. Maruyama, T. B. Grivas, and A. Kaspiris, “Effectiveness and outcomes of brace treatment: a systematic review.,” *Physiother. Theory Pract.*, vol. 27, no. 1, pp. 26–42, 2011.
- [143] J. Clin, C.-E. Aubin, and H. Labelle, “Virtual prototyping of a brace design for the correction of scoliotic deformities,” *Med. Biol. Eng. Comput.*, vol. 45, no. 5, pp. 467–473, 2007.
- [144] J. Clin, C.-E. Aubin, S. Parent, A. Sangole, and H. Labelle, “Comparison of the biomechanical 3D efficiency of different brace designs for the treatment of scoliosis using a finite element model,” *Eur. Spine J.*, vol. 19, no. 7, pp. 1169–1178, 2010.
- [145] J. Clin, C. É. Aubin, S. Parent, and H. Labelle, “Biomechanical modeling of brace treatment of scoliosis: Effects of gravitational loads,” *Med. Biol. Eng. Comput.*, vol. 49, no. 7, pp. 743–753, 2011.
- [146] F. Desbiens-Blais, J. Clin, S. Parent, H. Labelle, and C. E. Aubin, “New brace design combining CAD/CAM and biomechanical simulation for the treatment of adolescent idiopathic scoliosis,” *Clin. Biomech.*, vol. 27, no. 10, pp. 999–1005, 2012.
- [147] C.-É. Aubin, N. Cobetto, J. Clin, F. Desbiens-Blais, H. Labelle, S. Le May, and S. Parent, “Improved brace design combining CAD/CAM and finite element simulation for the conservative treatment of adolescent idiopathic scoliosis (AIS): preliminary results of a randomized control trial,” *Scoliosis*, vol. 10, no. Suppl 1, pp. O59–O59, Jan. 2015.
- [148] J. Dubousset, J. A. Herring, and H. Shufflebarger, “The crankshaft phenomenon.,” *J. Pediatr. Orthop.*, vol. 9, no. 5, pp. 541–550, 1989.
- [149] S. Delorme, H. Labelle, and C.-E. Aubin, “Is Cobb angle progression a good indicator in adolescent idiopathic scoliosis?,” *Spine (Phila. Pa. 1976)*, vol. 27, no.

- 6, pp. E145–E151, 2002.
- [150] C. E. Aubin, H. Labelle, and O. C. Ciolofan, “Variability of spinal instrumentation configurations in adolescent idiopathic scoliosis,” *Eur. Spine J.*, vol. 16, no. 1, pp. 57–64, 2007.
  - [151] S. D. Daffner, C. F. Beimesch, and J. C. Wang, “Geographic and demographic variability of cost and surgical treatment of idiopathic scoliosis,” *Spine (Phila. Pa. 1976)*, vol. 35, no. 11, pp. 1165–1169, 2010.
  - [152] R. R. Betz, A. Ranade, A. F. Samdani, R. Chafetz, L. P. D’Andrea, J. P. Gaughan, J. Asghar, H. Grewal, and M. J. Mulcahey, “Vertebral body stapling: a fusionless treatment option for a growing child with moderate idiopathic scoliosis,” *Spine (Phila Pa 1976)*, vol. 35, no. 2, pp. 169–176, 2010.
  - [153] R. R. Betz, J. Kim, L. P. D’Andrea, M. J. Mulcahey, R. K. Balsara, and D. H. Clements, “An innovative technique of vertebral body stapling for the treatment of patients with adolescent idiopathic scoliosis: a feasibility, safety, and utility study,” *Spine (Phila. Pa. 1976)*, vol. 28, no. 20, pp. S255–265, Oct. 2003.
  - [154] D. L. Skaggs, B. A. Akbarnia, J. M. Flynn, K. S. Myung, P. D. Sponseller, M. G. Vitale, W. Chest, G. Spine Deformity Study, G. Growing Spine Study, A. Pediatric Orthopaedic Society of North, and C. Scoliosis Research Society Growing Spine Study, “A classification of growth friendly spine implants,” *J Pediatr Orthop*, vol. 34, no. 3, pp. 260–274, 2014.
  - [155] P. R. HARRINGTON, “Treatment of scoliosis. Correction and internal fixation by spine instrumentation,” *J. Bone Joint Surg. Am.*, vol. 44-A, pp. 591–610, Jun. 1962.
  - [156] M. E. Cunningham, P. H. B. Frelinghuysen, J. S. Roh, O. Boachie-Adjei, and D. W. Green, “Fusionless scoliosis surgery,” *Curr. Opin. Pediatr.*, vol. 17, no. 1, pp. 48–53, Feb. 2005.
  - [157] J. S. Yang, M. J. McElroy, B. A. Akbarnia, P. Salari, D. Oliveira, G. H. Thompson, J. B. Emans, M. Yazici, D. L. Skaggs, S. A. Shah, P. N. Kostial, and P. D. Sponseller, “Growing rods for spinal deformity: characterizing consensus and variation in current use,” *J. Pediatr. Orthop.*, vol. 30, no. 3, pp. 264–270, 2010.

- [158] M. Yazici and Z. D. Olgun, "Growing rod concepts: State of the art," *Eur. Spine J.*, vol. 22, no. SUPPL.2, pp. 118–130, 2013.
- [159] T. Odent, B. Ilharreborde, L. Miladi, N. Khouri, P. Violas, J. Ouellet, V. Cunin, J. Kieffer, K. Kharrat, and F. Accadbled, "Fusionless surgery in early-onset scoliosis.," *Orthop. Traumatol. Surg. Res.*, vol. 101, no. 6 Suppl, pp. S281–8, Oct. 2015.
- [160] P. Kiely and M. Grevitt, "Recent developments in scoliosis surgery," *Curr. Orthop.*, vol. 22, no. 1, pp. 42–47, 2008.
- [161] K. M. C. Cheung, J. P. Y. Cheung, D. Samartzis, K. C. Mak, Y. W. Wong, W. Y. Cheung, B. a. Akbarnia, and K. D. K. Luk, "Magnetically controlled growing rods for severe spinal curvature in young children: A prospective case series," *Lancet*, vol. 379, no. 9830, pp. 1967–1974, 2012.
- [162] V. Cunin, "Early-onset scoliosis - current treatment.," *Orthop. Traumatol. Surg. Res.*, vol. 101, no. 1 Suppl, pp. S109–18, 2015.
- [163] J. Ouellet, "Surgical technique: modern Luque trolley, a self-growing rod technique.," *Clin. Orthop. Relat. Res.*, vol. 469, no. 5, pp. 1356–1367, May 2011.
- [164] Y. Floman, G. Burnei, S. Gavrilu, Y. Anekstein, S. Straticiuc, M. Tunyogi-Csapo, Y. Mirovsky, D. Zarzycki, T. Potaczek, and U. Arnin, "Surgical management of moderate adolescent idiopathic scoliosis with ApiFix®: a short peri- apical fixation followed by post-operative curve reduction with exercises," *Scoliosis*, vol. 10, no. 1, pp. 1–6, 2015.
- [165] A. D. SMITH, W. H. VON LACKUM, and R. WYLIE, "An operation for stapling vertebral bodies in congenital scoliosis.," *J. Bone Joint Surg. Am.*, vol. 36, no. A:2, pp. 342–348, Apr. 1954.
- [166] K. J. Hunt, J. T. Braun, and B. A. Christensen, "The effect of two clinically relevant fusionless scoliosis implant strategies on the health of the intervertebral disc: analysis in an immature goat model," *Spine (Phila Pa 1976)*, vol. 35, no. 4, pp. 371–377, 2010.
- [167] C. H. Crawford and L. G. Lenke, "Growth Modulation by Means of Anterior Tethering

- Resulting in Progressive Correction of Juvenile Idiopathic Scoliosis: A Case Report,” *J. Bone Jt. Surg.*, vol. 92, no. 1, pp. 202–209, 2010.
- [168] A. F. Samdani, R. J. Ames, J. S. Kimball, J. M. Pahys, H. Grewal, G. J. Pelletier, and R. R. Betz, “Anterior Vertebral Body Tethering for Idiopathic Scoliosis: Two-Year Results.,” *Spine (Phila. Pa. 1976)*, vol. 39, no. 20, pp. 1688–1693, 2014.
- [169] M. P. Shillington, R. D. Labrom, G. N. Askin, and C. J. Adam, “A biomechanical investigation of vertebral staples for fusionless scoliosis correction,” *Clin Biomech (Bristol, Avon)*, vol. 26, no. 5, pp. 445–451, 2011.
- [170] J. Clin, C.-E. Aubin, and S. Parent, “Biomechanical simulation and analysis of scoliosis correction using a fusionless intravertebral epiphyseal device.,” *Spine (Phila. Pa. 1976)*, vol. 40, no. 6, pp. 369–376, Mar. 2015.
- [171] N. Cobetto, C. E. Aubin, and S. Parent, “Biomechanical Simulation of the Immediate and Long Term 3D Correction of Anterior Vertebral Body Tethering in Pediatric Idiopathic Scoliosis,” in *9th International Congress on Early Onset Scoliosis (ICEOS)*, 2015.
- [172] S. B. Naique, R. Porter, A. A. Cunningham, S. P. Hughes, B. Sanghera, and A. A. Amis, “Scoliosis in an Orangutan,” *Spine (Phila. Pa. 1976)*, vol. 28, no. 7, pp. E143–5, 2003.
- [173] F. Schwab, A. Patel, V. Lafage, and J. P. Farcy, “A porcine model for progressive thoracic scoliosis,” *Spine (Phila Pa 1976)*, vol. 34, no. 11, pp. E397–404, 2009.
- [174] T. Odent, T. Cachon, B. Peultier, J. Gournay, E. Jolivet, and E. Viguier, “Porcine scoliosis model based on animal growth created with non-invasive off-set tethering,” *Comput. Methods Biomech. Biomed. Engin.*, vol. 12, pp. 199–200, 2009.
- [175] X. Zheng, X. Sun, Y. Qiu, Z.-Z. Zhu, W. Bin, Y.-T. Ding, and B.-P. Qian, “A porcine early-onset scoliosis model created using a posterior mini-invasive method: a pilot study.,” *J. Spinal Disord. Tech.*, vol. 27, no. 8, pp. E294–300, Dec. 2014.
- [176] J. G. Burke, E. Vettorato, G. Schoffmann, R. E. Clutton, T. S. Drew, and J. N. A. Gibson, “Creation of an ovine model of progressive structural lordo-scoliosis using

- a unilateral laminar tether.," *Eur. spine J. Off. Publ. Eur. Spine Soc. Eur. Spinal Deform. Soc. Eur. Sect. Cerv. Spine Res. Soc.*, vol. 24, no. 7, pp. 1382–1390, Jul. 2015.
- [177] J. T. Braun, J. W. Ogilvie, E. Akyuz, D. S. Brodke, K. N. Bachus, and R. M. Stefko, "Experimental scoliosis in an immature goat model: a method that creates idiopathic-type deformity with minimal violation of the spinal elements along the curve," *Spine (Phila Pa 1976)*, vol. 28, no. 19, pp. 2198–2203, 2003.
- [178] I. W. NACHLAS and J. N. BORDEN, "The cure of experimental scoliosis by directed growth control.," *J. Bone Joint Surg. Am.*, vol. 33 A, no. 1, pp. 24–34, Jan. 1951.
- [179] J. T. Braun, "The Efficacy and Integrity of Shape Memory Alloy Staples and Bone Anchors with Ligament Tethers in the Fusionless Treatment of Experimental Scoliosis," *J. Bone Jt. Surg.*, vol. 87, no. 9, pp. 2038–2051, 2005.
- [180] J. T. Braun, E. Akyuz, H. Udall, J. W. Ogilvie, D. S. Brodke, and K. N. Bachus, "Three-dimensional analysis of 2 fusionless scoliosis treatments: a flexible ligament tether versus a rigid-shape memory alloy staple," *Spine (Phila Pa 1976)*, vol. 31, no. 3, pp. 262–268, 2006.
- [181] E. J. Wall, D. I. Bylski-Austrow, R. J. Kolata, and A. H. Crawford, "Endoscopic mechanical spinal hemiepiphysiodesis modifies spine growth," *Spine (Phila Pa 1976)*, vol. 30, no. 10, pp. 1148–1153, 2005.
- [182] M. T. Coombs, D. L. Glos, E. J. Wall, J. Kim, and D. I. Bylski-Austrow, "Biomechanics of spinal hemiepiphysiodesis for fusionless scoliosis treatment using titanium implant.," *Spine (Phila. Pa. 1976).*, vol. 38, no. 23, pp. E1454–60, 2013.
- [183] P. O. Newton, F. D. Faro, C. L. Farnsworth, G. S. Shapiro, F. Mohamad, S. Parent, and K. Fricka, "Multilevel spinal growth modulation with an anterolateral flexible tether in an immature bovine model," *Spine (Phila Pa 1976)*, vol. 30, no. 23, pp. 2608–2613, 2005.
- [184] P. O. Newton, V. V Upasani, C. L. Farnsworth, R. Oka, R. C. Chambers, J. Dwek, J. R. Kim, A. Perry, and A. T. Mahar, "Spinal Growth Modulation with Use of a Tether in an Immature Porcine Model," *J. Bone Jt. Surg.*, vol. 90, no. 12, pp. 2695–2706,

2008.

- [185] P. O. Newton, C. L. Farnsworth, V. V Upasani, R. C. Chambers, E. Varley, and S. Tsutsui, "Effects of intraoperative tensioning of an anterolateral spinal tether on spinal growth modulation in a porcine model," *Spine (Phila Pa 1976)*, vol. 36, no. 2, pp. 109–117, 2011.
- [186] G. Demirkiran, C. Yilgor, M. Ayvaz, K. Kosemehmetoglu, K. Daglioglu, and M. Yazici, "Effects of the Fusionless Instrumentation on the Disks and Facet Joints of the Unfused Segments: A Pig Model.," *J. Pediatr. Orthop.*, vol. 34, no. 2, pp. 185–193, 2014.
- [187] H. T. Hee, Y. J. Chuah, B. H. M. Tan, T. Setiobudi, and H. K. Wong, "Vascularization and morphological changes of the endplate after axial compression and distraction of the intervertebral disc.," *Spine (Phila. Pa. 1976)*, vol. 36, no. 7, pp. 505–11, 2011.
- [188] V. V Upasani, C. L. Farnsworth, R. C. Chambers, T. P. Bastrom, G. M. Williams, R. L. Sah, K. Masuda, and P. O. Newton, "Intervertebral disc health preservation after six months of spinal growth modulation.," *J. Bone Joint Surg. Am.*, vol. 93, no. 15, pp. 1408–16, 2011.
- [189] E. C. Schmid, C.-E. Aubin, A. Moreau, J. Sarwark, and S. Parent, "A novel fusionless vertebral physeal device inducing spinal growth modulation for the correction of spinal deformities," *Eur. Spine J.*, vol. 17, no. 10, pp. 1329–1335, 2008.
- [190] M. Driscoll, C. E. Aubin, A. Moreau, Y. Wakula, J. F. Sarwark, and S. Parent, "Spinal growth modulation using a novel intravertebral epiphyseal device in an immature porcine model," *Eur Spine J*, vol. 21, no. 1, pp. 138–144, Jan. 2012.
- [191] M. Driscoll, C.-E. Aubin, A. Moreau, Y. Wakula, S. Amini, and S. Parent, "Novel Hemi-staple for the Fusionless Correction of Pediatric Scoliosis: Influence on Intervertebral Discs and Growth Plates in a Porcine Model.," *J. Spinal Disord. Tech.*, Mar. 2013.
- [192] R. M. Smith and R. A. Dickson, "Experimental structural scoliosis," *J Bone Jt. Surg Br*, vol. 69, no. 4, pp. 576–581, 1987.

- [193] P. O. Newton, C. L. Farnsworth, V. V Upasani, R. Chambers, S. H. Yoon, and P. Firkins, "Dual and single memory rod construct comparison in an animal study," *Spine (Phila Pa 1976)*, vol. 36, no. 14, pp. E904–13, 2011.
- [194] A. Patel, F. Schwab, V. Lafage, B. Ungar, and J.-P. Farcy, "Spinal Deformity Correction via an Anterior-Based Tether in a Porcine Scoliosis Model," *Spine J.*, vol. 10, no. 9, p. S142, Nov. 2010.
- [195] J. Burke, E. Vettorato, G. Schöffmann, R. E. Clutton, T. Drew, and J. N. A. Gibson, "Modulation of spinal shape with growth following implantation of a novel surgical implant," *Eur. Spine J.*, vol. 24, no. 7, pp. 1522–1532, 2015.
- [196] J. Liu, Z. Li, J. Shen, and X. Xue, "Spinal growth modulation with posterior unilateral elastic tether in immature swine model.," *Spine J.*, vol. 15, no. 1, pp. 138–145, Jan. 2015.
- [197] J. D. Bobyn, D. G. Little, R. Gray, and A. Schindeler, "Animal models of scoliosis.," *J. Orthop. Res.*, vol. 33, no. 4, pp. 458–67, 2015.
- [198] F. Cheriet, J. Dansereau, Y. Petit, C.-É. Aubin, H. Labelle, and J. A. U. De Guise, "Towards the self-calibration of a multiview radiographic imaging system for the 3d reconstruction of the human spine and rib cage," *Int. J. Pattern Recognit. Artif. Intell.*, vol. 13, no. 05, pp. 761–779, Aug. 1999.
- [199] S. Delorme, Y. Petit, J. A. de Guise, H. Labelle, C. E. Aubin, and J. Dansereau, "Assessment of the 3-D reconstruction and high-resolution geometrical modeling of the human skeletal trunk from 2-D radiographic images," *Ieee Trans. Biomed. Eng.*, vol. 50, no. 8, pp. 989–998, 2003.
- [200] F. Cheriet, C. Laporte, S. Kadoury, H. Labelle, and J. Dansereau, "A novel system for thE 3-D reconstruction of the human spine and rib cage from biplanar X-ray images.," *IEEE Trans. Biomed. Eng.*, vol. 54, no. 7, pp. 1356–8, 2007.
- [201] S. Kadoury, F. Cheriet, C. Laporte, and H. Labelle, "A versatile 3D reconstruction system of the spine and pelvis for clinical assessment of spinal deformities," *Med. Biol. Eng. Comput.*, vol. 45, no. 6, pp. 591–602, 2007.



- [202] S. Kadoury, F. Cheriet, J. Dansereau, and H. Labelle, "Three-dimensional reconstruction of the scoliotic spine and pelvis from uncalibrated biplanar x-ray images.," *J. Spinal Disord. Tech.*, vol. 20, no. 2, pp. 160–167, 2007.
- [203] S. Kadoury, F. Cheriet, and H. Labelle, "Self-Calibration of Biplanar Radiographic Images Through Geometric Spine Shape Descriptors," *Biomed. Eng. IEEE Trans.*, vol. 57, no. 7, pp. 1663–1675, 2010.
- [204] J. Dubousset, G. Charpak, I. Dorion, W. Skalli, F. Lavaste, J. Deguise, G. Kalifa, S. Ferey, M. C. H. Chouard, M. J. Picard, M. C. J. Menk??s, M. J. B. Paolaggi, M. J. D. Sraer, M. P. Vichard, M. C. Kenesi, M. M. Arthuis, and M. J. L. De Gennes, "Une nouvelle imagerie ostéo-articulaire basse dose en position debout: Le système EOS," *Bull. Acad. Natl. Med.*, vol. 189, no. 2, pp. 287–300, 2005.
- [205] H. Lin, C.-E. Aubin, S. Parent, and I. Villemure, "Mechanobiological bone growth: comparative analysis of two biomechanical modeling approaches.," *Med. Biol. Eng. Comput.*, vol. 47, no. 4, pp. 357–66, 2009.
- [206] N. M. Lalonde, C. E. Aubin, R. Pannetier, and I. Villemure, "Finite element modeling of vertebral body stapling applied for the correction of idiopathic scoliosis: preliminary results," *Stud Heal. Technol Inf.*, vol. 140, pp. 111–115, 2008.
- [207] N. M. Lalonde, I. Villemure, R. Pannetier, S. Parent, and C. E. Aubin, "Biomechanical modeling of the lateral decubitus posture during corrective scoliosis surgery," *Clin Biomech (Bristol, Avon)*, vol. 25, no. 6, pp. 510–516, 2010.
- [208] C. R. Driscoll, C. E. Aubin, F. Canet, H. Labelle, and J. Dansereau, "Impact of prone surgical positioning on the scoliotic spine," *J Spinal Disord Tech*, vol. 25, no. 3, pp. 173–181, 2012.
- [209] C. Driscoll, C.-E. Aubin, F. Canet, H. Labelle, W. Horton, and J. Dansereau, "Biomechanical study of patient positioning: Influence of lower limb positioning on spinal geometry," *J. Spinal Disord. Tech.*, vol. 25, no. 2, pp. 69–76, 2012.
- [210] A. Rohlmann, T. Zander, N. K. Burra, and G. Bergmann, "Flexible non-fusion scoliosis correction systems reduce intervertebral rotation less than rigid implants and allow growth of the spine: A finite element analysis of different features of

- orthobiomechanics,” *Eur. Spine J.*, vol. 17, no. 2, pp. 217–223, 2008.
- [211] J. P. Little, M. T. Izatt, R. D. Labrom, G. N. Askin, and C. J. Adam, “An FE investigation simulating intra-operative corrective forces applied to correct scoliosis deformity,” *Scoliosis*, vol. 8, no. 1, p. 9, 2013.
- [212] O. A. Abolaeha, J. Weber, and L. T. Ross, “Finite element simulation of a scoliotic spine with periodic adjustments of an attached growing rod,” *Conf. Proc. ... Annu. Int. Conf. IEEE Eng. Med. Biol. Soc. IEEE Eng. Med. Biol. Soc. Annu. Conf.*, vol. 2012, pp. 5781–5, 2012.
- [213] A. Agarwal, A. Zakeri, A. K. Agarwal, A. Jayaswal, and V. K. Goel, “Distraction magnitude and frequency affects the outcome in juvenile idiopathic patients with growth rods: finite element study using a representative scoliotic spine model,” *Spine J.*, 2015.
- [214] C. Vergari, G. Ribes, B. A. Menga, C. Adam, L. Miladi, B. Ilharreborde, K. Abelin-Genevois, P. Rouch, and W. Skalli, “Evaluation of a patient-specific finite-element model to simulate conservative treatment in adolescent idiopathic scoliosis,” *Spine Deform.*, vol. 3, no. 1, pp. 4–11, 2015.
- [215] M. Driscoll, J. M. Mac-Thiong, H. Labelle, M. Slivka, S. Stad, and S. Parent, “Biomechanical assessment of reduction forces measured during scoliotic instrumentation using two different screw designs,” *Spine Deform.*, vol. 1, no. 2, pp. 94–101, 2013.
- [216] H. Zhang, H. Hu, X. Yin, M. Tang, C. Guo, S. Liu, Y. Wang, A. Deng, J. Liu, and J. Wu, “Use of finite element analysis of a Lenke type 5 adolescent idiopathic scoliosis case to assess possible surgical outcomes,” *Comput. Aided Surg.*, vol. 18, no. 3–4, pp. 84–92, 2013.
- [217] P. Lafortune, C.-E. Aubin, H. Boulanger, I. Villemure, K. M. Bagnall, and A. Moreau, “Biomechanical simulations of the scoliotic deformation process in the pinealectomized chicken: a preliminary study,” *Scoliosis*, vol. 2, no. 1, p. 16, 2007.
- [218] B. Kumar, D. I. Bylski-Austrow, and Y. Liu, “Finite element model of spinal hemiepiphysiodesis: effect of contact conditions, initial conditions, and growth,”

*Stud Heal. Technol Inf.*, vol. 176, pp. 99–103, 2012.

- [219] C. E. Aubin, J. Dansereau, J. A. De Guise, and H. Labelle, “[A study of biomechanical coupling between spine and rib cage in the treatment by orthosis of scoliosis].,” *Ann. Chir.*, vol. 50, no. 8, pp. 641–50, 1996.
- [220] I. A. Stokes and J. P. Laible, “Three-dimensional osseo-ligamentous model of the thorax representing initiation of scoliosis by asymmetric growth.,” *J. Biomech.*, vol. 23, no. 6, pp. 589–595, 1990.
- [221] J. Carrier, C. E. Aubin, I. Villemure, and H. Labelle, “Biomechanical modelling of growth modulation following rib shortening or lengthening in adolescent idiopathic scoliosis,” *Med Biol Eng Comput*, vol. 42, no. 4, pp. 541–548, 2004.
- [222] T. Odent, T. Cachon, B. Peultier, J. Gournay, E. Jolivet, C. Elie, H. Abdoul, and E. Viguier, “Porcine model of early onset scoliosis based on animal growth created with posterior mini-invasive spinal offset tethering: a preliminary report,” *Eur Spine J*, vol. 20, no. 11, pp. 1869–1876, 2011.
- [223] E. Chay, A. Patel, B. Ungar, A. Leung, B. Moal, V. Lafage, J.-P. Farcy, and F. Schwab, “Impact of Unilateral Corrective Tethering on the Histology of the Growth Plate in an Established Porcine Model for Thoracic Scoliosis,” *Spine (Phila. Pa. 1976)*., vol. 37, no. 15, pp. E883–E889, 2012.
- [224] I. A. F. Stokes, D. D. Aronsson, and M. Jones, “Disc and vertebral wedging in patients with progressive scoliosis,” in *Studies in Health Technology and Informatics*, 1999, vol. 59, pp. 191–193.
- [225] J. T. Braun, J. W. Ogilvie, E. Akyuz, D. S. Brodke, K. N. Bachus, and R. M. Stefko, “Experimental scoliosis in an immature goat model: a method that creates idiopathic-type deformity with minimal violation of the spinal elements along the curve.,” *Spine (Phila. Pa. 1976)*., vol. 28, no. 19, pp. 2198–2203, 2003.
- [226] G. R. Buttermann and W. J. Mullin, “Pain and disability correlated with disc degeneration via magnetic resonance imaging in scoliosis patients,” *Eur. Spine J.*, vol. 17, no. 2, pp. 240–249, 2008.

- [227] I. A. Stokes and J. C. Iatridis, "Mechanical conditions that accelerate intervertebral disc degeneration: overload versus immobilization," *Spine (Phila Pa 1976)*, vol. 29, no. 23, pp. 2724–2732, 2004.
- [228] M. Cancel, G. Grimard, D. Thuillard-Crisinel, F. Moldovan, and I. Villemure, "Effects of in vivo static compressive loading on aggrecan and type II and X collagens in the rat growth plate extracellular matrix," *Bone*, vol. 44, no. 2, pp. 306–315, 2009.
- [229] A. Christe, R. Laubli, R. Guzman, U. Berlemann, R. J. Moore, G. Schroth, P. Vock, and K. O. Lovblad, "Degeneration of the cervical disc: histology compared with radiography and magnetic resonance imaging," *Neuroradiology*, vol. 47, no. 10, pp. 721–729, 2005.
- [230] S. Delorme, H. Labelle, B. Poitras, C. H. Rivard, C. Coillard, and J. Dansereau, "Pre-, intra-, and postoperative three-dimensional evaluation of adolescent idiopathic scoliosis.," *J. Spinal Disord.*, vol. 13, no. 2, pp. 93–101, 2000.

## APPENDIX A – SKELETAL GROWTH FEEDBACK LOOP

Figure A-1 illustrates the elaborate biological feedback loop involved in epiphyseal bone growth. Chondrocytes in the lower proliferative zone beginning hypertrophy secrete Ihh (Indian hedgehog), which signals juxta-articular cells (upper reserve zone) to increase PTHrP (Parathyroid hormone-related peptide) production through TGF- $\beta$  (transforming growth factor  $\beta$ ) secreted by perichondrial cells (1) [60], [63]. Ihh also acts locally by stimulating the increase of proliferation rate [63]. The increase in PTHrP is transmitted to late proliferating cells that express PTHrP receptor. These latter decrease Ihh producing cells (i.e. differentiating chondrocytes), which results in a control of the rate of proliferation [60], [63]. Chondrocytes in the lower proliferative zone undergo hypertrophy, a major factor contributing to the height gain of the growth plate, with the remainder gain within the proliferation and ECM synthesis [60], [64]. The hypertrophic cells then migrate to the lower hypertrophic zone and become terminal. At this stage, these apoptotic cells express collagen type X and vesicles containing high levels of alkaline phosphatase necessary for the calcification process as they constitute scaffolds for hydroxyapatite nucleation (2). Apoptotic chondrocytes also produce specialized ECM promoting cartilage calcification sites as templates for bone formation by osteoblasts from the vascular invasion zone (3) where collagen type X binds to the excreted vesicles, facilitating calcium deposition in the matrix. This complex feedback loop is maintained until skeletal maturity as growth promoting genes expression reduces with age while growth inhibiting genes increase. Growth rate and proliferation diminish resulting in reduced growth plate height due to diminished growth plate zonal and hypertrophic chondrocyte heights. Estrogen was found to be involved in growth plate closure and fusion at bone maturity [60], [63]. Yet, growth genetic, hormonal, and signaling pathways are not completely understood and future research will help elucidate involved factors. However, the cyclic process of endochondral ossification is well comprehended.

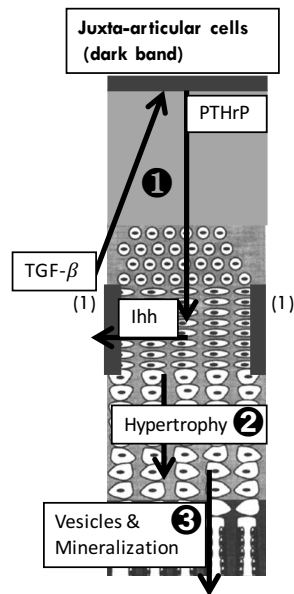


Figure A-1: Biology of the growth feedback loop

## APPENDIX B – SCOLIOSIS ETIOLOGY

Several investigations have attempted to narrow down the source of this spinal deformity by proposing theories as to its origin with most contemporary premises explaining its contributive and not primary causes. Figure B-1 summarizes the current proposed theories explaining the possible etiology pathways, which will be explored in more detail.

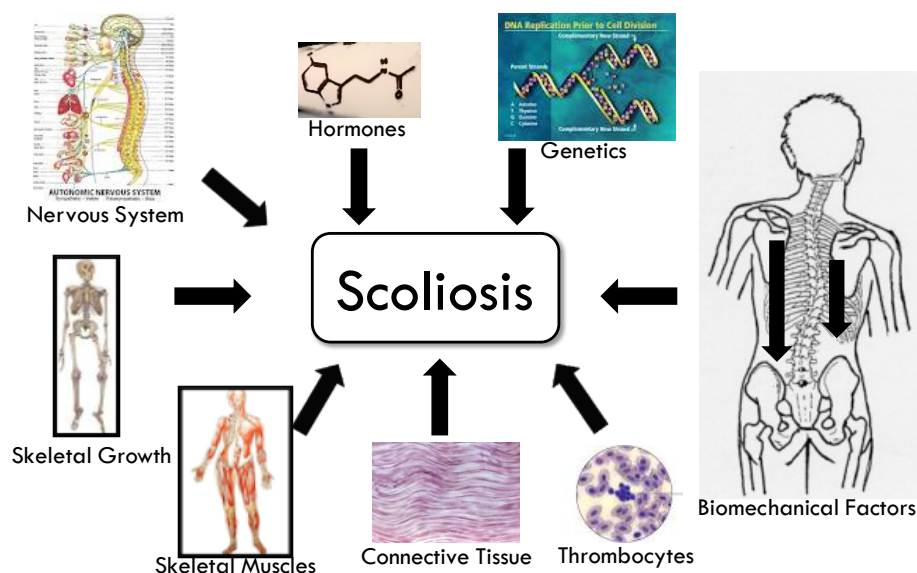


Figure B-1 : Current theories of the etiology of scoliosis

### B.1 Genetic and hormonal factors

As many of common human diseases, several investigators have tried to find the underlying genetic aspect of scoliosis. Specifically, first degree relatives are at most risk as concordance was observed in 73% of monozygotic and 36% in dizygotic twins suggesting a familial multifactorial inheritance pattern [103]. The prevalence was also reported as 11%, 2.4%, and 1.4% for first, second, and third degree relatives [104]. Yet, the mode of inheritance is not adequately confirmed and responsible genes yet to be identified as environmental and lifestyle factors may play a role in the development or genetic alterations leading to AIS initiation (such as calcium intake, diets, etc...). In a recent study, Patten *et al.* have identified three protein gene variant of POC5 present in a large family with multiple idiopathic scoliosis (IS) cases and multiple other independent IS

cases. The authors then successfully induced spinal deformity in zebrafish expressing any of the 3 (human) variants of POC5 indicating the contribution of the latter to the occurrence of IS [105]. Although promising, these findings succeed at indicating IS has genetic attributes but does not fully isolate the root cause of the expression of POC5 variants; though, its down-regulation may provide encouraging results as an exclusive IS causative factor. In another recent investigation, 4 new genes were identified as associated with AIS susceptibility; however, the authors conclude that further studies are required to better target pre-disposed genes [106]. The overall consensus reflects the important genetic aspect of AIS with extensive research focused on uncovering the gene(s) associated with AIS pre-disposition.

Hormonal factors have also been investigated as a possible metabolic root cause. Melatonin, a hormone secreted by the pineal gland, was extensively studied using animal models via removal of the pineal gland (pinealectomy). Scoliosis was consistently produced in pinealectomized chicken [107] and bipedal rats [108]; however, the pattern was not reproduced in quadrupedal rats nor nonhuman primates [109]. Additionally, scoliosis progression persisted in melatonin injected chicken after pinealectomy. These findings suggest melatonin deficiency may act differently between primate and small animals suggesting melatonin signaling pathways may be more important than melatonin levels [110], [111]. Conversely, no significant changes in melatonin levels were found in AIS patients [112], [113] with no link between melatonin levels and AIS progression [114]. Thus, these conflicting findings reflect the speculative role of melatonin signaling pathways as secondary factors with the exact role of melatonin and its signaling pathways requiring further in-depth research. Calmodulin was also investigated as it exhibits two properties: it is a second messenger of melatonin and it regulates contractile properties of muscles and platelets. As such, this molecule may mediate paraspinal muscle contractions and it was found that calmodulin distribution in the convex was higher than the concave paraspinal muscles in AIS [115]. Moreover, it was shown that platelet calmodulin levels were associated with curve progression in AIS with brace stabilization reducing these molecular levels in 90% of patients [116].



## B.2 Connective tissue and nervous system

Scoliosis development in connective tissue disorders suggest possible relation to soft tissue health (e.g. Marfan's syndrome) [104]. Moreover, intervertebral disc collagen fiber and proteoglycan changes were sometimes observed but not always consistent. Concave/convex muscles fibers asymmetry and elastic fiber change in AIS skin and ligaments are indicative of connective tissue disorder. However, speculations as to the secondary role of these changes may be warranted as no genetic association to collagen type I and II and elastin structural gene were noticed.

Further indications of regional brain and vestibular system volume differences were observed between AIS and normal [117]. Experimentally, scoliosis was induced in primates following spinal cord damage [118]. Spinal damage caused visual and proprioceptive functional impairment which may be associated with spinal alignment offset causing balance disruptions, and thus, resulted in scoliotic deformity secondary to an already existing spinal misalignment. In a well-written review, Hawasli *et al.* have summarized an established link between vestibular anomalies and scoliosis; however, their review does not pin a causative association rather a secondary or compensatory response [117].

## B.3 Skeletal growth and biomechanical factors

Relative anterior spinal overgrowth has been postulated as a causative factor. AIS patients had longer vertebral body heights, shorter pedicles, and larger interpedicular space suggesting anterior overgrowth [119]. Although hypothesized as etiological, this theory is arguably pathomechanistic as shown through numerical simulations where anterior overgrowth linked with lower IVD stiffness and gravitational loads resulted in progressive scoliosis in pre-existing spinal curvatures [120]. Moreover, girls with progressive curves showed lower bone mineral densities (BMD) compared to non-progressive, with unchanged BMD levels following brace treatment [121]. Likewise, AIS patients displayed lower BMD than age matched normal girls [103], [122], [123]. Nevertheless, these findings are associated with the progression rather than initiation of IS as no underlying source of low BMD has been found to date.

Biomechanical factors were believed to play a role in the etiology of scoliosis through irregular concave/convex loads (by-products of skeletal asymmetry). However, it is the etiology of this asymmetry that still eludes researchers, rendering biomechanical effects more of a pathomechanism factor. Numerous computational models have been developed supporting this pathomechanical hypothesis [34], [124]–[127].

Thus far, the etiology of idiopathic scoliosis is yet to be uncovered; however, countless research suggests IS is a multifactorial disease revolving around a complex interaction between genetic, biochemical, and biomechanical aspects. The following section will rather focus on understanding current concepts linked to the pathomechanism of scoliosis and the underlying mechanical or structural factors involved in its progression as most etiology theories succeed at attributing hypothesis as secondary to an unknown initiating cause. A thorough understanding of the progressive factors may help better target treatment strategies.

## APPENDIX C – THREE DIMENSIONAL RECONSTRUCTION OF THE SPINE

### C.1 3D reconstruction

Scoliosis is evaluated by means of biplanar radiographs to assess the severity of the deformity in the coronal and sagittal planes. Biplanar radiographic 3D reconstruction is predominantly explored to study the multi-planar geometric aspect of the deformed spine. Figure C-1 illustrates a procedural schematic for 3D reconstruction from biplanar radiographs.

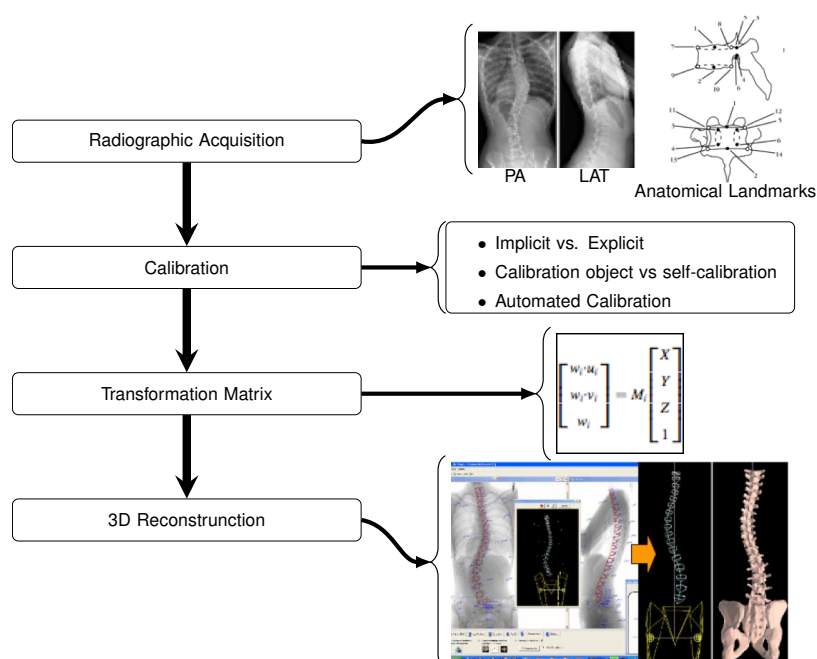


Figure C-1: Schematic of the procedure for biplanar spinal 3D reconstruction

First, radiographs are acquired in the Posterior-Anterior and Lateral views. The images are then calibrated via different techniques followed by geometric transformations of 2D landmarks to their 3D coordinates.

The biggest challenge resides within the calibration procedure with increasing attention towards automation. Early techniques relied on an implicit approach using a Direct Linear Transform (DLT) algorithm with a fixed calibration object of known 3D coordinates. Briefly, implicit calibration requires prior knowledge of the imaging setup parameters (distance from patient to source, distance between radiograph films and source). The patient is

positioned on a platform between 2 acrylic sheets with embedded steel marbles of known 3D coordinates (expressed in a global coordinate system). Radiographs are then taken in PA and LAT. Using DLT,  $M_i$  (transformation matrix) is then calculated from the 2D projection of the known 3D coordinates of the steel marbles in PA and LAT (Figure C-1) [198]–[200]. The transformation is then applied to the 2D coordinates of anatomical landmarks in each radiograph to obtain their respective 3D coordinates.

The DLT calibration method presents several shortcomings. The reconstructed geometry is highly sensitive to patient's motion between radiographic planes. As the platform and calibration marbles are fixed, patient's motion increases reconstruction error. Additionally, the calibration technique requires objects of known 3D spatial coordinates, spanning the entirety of the region of interest. Points outside the calibration object are prone to extrapolation errors.

Another calibration algorithm includes explicit descriptors of the radiographic setup, thus eliminating the need for a stationary calibration object and knowledge of radiographic setup. An object of known dimensions defines a reference plane. The 3D spatial coordinates of the object are no longer needed allowing for a mobile calibration setup (Figure C-2). Explicit calibration algorithm is based on a non-linear cost function minimizing the distance between observed and computed projections while changing the geometric descriptors of the radiographic setup [200]. The inherent benefits of explicit calibration is its ease of implementation with use of a calibration vest. Yet, this method still requires an external fixed object to establish a 3D global reference frame, with reconstruction accuracy comparable to the DLT method.

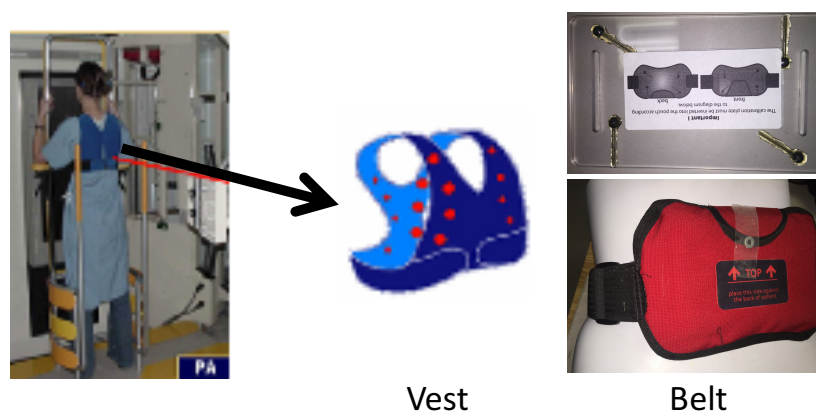


Figure C-2: Calibration vest and belt for explicit calibration

A calibration belt (Figure C-2) improved upon the calibration approach as it eliminates the need for a fixed external object. The reference plane is defined using the planar belt's coordinates. Weak-perspective is then used to estimate the distance between the image and the source, and thus, provide an initial estimate of geometrical parameters. The determined anatomical landmarks are reconstructed in 3D, then retro-projected on the PA and LAT radiographs using calculated projection matrices. Non-linear minimization reduces the error between retro-projected and initial landmarks with geometric parameters updated until the cost function is respected [201]. The procedure reduces errors from patient's motion between radiographs as the reference plane is defined by the wearable belt. However, the method is error-prone to the initial landmark identification, requiring a well-rounded operator. Anatomical landmarks were also proposed to eliminate the need for a calibration object. Using explicit calibration and minimization of retro-projected landmarks, the method is useful when the calibration object is undetectable on the acquired images. However, the scaling factor is not accounted for and typically required a small object of known dimensions, such as a screw or large marble, to establish a reference scale factor. Moreover, reconstruction errors increase for regions outside initially identified landmarks [202].

Each of these methods transforms the 2D coordinates of the selected vertebral landmarks and reconstruct their 3D coordinates. Seventeen vertebral, 21 on the pelvis, and 11 landmarks on each rib can be reconstructed, as needed, to obtain a 3D geometry of the

spine, thorax, and pelvis. A visual representation can be obtained by deforming primitives on high resolution CT scans reference anatomical structures through a process of dual-kriging to match 3D anatomical landmarks identified via the reconstruction technique. Reconstruction errors are in the order of 3 mm, with the largest error lying in reconstructing the posterior vertebral structures.

Another promising method ventures towards automatic calibration by using geometric shape descriptors, the vertebral bodies, to automatically recover vertebral contours via partial differential equation filtering. A silhouette of the vertebral bodies is then obtained in PA and LAT from which a visual hull 3D reconstruction is obtained with detection of the location and orientation of vertebral bodies. However, application of the method is prone to patient's motion between acquisitions[203].

The aforementioned methods require traditional radiographs; thus, exposing patients to a high dose of radiation. A low dose x-ray image machine, namely EOS, was developed [204]. Simultaneous biplanar low dose, calibrated radiographs of the entire body are acquired. Using SterEOS software, generic anatomical structures are then deformed and rotated to match their equivalent on the radiographs, with errors below 1.5mm.

## APPENDIX D – HISTOMORPHOMETRIC OBSERVATIONS

Currently, samples are fully polymerized but no analyses were performed. However, the following summarizes the prospective investigations for the polymerized samples. First, cut and grind method will be performed on the MMA embedded segments to trim at desired form-factors. Here, the intervertebral discs within the instrumented and internal control regions along with super and subjacent vertebral cuts will be extracted from instrumented and control samples (Figure D-1). Using a microtome, two 5  $\mu\text{m}$  mid-coronal slices will be extracted 30  $\mu\text{m}$  apart. Slices will then be stained using Safranin O to highlight the growth plate. Thus, hypertrophic zone and cell heights can be measured under optical microscopy set at 10 and 20 magnification, respectively, and via in-house custom algorithms. The procedure is well documents in previously published work [84], [191] (Figure D-1, B & C). Additional slices (5  $\mu\text{m}$  thick and 30  $\mu\text{m}$  apart) will be sampled and treated for type X collagen. Using an in-house protocol, type X collagen staining will be attained using a monoclonal antibody anti-collagen X for immunoperoxydase labelling followed by hematoxylin processing to highlight cellular content [191]. Type X collagen content reflects growth plate health sustainability [60], [228]. Finally, the intervertebral disc health will be assessed based on histological grading schemes quantifying the degree of nucleus necrosis and annulus fibre organization [229].

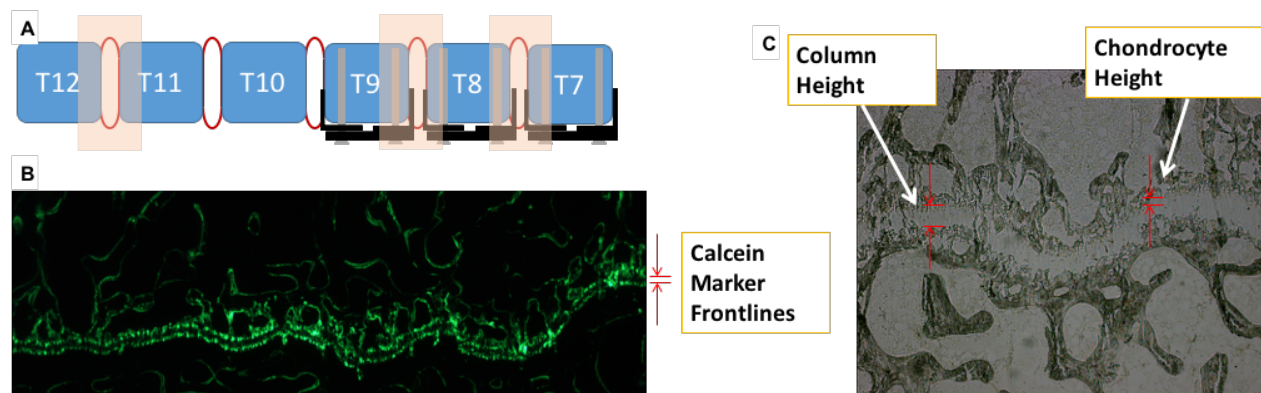


Figure D-1: A) Illustration showing extruded regions of interest (Shaded boxes). B) Calcein marker frontlines. C) Hypertrophic columnar and chondrocyte heights.

Calcein, a fluorescent marker, was injected 7 and 1 prior to animal sacrifice. These two injection time-points aid at visualizing calcein marker frontlines under fluorescent light. As such, growth rate changes is determined by measuring the distance between the marker

frontlines and dividing by the time interval between injections. This additional information will establish and quantify the growth modulating effect of the implant both ipsi- and contralateral to insertion site.



## APPENDIX E – CUSTOM SLING FOR STANDARDIZED RADIOGRAPHS

Some of the challenges involved in experimental medical imaging is standardized positioning between the postero-anterior and lateral views. In a clinical context, bi-planar radiographs are acquired by positioning the patient on an operating table and rotating the x-ray source between views. Similarly, conscious patients are asked to stand still while the x-ray source is rotated between views or, more traditionally with fixed source, patients typically turn 90 degrees while maintain the same posture as feasibly as possible. Thus, bi-planar 3D reconstructions can be performed as spinal shape changes are minimal between views. Yet, imaging is not standardized in experimental investigations. Investigators focus on quantifying changes within the coronal plane with little regard to sagittal plane modifications. Generally, animals are sedated and placed prone with limbs stretched forward and backwards for the postero-anterior radiograph then replaced on their lateral side for the side radiograph. These manipulations may alter the spinal form as it was evidenced that prone positioning under anesthesia results in 37% thoracic curve correction with flattening of the kyphosis and lordosis in human adolescent scoliotic spines [230]. With similar spinal biomechanics, it is expected that porcine spines behave similarly in prone positioning as the sagittal profile flattens and “stretches” the coronal deformity (if any exists). Nevertheless, published experimental works generally omit imperative details as to animal manipulation during x-ray imaging. To address this issues and to standardize the imaging protocol in our *in vivo* investigation, a custom sling was designed and a rudimentary prototype was hand fabricated (Figure E-1). In short, the sling consisted of a abdomen, sternum, and head resting clothes which slide independently along 2 aluminum hallow bars. The sternum resting clothe acted as an adjustable harness to support the chest area while also allowing for hand the front limbs to mimic, as closely as possible, the natural spine shape even under anesthetics. Furthermore, each clothe has a secondary opening to insert the metal rods for larger animals and eliminate rod x-ray obstruction during lateral exposure.

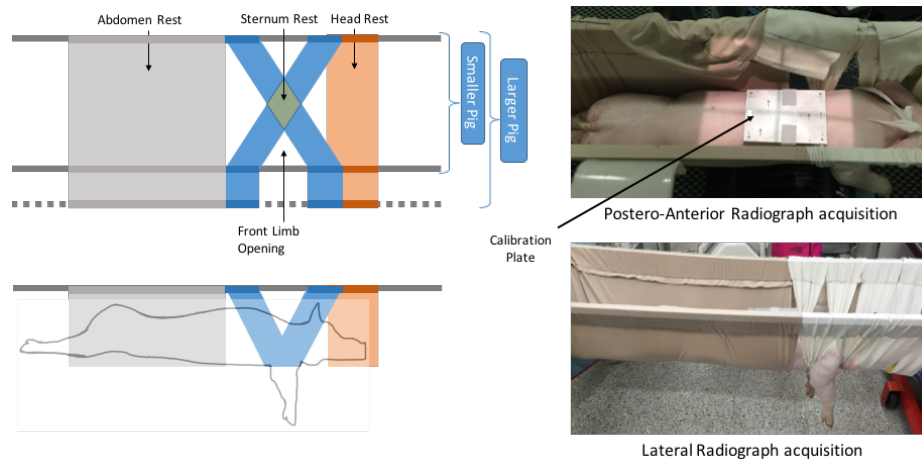


Figure E-1: Custom sling design (Left) and actual prototype (Right)

Finally, since no repositioning is performed between bi-planar views, a calibration plate (Figure E-1) was used to reconstruct the spine using bi-planar retro-projections [199]. Thus, 3D visualization of vertebral body changes can be evaluated over the study period. Preliminary reconstructions were performed; however, results are not presented within the context of this thesis work. All pigs in the dual-epiphyseal trials underwent x-ray imaging using the custom sling and calibration plate. The sagittal profile was measured between T6-T12 in all animals and showed comparable values between animals over 3 months follow-up with no variation over time (Figure E-2). Although no published data is available to obtain a direct comparison of the expected range in sagittal alignment of normal pigs, the measured values were within reported control animals using conventional imaging. Further experiments using this new sling may establish reference sagittal profiles as closely replicating normal quadrupedal stances. Reconstructing the imaged spines may reduce the measurement variations within the current measured values.

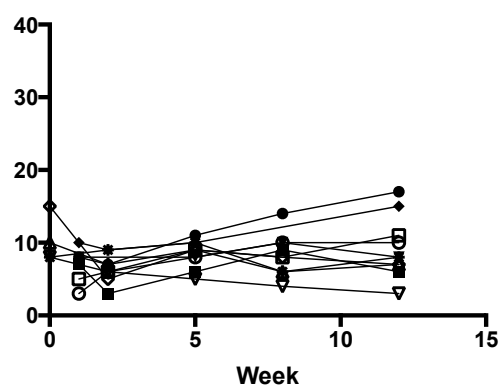
**Constrained Sagittal Cobb Angle All Pigs**

Figure E-2: Sagittal instrumented region angles for all pigs in the dual-epiphyseal trial